THE BEHAVIOUR OF THREE-PHASE SQUIRREL CAGE INDUCTION MOTORS WITH UNBALANCE IN THE ROTOR IMPEDANCE; IN PARTICULAR TWO POLE MOTORS

Itzhak Kerszenbaum

A thesis submitted to the Faculty of Engineering,
University of the Witwatersrand, Johannesburg
for the degree of Doctor of Philosophy
Johannesburg, 1983

DECLARATION

I hereby declare that this thesis is my own work and that no part or substance of it has previously been submitted for a degree at any University

I. KERSZENBAUM

01-07-83

To

my wife and children

Jacqueline

Livnat and Yigal

FOREWORD

It is well known, that in squirrel cage induction motors having non-insulated or partially insulated cages, relatively small inter-bar currents exist. It has been shown[15,30] that these small currents significantly affect the torque-speed characteristic of the motor and also give rise to additional losses. The existing theories, dealing with inter-bar currents, are all restricted to machines with healthy cages, ie with squirrel cages having no broken bars and/or endrings. It is surprising that despite the understanding that has been developed of inter-bar currents and their effects in healthy cage motors, to the best of the author's knowledge no such theory has been proposed for the case of the faulty cage.

The author became aware of certain characteristics in the behaviour of induction motors with faulty cages while working with these machines in industry. This behaviour indicated the possibility that large inter-bar currents were present, because burnt laminations were found, and also large axial and current dependent vibrations were measured. The existing theories do not offer satisfactory explanations of the phenomena observed. Therefore, it was decided that this aspect of the effects of broken rotor-bars and/or endrings, and the associated production of inter-bar currents should be thoroughly investigated. This forms the basis of the research outlined in this thesis.

Tests were conducted on a number of large industrial squirrel cage induction motors having outputs in the range half to one and a half megawatts. Initially these machines were specially constructed with broken cages and a series of measurements were taken. Subsequently the rotors were renewed with complete cages and the measurements were repeated. In this way, complete comparisons of the behaviours were obtained for the machines having both healthy and broken rotor-bars. In addition, laboratory tests were conducted on a number of small motors; in particular on an inverted experimental squirrel cage motor.

The evaluation of the inter-bar impedance is of prime importance to the understanding of the process of the production of inter-bar currents. The equations describing this inter-bar impedance are developed in Chapter 2, as well as in appendices B and C. Chapter 3 describes the methods and techniques used in the experimental measurements carried out on the industrial motors. Also the aims and objectives of these tests are fully disscused. The detailed results of the tests described in Chapter 3 are given in appendices A and D, while Appendix E gives a description of the industrial and the experimental motors. The equations describing the magnitude and distribution of the inter-bar currents are developed in Chapter 4, where the relevant background is also presented. Chapter 5 describes the effects that these inter-bar currents have on the vibration patterns produced by the motors. A new technique for detecting unbalance in the secondary impedance is presented in Chapter 6. It is interesting to note that simultaneously the same technique was proposed by other researchers in the United Kingdom[7]. This approach for fault detection was shown to be viable by both the author and the others, neither having any prior knowledge of the others work.

The basis of the theory regarding the inter-bar currents developed in this work has been accepted for publication by the South African Institute of Electrical Engineers. A later, and more comprehensive paper has been accepted for publication by the American IEEE (Power Apparatus and Systems).

ACKNOWLEDGMENTS

The Author extends his sincere thanks and appreciation to the following people and institutions who in a variety of ways have contributed to the fulfilment of this investigation:

- Professor C.F. Landy of the Department of Electrical Engineering, University of the Witwatersrand, the project supervisor. The advice, guidance, assistance and friendship offered by him throughout the duration of this research project has been invaluable.

- Mr. A.S. Meyer, Technical Director, GEC Machines SA, whose personal involvement and never failing interest made it possible for this project to be undertaken.

- GEC Machines (Pty) Ltd. SA., for building the core of the inverted experimental motor, for allowing the Author to specially modify industrial motor A for the purposes of this research, and for allowing the Author to carry out tests on several other motors.

- The Council for Scientific and Industrial Research, SA (CSIR), for the substantial financial assistance provided. Without this support this project could not have been undertaken.

- Mr. V. Franzsen, for his invaluable assistance in carrying out the vibration tests on both industrial machines.

- Mr. J. de Lima, GEC Machines, for his help with all the technical aspects related to the design and testing of both industrial machines.

- Mr. K. Gray and the workshop staff of the Department of Electrical Engineering of the University of the Witwatersrand, for their help rendered during the course of this project.

Finally I would like to thank my wife, Jacqueline, for her never failing encouragement and support during the course of this project.

LIST OF PRINCIPAL SYMBOLS

Ac	- effective conducting area in rotor-bar due to the 'depth of penetration' effect
B	- flux density
CACA	- cooler-air/cooler-air (type of motor enclosure)
DE	- drive-end side of motor
DOL	- direct-on-line
$\vec{E}$	- electric field (vector)
f	- frequency in Hz unless otherwise specified
f_o	- frequency of the fundamental
fn	- frequency of negative sequence components
fp	- frequency of positive sequence components
fsr	- frequency of pulsation arising from the interaction between a stator produced space harmonic and a rotor asymmetry
ftr	- frequency of currents induced in the rotor
FLT	- full-load-torque
g	- radial airgap length
$\vec{H}$	- magnetic field (vector)
I	- rotor rotational inertia
I1	- primary current per-phase
I2	- secondary referred current per-phase
2.Ib(x)	- actual rotor-bar current flowing in the 'broken' bar at a distance x of the 'healthy' endring
Ibb	- actual current flowing into the 'broken' bar from the 'healthy' endring

In - actual average current flowing in the squirrel cage

It - actual total current flowing in the system comprising the 'broken' bar and the two adjacent bars

$2\Delta Ic(x)$ - actual current flowing from the 'broken' bar into the core at a distance x from the 'healthy' endring

$\delta Ic(x)$ - function of the distribution along the core of the inter-bar current

J - current density

kd - winding distribution factor

kp - coil pitch factor

kws - stator winding factor = kd.kp

kwr - rotor winding factor

km - 'measurement constant', equal to the tangent of the line passing through the points of rotor-bar currents drawn against the primary current for each toroid

ℓ - gross length of core

ℓ' - effective length of core

L - inter-bar inductance

mmf - magneto-motive-force

N1 - number of stator turns in series per-phase

NDE - non-drive end side of motor

OD - overall diameter

p - number of pairs of poles

POT - pull-out-torque

q - order of secondary produced space harmonic

r_e - rotor bar-to-core resistance per unit of core length

R - equivalent radius of rotor-bar

R1 - primary resistance per-phase

R2 - referred secondary resistance per-phase

Rb - rotor-bar resistance

Rc - inter-bar resistance (Rc = $R_{MN}(\theta_0)$.l)

Rcbr - contact resistance between rotor-bar and endring

$R(\theta)$ - resistance of the iron between two points in the periphery of the rotor core (per unit of core length)

$R_{MN}(\theta_0)$ - total resistance per unit of core length between two bars with an angle θ_0 in between them [$R_{MN}(\theta_0) = r_0 + R(\theta_0)$]

rpm - revolutions per minute

n.RPM - `n' multiples of the actual rotor speed

s - slip of the motor

st - slip of the space harmonic of order `t'

S1 - number of stator slots

S2 - number of rotor slots (single cage)

ST - starting torque

t - order of primary produced space harmonic field

Tnett - nett available torque at shaft

Tm - electromagnetic torque (airgap torque)

Tfr - friction torque

Tw - windage torque

Tfw - combined friction and windage torque (Tfw = Tfr + Tw)

U1 - primary phase voltage

UMP - unbalanced magnetic pull

U.V. - ultra violet (for torque-speed measurements)

[illegible] - velocity of the mmf waves existing in the airg p

Vr - peripheral velocity of rotor w.r.t. the stator

Vls - velocity of the fundamental field produced by the stator

Vlr - velocity of the fundamental field produced by the rotor

Vts - velocity of the `t'th space harmonic field produced by the stator

Vqr - velocity of the `q'th space harmonic field produced by the rotor

X1 - primary leakage reactance per-phase

X2 - referred secondary leakage reactance per-phase

Xm - magnetizing reactance

Xb - secondary slot leakage reactance

Xc - inter-bar reactance

Zb - rotor-bar impedance

Zc - inter-bar impedance

Zring - endring impedance

[illegible] - angle between two given rotor-bars

[illegible] - conductivity ($\sigma = 1/\rho$)

μ - permeability ($\mu = \mu_0 . \mu_r$)

μ_r - relative permeability of the material

[illegible] - permeability of free space ($4\pi . 10^{-7}$ H/m)

[illegible] - inter-bar current distribution factor ($1 \pm \sqrt{3|Zb/Rc|}$)

[illegible] - wavelength of the fundamental field

λ_t - wavelength of the space harmonic field of order `t'

ω - angular speed in radians/sec

ω_r - angular speed of rotor

ω_{st} - angular speed of the stator produced space harmonic field of order `t'

ω_o - angular speed of the fundamental field

ϵ - permittivity ($\epsilon = \epsilon_r . \epsilon_o$)

ϵ_r - relative termittivity

ϵ_o - permittivity of free space ($=8,854.10^{-12}$ F/m)

CONTENTS

CHAPTER 1

INTRODUCTION

The earliest record of serious consideration being given to the effects of unbalance in the impedance of the secondary of an induction motor (almost always the rotating member) was in 1896, which is approximately ten years after Tesla and Ferraris invented this machine. This was observed by Gorge[1,2], the so called Gorges phenomenon, where the induction motor runs at half the normal speed when one phase of the secondary circuit is left open. Since then, much has been written on the behaviour of induction machines having unbalanced secondary impedances; the overwhelming majority dealing with wound rotors[2,27,28]. Until fairly recently little interest was shown in the electromagnetic unbalance effects present in squirrel cage rotors. The main reason for this lack of interest was due to the fact that the earlier squirrel cage motors were over-designed, by todays standards (the output per frame size is approximately ten times greater today). Therefore, many vibration problems did not rear their heads due to the lower fields strength used, and also due to the mechanical robustness of the overall structure. Most of the research carried out on the effects of unbalanced secondary impedance of squirrel cage motors, in those times, was confined to the search for some special characteristic (eg Weichsel's[3] work on split endrings to achieve an increase in starting torque).

Nowdays, induction machines have become the prime source of electromechanical energy conversion in modern society; from miniature drives to the large industrial motors well into the megawatt region. Of more recent times synchronous machines are also being used for variable speed drives, previously reserved for DC machines. This has been made possible by modern electronic technology, which in conjunction with the AC machine provides a drive having similar characteristics to these of the DC systems, at very competitive prices. This is particulary true in the case of squirrel cage motors which also offer higher reliability and lower maintenance.

Owing to the higher reliability and lower maintenance requirements, squirrel cage motors form the vast majority of induction machines manufactured. This, coupled to the ever increasing demand for more efficient, less noisy and less expensive (more kW output per kg mass) machines, has created the necessity to look for improvements in places that heretofore have received little attention. The higher, and still growing outputs, obtained from smaller frames has created the situation where the main factors limiting any further increase in the ratio output/mass are mechanical in nature (shaft diameter, bearings, etc), and not electrically related (insulation, current density, etc.). Vibration, which has a direct detrimental effect on material fatigue, has became the subject of intensive study by many researchers. The same can be said about the related noise emission from electrical machines which is coming more and

Nowdays, induction machines have become the prime source of electromechanical energy conversion in modern society; from miniature drives to the large industrial motors well into the megawatt region. Of more recent times synchronous machines are also being used for variable speed drives, previously reserved for DC machines. This has been made possible by modern electronic technology, which in conjunction with the AC machine provides a drive having similar characteristics to these of the DC systems, at very competitive prices. This is particulary true in the case of squirrel cage motors which also offer higher reliability and lower maintenance.

Owing to the higher reliability and lower maintenance requirements, squirrel cage motors form the vast majority of induction machines manufactured. This, coupled to the ever increasing demand for more efficient, less noisy and less expensive (more kW output per kg mass) machines, has created the necessity to look for improvements in places that heretofore have received little attention. The higher, and still growing outputs, obtained from smaller frames has created the situation where the main factors limiting any further increase in the ratio output/mass are mechanical in nature (shaft diameter, bearings, etc), and not electrically related (insulation, current density, etc.). Vibration, which has a direct detrimental effect on material fatigue, has became the subject of intensive study by many researchers. The same can be said about the related noise emission from electrical machines which is coming more and more under the whip of industrial regulations.

Vibration becomes a problem of acute dimension in the case of two pole machines. It is becoming common practice for customers to demand machines with levels of vibration far more stringent that those quoted in the relevant international specifications.

All these factors have now made it important to analyse impedance unbalance effects in squirrel cage rotors. The first authors to investigate this problem only considered faults that are symmetrically distributed around the rotor[4,5]. As a result of this simplification, the mathematical models developed were incomplete in that they do not take account of many phenomena which are likely to occur in reality. The more recent work by Williamson and Smith[6] proposes what is probably the most versatile model published todate. It allows for the current distribution in the rotor-bars to be solved for any kind of cage fault, by means of an impedance matrix in which each of the rotor-bars is represented as well as each portion of the endring between the bars.

The assumption that is common in all the studies so far undertaken on squirrel cage impedance unbalance effects, as described in the literature surveyed, is that there are negligible inter-bar currents present. This means that the cages have been assumed to be insulated. Obviously this assumption greatly reduces the complexity of the problem, but the question arises as to whether this assumption is still valid in the case of modern squirrel cage machines where there is no insulation. The squirrel cages of these machines may be roughly divided into two categories. Firstly the die-cast aluminium rotors used in the smaller machines, where in some cases partial insulation is achieved via oxidation of the aluminium. This process has its own associated problems in that the oxidation is not uniform and this gives large variations in the magnitude of the insulation achieved for different points in the same rotor. Secondly, in the large machines the rotor-bars are tightly fitted into the slots without any insulation in between the bars and the iron, and, as is shown further on, the resulting inter-bar impedance is of similar order to that of the normal rotor-bar impedance. This research is concerned with these machines where the rotor-bars are tightly fitted in the core.

It is shown further on, both analytically and experimentally, that this low ratio of inter-bar to rotor-bar impedance is the cause of large inter-bar currents flowing in non-insulated cages having broken bars and/or endrings. The experimental verification of the existence of these inter-bar currents was achieved by actually measuring the currents flowing in the rotor of a large industrial motor in which a fault was introduced into the cage. Measurements were also taken on an experimental inverted induction motor; and also the damage found in a large motor that had failed due to broken bars was examined. As is shown, the results of these measurements and observations confirms the presence of large inter-bar currents, and also proves the validity of the mathematical model proposed.

Two different approaches could be taken to establish the mathematical model mentioned above that is used to determine the magnitude and distribution of the currents flowing in a faulty cage. The first is to modify that proposed by Williamson and Smith[8] to take account of the fact that the cage is not insulated. This will lead to a very general and elaborate model. The second approach is to concentrate on the currents in the region of the fault. In this project the second approach was followed because, as is shown further on, in the large induction machines the current distribution in the cage away from the fault is no different, for all practical purposes, than that found in a healthy cage. It is in fact only the currents in the few bars adjacent to the fault that are affected.

There are other factors beside cage faults that can give rise to secondary impedance unbalance, namely: non-homogeneous lamination material, poor inter-laminar insulation, shaft keyways, number of `spider' ribs, loose core,etc. The effects produced by these peculiarities are accentuated by the high flux densities existing in the modern induction motors, in particular two pole machines. Obviously it is not easy to implement these anomalies experimentaly, but since the effects they produce are similar to those produced by a faulty cage, only this type of fault was investigated.

It is shown in this project that the presence of large inter-bar currents, which flow tangentially, give rise to several phenomena which can be observed but cannot be explained by the models proposed by the previous researchers. These currents give rise to axial mmfs in the machine which produce abnormally large axial vibrations, which are load dependent. This has been demonstrated by a comprehensive set of vibration measurements taken on a number of large induction motors having faulty cages. Also these inter-bar currents indirectly affect the starting and pull-out torques of the motor. This is so because as a result of the presence of the inter-bar current [illegible] rent must flow into the broken bar. Consequently, the reduction in starting torque is not as large as would normally be expected. It was found by measurements taken on a 475 kW motor (motor A in this work) having a broken bar, that there was no noticable reduction in the starting torque, but the pull-out torque was substantially reduced. This is due to the change in the degree of secondary unbalance with the motor slip.

The increasing volume of work done on the behaviour of squirrel cage induction motors with unbalance in the secondary impedance has been accompanied by an increasing amount of research into developing techniques for detecting rotor faults. The emphasis has been on the detection of faults that are developing, thereby avoiding the excessive damage that usually occurs when the motor finally fails.

The usual techniques used for monitoring whether such faults are present are: (i) to monitor speed fluctuations and torque or current pulsations[7,8], (ii) to monitor electromagnetic noise emission[9,10], and (iii), to monitor the axial flux[10,11,12]. A new technique was developed during the course of this investigation, which entails analysing the spectrum of the primary current, to assess whether there is a cage fault. A simple expression is developed which allows the additional primary current harmonics, which appear when the fault occurs (primary or secondary) to be identified, thereby allowing the source of the unbalance to be pinpointed as being either in the primary or the secondary. The main feature of this technique is that it is independent of any effects that may be introduced by the driven load. Also it is simple to carry out in an industrial environment. It is interesting to note that other researchers in England[7,13] proposed the same technique just two months after this was established as viable in this study. Their research also showed that this method of detection has practical application, but they did not go as far as to actually identify the origin of the respective harmonic components (see Table 6.1 and equations 6.5 and 6.6, page 6.6)

CHAPTER 2

ROTOR INTER-BAR IMPEDANCE AND FLUX DISTRIBUTION IN THE SHAFT

Two basic phenomena associated with the presence of broken bars and/or endrings in the squirrel cage rotor are the production of axial fluxes and inter-bar currents, ie currents flowing between bars through the core laminations. In induction machines, in particular two pole motors, impedance unbalance may arise from the presence of keyways in the shaft or other mechanical asymmetries. This is due to the relatively high flux densities used in modern machines. Hence a pre-requisit for the understanding of these phenomena is to analyse the inter-bar impedances and the flux distribution in the shaft and core.

2.1 - Inter-bar impedance

All authors of previous work related to the performance of induction machines having broken rotor-bars and/or endrings disregarded the presence of inter-bar currents in unskewed rotors. Results of measurements done in this project show that this assumption does not hold for motors with non-insulated rotor-bars. This is also relevant to machines having die-cast aluminium squirrel cages, because imperfections commonly occur during the casting process. These result in an odd distribution in the bar-iron contact resistance around the machine. In particular these machines were studied by Vas[4]. Weichsel[3] developed the theory of a squirrel cage induction motor having symmetrically split endrings. He uses this theory to calculate the new resultant torque developed. Again in this theory the distribution of the rotor-bar and endring currents is evaluated without taking into account any possible inter-bar currents that may flow in the core and thereby bypass the split in the ring.

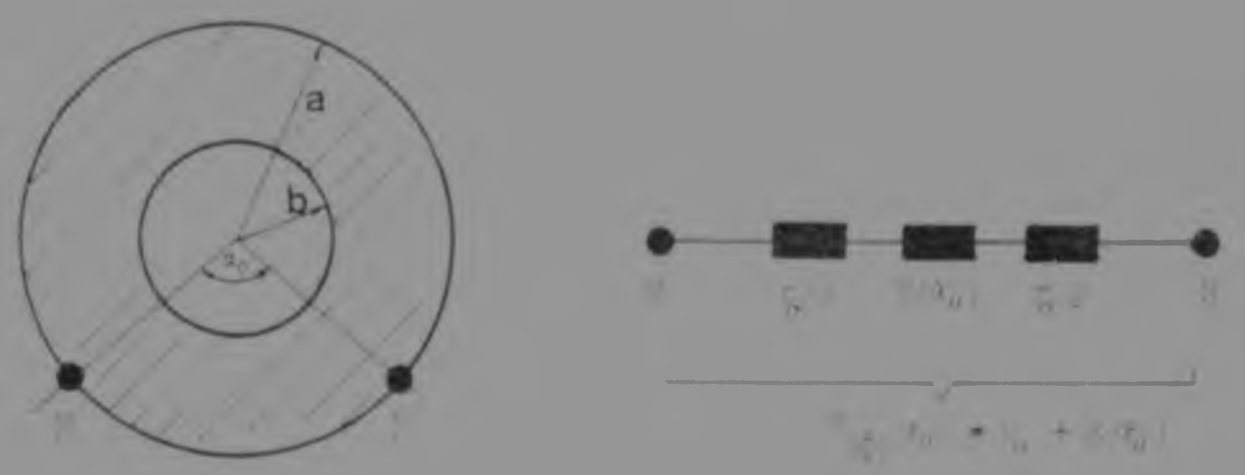

Figure 2.1 - Cross-sectional view of a squirrel cage laminated core with two bars shown as M and N. The equivalent circuit for current flow between M and N is also shown.

$r_\theta/2$ = bar-core resistance per bar per unit of length

$R(\theta_0)$ = resistance of core between M and N pe metre of effective core length

One simple representation of a squirrel cage rotor core is that of an annular shape or ring of magnetic iron with the conductors distributed around the periphery (see Figure 2.1).

An accurate calculation of the inter-bar impedance will have to take into account the bar and slot dimensions and the influence of all other rotor elements, such as keyways, ribs, etc.. This may be accomplished by using one of the several finite element analysis techniques available. However, in this work a general analytical method is developed which yields a first approximation for the actual inter-bar impedance.

The contact resistance is of non-linear nature[15] and depends on the voltage developed across the area of contact (or equally, on the inter-bar current flowing through the area of contact). As is shown by Christofides[15], relatively large inter-bar currents will have to flow before the resistance becomes non-linear. Usually such large inter-bar currents will only flow under run-up conditions in unskewed rotors having a faulty cage. Therefore the contact resistance may be assumed to be linear when the motor is running at rated speed.

The inter-bar impedance is found to be largely resistive for frequencies within the normal operating range of the motor, ie from no load to full load. This was demonstrated by Christofides[15] and also in this project, were similar tests were performed on rotors of relatively large machines (several hundreds of kilowatts).

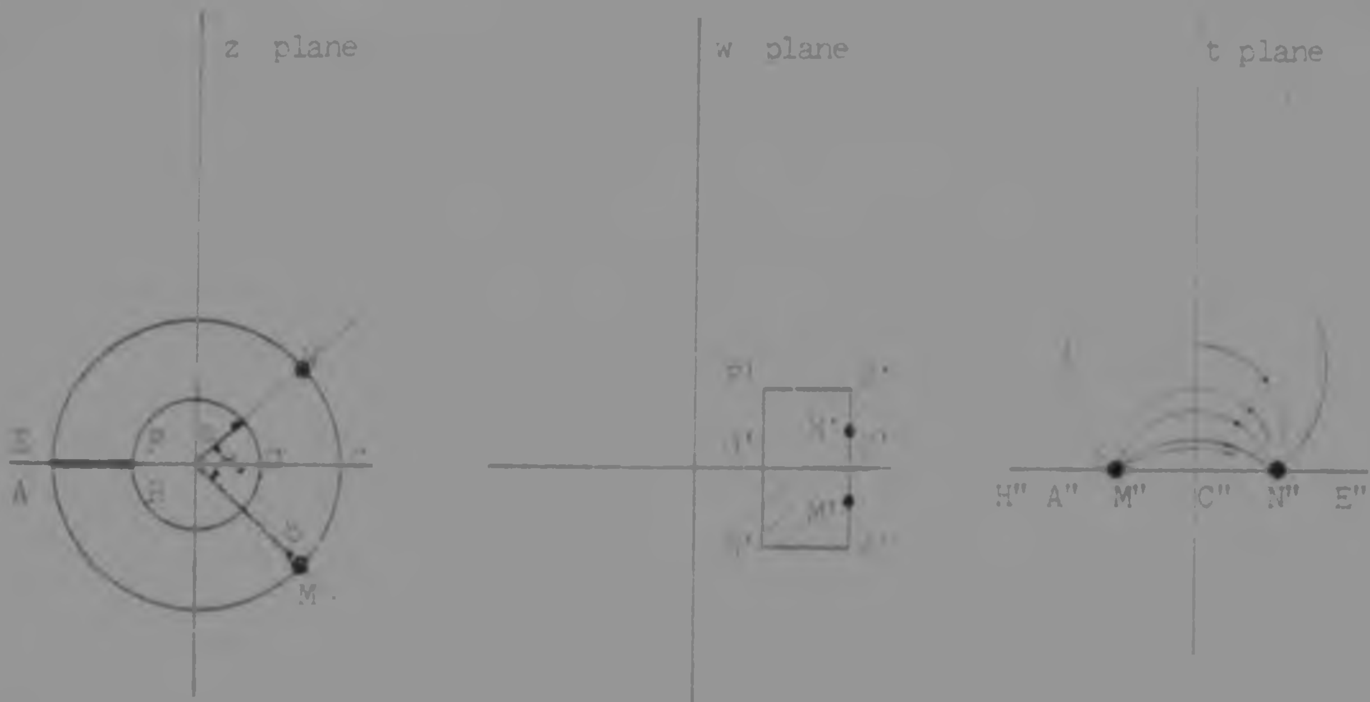

$$w = \ln z \qquad \text{and} \qquad w = \int_0^t \frac{dt}{\sqrt{(1-t^2)(1-k^2t^2)}} \qquad 0<k<1$$

Figure 2.2 - Conformal mapping transformations used to determine the electric field configuration and hence current density distribution in the core between rotor-bars M and N.

As shown in Figure 2.1 the resistance between any two rotor-bars may be divided into the two resistances $r_g/2$ (ie between one bar and the core) and the core resistance $R(r_0)$ between the two bars. (In this analysis $R(r_0)$ has been taken as purely resistive. In certain special cases -eg when higher than normal frequencies are involved- $R(r_0)$ will have a reactive component as well. This is discussed further on in this chapter as well as in Appendix C).

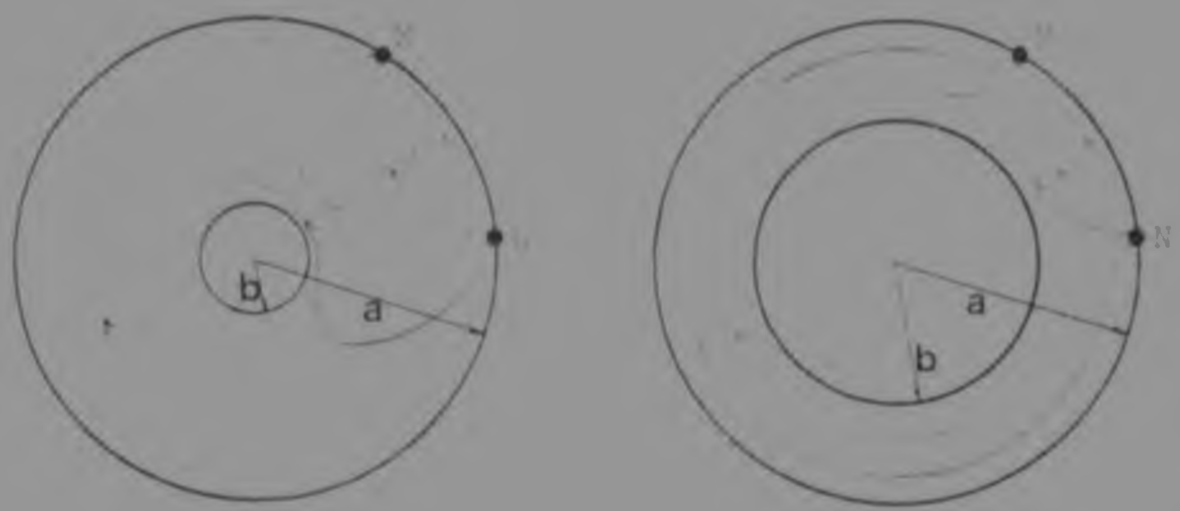

2 pole case multipole case

Figure 2.3 - Schematic diagrams of current density distributions within the rotor core for 2 pole and multipole machines.

An exact analytical solution for determining the core resistance $R(\nu_0)$ may be found by using double conformal mapping transformations (Figure 2.2). This allows the electric field configuration within the laminations to be found and hence also the current density distribution ($\vec{J} = \sigma \vec{E}$) present in the core. This method entails using "elliptic" functions whose solutions are given in tabulated form. This method proved to be cumbersome and thus a more practical approach was devised by dividing the analysis into two cases as follows:

(i) For two pole machines: The rotor cross-sectional area is taken as that of a full circle because the area occcupied by the shaft is small when compared with that of the full area (ie the diameter of the shaft is significantly smaller than the overall outside diameter of the lamination -see Figure 2.3-). As shown in Appendix B, page B.4, based on this assumption the core resistance $R(\alpha_0)$ is given by

$$R(\alpha_0) = \frac{[illegible]}{\pi\sigma} \ln \left\{ \frac{[illegible]}{[illegible]} \right\} \quad \text{(per metre)..[2.1]}$$

where

R = radius of equivalent conductor representing the rotor-bar

$\sigma = 1/\rho$ = conductivity of the lamination material

Hence the total inter-bar resistance is given by

$$R_{MN}(\alpha_0) = 2(r_0/2) + R(\alpha_0)$$
$$= r_0 + R(\alpha_0) \qquad \text{....[2.2]}$$

where $R(\alpha_0)$ is as given in equation [2.1]

(ii) For machines with four or more poles: For these machines the ratio a/b (rotor core outer radius/inner radius) tends to unity as the number of poles increases. Associated with this is the fact that the current density distribution then follows more closely the circumferential paths as shown in Figure 2.3. Because of this, the total core resistance $R(\theta_0)$ between the bars M and N can be given by the parallel combination of the resistances of the two paths between M and N (see Figure 2.3). The accuracy of this approximation for $R(\theta_0)$ increases with the number of poles. Calculations done for several rotors having different number of poles, show that both methods yield similar results when applied to four pole machines.

From inspection of Figure 2.4 the following expression may be written:

$$R(\theta_0) = \frac{\rho}{[illegible]} \frac{a+b}{[illegible]} [illegible] \theta_0 \qquad \text{(per metre)..[2.3]}$$

Therefore the total inter-bar resistance is given by

$$R_{MN}(\theta_0) = r_\emptyset + R(\theta_0) \qquad \text{....[2.4]}$$

where $R(\theta_0)$ is as given by equation [2.3].

2.1.1 - Assessment of the contact resistance ($r_{\emptyset}$)

All the parameters in the above expressions for $R_{MN}(\gamma_0)$ are known for any particular rotor with exception of $r_{\emptyset}$, the bar-core contact resistance. This may be found by comparing the calculated value for $R(\gamma_0)$ and the measured value of the total inter-bar resistance R_{MN}.

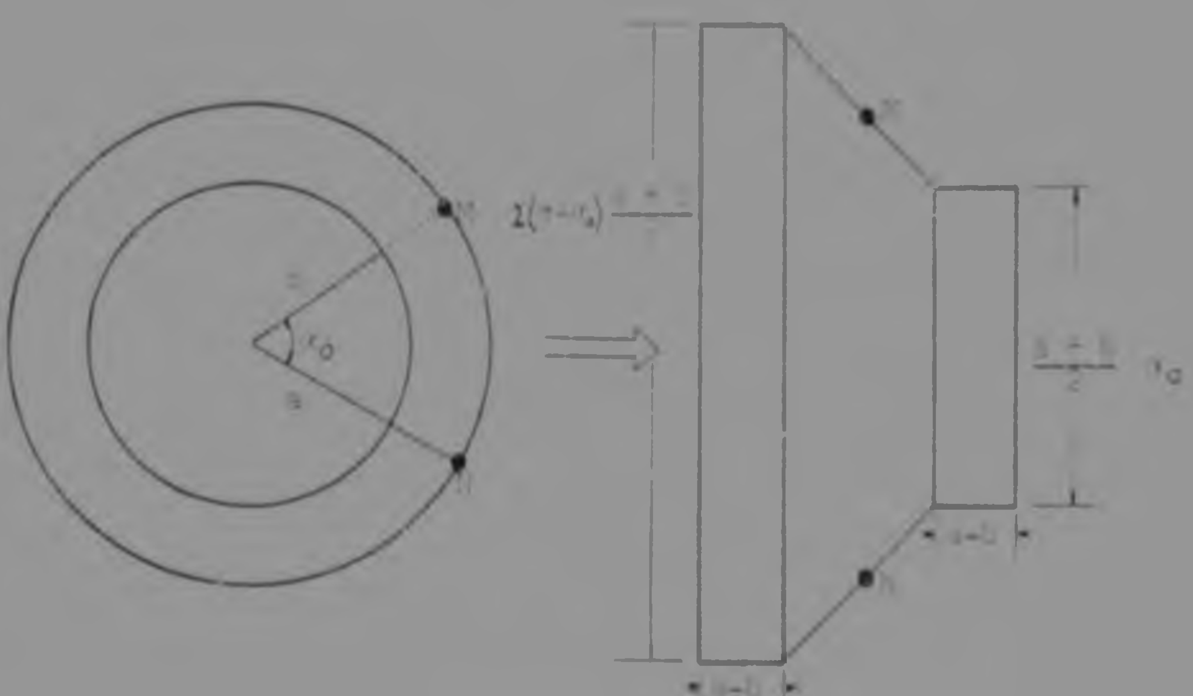

Figure 2.4 - Schematic diagram showing the annular shape of the rotor core for machines having four or more poles.

In order to facilitate the evaluation of $r_{\emptyset}$ measurements of $R_{MN}(\gamma_0)$ were taken on a number of rotors. The resistance was measured at zero frequency on the rotors during manufacture and prior to the fitting of the endrings. It was found that even though the construction of the rotors differed considerably, the resistance value obtained differed very little from rotor to rotor. To illustrate this the results obtained on a two pole rotor and six pole rotor are given below. In both cases the rotor laminations were made from 2% Si steel giving a resistivity of 35×10^{-8} Ωm. The core stacking factor was taken as 0,95.

<u>ROTOR 1 (two pole motor)</u>

gross core length (ℓ) = 0,355 m

effective core length (ℓ') = 0,337 m

$\rho = 0{,}35 \times 10^{-6}$ Ωm

a = 0,151 m; a/b (outer radius/inner radius) = 2

radius of equivalent conductor (R) = 0,017 m

number of rotor slots (S2) = 46

angle between adjacent bars = 7,826 degrees

Table 2.1 - <u>ROTOR A</u>

Measured and calculated values of $R_{MN}(\alpha_0)$ and $R(\alpha_0)$.

Angle between bars M,N in degrees	Measured values of $R_{MN}(\alpha_0)$ for six different pairs of bars chosen at random $\mu\Omega$						Average $R_{MN}(\alpha_0)$ $\mu\Omega$	Calculated value of $R(\alpha_0)$ $\mu\Omega$
7,826	50	50	50	52	47	45	49	0,0
15,652	46	58	55	55	50	50	52	0,2
23,478	55	58	57	57	57	52	56	0,3
31,304	65	55	57	57	52	50	56	0,3
39,130	56	52	52	58	57	52	55	0,4
180,000	46	48	49	49	49	58	50	1,8
bar-shaft	36	34	34	35	35	36	35	---

Table 2.1 shows the measured values of $R_{MN}(\alpha_0)$ and the calculated values of $R(\alpha_0)$ for six different angles (using equation [2.1]). It can be seen from this table that the core resistance is much less than the bar-core contact resistance and therefore it forms a very small portion of the total bar-bar resistance. The average values of $R_{MN}(\alpha_0)$ obtained show some scatter, as expected, but the values of $R(\alpha_0)$ are so small that they are in effect swamped by this scatter. Clearly then, to a good approximation, the bar-bar resistance $R_{MN}(\alpha_0) \approx r_0$. Bearing in mind that the total

bar-bar resistance is the parallel summation of the bar-bar resistance per elemental core length, gives the bar-bar resistance per unit length as:

$$r_\theta \Big|_{\substack{\text{per metre of} \\ \text{eff. core length}}} = R_{MN}(\alpha_0) \cdot \ell'$$

For α_0 = [illegible],826 degrees (adjacent bars)

$$r_\theta \Big|_{\substack{\text{per metre of} \\ \text{eff. core length}}} = 49 \times 0,337 = 16,5 \ \mu\Omega m$$

$$= 17 \ \mu\Omega m \qquad \ldots.[2.5]$$

$$= R_{MN}(\alpha_0)$$

ROTOR B (six pole motor)

gross core length (ℓ) = 0,720 m

effective core length (ℓ') = 0,524 m

ρ = 0,35 x 10^{-6} Ωm

a = 0,22[illegible] = OD/2 - depth of bar - bridge = 0,239 m

b = 0,191 m; a/b = 1,45

number of rotor slots (S2) = 58 slots

angle between adjacent bars = 6,207 degrees

Note: The resistance value of $R(\alpha_0)$ for this machine was calculated using equation [2.3] since it was a six pole motor. In this case the rotor was constructed with a `spider' giving the rotor core thickness as 0,277 - 0,191 = 0,086 m. When the angle α_o is large (bars far apart) the current path in the iron will be in the section below the slots. Therefore when performing calculations the effective outside radius has been taken as the radius at the bottom of the slots. Clearly this assumption breaks down when two adjacent bars are considered because here the current will mainly flow from bar side to bar side. The value for the core resistance in this instance will be less than that when α_o is large and since the core resistance is almost negligible, the error introduced by the above assumption is very small indeed.

Table 2.2 shows measured values of $R_{MN}(\alpha_o)$ and the calculated values of $R(\alpha_o)$ (using equation [2.3]). As before for α_o =6,207 degrees,

$$r_0 \Big|_{\substack{\text{per metre of} \\ \text{eff. core length}}} \approx 18 \ \mu\Omega\text{m} \qquad \text{....[2.6]}$$

$$\approx R_{MN}(\alpha_o)$$

Table 2.2 - ROTOR B

Measured and calculated values of $R_{MN}(\alpha_0)$ and $R(\alpha_0)$.

Angle between bars M,N in degrees	Measured values of $R_{MN}(\alpha_0)$ for six different pairs of bars chosen at random $\mu\Omega$						Average $R_{MN}(\alpha_0)$ $\mu\Omega$	Calculated value of $R(\alpha_0)$ $\mu\Omega$
6,207	30	30	28	35	40	41	34	0,0
12,414	35	35	34	35	36	35	35	0,6
18,621	41	35	34	32	32	35	35	1,0
180,000	42	45	43	42	--	--	43	5,0
bar-shaft	22	26	23	19	25	25	23	---

Obviously $R_{MN}(\alpha_0)$ will differ from rotor to rotor even for identical designs due to the following factors; fit between bars and core, change in the silicon content of the laminations, staggering of the laminations, etc.. Nevertheless, the previous examples show that even with the two rotors which have different constructions, the value of the inter-bar resistance was consistent. Therefore this value of $R_{MN}(\alpha_0)$ can be taken as representative of the inter-bar resistance, at zero frequency, for large industrial squirrel cage induction motors.

The resistance was measured at normal ambient temperatures. (~20°C) A reduction in the value of r_g, and therefore $R_{MN}(\alpha_0)$, may be expected with an increase of temperature due to the higher coeficient of thermal expansion of the copper (or aluminium) bars than the core. This results in an increase in the contact pressure.

2.1.2 - The effect of frequency on the inter-bar impedance

Results of measurements published by Christofides[15] show that the value of the inter-bar impedance is almost independent of frequency for frequencies up to several hundreds of hertz. This implies that the reactive component of the inter-bar impedance is small when compared with the resistive component. This is true for machines with aluminium cages, such as those studied by Christofides, because of the oxidation build up on the bar surfaces giving rise to higher bar/core contact resistances. In the case of the large machines, as in this work, the reactive component of the inter-bar impedance may be, in certain cases, of similar magnitude to that of the resistive component and thus may not be neglected.

In view of the fact that the reactive component of the inter-bar impedance may not always be neglected, it became necessary to develop an expression describing this parameter. This was done by considering two rotor-bars of width a and length b being parallel to each other and spaced h apart. Clearly the two bars are surrounded by laminated ferromagnetic material of permeability μ . This leads to the following expression for the inductance between the two bars:

$$L \cong \frac{\mu h b}{\pi \sinh\left(\frac{\pi a}{2b}\right)} \left\{\cosh\left(\frac{\pi a}{2b}\right) - 1\right\} \qquad [2.7]$$

The detailed derivation of this expression is given in Appendix C together with the approximations necessary when round bars are considered, such as those of the experimental inverted motor. Also the experimental verification of this expression is given in Appendix C, page C.5.

Generally the inter-bar inductance is a function of frequency due to the skinning effects of inter-bar currents in the iron laminations. For frequencies up to 50 Hz the penetration depth in the iron is approximately equal to 0,7 mm. Therefore for frequencies in this range and for laminations of thickness not more than 0,7 mm, the inductance will not vary with frequency. For higher frequencies and for thicker laminations, the value of the inductance will decrease due to the skin effect. The normal working range for the machines considered, and the usual lamination thicknesses used, lie within the fifty hertz and 0,7 mm bounds. Therefore, the expression in equation [2.7] has been simplified by neglecting the frequency dependence.

The actual influence of the inter-bar reactance on the inter-bar impedance must be assessed for each case, especially when higher frequencies are considered (as was the case in the inverted experimental motor). However, it was found from the measurements taken on the large machines, that the <u>magnitude</u> of the inter-bar impedance did not differ significantly from the inter-bar resistance measured at zero frequency. Therefore, for most practical cases, for frequencies up to fifty hertz the measured value of the inter-bar resistance can be taken to be that of the inter-bar impedance.

2.2 - The effect of flux penetration into the shaft

When designing two pole induction motors, designers show a tendency to use the shaft to increase the effective area at the back-of-the-core for the magnetic flux. This is as a result of the lack of space in the back-of-the-core in rotors of two pole motors, due to the high curvature present in these machines[17]. This would not represent a problem on its own, but the presence of keyways in the shaft (for attaching the core to the shaft), introduce restrictions in the path of the flux. These restrictions, which are distributed around the machine, may give rise to a net circumferential flux, see Figure 2.5, which is the source of vibrations, torque fluctuations, shaft voltages, etc..

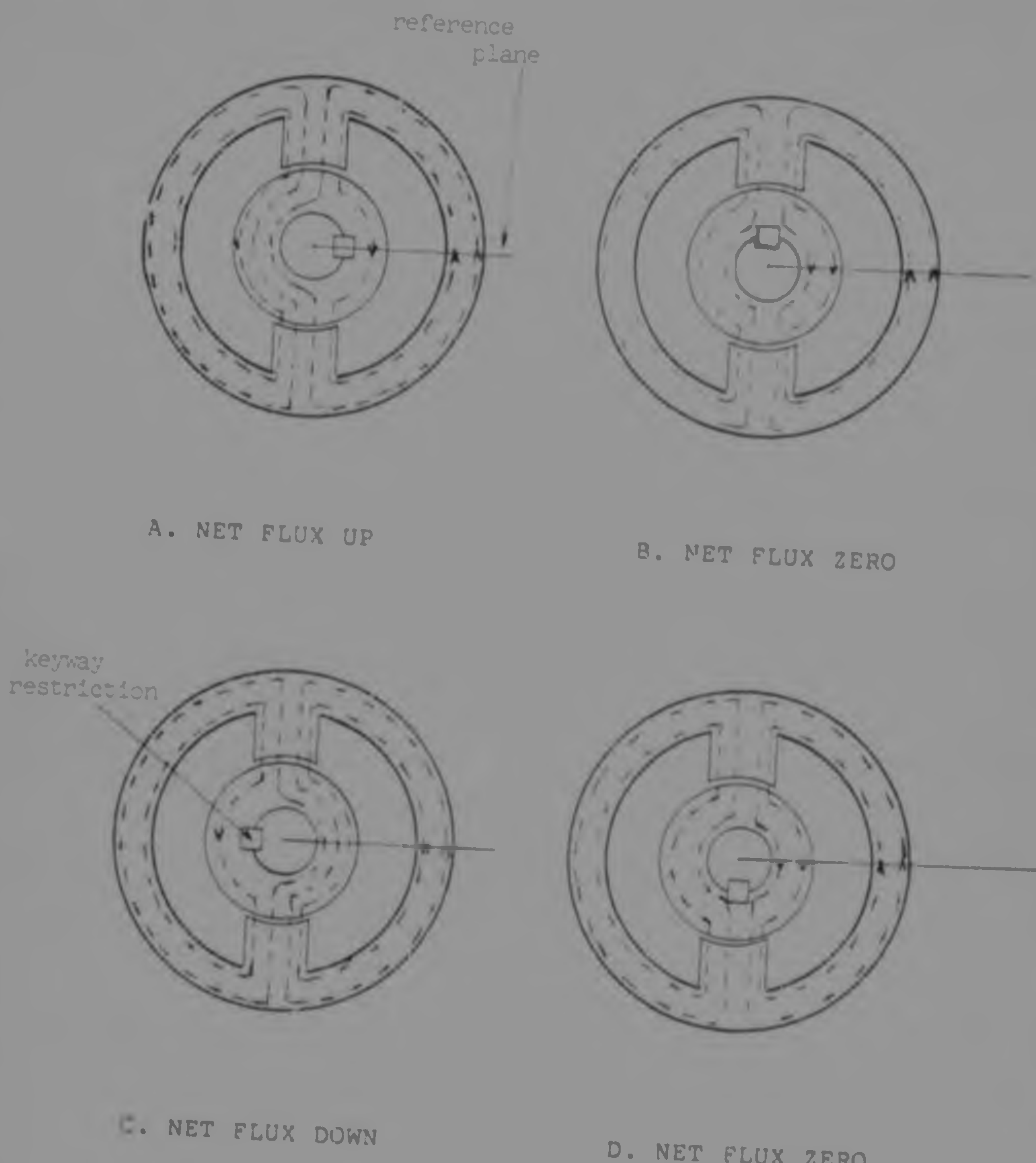

Figure 2.5 - Flux patterns for single restriction in rotating core and shaft, drawn for successive positions of rotation of a two-pole D.C. machine. (After Stringer[16])

Stringer[16] showed schematically how keyways and "spiders" produce a net circumferential flux. It is shown that in the case of 'n' multiple restrictions equally spaced around the shaft/core the following applies:

(i) If the numerator of the ratio n/p (p = pairs of poles) reduced to its lowest term is even, then no net circumferential flux is generated.

(ii) If the numerator is odd, net circumferential flux is generated having a frequency equal to that of the fundamental flux multiplied by this reduced numerator and the slip of the motor.

(iii) When n/p = 1 the generated circumferential flux is a maximum (other things being equal) and its frequency is that of the fundamental flux times the slip of the motor.

In the case of the large industrial two pole motors tested having only one keyway each in the shaft the equation gives:

$$n/p = 1/1 = 1$$

This corresponds to the worst case for the generation of net circumferential flux with a frequency equal to the fundamental times the slip of the motor.

Another effect of the presence of net circumferential flux is the uneven saturation of the iron. This gives rise to an unbalance in the secondary impedance, due to the leakage reactances being different around the machine. The degree of this unbalance is negligible when compared with the unbalance produced by a faulty cage, as it is shown in Chapter 5. Nevertheless, this unbalance is the source of undesirable phenomena, in particular in two pole machines running with relatively high slip and high flux densities.

CHAPTER 3

MEASUREMENTS PERFORMED ON THE INDUSTRIAL MACHINES

A description of the tests and measurements carried out on the industrial motors, as well as an account of the aims and objectives of each of the tests is given in this chapter. The actual results obtained from the tests are given in Appendix D, and these are fully discussed in the following chapters.

The tests carried out on the industrial motors were adapted to the particular constructional characteristics of eacn motor. Also the tests were tailored to fit in with the normal manufacturing schedule.

The essence of the present research (to study the behaviour of induction machines with unbalance in the rotor impedance), required that the test machines be almost perfectly balanced electromagnetically and mechanically, besides the asymmetries intentionally introduced for the purpose of this study. The motors chosen for the tests had symmetrical stator windings the particulars of which are given in Appendix E. These consist of pre-moulded "diamond" type coils wound in an integral slot/pole/phase (s/p/p) arrangement. The winding is double layer with a narrow phase belt distribution. The stator bore was carefully machined to ensure that the airgap was concentric to the geometric centre of the laminations. This ensured that the tooth-lip dimension was kept constant around the stator. The rotor was also carefully machined and balanced and special care was taken during all stages of manufacture and assembly to ensure symmetry. The motors were supplied from a synchronous generator via a step-down transformer loaded only with the motor under test. In this way it was possible to ensure that the supply to the test motors was balanced and was free from mains borne disturbances.

3.1 - Tests on industrial motor A

One bar of the cage of this motor was cut short from one of the endrings to introduce a `broken' bar and with it secondary impedance unbalance, see figures 3.2 and E.5 pages 3.5 and E.5 respectively. Subsequently the endring was removed, all the bars were machined to the normal length and the endring replaced. This then allowed measurements to be taken on a healthy cage. The bar that was actually cut was chosen to be that bar which lined up with the keyway in the shaft extension thereby allowing its position to be readily identified.

3.1.1 - Measurement of the locked-rotor rotor-bar currents

This test was carried out to measure the actual currents flowing in the `healthy' rotor-bars at various peripheral positions from the `broken' bar. Also the current flowing into the `broken' bar from the `healthy' side, ie the side brazed to one of the endrings, was measured. It is very difficult to measure the squirrel cage currents when the rotor is rotating. Therefore direct measurement of the rotor-bar currents in the industrial motor was done only with the rotor at stand-still. However the actual cage currents were measured with the motor operating in the inverted-geometry experimental motor as explained in Chapter 4.

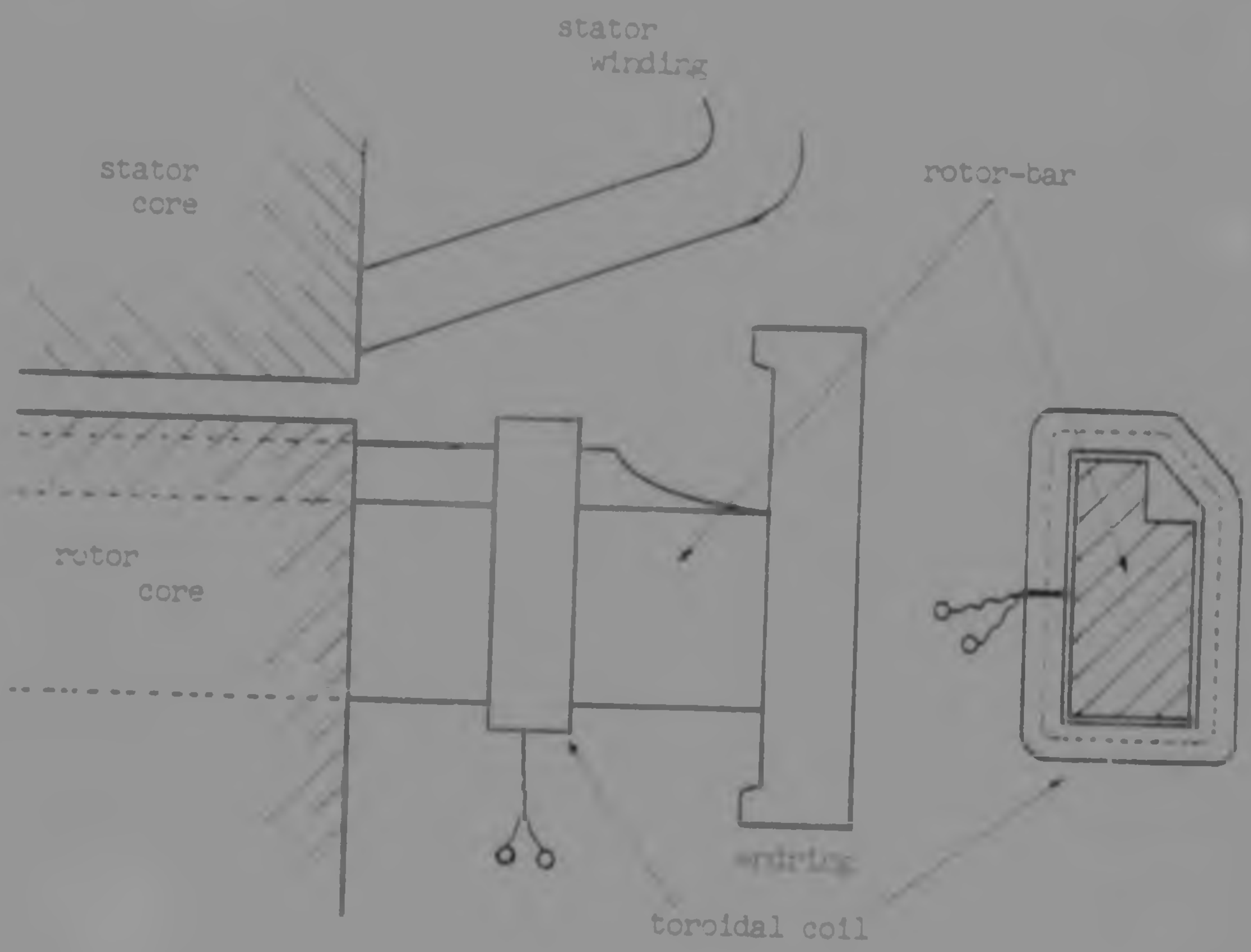

Figure 3.1 - Location of the toroidal coils on the rotor-bars for the measurement of the rotor-bar currents at stand-still.

The secondary bar currents were measured by using

Rogowsky transducer coils. Toroidal coils having approximately 300 uniformly wound turns were constructed on flexible PVC sleeving and then secured around the bar with the ends butting together. Care was taken to thread the return wire back down the centre of the PVC tube because only one layer was wound. The coil outputs were fed to an integrator giving an accurate reproduction of the current waveform. An assessment of the performance of this method is given by various authors[19,20,21,22] and has been used very successfully[20]. Landy[20] and Ellison[21] show by different techniques that the toroidal coils are largely insensitive to currents other than those flowing in the conductor around which the toroid is wrapped. Also the coils are insensitive to currents flowing in conductors that are not parallel to the conductor of concern. Ellison[21] found a maximum interference of less than 0,03 % at an angle of 120 degrees. This interference can be expected to be even less than the 0,03 % when the return wire is brought back through the centre of the tube as was done in the course of the present measurements. From the above it can be safely assumed that the toroidal coils were free from interference from currents flowing in conductors other than their own conductor and also from currents flowing in the adjacent short circuit endring.

Each of the five manufactured toroidal coils was calibrated by initially wrapping it around a similar bar to those used in the motor. Subsequently known sinusoidal currents were passed through the bar and the output of the integrating circuit was monitored. The details of the measuring systems are given in Appendix A together with the calibration constants obtained for all the coils used. Figures 3.1 and 3.2 show the typical constructic and positioning of the coils on the rotor and on the different bars.

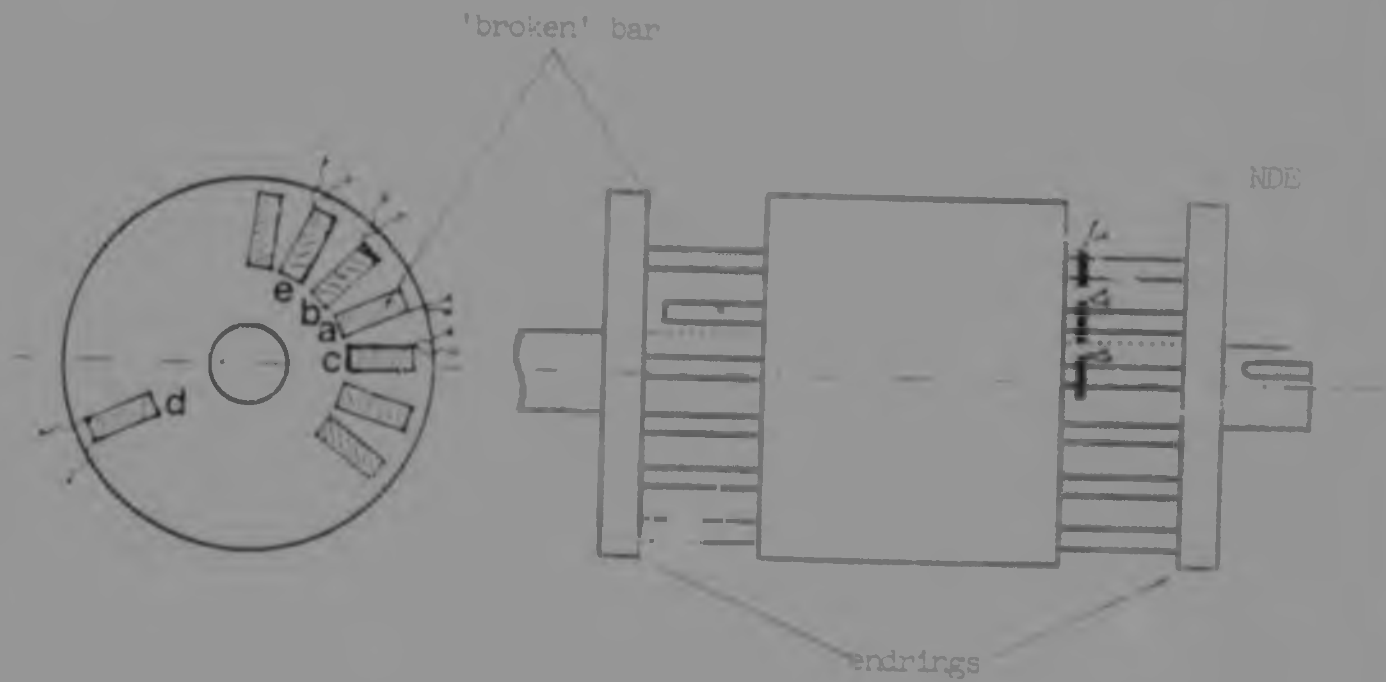

Figure 3.2 - Industrial motor A - The toroidal coils were fitted on five different bars, positioned as shown, next to the core on the NDE side of the motor. The unbrazed side of the `broken' bar is on the DE side next to the endring.

The output of the amplifier/integrator was fed into an oscilloscope, a spectrum analyser and a voltmeter. Both the oscilloscope and the spectrum analyser have the facility of storing the traces so that photographic records of the actual current waves shapes and spectra could be taken. Typical examples of these records are shown in Appendices A and D, pages D.16 and D.18.

3.1.2 - Effect of temperature on the rotor-bar resistance

The measurements of the currents in the five rotor-bars having toroids were taken consecutively. Clearly there was a time lapse between measurements and consequently the bar temperatures must have been different for each of the measurements. As all these current magnitudes were to be compared it was important to establish how the temperature differences affected these magnitudes. The following analysis verifies that in fact this introduced a negligible error.

During the locked rotor test the impedance seen by the supply is mainly inductive. The change in the resistance of the stator winding is negligible as the rise in temperature of the stator copper is well below that of the rotor-bars. To assess the expected temperature rise of the rotor-bars the curves in Figure 3.1 were ploted which show the adiabatic temperature rise of the conductors when the rotor is locked. The equation describing the behaviour of these curves takes into account the skin effect in the bars and assumes that the whole section of the bar absorbs the heat generated. It does not take into account any heat dissipation to the surrounding environment and as such it gives a pessimistic result. The time for each measurement was approximately 30 seconds and the current in each bar was measured six times; twice at 25 Amps primary current, twice at 50 Amps and twice at 75 Amps. Taking into account the time elapsed between each measurement and in particular between measurements taken on different bars, the estimated maximum temperature rise was 50 degrees Celsius.

The increase in resistance for a 50 degrees temperature rise of copper is approximately 12 % for an ambient temperature of 20 degrees Celsius. Figure 3.4 shows the elementary equivalent circuit for stand-still conditions for industrial motor A. The values used for the resistances and reactances were obtained from computer calculations for this machine and were supplied by the manufacturer. From Figure 3.4 it is seen that a 12 % increase in the secondary resistance causes the current to change by approximately 0,4 %. The values of the reactances used in the circuit of Figure 3.4 are for saturated conditions at rated voltage. The tests were performed at reduced voltage where saturation is negligible. Therefore the actual values of the reactances must have been larger than those used and as such the change in the current was smaller than the 0,4 % calculated above.

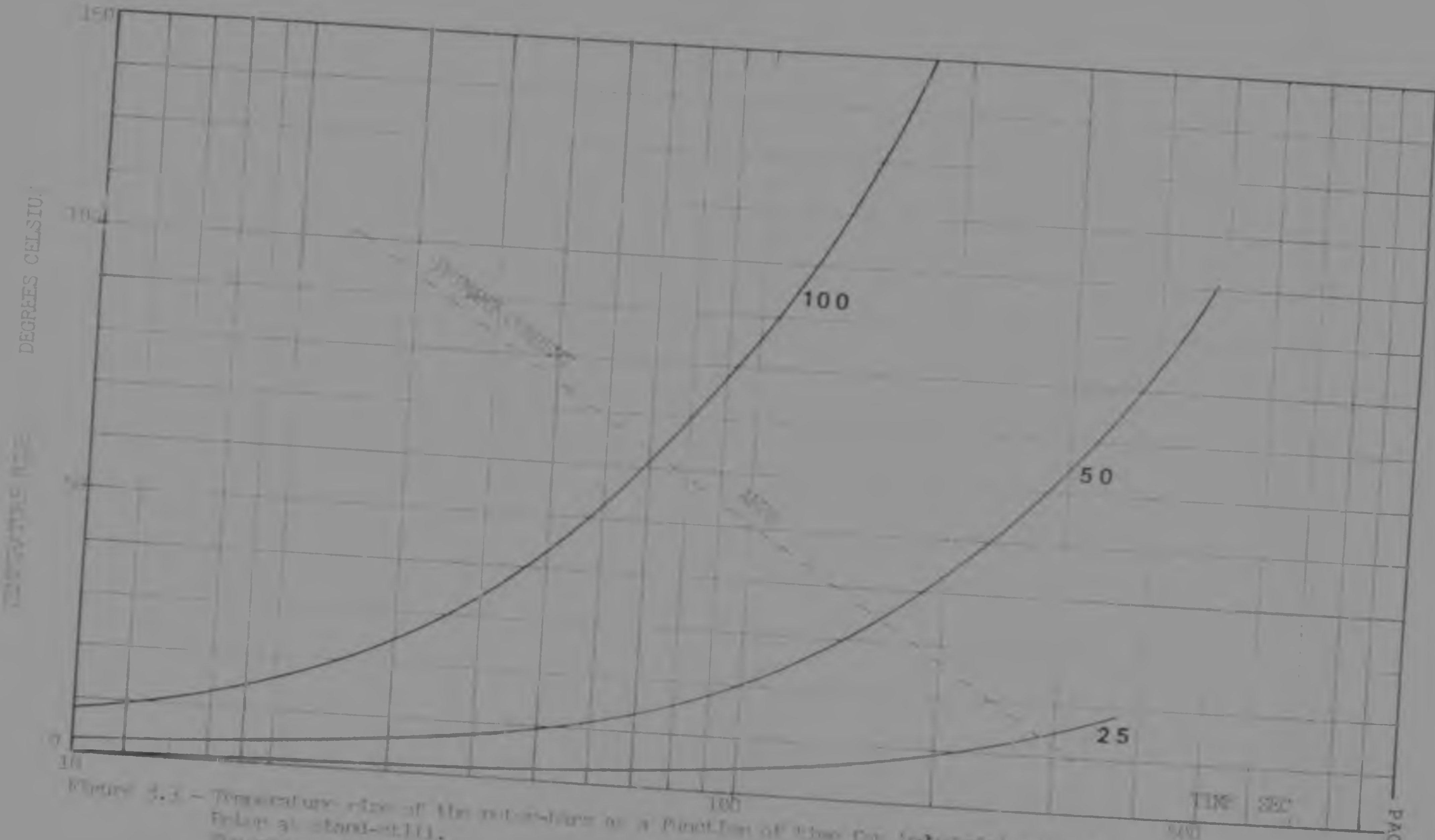

Figure 3.3 – Temperature rise of the rotor-bars as a function of time for industrial motor A (rotor at stand-still).
The curves are drawn for three different values of the primary current.

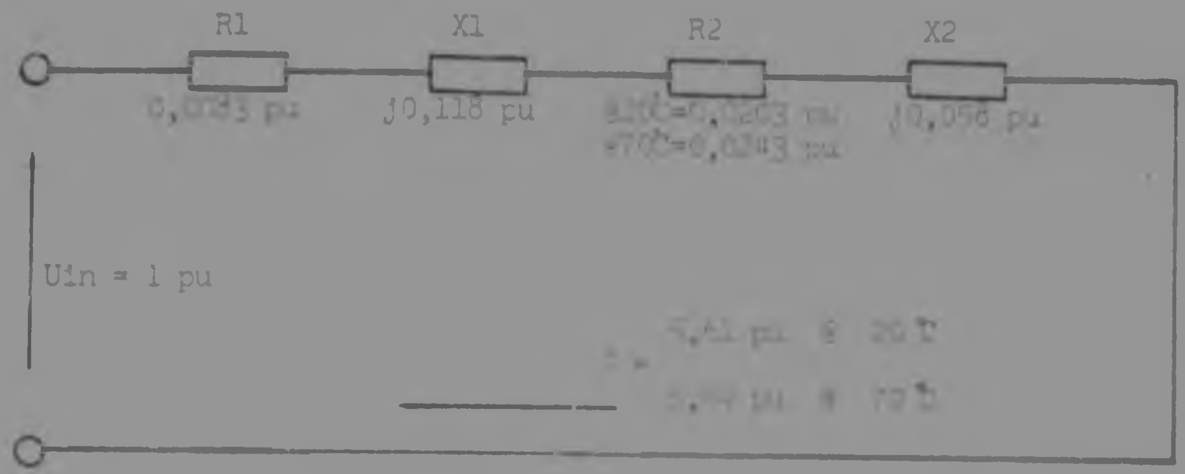

$$\text{Change in } I = \frac{I(@\ 70\,^{\circ}C) - I(@\ 20\,^{\circ}C)}{I(@\ 20\,^{\circ}C)} \times 100 = 0{,}36\ \%$$

Figure 3.4 - Simplified equivalent circuit for stand-still conditions for industrial motor A. The change in $|I|$ for a 50 °C rise in temperature is approximately 0,4 %.

3.1.3 - Locked-rotor torque measurement

The objective of the locked-rotor torque measurement was to assess the influence of the rotor impedance unbalance on the magnitude of the starting torque. These results were also used to calibrate the measured torque-speed characteristic of the machine.

There are two methods of determining the starting torque and both were used and the results compared.

(i) <u>The direct method:</u> The starting torque is measured by means of a torque-arm and a scale.

(ii) <u>The indirect method:</u> The starting torque is calculated from the input power measured during the test after the stator copper and other losses have been subtracted.

In the indirect method the assumption is made that the total power transferred to the rotor is the input power minus the stator losses and this is responsible for the production of the torque. This method does not take into account the stray losses. Nevertheless an empirical factor for stray losses is introduced (see Appendix D, page D.19). This factor, which is based on experience from measurements taken on a large number of motors is found to improve the predictions and gives good correlation with the values obtained from the direct method. When taking measurements using the direct method, in the case of motors having anti-friction bearings (as is the case with industrial motor A) the static friction force may be safely disregarded. This is not the case with motors having sleeve bearings (as with motor B). In this case the stiction may become appreciable when compared with the starting torque, a fact which may introduce significant differences between the calculated torque value and the measured value. This is particularly acute when the locked rotor test is done at a very reduced voltage, as was done with industrial motor B.

The use of reduced voltage for the measurement of the starting torque was necessary because of practical limitations, eg over-heating, torque-arm and scale limitations, etc.. The values measured were then related to full voltage by the square of the ratio Vrated/Vtest . This does not take account of saturation effects, but as all torque measurements, including the torque-speed characteristic, were done at reduced voltage, the conditions of saturation were similar to all of them. These tests were performed twice, once with the `broken' bar and then again when the cage had all the bars perfectly brazed to the endrings. The actual results obtained from the measurements are given in Appendix D.

3.1.4 - Vibration measurements

As with the locked rotor tests, all vibration tests were also done twice, once with the `broken' bar and once with the `normal' cage. The equipment used for the vibration measurements consisted of a velocity magnetic contact probe (pick-up), a vibration meter, an X-Y recorder, and a stroboscope.

Basically the sources of vibration in electrical rotating machines can be subdivided into two categories, namely, those produced mechanically and those produced electrically. In most cases the sources of vibration are interrelated and it is difficult to determine the origin as being either electrical or mechanical. However, vibrations due to impedance unbalance can certainly be classified as electrical in origin. A typical example of vibration being both electrical and mechanical in origin is that produced due to Unbalanced Magnetic Pull (UMP). This is so because when no excitation is applied even if the airgap is eccentric, no vibration occurs. Bearing misalignment or mechanical unbalance on the rotor will give rise to vibration when the rotor rotates even if the machine is not excited and as such these vibrations are mechanical in origin.

Clearly the magnitudes of the vibrations due to the various sources are dependent on certain parameters, such as voltage, current, speed, temperature, etc.. Therefore to identify the different origins, where possible, measurements were taken with several of the parameters changed, eg different voltages, different loads, etc.; see results in Appendix D.

Figure 3.5 shows the locations on the industrial machines where the vibrations were measured. As shown, measurements were taken in the vertical (V), horizontal (H) and axial (A) directions on both the NDE and DE sides.

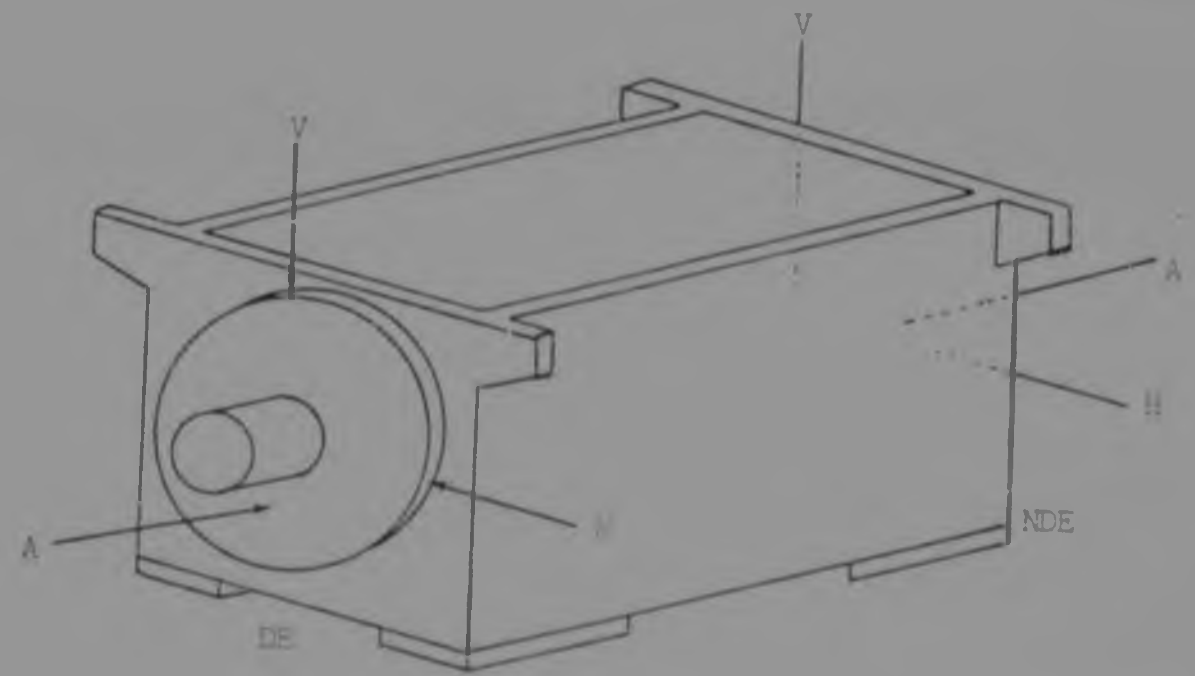

V - Vertical
H - Horizontal
A - Axial

Figure 3.5 - Position of vibration measurements used for both industrial motors.

Note: Industrial motor A had a locating "ball" bearing on the NDE side and a "roller" bearing on the DE side. Industrial motor B had non-locating "sleeve" bearings on both sides.

3.1.5 - No-load vibration measurements (motor uncoupled)

The objectives of the vibrations test were:

(i) to identify those vibrations of mechanical origin and

(ii) to identify those vibrations as a result of

UMP.

Vibrations of mechanical origin are largely due to the physical unbalance of the rotor, bearing misalignment and induced vibration from the outside enviroment. During the no-load test the motor was uncoupled from the load and therefore induced vibrations through the shaft were not present. Induced vibrations through the foundations were negligible and thus only internally produced vibrations were present. The internal vibrations of mechanical origin are, by and large, only dependent on the running speed of the motor. The UMP dependent vibrations are basically sensitive to changes in voltage. Generally when the voltage varies the speed of the induction motor does not change significantly (especially when the motor is running uncoupled). Therefore vibrations that are of mechanical origin will not be dependent on voltage. However, large changes in UMP induced vibrations will result by changing the voltage. Therefore when the motor is run uncoupled and the voltage is varied, it is possible to separate the vibrations due to UMP from those of mechanical origin.

As it is shown further on, vibrations produced by having a broken bar or endring in the cage are only dependent on the actual rotor-bar currents. Also it is shown that these vibrations increase dramatically with increased bar currents. However, when the machine is run uncoupled, the bar currents are very small and remain so even if the voltage is varied (except when the voltage is very low which was not the case during the course of these measurements). Hence, when the motor was run under these conditions, the vibrations produced by the 'broken' bar were negligible, so that no-load vibration measurements were only done once, ie when the machine was tested with the 'broken' bar. It is worthy to note that no-load tests were carried out on identical motors that obviously had 'healthy' squirrel cages. The results of these tests confirmed that the 'broken' bar has practically no effect on the vibration pattern of the machine <u>at</u> <u>no-load</u>.

3.1.6 - <u>Vibration measurements on load</u>

As previously discussed, when a rotor-bar is broken and the rotor current is large (machine on load), the vibrations produced likewise are large. Therefore to assess this phenomenon the motor was coupled to a load which could be varied. The UMP induced vibrations were essentially kept constant because the voltage applied to the motor was kept constant. Also, as the motor speed changed very little with changes in load (motor only partially loaded because the vibrations were already excessive, see vibration recordings, Appendix D) the charges in mechanically induced vibrations were very small.

Measurements were taken of the vibration levels present in the gearbox which was used to couple the motor to the load. It was found that these vibration levels were far lower than those measured on the motor (see figures D.28 and D.29, pages D.59 and D.60 respectively) and therefore the driven machinery had very little effect on the vibrations measured on the motor under test.

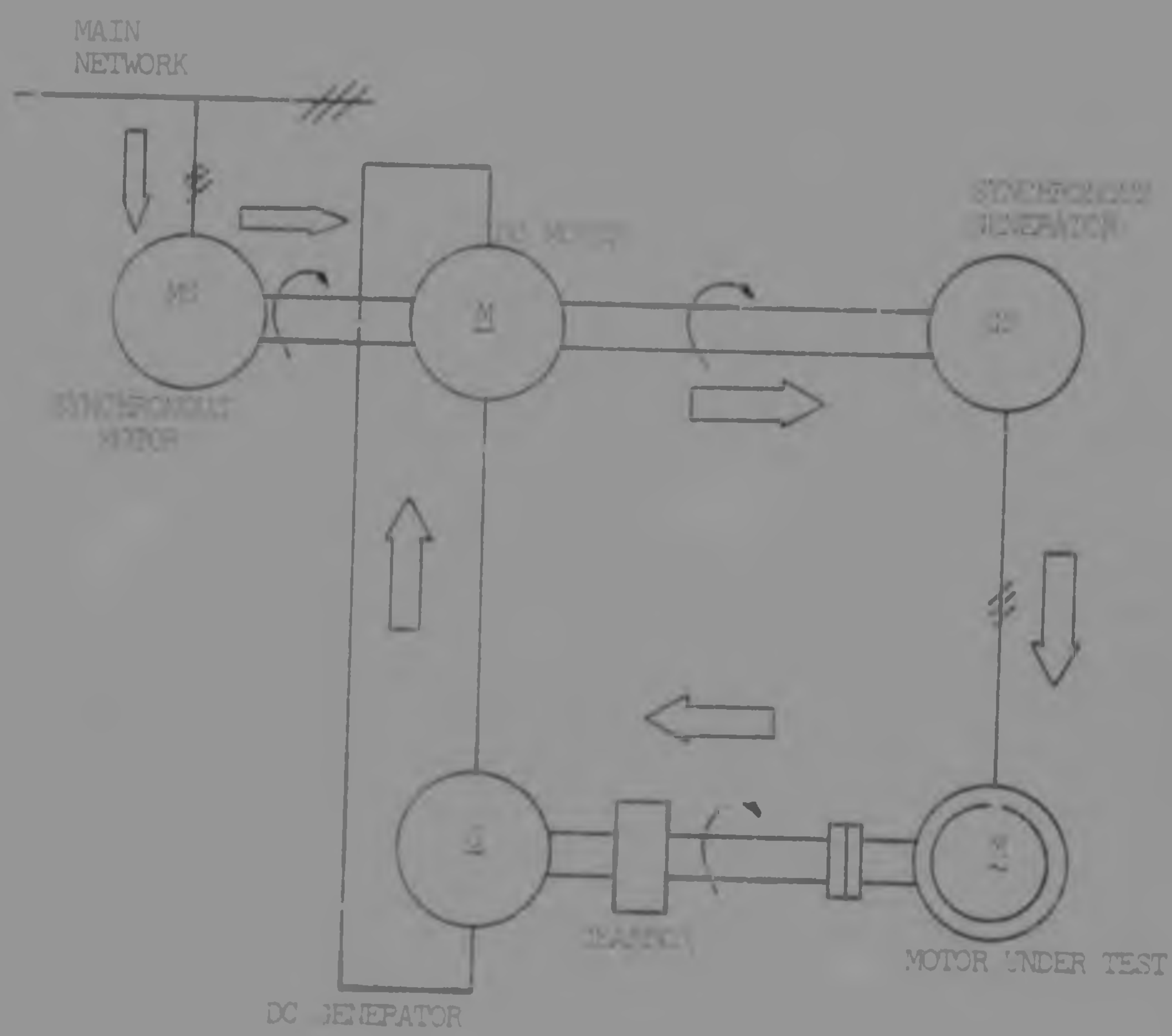

Figure 3.6 - Schematic layout of the test system used to do the load tests. The large arrows show the active power to and from the motor under test. The small arrows show the active power supplied by the main network which is only that required to overcome the losses in the system.

The driven equipment consisted on a DC generator coupled to the motor under test via a gearbox. The load on the motor was changed by changing the field of the DC generator. The test system used forms a closed loop, see Figure 3.6, where the motor under test drives a DC generator via the gearbox. The output of the DC generator is feed back to the DC busbar so the power drawn from the main supply is only that required to overcome the losses.

3.1.7 - Measurement of the torque-speed characteristics

The circuit used for the measurement of the torque-speed characteristics was developed and successfully used by Landy[22]. It was adapted from the system originally developed by Metropolitan Vickers Electr. Corp.[23]. The method is based on the fact that if an electrical motor accelerates slowly, ie the acceleration time is much smaller than the electrical time constants of the motor, then for all practical purposes the currents and fluxes are always in the sinusoidal steady state and the torque produced at every speed is the steady state torque. To achieve long acceleration times the tests were done at reduced voltage and the motor was allowed to decelerate and accelerate against its own rotor inertia. The measuring circuit used is shown in Figure 3.7 and the frequency response of the circuit in Figure 3.8.

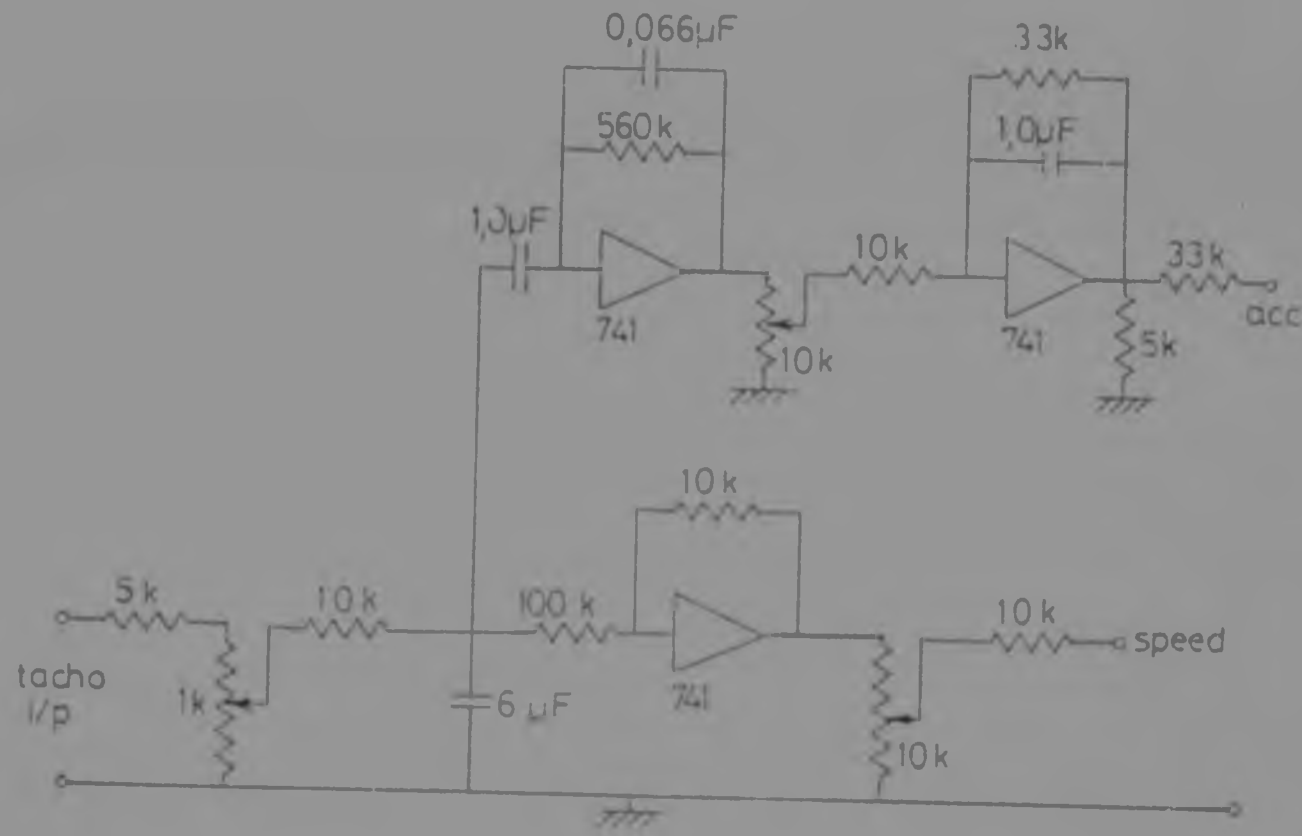

Figure 3.7 Circuit diagram of unit developed for measurement of speed and acceleration of large practical motor. (After Landy)

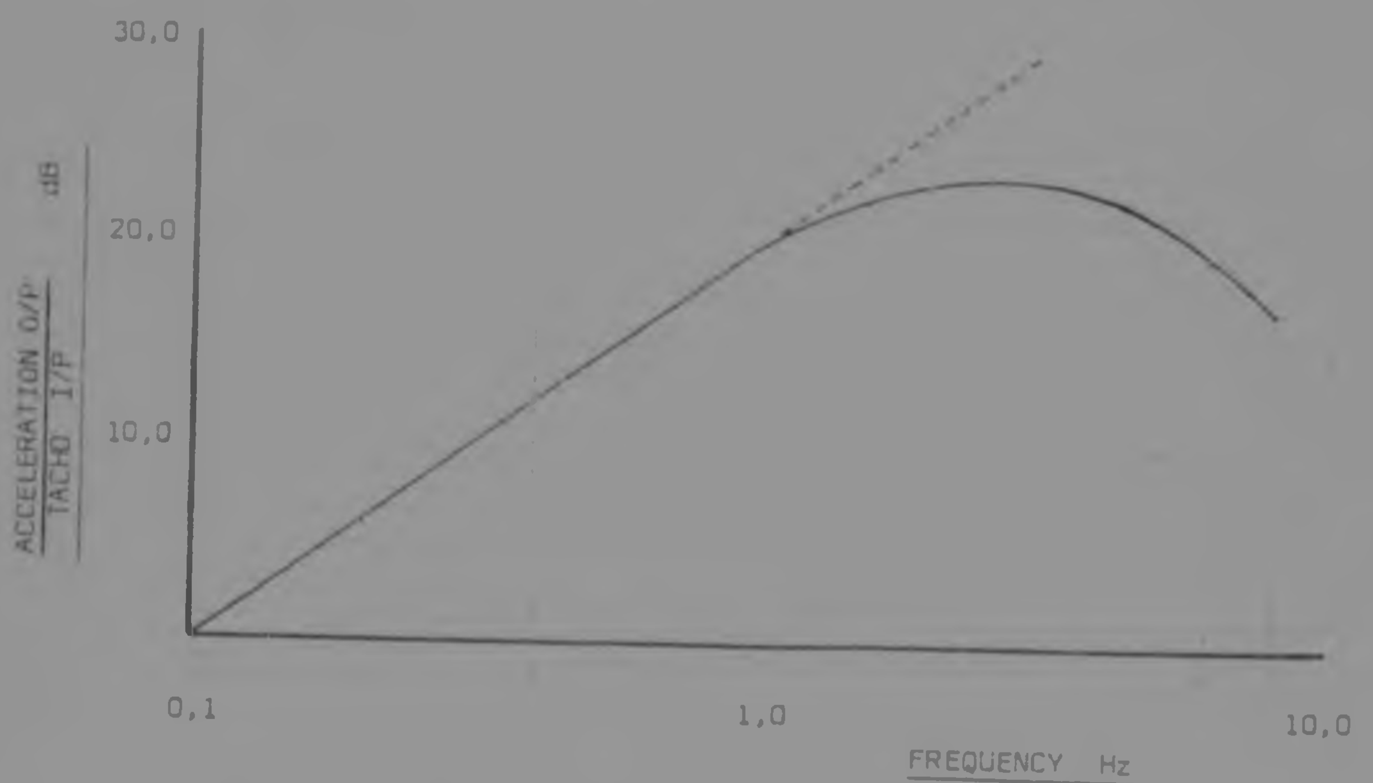

Figure 3.8 Frequency response of acceleration system taken with the input signal applied to the TACHO input terminals. The bandlimited differentiator properties are clearly shown.
(After Landy)

The system basically comprises a tachometer which is coupled to the shaft of the motor under test. The output is filtered for high frequency noise and differentiated. The low-pass filter output gives a direct measure of the speed and the output from the differentiator gives the acceleration. Both speed and acceleration are recorded on an Ultra violet (U.V.) recorder from which the torque-speed curve is reproduced. An assessment of the whole circuit is given by Landy[24]. Using this apparatus torque-speed characteristics were taken both with one `broken' bar and with all the bars normally brazed. (the actual measured traces obtained are given in Appendix D, page D.63).

3.1.8 - Friction and windage effects on the torque-speed measurements

The mathematical expression describing the motion of the rotor with the machine running light (uncoupled) is given by:

$$T_{nett} = T_m - T_{fr} - T_w = I\frac{d\omega}{dt} \qquad \text{....[3.1]}$$

for $0 < s < 1$ (motoring region)

and

$$T_{nett} = T_m + T_{fr} + T_w = I\frac{d\omega}{dt} \qquad \text{....[3.2]}$$

for $1 < s < 2$ (braking region)

where

T_{nett} = nett accelerating torque

T_m = electromagnetic torque (airgap torque)

T_w = windage torque

Tfr = friction torque (approximately constant for all $s \neq 1$)

I = rotor rotational inertia

s = slip of the motor

ω = angular speed of the motor

Equations [3.1] and [3.2] can be reduced to one equation

$$Tnett = Tm \pm Tfw = I \quad \text{for } 0 < s < 2 \qquad ....[3.3]$$

where

$$Tfw = Tfr + Tw$$

and the sign of Tfw is positive for $1 < s < 2$

negative for $0 < s < 1$

For the point $s = 1$ the windage torque is zero and the friction torque is the static friction torque which is different from the dynamic friction torque. As this only occurs at one point and is an instantaneous transitional effect, it may be disregarded for all practical purposes with regard to these measurements.

The speed signal ($\propto \omega$) and acceleration signal [$\propto (d\omega/dt)$] obtained from the measurement system were recorded on an UV recorder . From this an XY plot of acceleration vs speed is obtained as illustrated in Figure 3.9.

Figure 3.9 - Typical acceleration-speed characteristic obtained from the measurements recorded on the UV recorder

As explained above the test is done at reduced voltage. The electromagnetic torque varies as the square of the applied voltage, and therefore to obtain the torque produced at full (rated) voltage the following scaling must be done:

$$Tm\Big|_{\text{rated voltage}} = Tm\Big|_{\text{test voltage}} \left\{\frac{\text{rated voltage}}{\text{test voltage}}\right\}^2 \quad \ldots.[3.4]$$

$$= Tm(\text{test voltage}).k^2$$

The torque obtained from the measurements (Tnett) includes the friction and windage effects. Therefore when the measured curves are scaled to full voltage values, the friction and windage torques (which are independent of voltage) are also scaled. To avoid this, the friction and windage torques must be added or subtracted (depending on the value of s) before any scaling is done. In this way a true picture of the developed torque at full voltage is obtained.

In two or four pole, CACA type machines having externally mounted fans, the friction and windage torques may become a significant part of the measured torque at high speeds and reduced voltage. As industrial motor A falls into this category, these effects were carefully assessed and accounted for as shown in Appendix D.

3.2 - Tests on industrial motor B

The rotor asymmetry introduced into the squirrel cage of industrial motor B was different to that introduced into the rotor of industrial motor A. In rotor B a bar was cut at both ends adjacent to the endrings, while in rotor A a bar was cut only at one end. This was done to allow the effects of any inter-bar currents that may be present to be assessed. (These could only occur in motor A). Therefore differences between the results of the measurements obtained on the two motors must be expected. All the on-load vibration measurements taken on motor A were repeated on motor B with motor B coupled to the gearbox in the same position as was motor A. These measurements show up the differences in the vibration pattern produced when a rotor-bar is completely isolated from both endrings or when it can carry current from one endring, as it is shown in Chapter 5.

CHAPTER 4

THE PRODUCTION OF INTER-BAR CURRENTS

Gorge[1] was the first to study the operation of a three-phase induction motor having an asymmetrical rotor circuit. Since then, many investigators have studied the effects of rotor asymmetries in slip-ring induction motors, however few papers deal with rotor asymmetries in three-phase squirrel cage induction motors. Analysis of machines having broken endrings was done by Mishkin[36] and for machines having symmetrically split endrings by Weichsel[3]. Different aproaches for the calculation of the current distribution in a squirrel cage having broken bars are presented by Shuisky[37], Hiller[38], D'Alessandro and Pagono[39], Vas[4,35],and Williamson and Smith[6]. In all these works the authors assumed that there were no inter-bar currents present in the rotor. However, as it is shown in this Chapter, this assumption does not hold for most modern squirrel cage industrial machines in which the bar-to-bar impedances are relatively small. It is interesting to note that in the literature surveyed, it has been shown that inter-bar currents exist in healthy squirrel cages (even in unskewed cages)[15,30]. However, no theory is put forward describing the consequences of having a faulty cage where, as is shown here, the inter-bar currents may become large.

An asymmetrical rotor winding may be represented by a set of three symmetrical component impedances. In the case of squirrel cage motors, the assumption that currents can flow only in the rotor-bars implies that no zero-phase sequence currents can exist. These zero-phase sequence currents are in phase in all the bars and as such will return via the laminations and the shaft. These currents do not produce any average torque but certainly produce additional losses. In this work no expression for the zero-phase sequence currents is presented because this investigation concentrated on the asymmetry present only in the region of the 'broken' bar. The analysis including zero-phase sequence currents follows a completely different aporoach which is outside the objectives of this work. However, it is felt that Williamson and Smiths model can form a good basis for such an analysis and in fact further work in this direction has already been initiated.

4.1 - Calculation of the current flowing into the 'broken' bar

This analysis is restricted to a particular type of fault and to the effects that occur in the region of this fault. This fault, namely that of a bar broken next to one of the endrings, is the most common fault that occurs in squirrel cages. Although the mathematical expressions derived are not strictly applicable to other types of cage faults, it is felt that the general conclusions reached are also representative of most other types of faults.

Figure 4.1 shows the simple model used for the calculation of the current distribution in the bars and the iron in the region near the `broken' bar.

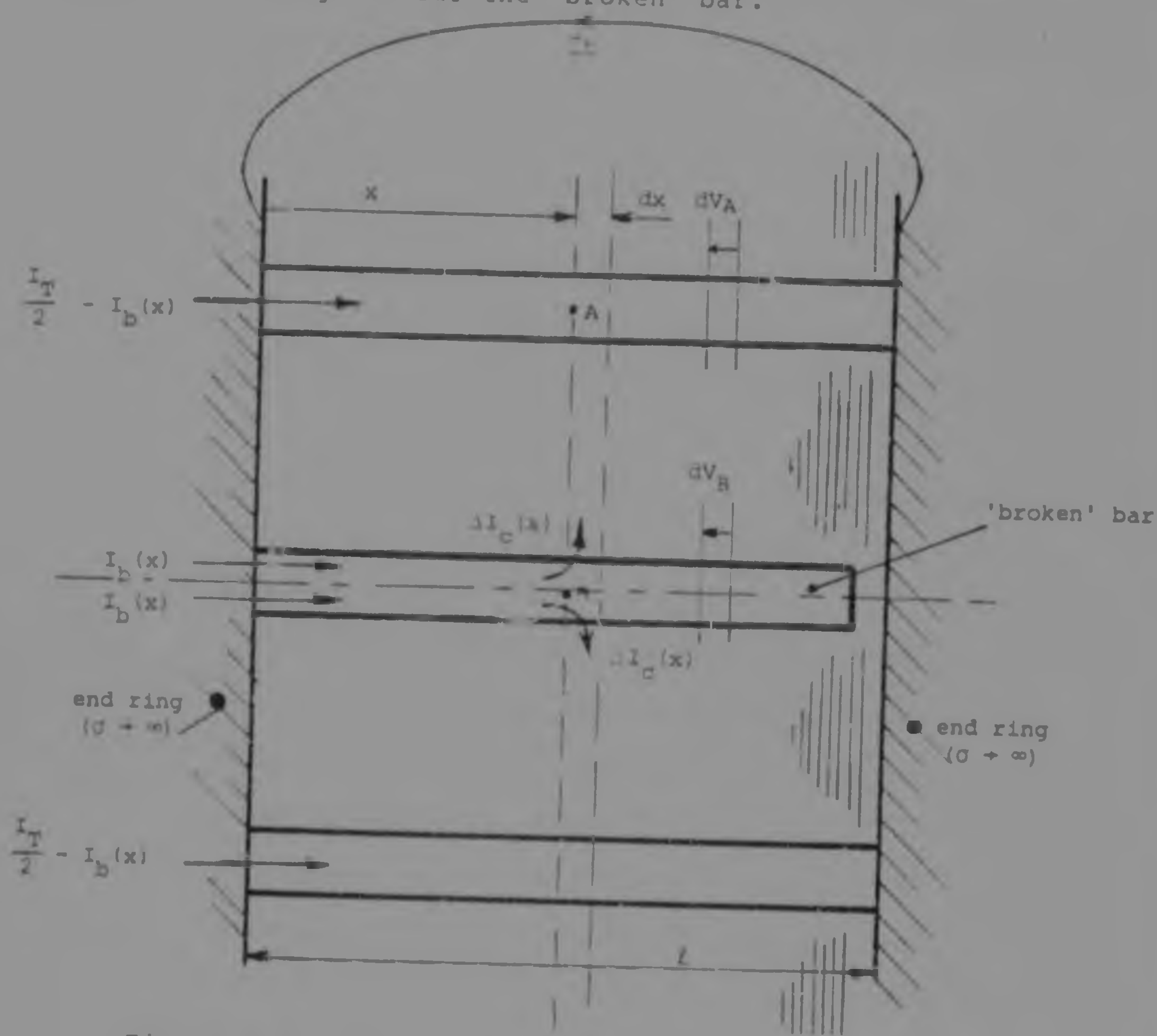

Figure 4.1 - Current flowing in the region of the `broken' bar.

In this analysis the following assumptions have been made:

(a) The inter-bar laminar currents flow only between the `broken' bar and the two adjacent bars. (Actually the currents flow between the `broken' bar calculation of the current distribution in the bars and the iron in the region near the `broken' bar.

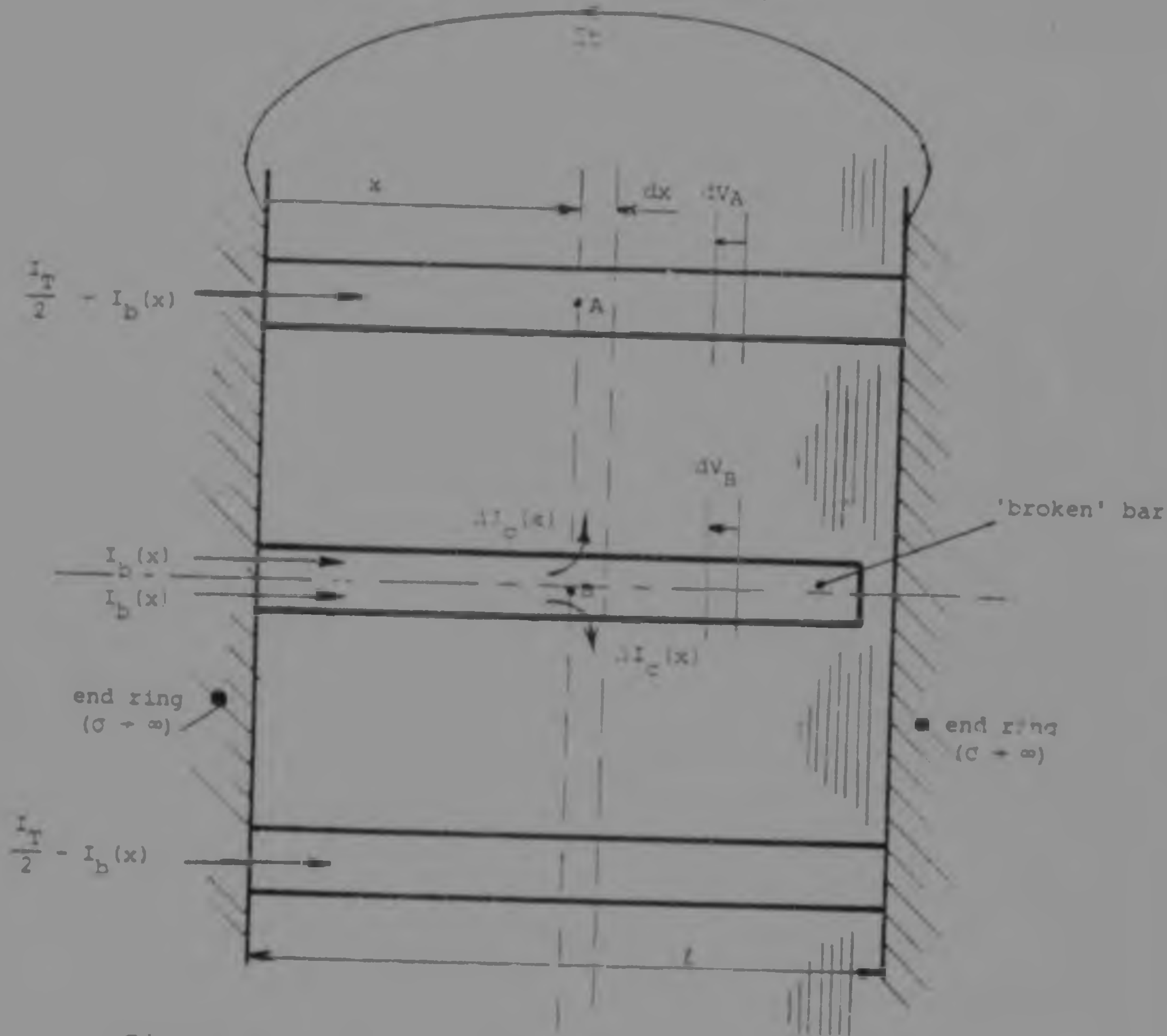

Figure 4.1 - Current flowing in the region of the `broken' bar.

In this analysis the following assumptions have been made:

(a) The inter-bar laminar currents flow only between the `broken' bar and the two adjacent bars. (Actually the currents flow between the `broken' bar and several adjacent bars, the number of which is a function of the relationship between the endring impedance (Zring) and the total secondary impedance[6]. Nevertheless, as is shown, the assumption still holds because in large machines the endring impedance is a small portion of the total secondary impedance. Therefore the total current of all the bars, which carry current compensating for that of the 'broken' bar, divided by this number of bars (including the `broken' bar) gives an average value very close to In, ie to the average bar current that would flow in a healthy cage under the same slip and voltage conditions).

(b) The voltages induced in the three bars are equal in magnitude and are in phase with one other. (This is valid when the number of rotor slots per pole is relatively high, as is the case in most two pole motors. If the slot angle is large enough to be included the effect will be that the magnitude of the current flowing from the `broken' bar to either of the adjacent bars will fluctuate with the slip; ie at some time more current will flow from the 'broken' bar to, say, adjacent bar A and less will flow to adjacent bar B while at a short time later the roles reverse).

(c) The inter-bar impedance is mostly resistive at the frequencies dealt with. (This fact has been verified by measurement, see Chapter 2, page 2.14).

(d) The endring impedance between the bars is negligible. (See assumption `a'). The value of the endring impedance of large machines is typically about 0,2 pu of the secondary impedance at full speed. The magnitude of this impedance does affect the small inter-bar currents present in squirrel cage motors as discussed by Weppler[30] when dealing with `healthy' cage motors. However, in the case of a broken bar, the main parameter affecting the inter-bar currents is the ratio between the bar impedance and the distributed inter-bar impedance (contact and core impedance). This holds true particularly in the case of normal machines where the endring impedance is low, ie approximately equal to 0,2 pu.

(e) The portion of the bars between the endring and the core is disregarded.

Assumption (b) implies that the current distribution in the three bars and the core in between them depends only on the impedance configurations and not on any voltage distribution. From inspection of Figure 4.1 and taking into account the current and voltage directions, the differential voltage drops along bars A and B are given by:

$$dV_B(x) = -2\, Ib(x).Zb.dx$$

$$dV_A(x) = -\,[(It/2) - Ib(x)].Zb.dx$$

where It is the total current flowing in the system composed of the currents in the 'broken' bar and the two immediate adjacent bars, and 2Ib(x) is the current flowing through the 'broken' bar at a distance x from the 'healthy' side endring. Therefore:

$$V_A(x) = \int_0^x -[(It/2) - Ib(x)].Zb.dx \qquad \ldots\ldots[4.1]$$

$$V_B(x) = \int_0^x -2Ib(x).Zb.dx \qquad \ldots\ldots[4.2]$$

where $V_A(x)$ and $V_B(x)$ are the voltage drops along the bars between the 'healthy' side endring and points A and B respectively. The current flowing into the portion dx of the core from the 'broken' bar at a distance x is given by

$$dIc(x) = [V_{BA}(x)/Rc].dx \qquad \ldots\ldots[4.3]$$

It is important to note that in equation [4.3] the resistance of the portion of the core and the contact between bar and core for the length dx through which the current dIc(x) flows has a resistance given by Rcdx = Rc/dx . This is so because Rc is the total value for one metre of effective core length and is inversely proportional to the axial length.
The applicable boundary conditions are as follows:

(i) $Ib(x=1) = 0$ (ie no current flows out at the end of the `broken' bar)

(ii) $V_{BA}(x=0) = 0 \implies dIc(x=0) = 0$ (assumption (d))

The solution for $Ib(x)$ is obtained from equations [4.1], [4.2] and [4.3] together with the boundary conditions (i) and (ii) given above as follows: From equations [4.1] and [4.2] it can be written

$$V_{AB}(x) = V_A(x) - V_B(x) =$$

$$= - Zb.(It/2).x + 3Zb \int_0^x Ib(x).dx$$

and $\quad dIc(x) = - [V_{AB}(x)/Rc].dx = [dIb(x)/dx].dx$

Therefore

$$dIb(x)/dx + (It.Zb/Rc).x - (3Zb/Rc) \int_0^x Ib(x).dx = 0$$

$$\implies \quad Ib(x)'' - (3Zb/Rc).Ib(x) = - It.Zb/2Rc$$

The general solution for this equation is

$$Ib(x) = C1.\exp\{\ x\} + C2.\exp\{-\ x\} + C3$$

The constants C1, C2 and C3 are found using the boundary conditions (i) and (ii). The resulting expression for $Ib(x)$ is then:

$$Ib(x) = (It/6).[1 - (\cosh \lambda x/\cosh \lambda \ell)] \qquad ....[4.4]$$

where $\lambda = \sqrt{3|Zb/Rc|}$

The change in the airgap mmf distribution in the radial direction in the region of the `broken' bar will be compensated for by the increased currents flowing in the adjacent bars, such that the total ampere-turns produced by the three bars will remain almost constant. That is the total current will be $It \cong 3In$. Therefore from equation [4.4]

$$Ib(x) = In/2.[1-(\cosh \lambda x/\cosh \lambda \ell)] \qquad ....[4.5]$$

The current entering the `broken' bar at $x = 0$ is

$$2Ib(x=0) = Ibb$$

Hence from equation [4.5]

$$Ibb/In = 1 - 1/\cosh \lambda \ell \qquad ....[4.6]$$

This variation of the current flowing into the `broken' bar, taken as a percentage of the current that would flow into a `healthy' bar under identical voltage and slip conditions (equation [4.6]) is plotted against the ratio |Zb/Rc| in Figure 4.2.

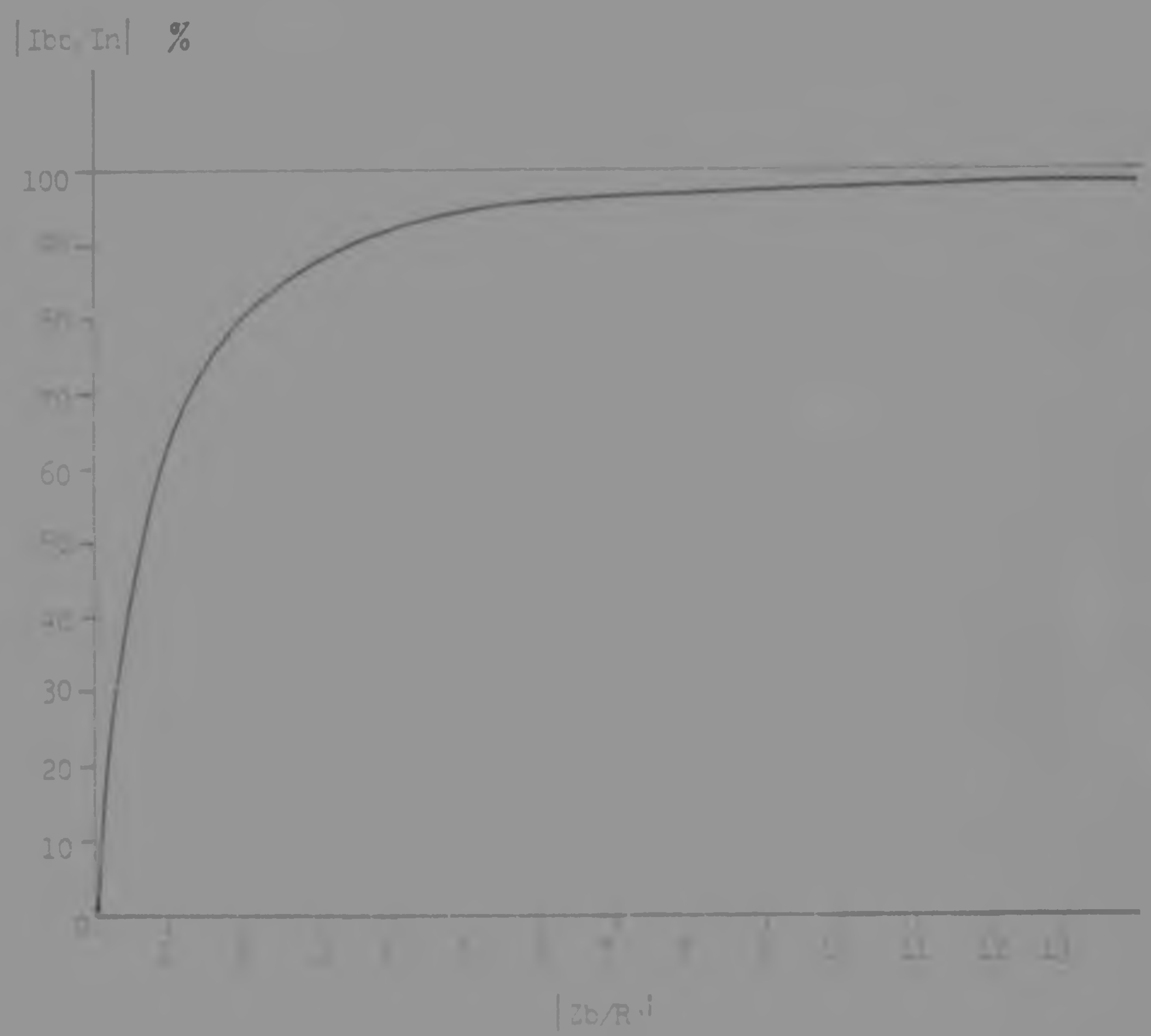

Figure 4.2 - Plot of |Ibb/In| as a function of |Zb/Rc| as per equation [4.6]

4.1.1 - Experimental verification of the ratio |Ibb/In| (equation [4.6])

The actual rotor-bar currents were measured on industrial motor A under locked rotor conditions as described in Chapter 3, section 3.1.1. The results of these measurements are given in Appendix D, section D.1.1, page D.12, where it is shown that the magnitude of the current entering the `broken' bar is practically the same as that of the currents flowing into the `healthy' adjacent bars (see Figure 4.4). This somewhat surprising result can be predicted from equation [4.6] by first evaluating the ratio of |Zb/Rc|, as follows:

(a) Calculation of Rb:-

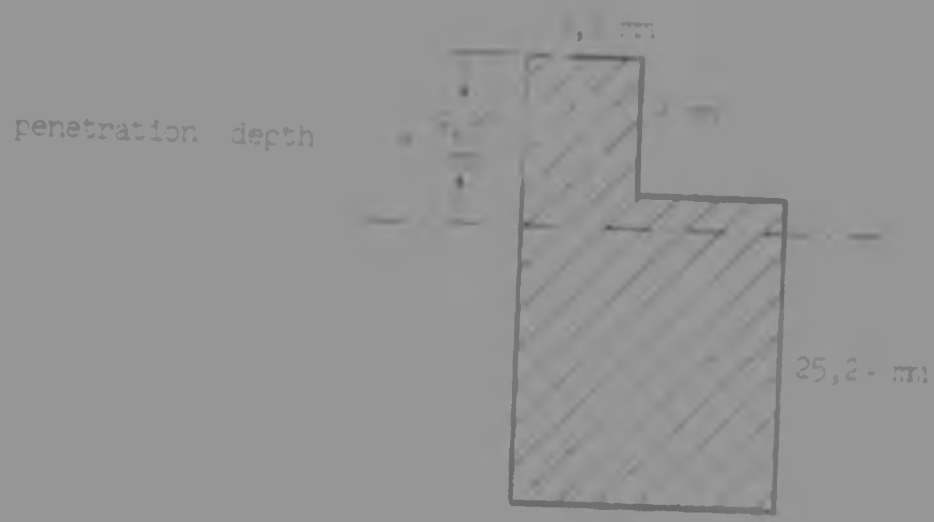

Figure 4.3 - Cross section of a bar of the squirrel cage of industrial motor A.

The depth of penetration at 50 Hz for 100% conductivity copper is equal to 9,37 mm. Therefore the effective conducting area Ac at 50 Hz, ie under locked rotor conditions is (see Figure 4.3):

$$Ac = 3,2 \cdot 9 + 7,91 \cdot 0,37 = 31,73 \text{ mm}^2$$

Hence, the bar resistance under this condition is

$$Rb(\text{at } 50 \text{ Hz}) = 1,732 \cdot 10^{-6} \cdot 45 \cdot (1/0,3173)$$
$$= 246 \, \mu\Omega$$

(b) Calculation of Xb:-

$$Xb(\text{at } 50 \text{ Hz}) = 2\pi f.(\text{length of core}).4\pi.10^{-9}.$$
$$.(\text{slot permeance at } 50 \text{ Hz}) \quad \text{ohms}$$

bridge permeance = 3/3,7 = 0,8108

slot permeance = 9/(3 x 3,7) = 0,8108

total slot permeance = 0,8108 + 0,8108 = 1,622

Therefore

$$Xb(\text{at } 50 \text{ Hz}) = 2\pi \cdot 50 \cdot 45 \cdot 1,622 \cdot 4\pi \cdot 10^{-9}$$
$$= 288 \, \mu\Omega$$

Therefore the bar impedance is

$$Zb = Rb + jXb = 246 + j288$$

ie $|Zb| = 379 \, \mu\Omega$

(c) Calculation of Rc:-

The total inter-bar resistance is

$$Rc = 19,5/(0,45 \cdot 0,95)$$
$$\simeq 46 \, \mu\Omega$$

In this calculation (0,45 . 0,95) represents the effective core length and 19,5 $\mu\Omega$ has been taken as the inter-bar resistance per metre of effective core length. (This value of 19,5 $\mu\Omega$ was the value measured for this rotor, cf 18 $\mu\Omega$ page 2.12).

Hence $|Zb/Rc| = 379/46 = 8,24$

$\simeq 8$

By inspection of Figure 4.2 it is seen that for this value of $|Zb/Rc|$ the ratio of $|Ibb/In|$ is approximately equal to 100%, ie the current entering the 'broken' bar is almost equal in magnitude to the currents that would exist in all the bars were the cage complete. This means that in this machine, and for this slip, the current distribution pattern around the machine is hardly affected by having a broken bar. The measurements taken of the actual bar currents bear this out, see Figure 4.4, where it is seen that the current entering bar A, the 'broken' bar, is of comparable magnitude to the current entering any other bar.

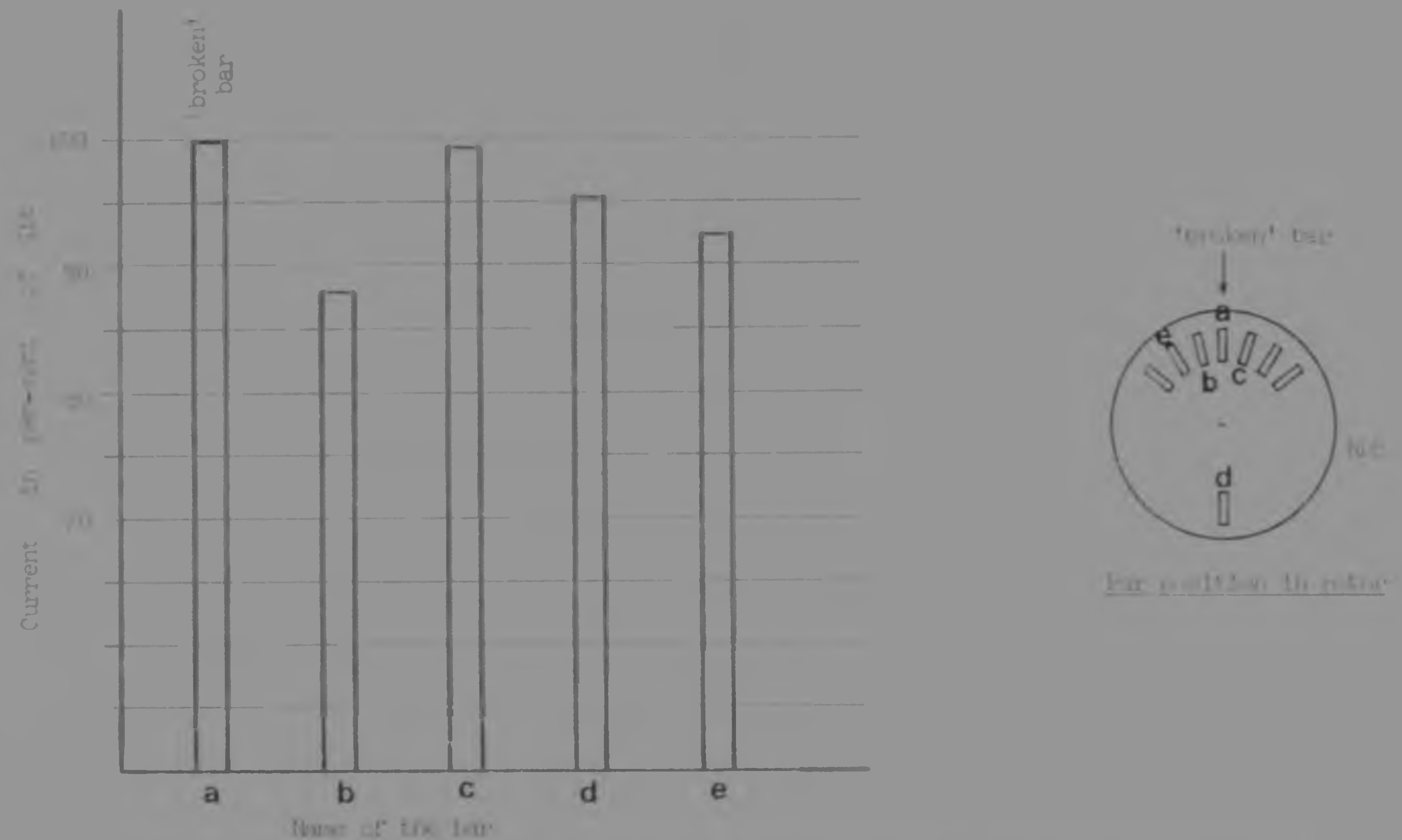

Figure 4.4 – Measured valu   ...ou/ml for industrial motor A. The bars were positioned
around the mac   ...hown.
(Figure also r...   ...as D.5 in Appendix D)

The actual differences between the values of the currents in the various rotor-bars shown in Figure 4.4 can be attributed to the change in the permeability of the airgap around the machine due to the variation of the relative position of the stator and the rotor slots. (The detailed assessment of this aspect is given in Appendix D, page D.13). Also, as is shown further on, the fact that the current in the 'broken' bar is slightly larger than the currents in the other bars can partly be attributed to the small finite endring impedance that exists. However, this impedance is small enough to have been taken as zero in the calculations.

4.2 - Axial distribution of the current entering the core from the 'broken' bar

The distribution of the current magnitude in the 'broken' bar expressed as a function of the axial position along the bar is given by equation [4.5]. This is plotted in Figure 4.5 where clearly as x->l (l = normalized bar length) the magnitude of the current Ib(x) tends to zero.

Note: In Figure 4.5 the current plotted is 2Ib(x) which is the total bar current at position x . As shown in Figure 4.1 Ib(x) represents half the bar current as the system has been symmetrically divided.

From the above it can be seen that the magnitude of the inter-bar current in the rotor core at some position x can be expressed as:

$$\Delta Ic(x) = Ib(x) - Ib(x + \Delta x)$$

$$\Longrightarrow \quad \Delta Ic(x)/\Delta x = (Ib(x) - Ib(x + \Delta x))/\Delta x$$

As $\Delta x \rightarrow 0$

$$dIc(x)/dx = - dIb(x)/dx$$

Therefore the magnitude of the distribution of the current flowing in the core is given by

$$\begin{aligned} |\delta Ic(x)| &\doteq |dIc(x)/dx| \\ &= |dIb(x)/dx| \\ &= |(In. \lambda/2)(\sinh \lambda x/\cosh \lambda \ell)| \qquad \ldots.[4.7] \end{aligned}$$

This distribution of the magnitude of the inter-bar current in the core $|\delta Ic(x)|$ is also plotted in Figure 4.5. This shows that the core currents are largest at the end of the core adjacent to the fault.

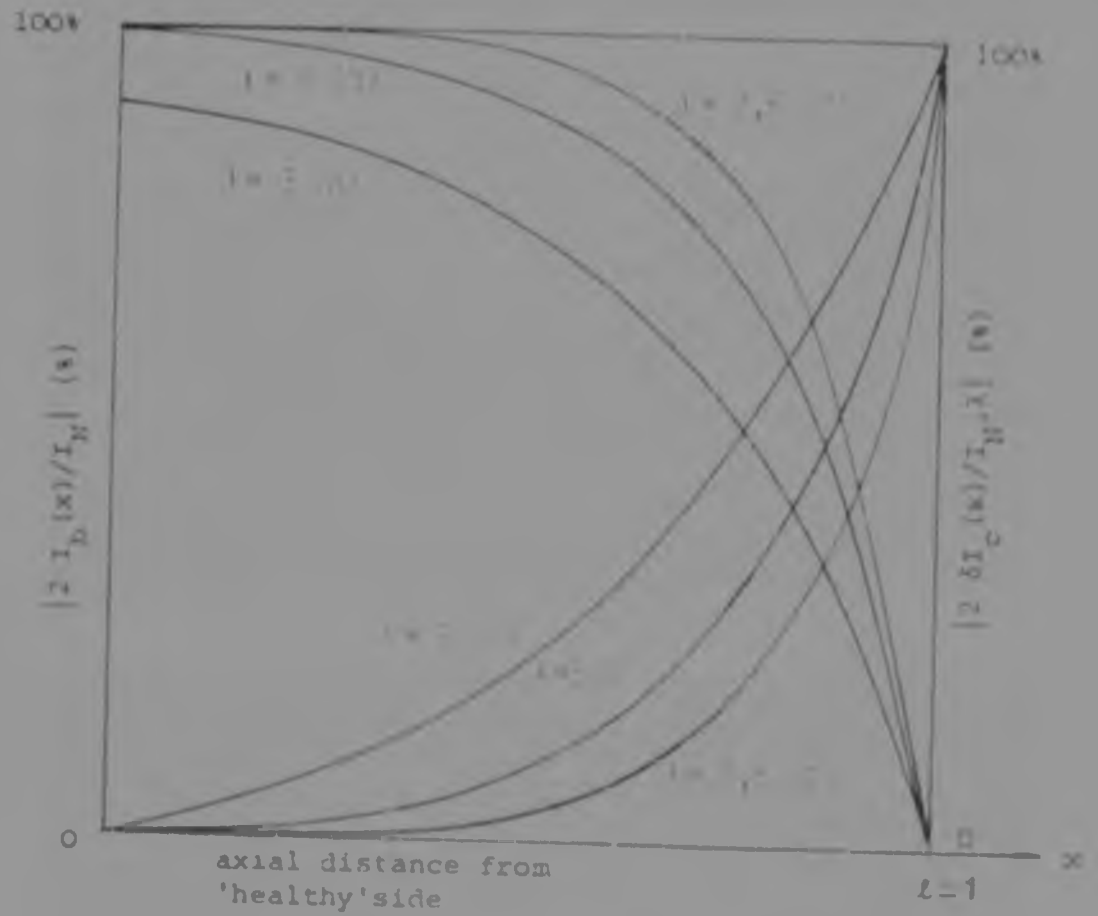

Fig.4. Current distribution along the rotor in the region of the 'broken' bar.

Curves A, B, C show the distribution of the current magnitude in the 'broken' bar for 3 different values of λ as a function of position along the bar.

Curves D, E, F show the distribution of the magnitude of the current flowing from the 'broken' bar into the core for 3 values of λ, as a function of position along the bar/core.

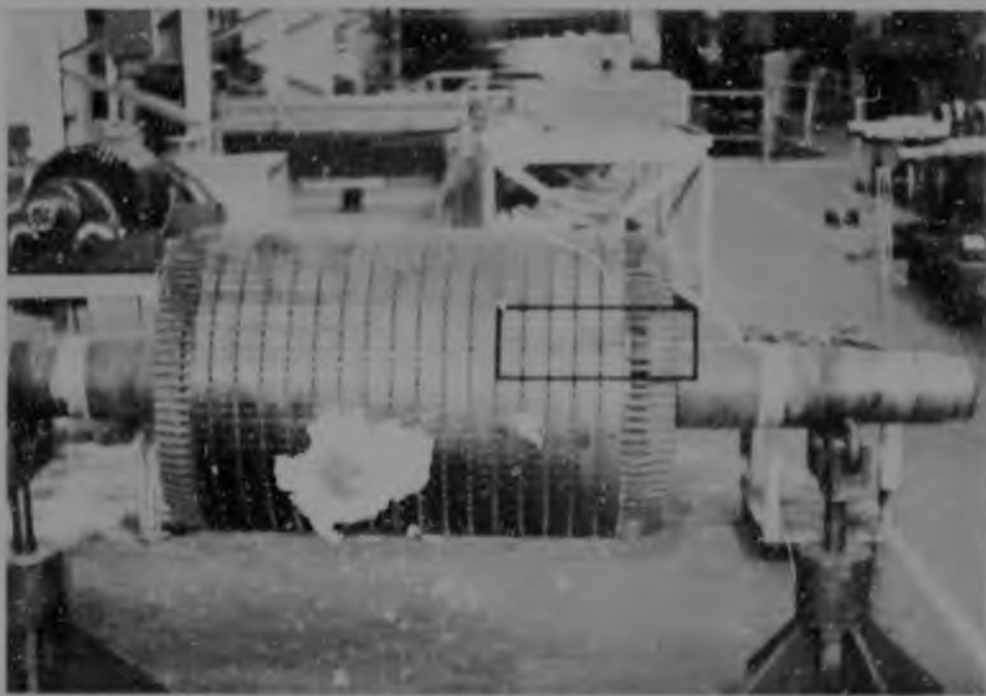

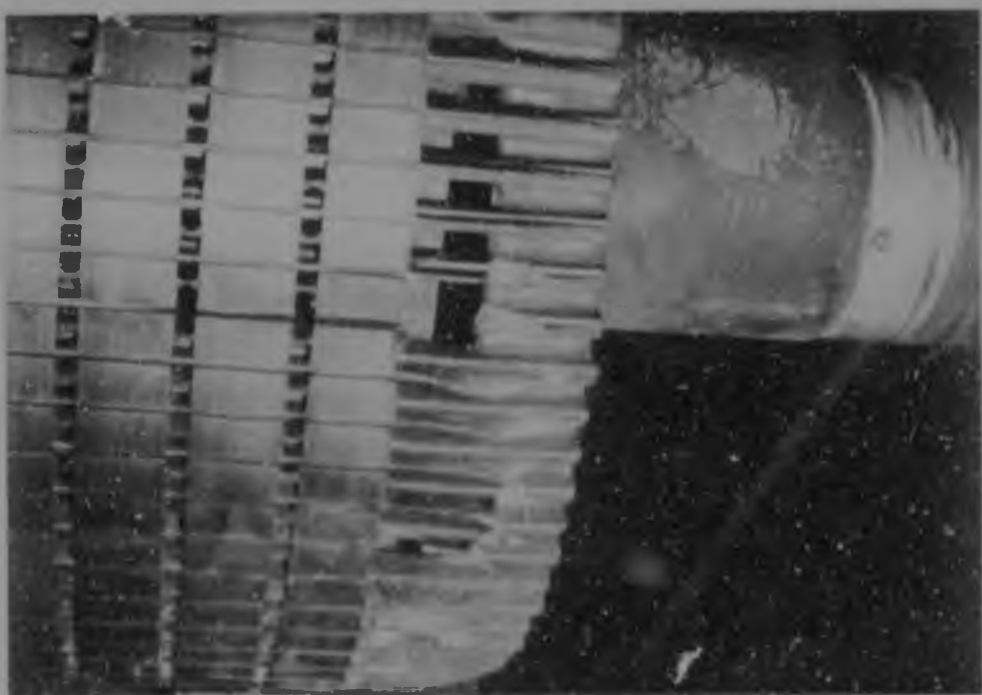

Photographs of faulty rotor of a [illegible] induction motor. [illegible] enlarged view of the faulty section [illegible]

4.2.1 - Experimental verification of equation [4.7]

Figure 4.6 shows photographs of a rotor of a 1300/400 kW, 4/6 pole, 6600 Volts induction motor having a cage fault similar to that described above. The rotor of this motor has 58 slots which house a single cage winding of `T' shaped bars made of 100% conductivity copper. This motor was subjected to severe starting conditions (relatively short periods between DOL starting with a load having a large inertia). As a consequence most of the inter-bar current effects must have occurred at low speeds, ie with rotor frequencies close to 50 Hz. Therefore in doing predictions λ has been calculated for 50 Hz. Also for this machine:

$Rc \simeq 33\mu\Omega$ (taking $20\mu\Omega$ per metre of effective core length)

$Rb = 194\ \mu\Omega$

$Xb = 603\ \mu\Omega$

$\therefore\ |Zb| = 634\ \mu\Omega$

Hence $\lambda = \sqrt{3|Zb/Rc|} = 7,6$

From inspection of Figure 4.5, curves C and F, it can be seen that for $\lambda = 7,6$ the current flowing from the `broken' bar into the core will be largely concentrated at the end of the core next to the fault. This is totally in accordance with the severe burning of the core laminations and the web of the bar as can be seen in the photographs of the damaged rotor in Figure 4.6.

4.3 - The inverted experimental motor

The direct measurement of rotor-bar currents on conventional machines for slips other than unity is a difficult task. This requires sophisticated transmission equipment so that the information can be transmitted from the rotating member to the stationary outside environment. This difficulty can be overcome by performing measurements on an inverted machine where the squirrel cage is housed on the stationary member and the conventional three phase winding (the primary) on the rotating member, being fed via three sliprings from the supply. The inverted squirrel cage induction motor used for this purpose is described in Appendix E, section E.3.

By controlling the slip of the motor and the frequency of the supply, a series of rotor-bar current measurements were taken on the inverted machine for frequencies varying up to 400 Hz. The current measurements were also done by using 'Rogowsky' type toroid coils. As the measurements were taken for frequencies well in excess of 50 Hz the assumption that the inter-bar impedance remains almost purely resistive no longer holds. Consequently the measurements of this impedance were done using the same methods as described by Christofides[19] for various frequencies in the range 0-400 Hz. The magnitude of the measured inter-bar impedance varied considerably from bar to bar, and for each frequency the average value of a large number of measurements taken between a number of pairs of rotor-bars was determined and these results are plotted in Figure 4.7. The calculated values of the rotor-bar impedances |Zb| and the ratio |Zb/Zc| are also plotted in Figure 4.7 as functions of the frequency.

Approximately one third of all the rotor-bar currents were measured by placing Rogowsky coils at both ends of the bars close to the endrings. The side of the cage having all the bars connected to one endring is called the `healthy' side while the side where one bar is left unconnected is called the `faulty' side.

Figures 4.8 to 4.12 show the results of the rotor-bar current measurements taken at frequencies of 25, 50, 225, 320 and 400 Hz respectively. In each of these figures the currents measured at the `healthy' (curve b) and `faulty' (curve a) sides are shown. The current flowing into the `broken' bar from the `healthy' side is also shown. The scattering of the points is due to the large deviation that exists in the value of Zc for different pairs of bars around the rotor, as well as to the difference in the values of the endring/rotor-bar resistance for different bars. Nevertheless, the trends are clearly visible, ie that the currents in the `healthy' bars adjacent to the `broken' bar are far larger than the currents in the `healthy' bars further away from the `broken' bar. In the region away from the fault not many transducer coils were placed around bars, and consequently smooth curves have been drawn through these few points (eg from bars 36 to 9 to 13 and bars 20 to 27 to 36). Clearly this averages out the expected deviations in these regions. Also the average rotor-bar current In is shown; this being determined graphically from the respective curves.

Figure 4.13 shows the magnitude of the ratio of the current in the 'broken' bar (Ibb) to the average current (In) plotted against frequency. The measured values (obtained from figures 4.8 to 4.12) are shown in curve a. Curve b is the theoretical characteristic of this ratio derived directly from equation [4.6], ie assuming the endrings have zero impedance. It is seen that the measured curve is shifted upward in relation to the calculated characteristic. This is due to the fact that the endring impedance of this machine is relatively large, which means that the assumption of zero endring impedance no longer holds. Landy[20] has shown that the endring-to-bar contact resistance (Rcbr) for this machine is approximately:

$$Rcbr \approx 100\ \mu\Omega \qquad \text{for} \leq 106\ \text{Hz}$$

$$Rcbr \approx 100\ \sqrt{f/106} \qquad \text{for} > 106\ \text{Hz} \qquad \ldots.[4.8]$$

This means that the endring/bar contact resistance approximately equals the rotor-bar impedance Zb at 50 Hz. Also the actual endring (made of brass) impedance must still be added to this endring/bar contact resistance. The effect of this large endring impedance is to emphasize the asymmetry in the distribution of the rotor-bar currents around the rotor[6], thereby raising the magnitude of the bar currents in the region of the 'broken' bar as shown in Figure 4.14.

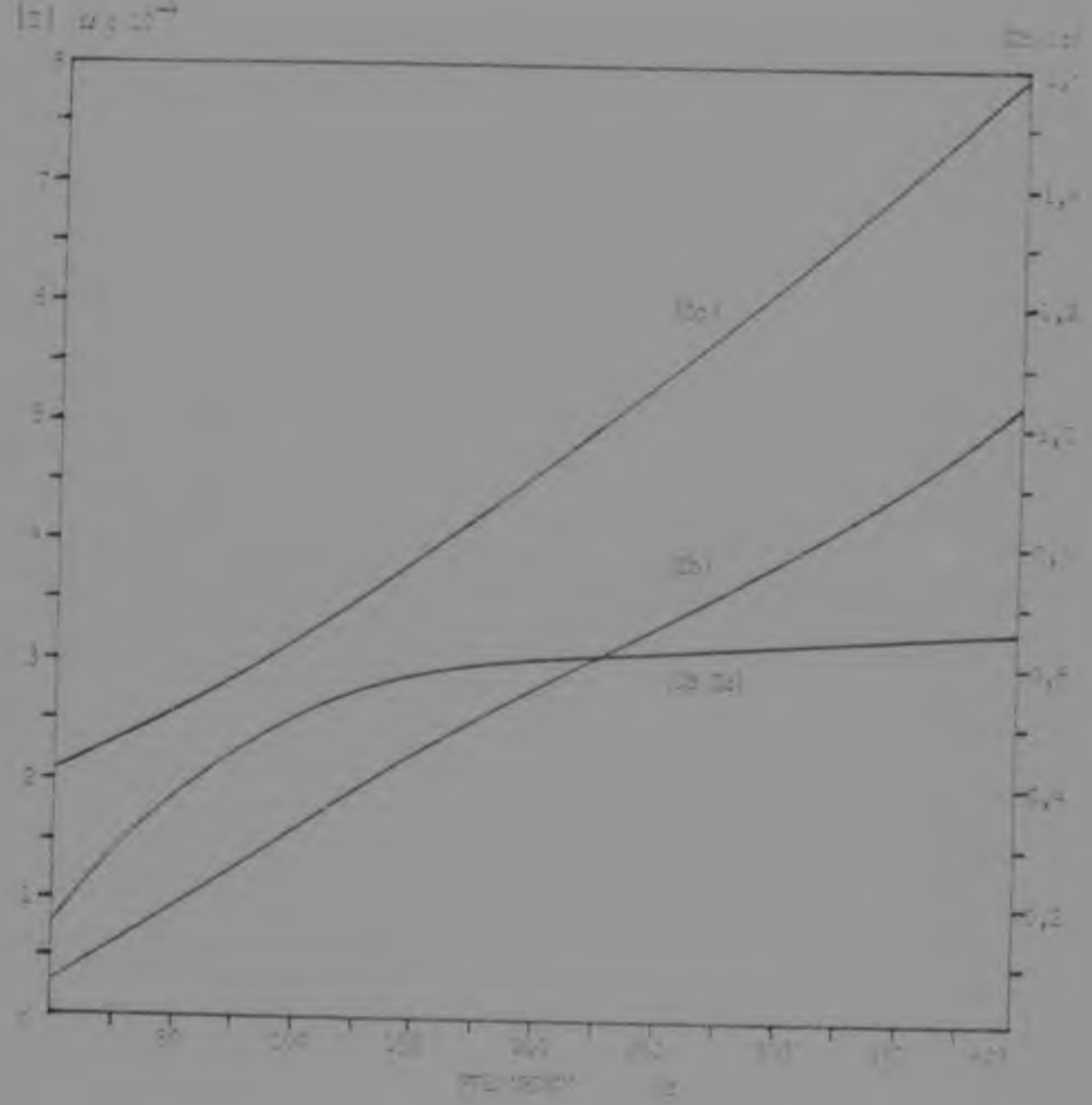

Figure 4.7 – Variation of the measured inter-bar impedance |Zc| with frequency for the inverted experimental motor. Also the calculated variations of |Zb| and |Zb/Zc| with frequency are shown.

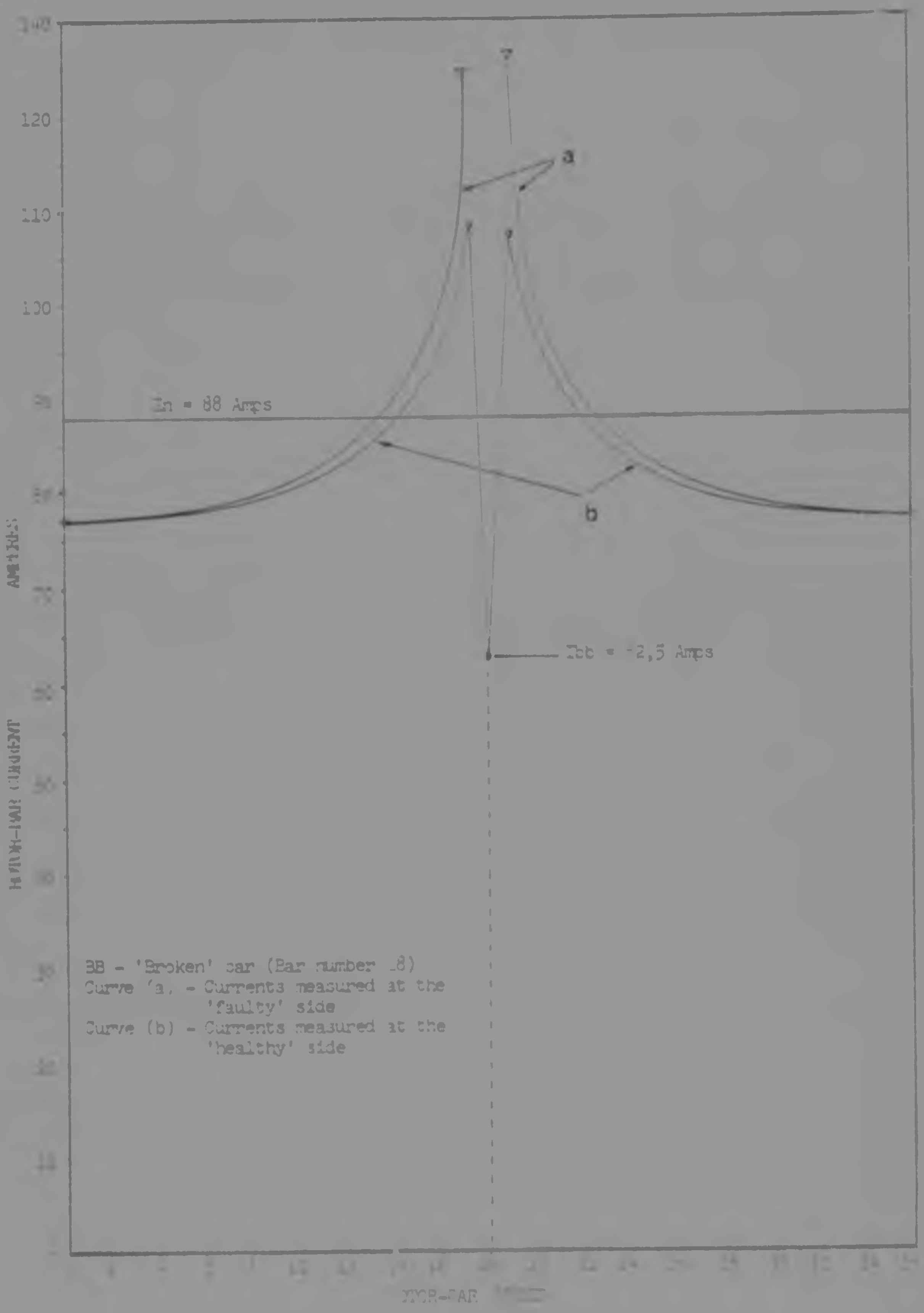

Figure 4.8 - Inverted Geometry Motor.

Measurement of rotor-bar currents for 25 Hz.

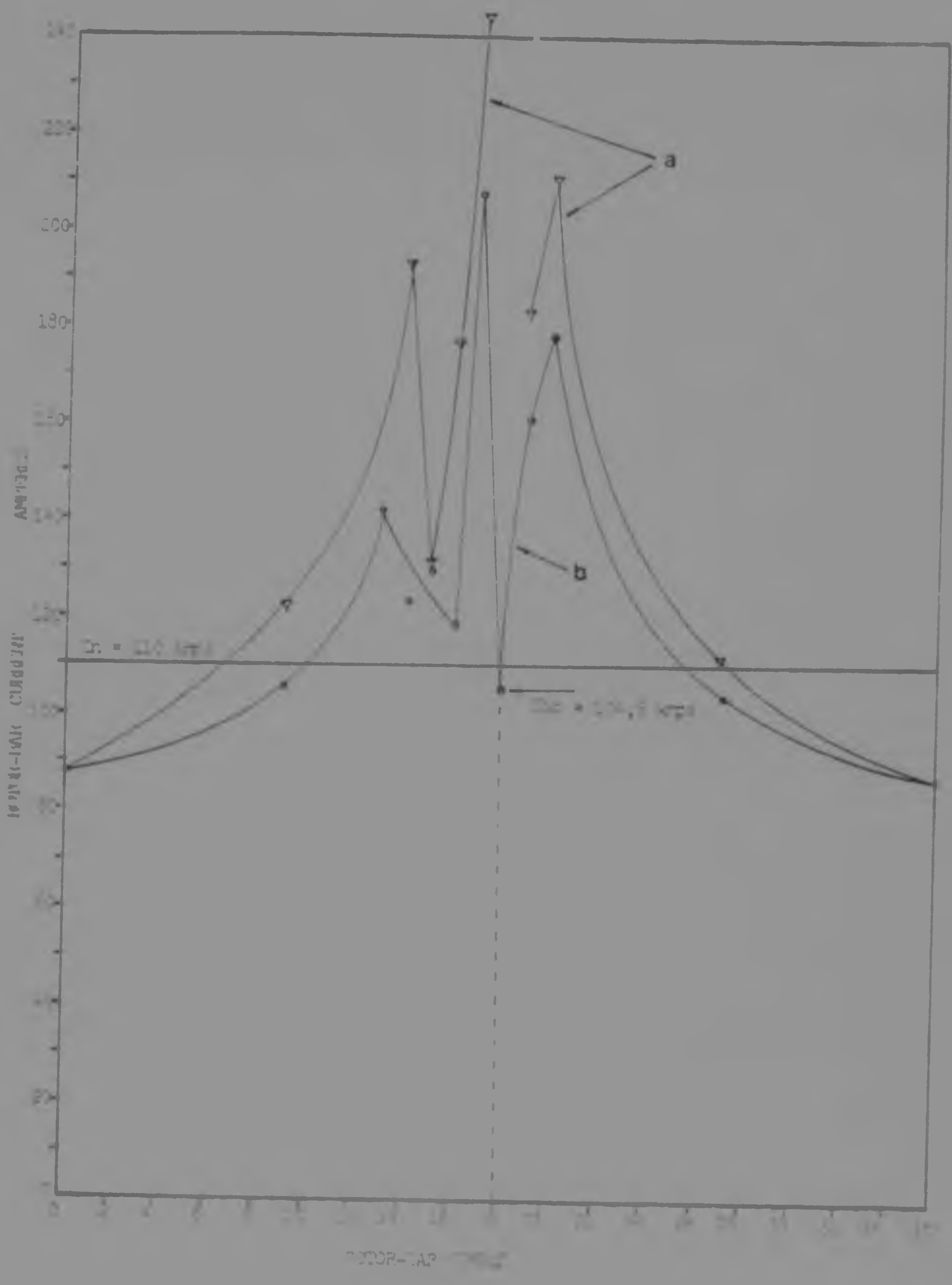

Figure 4.9 - As for Figure 4.8, but for 50 Hz.

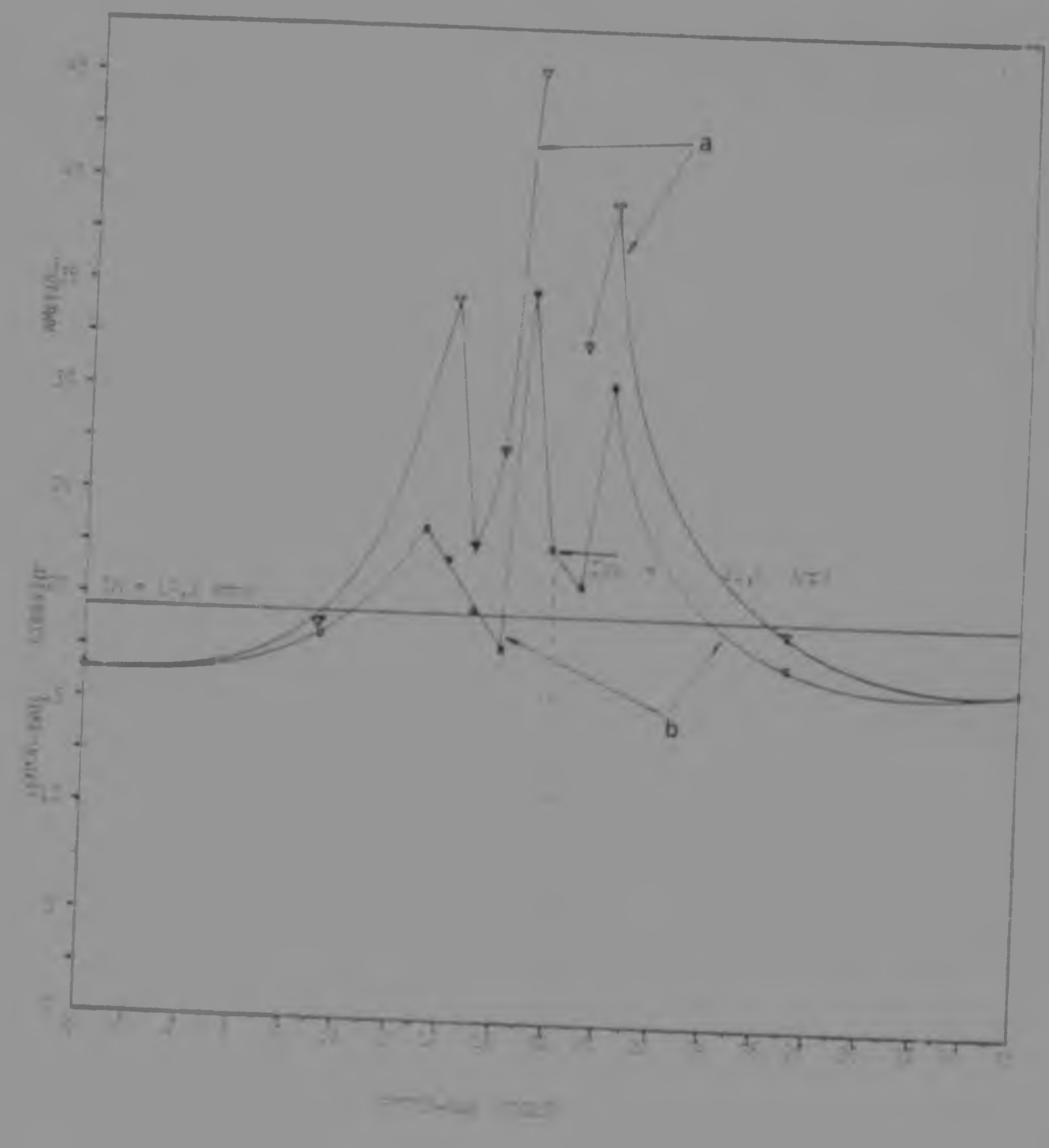

Figure 4.10 – As for Figure 4.9, but for [illegible] m.

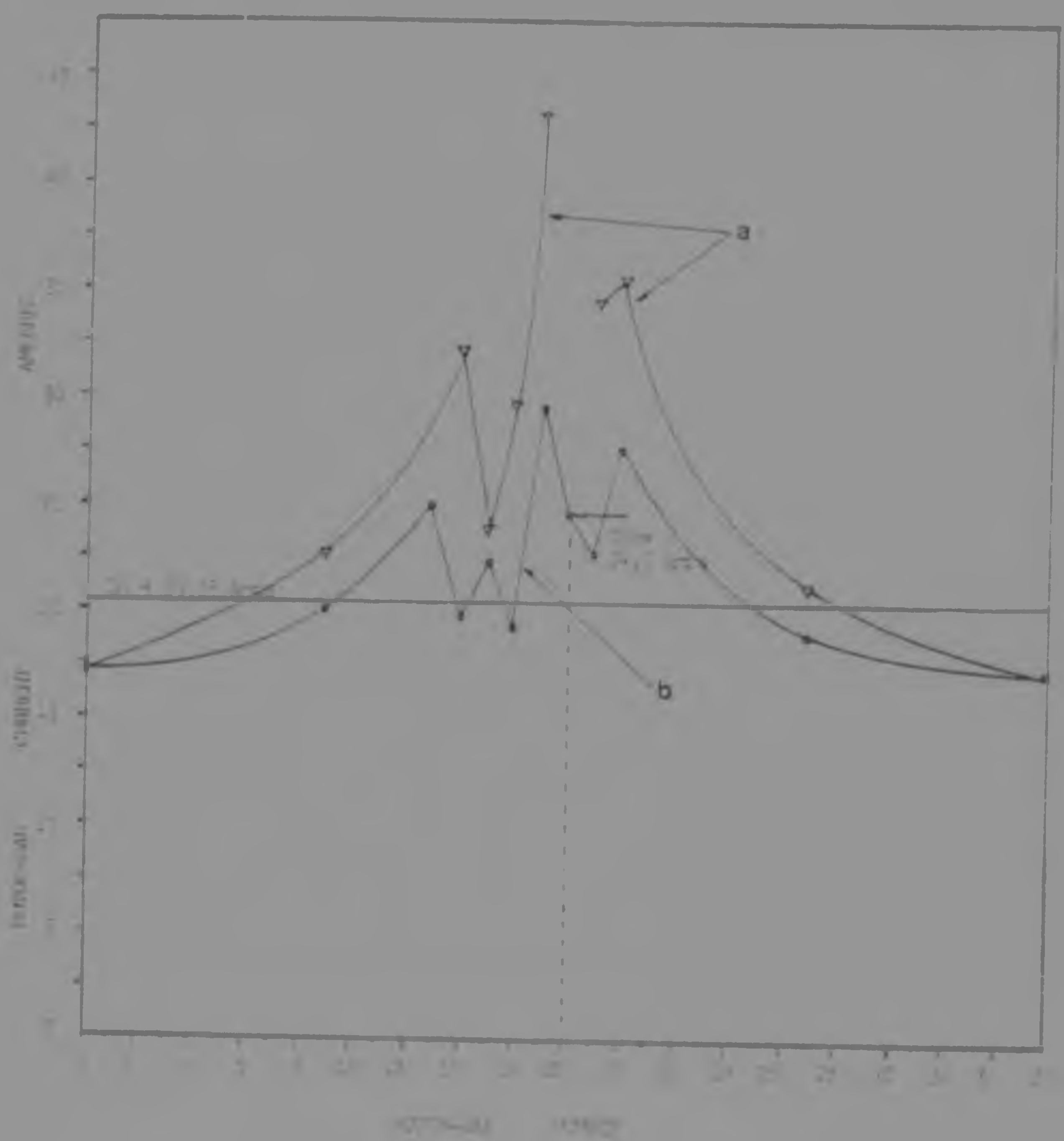

Figure 4.11 - As for Figure 4.9, but for 320 Hz.

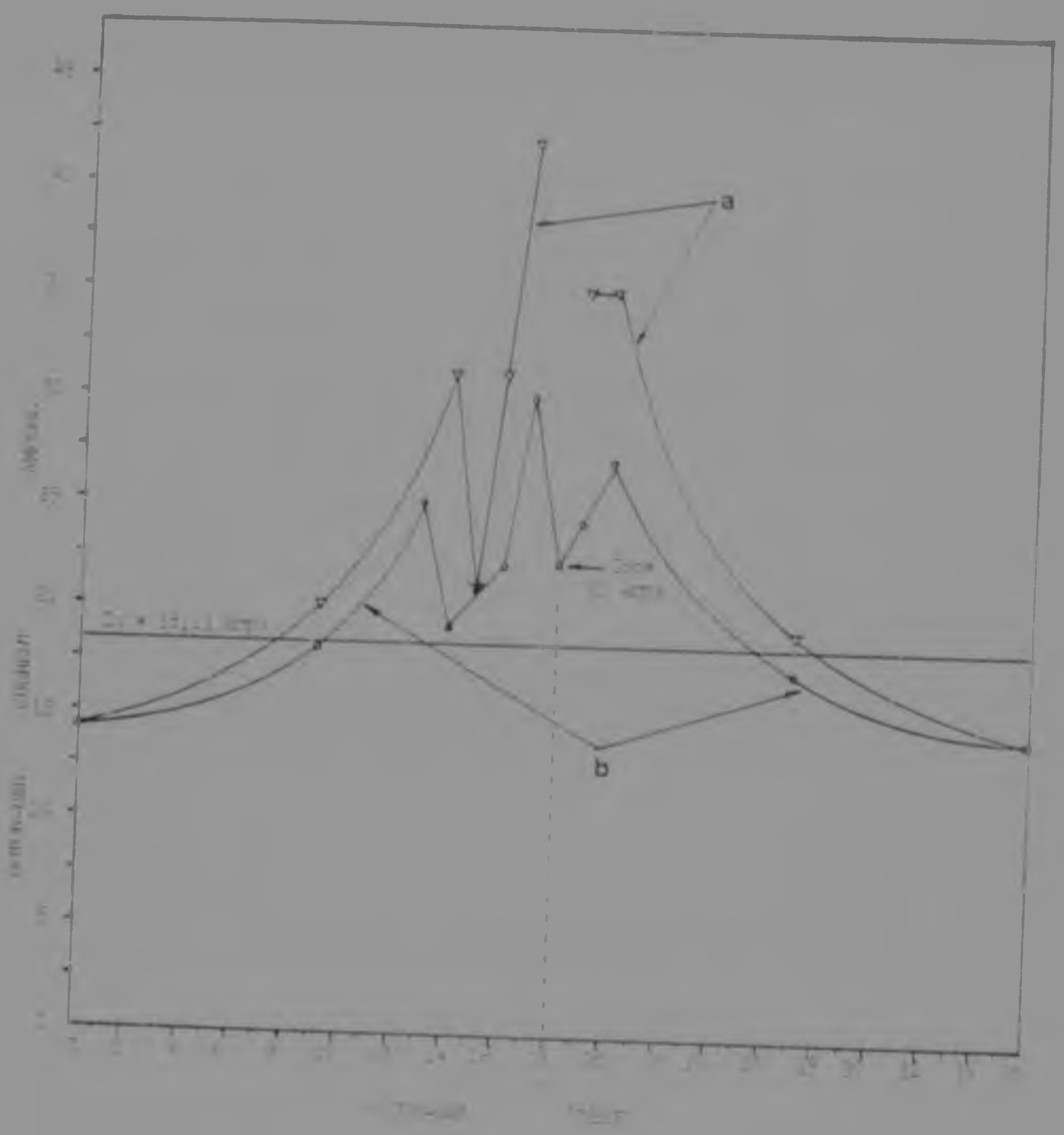

Figure 4.12 - As for Figure 4.8, but for 468 Hz.

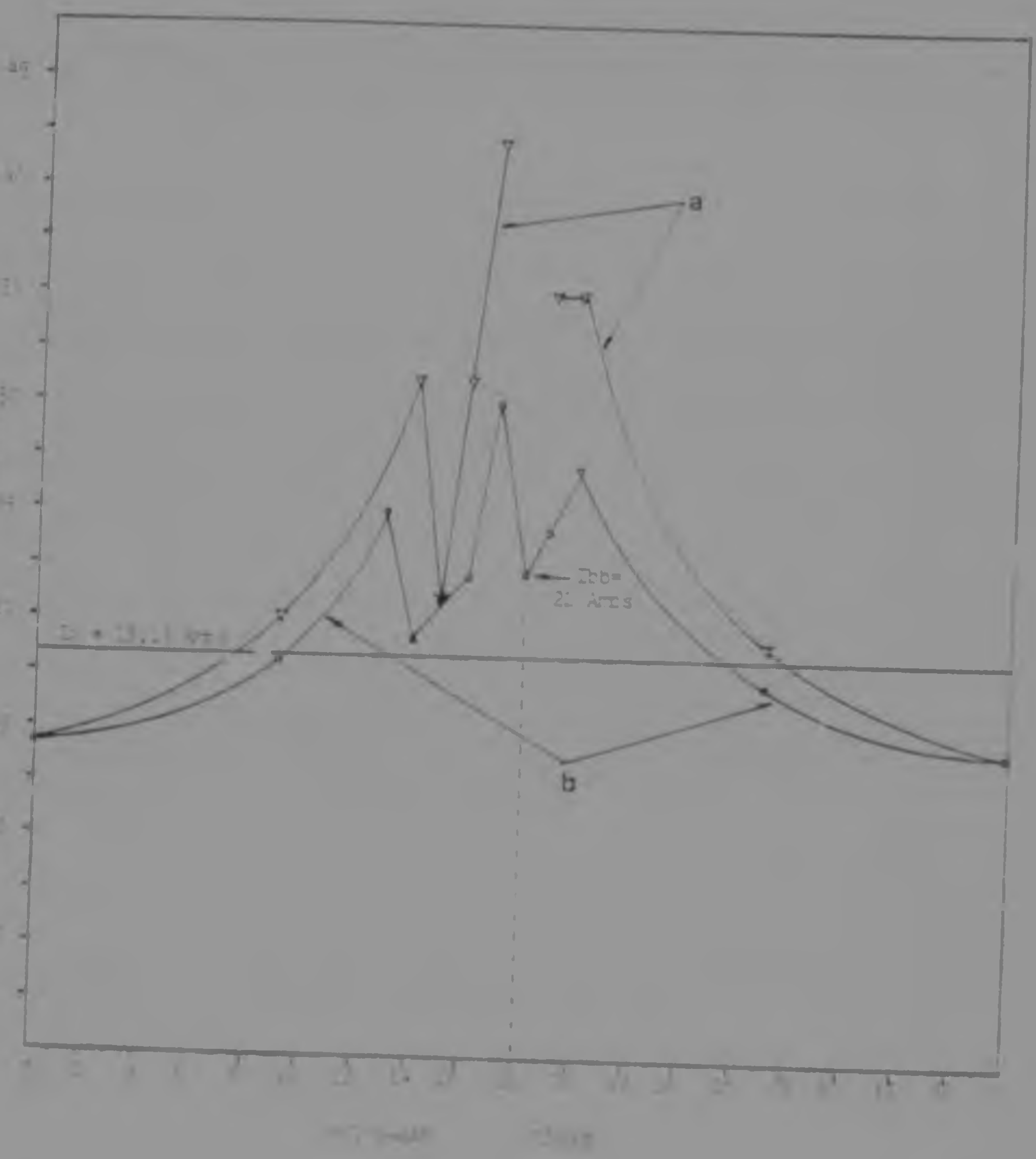

Figure 4.1[illegible] – As for Figure 4.[illegible], but for [illegible]

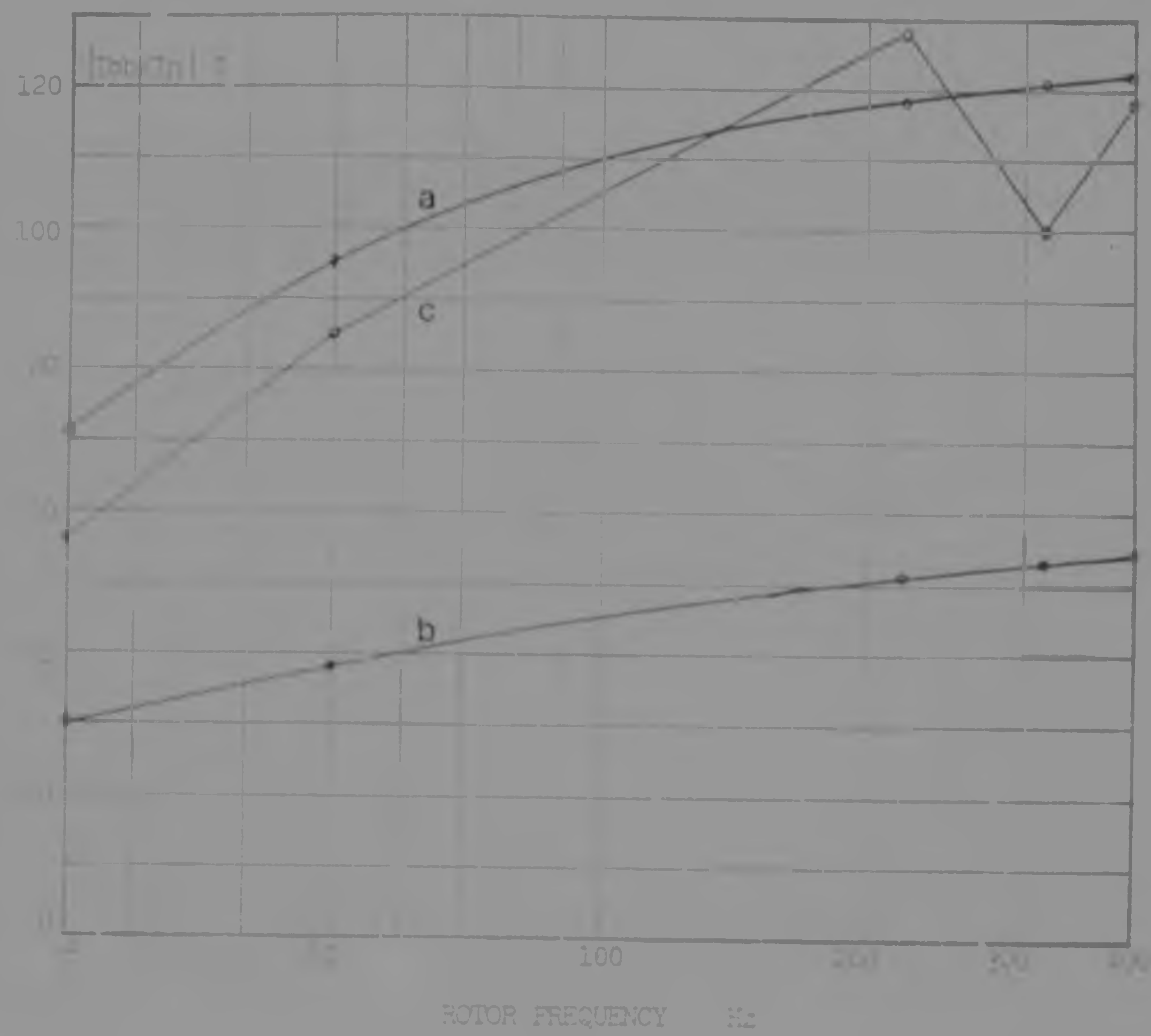

[illegible] - [illegible] values [illegible] $|Ibb/In|$ for the [illegible].

Curve (a) - Measured characteristic
Curve (b) - Calculated characteristic assuming Zring=0
Curve (c) - Predicted characteristic after correction for large Zring

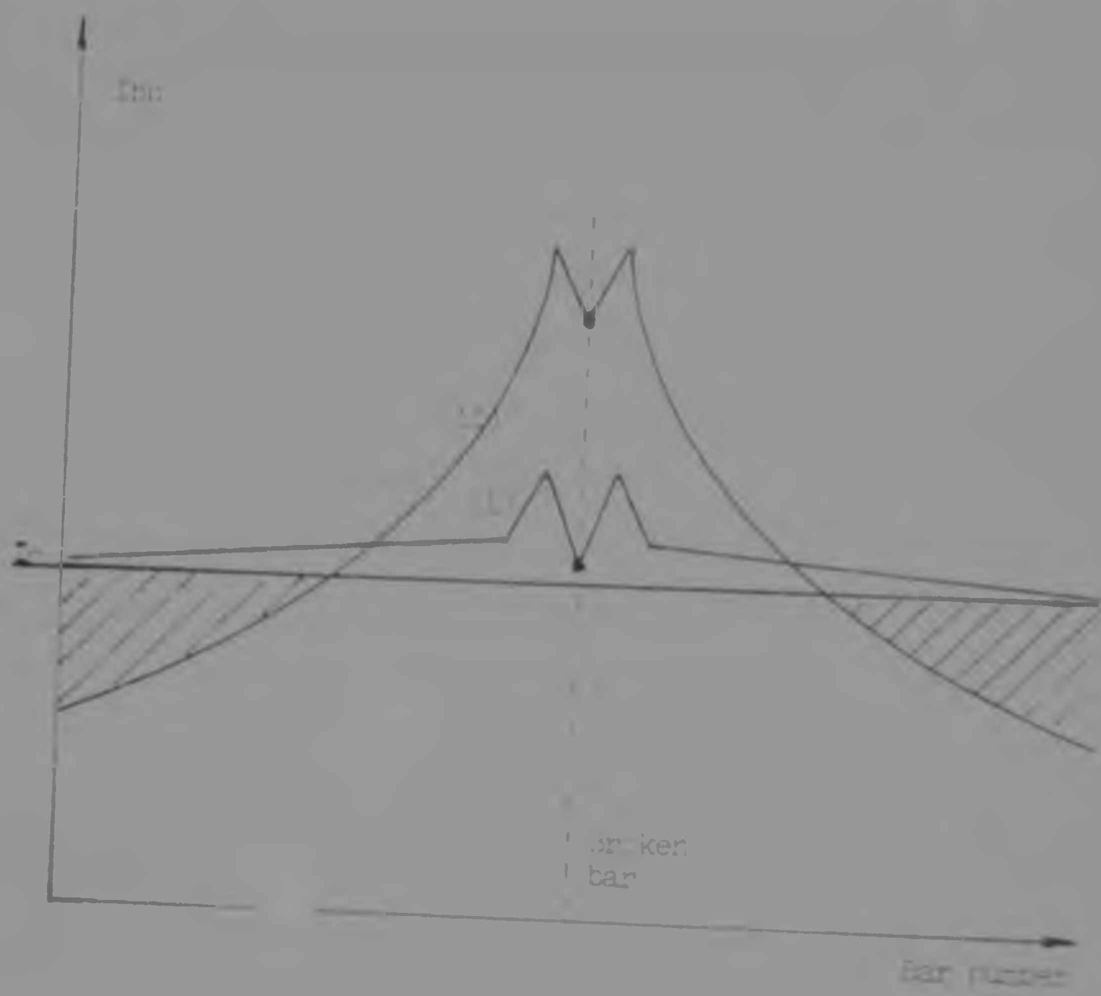

Figure 4.14 - Illustration of typical rotor-bar current distribution around the rotor for different endring impedances.

(i) zero impedance (note: distribution very close to In)

(ii) large endring impedance

Clearly, as previously explained, when the endring impedance is small the currents in the bars away from the `broken' bar all equal In (for all practical purposes). It is only the currents entering the `broken' bar and the adjacent bars that differ from In and, as shown in equations

[4.4] and [4.5], It ≅ 3In. Whe he ring imped.nce is large it is clear that the currents in the bars away from the 'broken' bar are less than In, and therefore the sum of the currents entering the 'broken' bar and the two adjacent bars, ie It, must now be greater than 3In. The amount by which It exceeds 3In is equal to the sum of the difference between In and the actual bar current for all bars having currents less than In. This correction has been evaluated from all the measured values (figures 4.8 to 4.12) and the corrected predicted characteristic is shown as curve c in Figure 4.13. The agreement achieved is quite acceptable, especially when it is realized that the values of the magnitude |Zb/Zc| give points on the steep portion of the characteristic shown in Figure 4.2. Also it is seen that as the frequency tends to zero the difference between curves a and b becomes less. This is as expected because the endring impedance -in particular Rcbr- has been shown to be a function of frequency (see equation [4.8]). The emphasis of this research is on the effects that occur in large machines when, almost always, Zring (the ring impedance) is a small portion of the secondary impedance. Consequently the correction referred to above is usually unnecessary.

The foregoing discussion clearly points to the interesting fact, that <u>given a relatively high endring impedance the current flowing into the healthy side of a broken bar</u> of a squirrel cage induction motor <u>may be substantially larger than the average rotor-bar current</u>.

4.4 - Effect of the inter-bar currents on the starting torque and pull-out-torque

It is well known that a reduction of the starting torque (ST) and pull-out-torque (POT) can be expected to occur in a squirrel cage induction motor with a faulty cage. This is mainly due to the torque produced by the negative sequence stator and rotor currents which themselves are a product of the unbalance in the secondary impedance. Another result of having a large concentrated asymmetry in the rotor is that the starting torque will now be largely dependent on the relative angle existing between stator and rotor. This is so because of the asymmetry in the distribution of the airgap fields and the large changes that occur in the field, in the region of the asymmetry, with changes in the relative position between stator and rotor teeth. (Ito[31], presents a good illustration of the measured airgap flux around a motor with a broken bar). In Figure 4.15 the various curves show the measured values of starting torque and their variation as a result of changes in the relative angle between stator and rotor of a 8 pole, 10 BHP, 220 Volt squirrel cage motor with an insulated cage. These measurements were taken with the cage being complete, ie without any faults and then repeated when the cage had one, two and three adjacent bars broken (all bars being isolated from the same endring). The figure also shows the mean value of the starting torque for each of the above conditions. As expected the average starting torque decreased when the amount of asymmetry introduced into the rotor was increased. Also it is shown that the dependence of the starting torque on the angle between stator and rotor is a function of the amount of the rotor asymmetry.

Figure 4.16 shows the average of the measured values of the starting torque and the pull-out-torque (in pu of the values measured with the cage complete) for the above mentioned motor plotted as a function of the number of adjacent broken bars. It is interesting to note that the characteristics for the ST and POT follow a similar trend(in the case of the cage being insulated). It is evident from the figure that very large reductions in the starting torque and pull-out-torque may be expected in motors having a faulty cage. In the case of an uninsulated cage where inter-bar currents can flow, the changes in the starting torque and pull-out-torque will be different from those that would occur were the cage insulated. This can be illustrated as follows:

It is seen from Figure 4.2 that the percentage of current flowing into the 'broken' bar |Ibb/In| is a function of the ratio |Zb/Rc|. For any particular core length Rc is practically constant and does not vary with frequency in the motoring region. Rc will however be different for other core lengths. Zb, the bar impedance, will vary with frequency and therefore for any particular machine |Zb/Rc| will vary with the frequency. Hence, for any given rotor length and bar dimensions the region around which |Zb/Rc| varies with the frequency will be set by Rc, see Figure 4.17.

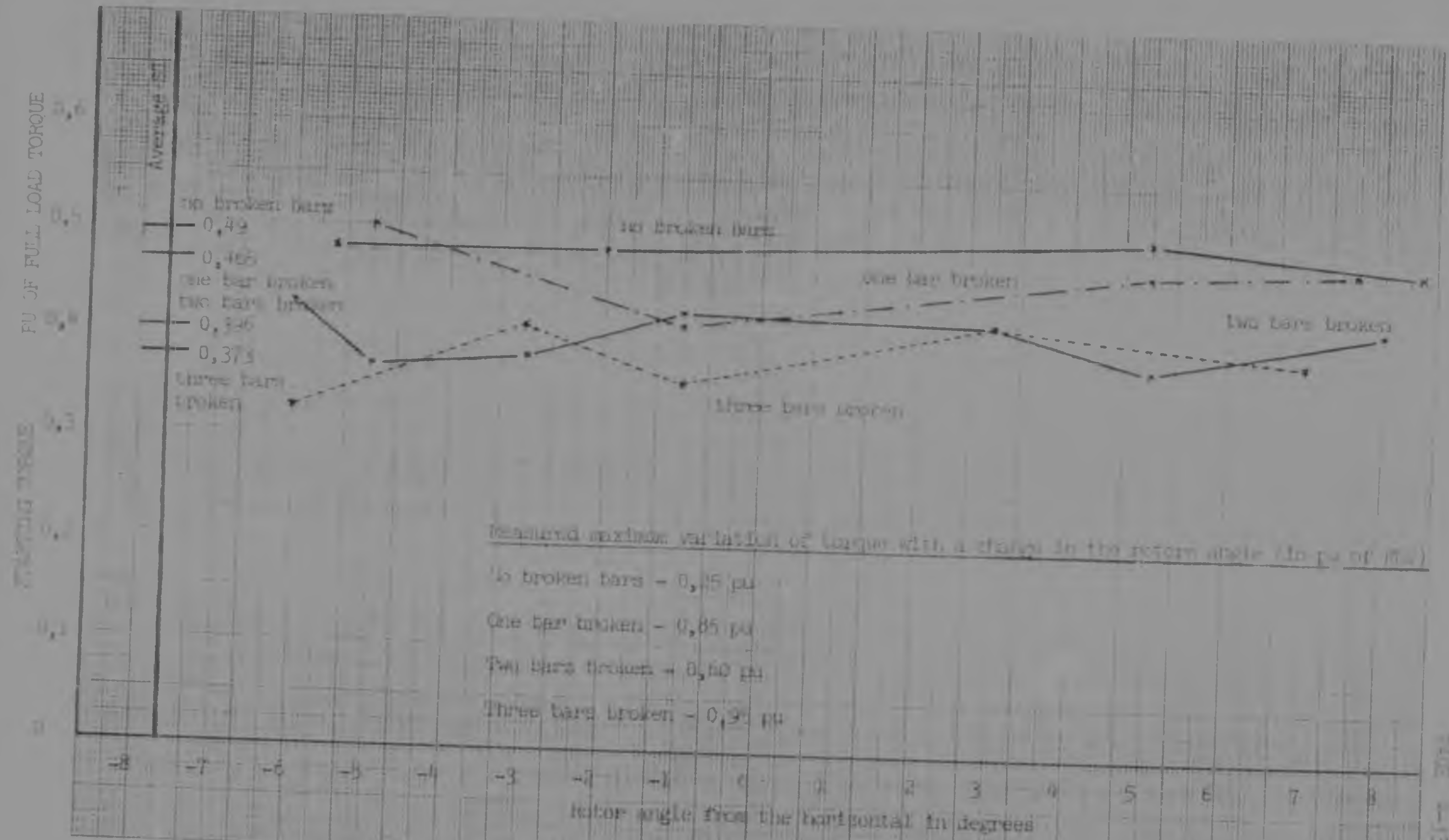

Figure 4.15 - Change in the starting torque of a 8 pole, 10 kW squirrel cage induction motor having an insulated cage, as a function of the number of adjacent bars broken and a change in the relative stator-rotor angle.

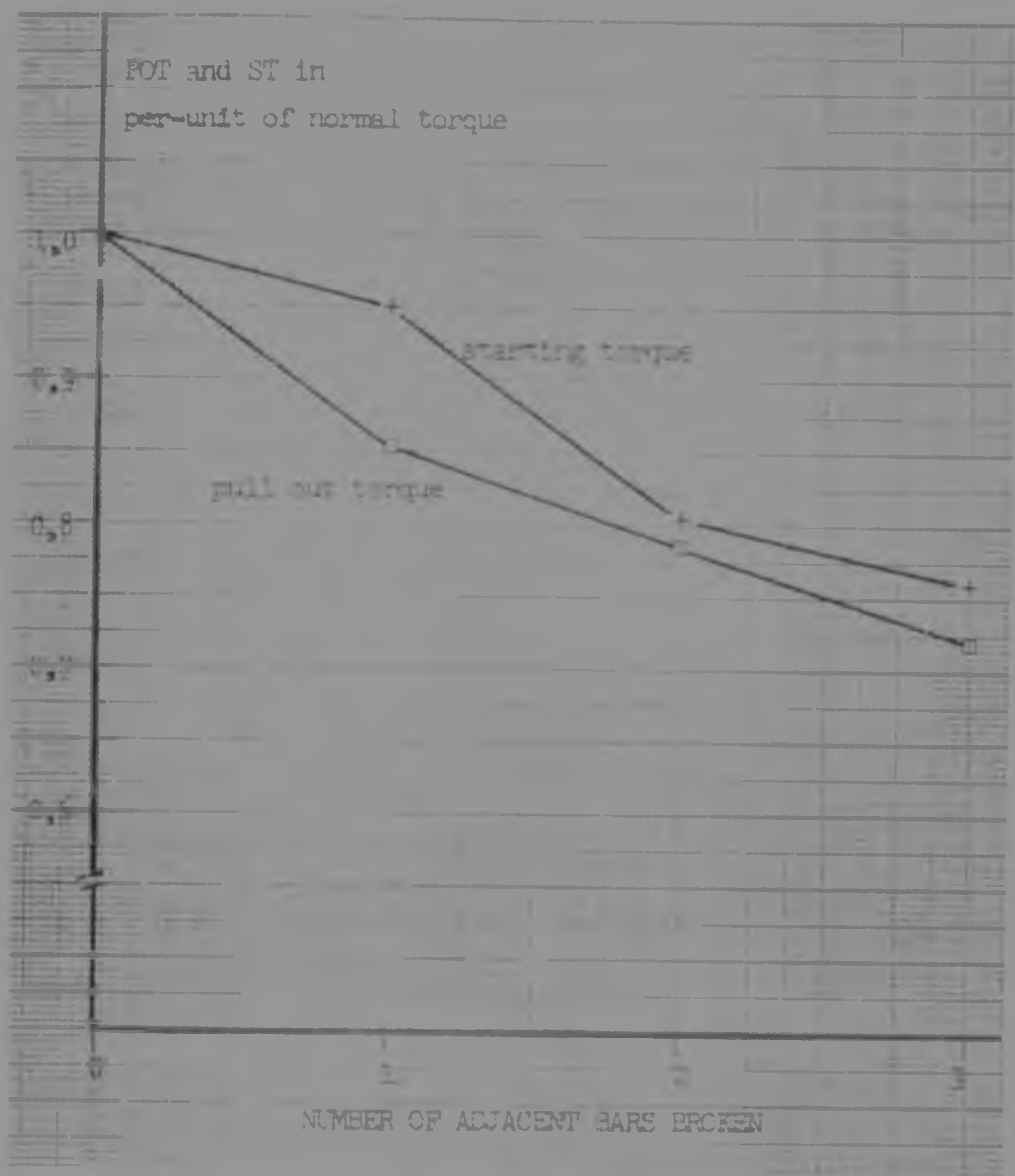

Figure 4.15 - Measured changes of starting torque and pull-out-
torque as a function of the number of adjacent
bars isolated from the same endring.
(Measurements performed on a 8 pole, 10 BHP squirrel
cage induction motor having an insulated cage).

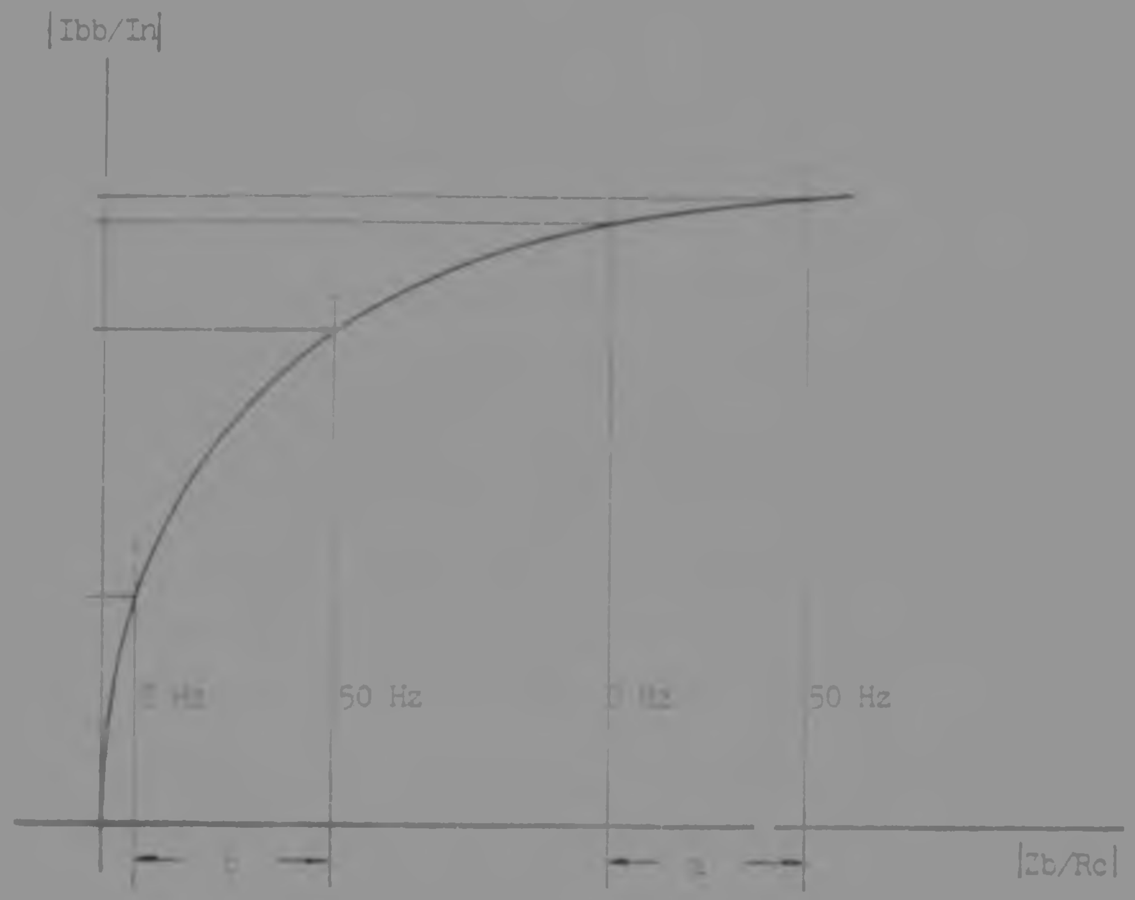

Figure 4.17 - Variation of |Ibb/In| as a function of |Zb/Rc| (as per Fig. 4.2).
For one motor |Zb/Rc| may vary with frequency over region `a' whereas for another motor |Zb/Rc| may vary over region `b'.

Clearly it is seen that in some cases |Ibb/In| may not vary much with the slip whereas in others the variation will be large. For example consider industrial motor A.

It has already been shown on page 4.1Ø that at starting the current flowing into the `broken' bar was practically the same as the current flowing into the `healthy' bars. As a consequence it can be expected that the reduction in the starting torque due to the fault would be small and that the starting torque would not vary with the angle between the stator and rotor. Chapter D, section D.1.2, page D.19 shows the results of starting torque measurements done on industrial motor A under both 'healthy' and 'faulty' conditions. The results obtained from both methods of measurement show no difference at all between the measured starting torque under both conditions. This is in contrast to the measured 5% torque reduction obtained for the 8 pole motor with the insulated cage and having one broken bar, see Figure 4.16.

In the case of the pull-out-torque the ratio |Zb/Rc| must be calculated for low slip. The recordings of the torque-speed characteristics for industrial motor A (see Figure D.30, page D.63) show that the slip in the region of the POT was approximately equal to 125 rpm, ie the rotor frequency was approximately equal to 2 Hertz.
For this frequency the bar resistance Rb is

$$Rb(\text{at } 2\ Hz) = 1,732 \ .\ 10^{-6} \ .\ 45 \ .\ 1/2,28$$
$$= 34,1\ \mu\Omega$$

where 2,28 is the total cross sectional area of the rotor-bar in cm^2.
The slot leakage reactance Xb is

$$Xb(\text{at } 2\ Hz) = 2\pi \ .\ 2 \ .\ 45 \ .\ 3,51 \ .\ 4\pi \ .\ 10^{-9}$$

$= 24,9\ \mu\Omega$

where 3,51 is the value of the bridge and slot permeance at this frequency.

Hence $|Zb| = 42,22\ \mu\Omega$

Rc is again taken as approximately equal to 46 $\mu\Omega$

Therefore $|Zb/Rc| = 0,92$

From Figure 4.2 it is seen that for $|Zb/Rc| = 0,92$ the magnitude of Ibb/In will be approximately equal to 60%. In the region of the POT the rotor currents are relatively high and the fact that Ibb is only 60% of In means that the unbalance will be significant and will give rise to substantial negative sequence currents. These negative sequence currents produce negative torques which result in a large reduction in the value of the POT (See Figure 4.18). This is confirmed by the measured torque speed characteristics of industrial motor A (figures D.31 and D.32, pages D.64 and D.65 respectively) taken under `healthy' and `faulty' conditions. It is seen from the figures that a reduction of 26% in the POT occured.

The observed characteristics of industrial motor A, namely no change in starting torque but a large reduction in pull-out-torque, can only be attributed to the presence of the inter-bar currents. The agreement achived between the theory

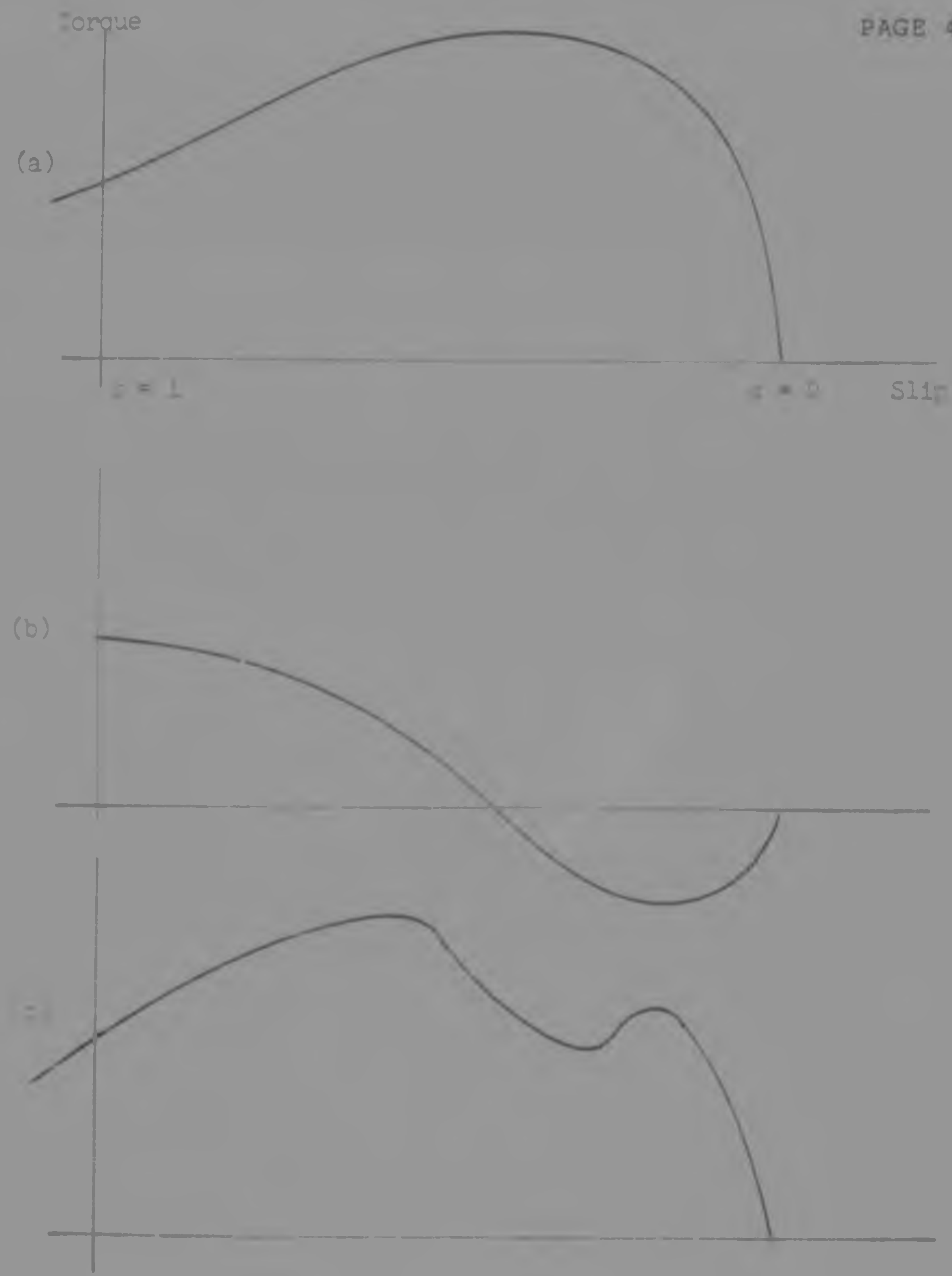

Figure 4.18 - Illustration of the effect of the negative sequence current on the torque of an induction motor.

(a) Fundamental positive sequence torque

(b) Fundamental negative sequence torque

(c) Resultant torque

and the observations lends weight to the validity of this argument. Clearly it is seen that in other machines, there may not be any significant reduction in POT because as the frequency varies $|I_{bb}/I_n|$ does not change significantly.

CHAPTER 5

VIBRATIONS DUE TO UNBALANCE IN THE ROTOR IMPEDANCE

The topics related to the study of vibration patterns in induction motors are probably the most complex to analyse of all topics concerned with this type of machine. The trend to increase the output from ever smaller frame sizes is giving rise to the situation where the limits in the motor design are becoming more and more mechanical in nature. Therefore vibration (and the associated noise), which is the main cause of mechanical failure due to fatigue of the material, is nowdays a main source of concern for motor designers. This problem is further accentuated when induction motors supplied from thyristor controlled inverters run at speeds higher than 3000 rpm (or 3600 rpm with 60 Hz supply). The study of vibrations produced in induction machines is highly complex due to the interaction between electromagnetic and mechanical sources. A comprehensive study of the vibration and noise patterns produced entails analysing all the magnetic fields existing in the airgap, which include the slot ripple harmonics, primary and secondary produced space harmonics, harmonics due to saturation of the iron, homopolar fluxes, etc., as well as all the relevant mechanical characteristics of the machine.

Many authors have studied these phenomena resulting in a large amount of literature being published. In this project the investigation of vibration has been confined exclusively to those vibrations which are a direct consequence of unbalance in the impedance of the secondary (normally the rotor). In particular two pole machines have been considered as these are more prone to suffer from these effects.

It has been pointed out in Chapter 2 how rotor asymmetry gives rise to an asymmetric flux distribution in and around the rotor. The effects on vibration, noise, and speed fluctuations produced by rotor impedance asymmetry are qualitatively similar, irrespective of the exact origin of the unbalance. Hence the results of the investigation done for the unbalance due to broken bars in the rotor cage are, to some extent, applicable to any other type of secondary impedance asymmetry. Broken bars and/or endrings are the most common cause of unbalance in the rotor impedance and are the simplest of all to study experimentally. Therefore this approach was followed in this project.

5.1 - Vibration due to rotor asymmetry and airgap eccentricity. Change in the normal UMP

The more important magnetic forces that are sources of vibration and noise in electrical machines are due to the flux existing in the airgap of the machine. The force of attraction that exists between two infinitely permeable media, which are separated by a vacuum, has the same direction as the magnetic flux and its magnitude per unit of area is given by

$$F = B^2/2\mu_0 \qquad \text{....[5.1]}$$

where B is the flux density and μ_0 the permeability of free space. For all practical purposes related to this work, the core of an induction motor may be considered to be of infinite permeability. This avoids the complication of dealing with the tangential components of the force of attraction which are of secondary importance. The rotor and the stator are both assumed to have smooth surfaces which eliminates the effects introduced by the slots in the airgap flux distribution. Under the above mentioned conditions, and with the rotor being totally concentric with the stator and of perfect circumferential perimeter, the flux shows a pure sinusoidal distribution. If the rotor is slightly off-centered UMP will arise. This exists in differing degrees in every motor, mainly due to the bending of the shaft and the displacement in the vertical direction inside the bearings as a result of the weight of the rotor. Every time a pole of the airgap flux wave passes through the vertical position a physical displacement of the rotor occurs giving rise to vibration having a frequency equal to two times the line frequency. Summers[31] shows that all stator produced space harmonics will give rise to vibrations at twice line frequency worsening this particular type of vibration.

It has been shown by various authors[31,32,33], that broken bars create an asymmetry in the airgap flux distribution which is stationary with respect to the rotor, ie it has the same speed with respect to the stator as does the rotor (1xRPM). This can be explained briefly in the following manner: the ampere-turns of th rotor and the stator tend to balance one another except for the excitation ampere-turns. If a rotor-bar is open circuited and it is assumed that the current flowing in it is less than the normal current, then the ampere-turns produced will also be reduced. The net unbalanced stator ampere-turns will produce an airgap flux density greater than normal at the point of the defective bar. This increased flux density will cause a higher induced voltage and, thus, a higher current in the bars adjacent to the defective bar. Hence, the net effect is that the stator and rotor ampere-turns still balance one another, but the flux distribution in the airgap is altered. This change in flux distribution is most pronounced when the defective bar is under a magnetic pole and least effective when it is between poles. Since the defective bar is passed by a magnetic pole twice for each revolution of slip, inherent 2xRPM frequency vibration is modulated at two times slip frequency. In the analysis of two pole induction motor vibrations, Maxwell[32] shows qualitatively how the vibration caused by an asymmetry in the airgap flux distribution produced by a broken bar may be discerned from that produced by normal UMP. The first produces vibrations at one and twice running speed (ie 1xRPM and 2xRPM), when the later produces vibration at twice line frequency (or twice synchronous speed). Figure 5.1 shows both conditions, ie a stationary airgap asymmetry and a rotating asymmetry, when they exist separately within the motor and when they exist together.

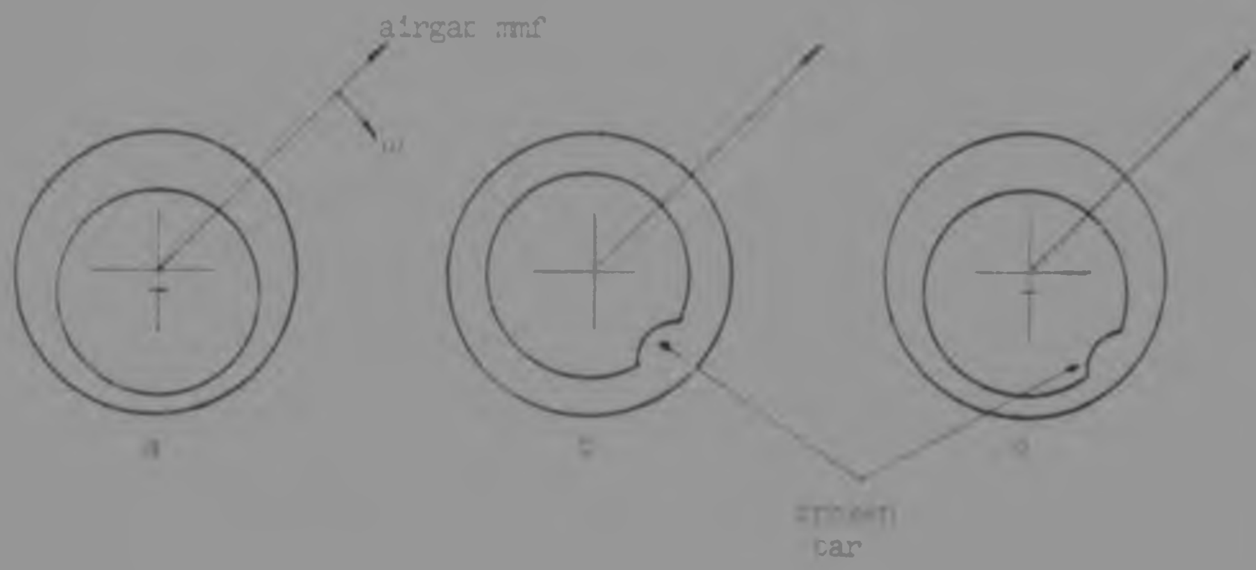

Figure 5.1 - Conditions for vibrations arising from normal UMP interacting with an asymmetry in the airgap due to a broken bar.

(a) Stationary airgap asymmetry: vibration at 2x line frequency

(b) Rotating asymmetry: vibration at 1xRPM and 2xRPM and modulation at 2x slip frequency

(c) Combined unbalance: vibration at all previous modes

In a recent paper, Ito, Fujimoto, Okuda, Takahishi and Watahiki[33] develop a method for the derivation of a quantitative expression for the change in the UMP of squirrel cage induction motors due to broken bars. The method is based on a 'finite element analysis' which is used to solve the fundamental equations of electromagnetism when applied to the airgap of the machine. One of the most interesting results of their research, which is relevant to this work, is an analytical and experimental demonstration of an almost linear relation between the maximum value of UMP and the number of broken bars.

From the comprehensive set of vibration measurements carried out in this project on industrial motors A and B (see figures 5.2 and 5.3 in this Chapter and figures D.11 to D.29, pp.D.23-D.60 and figures D.34 to D.36, pp.D.69-D.71 in Appendix D) experimental confirmation of the items discussed above can be shown. Figures 5.2 and 5.3 show the axial vibration recordings taken on industrial motor A at the non-drive end for two different load conditions. Figure 5.2 is for the case of the 'faulty' cage while Figure 5.3 is for the 'healthy' cage. Comparing the vibration patterns of figures 5.2 and 5.3, shows the increase in the 1xRPM frequency vibration due to the rotating asymmetry created by the broken rotor-bar in he squirrel cage. In Figure 5.2 (the record taken with the 'faulty' cage) a very large increase in the 1xRPM frequency vibration is observed when the load is increased, ie when the slip increases. This is due to the increase in the rotor currents giving a larger degree of unbalance. In the case of the 'healthy' cage, Figure 5.3, when the load is increased the vibration at 1xRPM decreases. This is the normal pattern for large machines due to the forced seating of the rotor in the bearings when the load increases (more prevalent in machines having sleeve bearings, although also present in machines with anti-friction bearings, as is the case with industrial motor A). The increased load currents also slightly reduce the UMP (at 2xRPM frequency) due to the increased saturation. The same phenomenon can be seen on all the other pairs of recordings taken at different locations on the same motor.

On industrial motor B records were taken only for the 'broken' bar condition (see figures D.34-D.36, pp.D.69-D.71). These all show an increase in the 1xRPM frequency vibrations due to the increase of the rotor currents with load.

It must be pointed out that parallel connections of the primary winding which help to reduce the normal UMP are equally effective in reducing the vibrations produced by a faulty cage.

5.2 - Vibration due to interaction between rotor asymmetry and space harmonic fields

The previous analysis concerned itself with vibrations produced due to the rotating main field and also due to an asymmetry in the rotor that rotates with the rotor interacting with the stationary airgap eccentricity. There is, however, another interaction which gives rise to vibration. This is the interaction between the rotating rotor asymmetry (due to the 'broken' bar) and the higher harmonics of the airgap field. These are generally small due to the low magnitudes of the space harmonic fields.

Figure 5.2 - On-load vibration test on industrial motor A (reproduction of Fig. B.7(a))
Red trace = 300kW load; Black trace = 50 kW load.

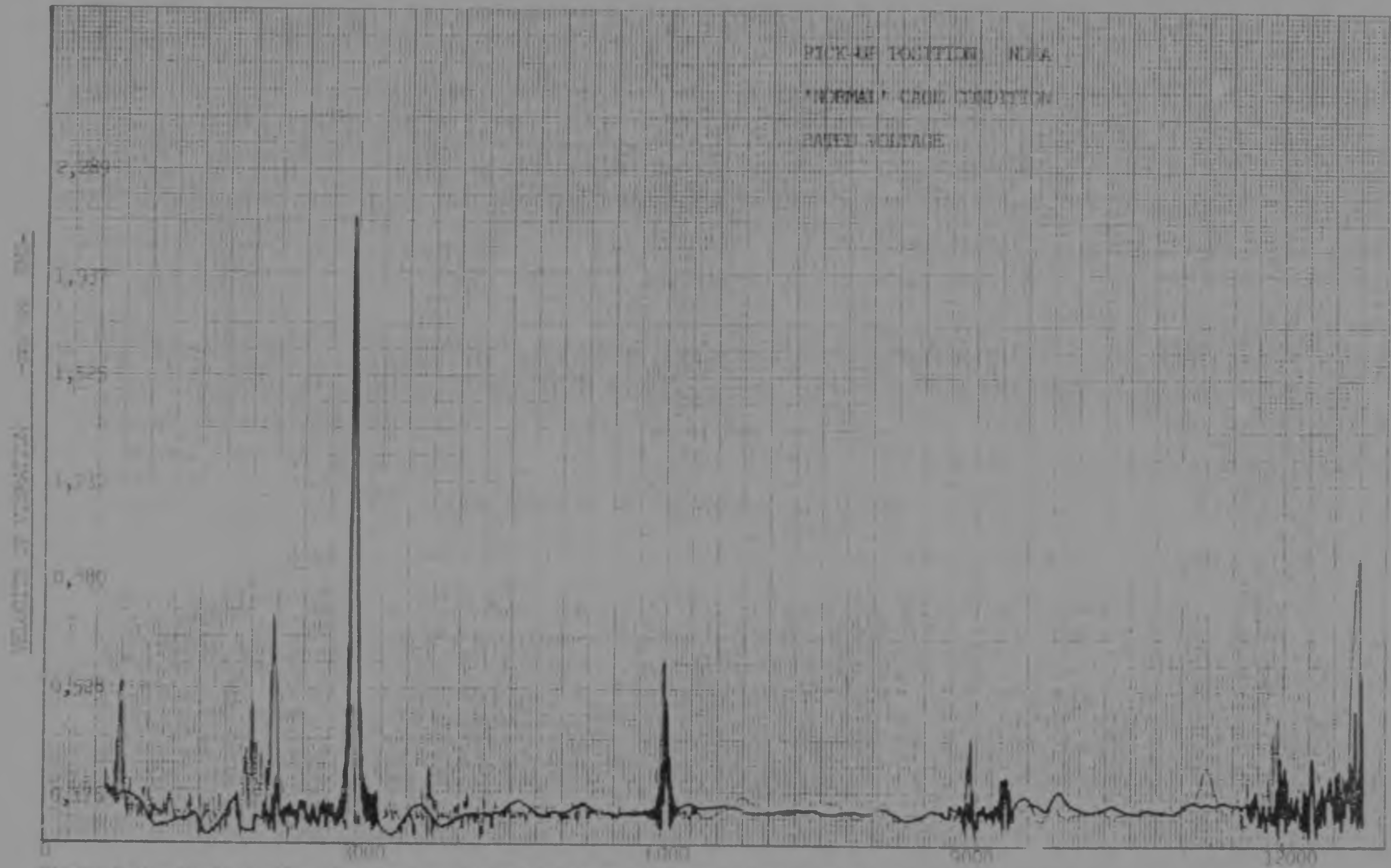

Figure 5.3 - On-load vibration test on industrial motor A (reproduction of Fig. D.21b)
Red trace: 300 kW load; Black trace: 50 kW load.

The frequency of the vibration due to any one space harmonic field is clearly related to the harmonic order and to the speed of the motor. These vibrations are usually insignificant but they do add their share to the overall stress experienced by the faulty machine. This is emphasized if the frequency of one of these vibrations coincides with a mechanical natural frequency of the stator structure.

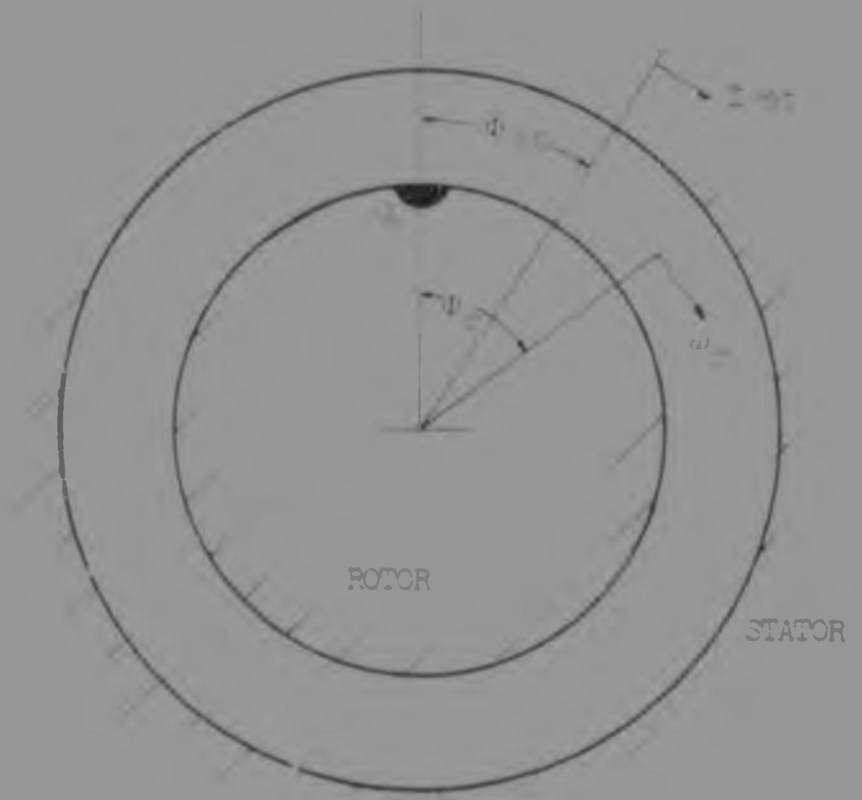

Figure 5.4 - Interaction between stator produced space harmonic of order "t" and the rotating asymmetry "A".

ω_r : angular speed of motor

ω_{st} : angular speed of the stator produced "t"th space harmonic

Φ_{st} and Φ_r : angles swept by the "t"th space harmonic and the rotor in a given time.

The frequency of vibration due to a particular harmonic field will be equal to the number of times the rotating asymmetry (indicated as `A' in Figure 5.4) passes a pole of the harmonic field in one second. If the angular velocity of the rotor is ω_r and that of the "t"th harmonic field is ω_{st}, then the angle covered by each of them in one second will be:

Φ_r (angle covered by the rotor) $= \omega_r .1$

Φ_{st} (angle covered by the "t"th space harmonic field) $= \omega_{st} .1$

Therefore the relative change in the angle between them in one second will be

$$|\Delta\Phi| = |\Phi_r - \Phi_{st}| = |\omega_r - \omega_{st}| \quad \text{radians}$$

But $\omega_{st} = \omega_s / t$

and $\omega_r = (1-s) . \omega_s$

where ω_s is the angular speed of the fundamental field and s is the motor slip.

Therefore $|\Delta\Phi| = |(1-s) . \omega_s - \omega_s /t| = |\omega_s/t[t(1-s)-1]|$ rad.

The angle between two consecutive poles of the "t"th space harmonic field is π/t, so the number of pulsations per second resulting from the interaction of this field and the rotor asymmetry will be:

$$fsr = |\Delta\phi|/|\pi/t|$$
$$= \frac{\omega_0}{\pi}|t(1-s) - 1| \qquad Hz$$

For a two pole motor $\omega_0 = 2\pi f_0$, where f_0 is the frequency of the fundamental field

Therefore $fsr = 2f_0|t(1-s) - 1|$ Hz ....[5.2]

From these results it is clear that the interaction between the stator space harmonic fields and the rotating asymmetry, for motors running close to synchronous speed, will yield vibrations having frequencies high enough to be of practical importance. For example consider the following space harmonic fields: 1; -5; 7; -11; 13. (In two pole motors some of the higher harmonic fields may be large due to the excessive chording of the stator winding). Equation [5.2] gives the frequencies of the vibrations produced by these fields and the values tabulated in Table 5.1 are for those at full speed (ie $s \approx 0$).

The values tabulated in Table 5.1 show that for this phenomenon the frequencies of vibration are relatively high for machines supplied from 50 or 60 Hz networks (and running in the region of rated speed). In the table only one value of frequency appears for each pair of harmonics.

Table 5.1 - Frequencies of vibration for a two pole motor running at synchronous speed resulting from the interaction of the stator created space harmonic fields and the rotating asymmetry due to a broken bar.

harmonic order "t"	fsr (for 50 Hz supply) Hz	fsr rpm
1 (fundamental)	[illegible]	0
-5	600	36000
7	600	36000
-11	1200	72000
13	1200	72000

This is so because in the calculations the slip was taken to be equal to zero. When the machine is running at full speed for each pair of harmonics two values of frequency will be produced, but because the slip is small these frequencies will remain close to the values tabulated in Table 5.1. As already stated these vibrations are small in magnitude, but they may coincide with one of the natural frequencies of the core, in which case resonance occurs resulting in relatively large amplitudes of vibration. It is interesting to note that in their series of papers, Verma and Girgis[34] give theoretical and experimental results for the natural frequencies of stators of electrical machines, and some of the frequencies quoted are of the same order as those in Table 5.1. Some of these vibrations can be annoying as their frequencies fall well within the audio range.

5.3 - Vibrations due to the tangential inter-bar currents

The only mechanical causes of axial vibration in a motor coupled to a load on a test-bed are misalignment of the couplings, misalignment of anti-friction bearings, certain types of rotor unbalance (eg fan mounted skew), and misalignment of friction (sleeve) bearings combined with physical unbalance in the rotor, see Figure 5.5. These result in vibrations having a frequency at one times running speed (1xRPM) and, if the misalignment is severe, at 2xRPM and in some cases at 3xRPM. Vibrations produced by misalignment are exclusively dependent on the actual speed of the motor and will remain practically constant as long as the speed is only slightly changed. As changes in the load of induction motors cause small changes in the speed of the motor, the magnitude of the axial vibration from mechanical sources will remain practically constant once the motor reaches the normal working speed region.

The vibration measurements taken on industrial motor A (Figure 5.2) show that an extremely large axial vibration was present at 4xRPM in the case of the `faulty' cage. The magnitude of this component was totally dependent on the slip of the machine, ie on the magnitude of the rotor-bar currents. This phenomenon occured only when the motor was tested with the 'faulty' cage (ie having one bar open circuited on one side). The vibration patterns in figures 5.2 and D.26 should be compared with those in figures 5.3 and D.27 (figures D.26 and D.27 are in Appendix D, pages D.57 and D.58) which are for the 'healthy' cage condition. The relative changes with load observed in the vibration levels in these figures are tabulated in Table D.27, page D.61.

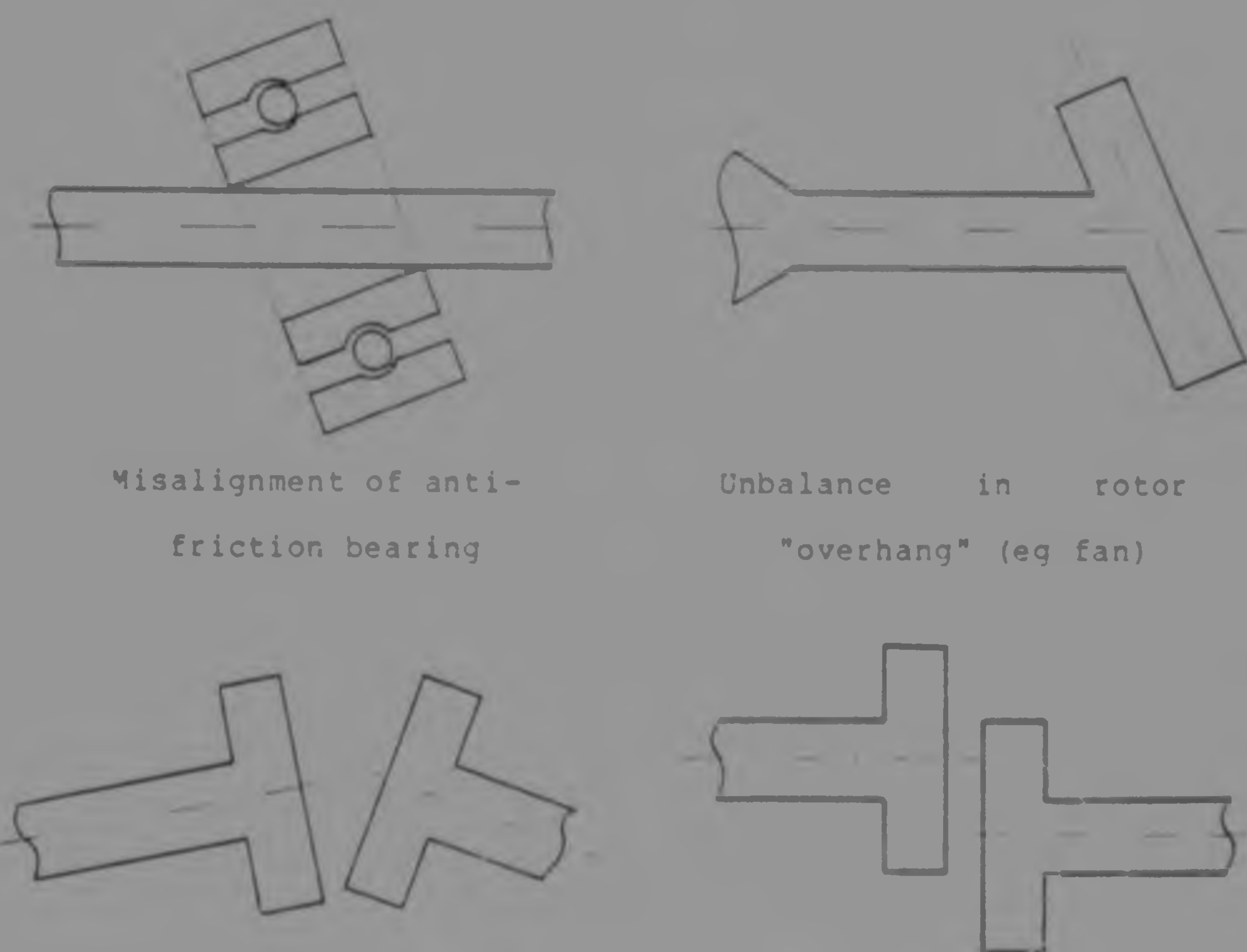

Misalignment of anti-friction bearing

Unbalance in rotor "overhang" (eg fan)

angular offset in coupling

axial offset of coupling

Figure 5.5 - Some of the mechanical sources of axial vibration

As previously stated, mechanical sources cannot give rise to the large magnitude of vibration measured at 4xRPM. Also this cannot be the cause of the vibration being current dependent. Clearly then, the origin of this vibration must be electromagnetic and is closely related to the `broken' bar. A 4xRPM frequency vibration can also be created by a combination of two other vibrations, one at two times line frequency (caused by normal UMP) and the other at 2xRPM (caused by the rotating asymmetry from the `broken' bar). However, the amplitude of the vibration measured at 4xRPM is far larger than the direct summation of these two components and therefore cannot, in any way, account for the large magnitude measured. Furthermore, vibration recordings taken on industrial motor B under `faulty' cage conditions (Figure D.35, page D,70) show that the machine was free from this 4xRPM vibration. There is, however, a very significant difference between these two motors. Motor A had very large inter-bar currents flowing, but because the broken bar in motor B was isolated from both endrings no inter-bar currents could flow. Therefore, it may be concluded, that the large axial vibrations present at 4xRPM in motor A are due to the presence of the large inter-bar currents in the rotor. These currents, which flow tangentially, produce axial fluxes similar to the homopolar fluxes produced by other asymmetries in the motor, but the magnitude is far larger. These fluxes due to the inter-bar currents are totally dependent on the motor slip because the magnitude of the inter-bar currents is dependent on the slip. This explains the strong correlation measured between the 4xRPM axial vibration and the motor load. To date several papers[10,11,12,13] have been written on the production of homopolar fluxes in induction machines. Some of these examine how rotor-stator eccentricity affects the creation of homopolar flux[13], and others propose methods to detect machine unbalance through the analysis of the homopolar axial flux[11,12]. However, in the literature surveyed, there is no mention of inter-bar currents being a source of axial flux and consequently of axial vibration. This is hardly surprising as the presence of large inter-bar currents in faulty cages has previously not been accounted for.

In Chapter 4, an expression for the current flowing into the `broken' bar was developed, namely:

$$Ib(x) = (In/2)[1 - (\cosh \lambda x/\cosh \lambda \ell)]$$

and the distribution of the magnitude of the current flowing from the `broken' bar into the core was given as:

$$|\delta Ic(x)| = |dIb(x)/dx| = |(\lambda In/2).(\sinh \lambda x/\cosh \lambda \ell)|$$

From Amperes law ($\oint H.dl = \int (Jc + \partial D/\partial t).ds$) it can be shown that if $J(x)$ is taken as a two dimensional sheet of current density flowing from bar-to-bar, and if a point $x = a$ is choosen such as $0 \leq a \leq \ell$, then it can be shown that the intensity of the magnetic field at $x = a$ produced by an element of inter-bar current of magnitude $\delta Ic(x).dx$ flowing into the core at a point x is given by

$$dH(x=a) = [\ \delta Ic(x).dx/2\pi(a-x)]$$

for any x between zero and "a", and

$$dH(x=a) = [\ \delta Ic(x).dx/2\pi(x-a)]$$

for any x between "a" and "ℓ".

Therefore the value of the flux density $B(x=a)$ due to the total inter-bar current flowing along the entire core is given by

$$B(x=a) = \mu_o \int_0^a [\ \delta Ic(x)/2\pi(a-x)].dx \; - \; \mu_o \int_a^{\ell} [\ \delta Ic(x)/2\pi(a-x)].dx \qquad \ldots.[5.3]$$

It is evident from equation [5.3] that the flux distribution created by the inter-bar currents varies axially along the motor (as a result of the function $\delta Ic(x)$ being asymmetric along the machine). This gives rise to axial asymmetry in the radial flux distribution which cannot be compensated for by the primary winding current, see Figure 5.6. This phenomenon gives rise to the axial vibrations present. A most interesting feature arising from this axial distribution of the flux is that the axis of the so produced axial field is not parallel to the axis of the machine, see Figure 5.7.

As the currents flow from the 'broken' bar into the core in opposite directions, four poles of axial flux are produced which are not evenly distributed around the circumference of the machine (see Figure 5.7). These four poles which rotate at full speed are the cause of the axial vibrations having their largest magnitude at 4xRPM frequency.

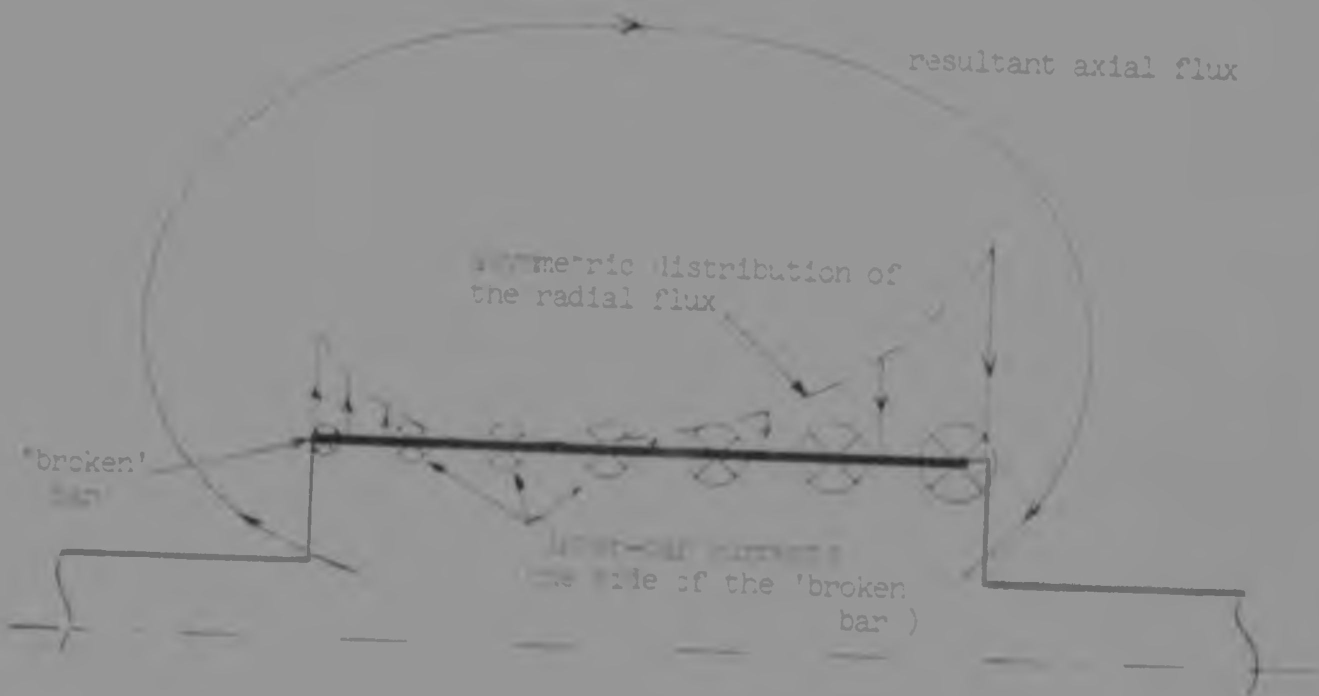

Figure 5.6 - Schematic diagram showing how the non-linear distribution of the inter-bar currents gives rise to an asymmetric distribution of the radial flux density.

The frequency of the rotor currents is slip frequency, hence the vibration at 4xRPM is modulated at twice slip frequency, see Figure D.26, page D.57. As a result of this axial flux being asymmetrically distributed around the circumference, large harmonic and subharmonic vibrations can be expected (see Figure D.23a, page D.54). These vibrations appear only

As the currents flow from the `broken' bar into the core in opposite directions, four poles of axial flux are produced which are not evenly distributed around the circumference of the machine (see Figure 5.7). These four poles which rotate at full speed are the cause of the axial vibrations having their largest magnitude at 4xRPM frequency.

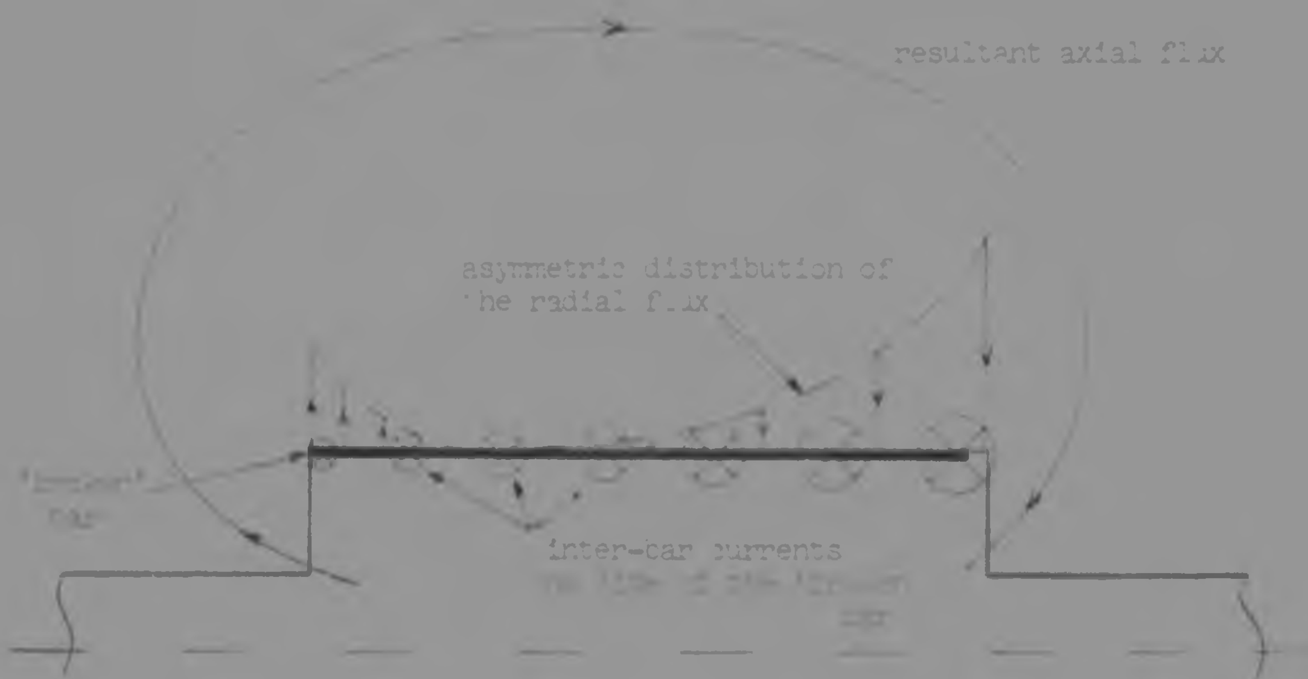

Figure 5.6 - Schematic diagram showing how the non-linear distribution of the inter-bar currents gives rise to an asymmetric distribution of the radial flux density.

The frequency of the rotor currents is slip frequency, hence the vibration at 4xRPM is modulated at twice slip frequency, see Figure D.26, page D.57. As a result of this axial flux being asymmetrically distributed around the circumference, large harmonic and subharmonic vibrations can be expected (see Figure D.23a, page D.54). These vibrations appear only in the axial direction which tends to confirm the above theory. It must be realized that the frequency of 4xRPM is a direct result of having only one bar broken (or a group of adjacent bars broken). Other configurations of faults in the cage will probably produce axial vibrations having frequencies equal to different multiples of the running speed.

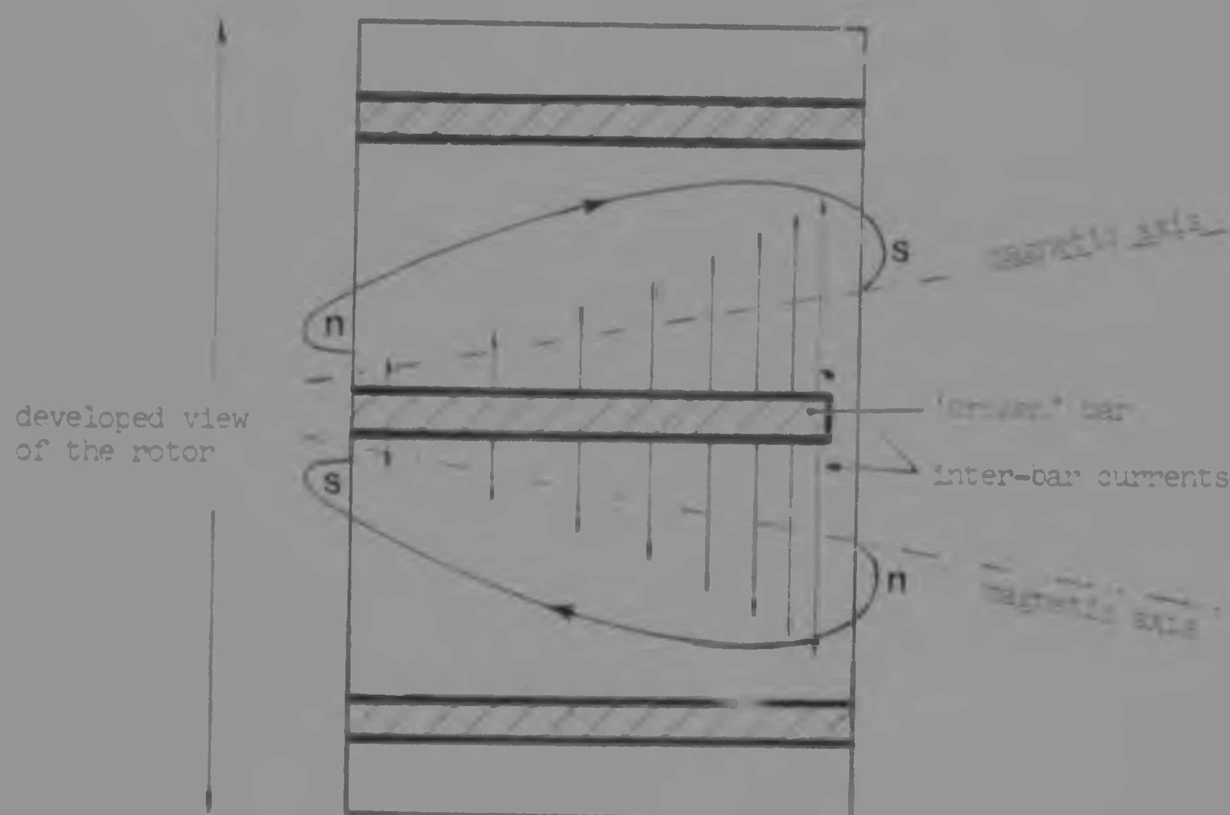

Figure 5.7 - Developed view of the rotor showing the axial fluxes produced by the inter-bar currents flowing from the `broken' bar into the core.

Therefore the strongest indication of a faulty cage is not the actual frequency of the axial vibrations, but the fact that they will always be largely dependent on the magnitude of the rotor current (or the slip of the machine).

CHAPTER 6

CHANGES IN THE HARMONIC SPECTRUM OF THE PRIMARY CURRENT DUE TO BROKEN CAGE-BARS AND/OR ENDRINGS

A great deal of work has been done during recent years to develop reliable techniques which allow faults in the squirrel cage of induction motors to be detected, particularly in large industrial motors working under harsh conditions (eg many DOL startings per hour, high inertia loads, etc.). The aim is to achieve early detection of developing faults to avoid extensive and expensive overall damage to the motor. The existing practical approaches to the solution of the problem fall into three main categories; speed fluctuation monitoring[7,8], vibration and noise monitoring (including electromagnetic noise)[9,10] and axial flux monitoring[10,11,12]. The first two techniques are based on monitoring the mechanical effects produced by the rotor unbalance while the last one monitors the electromagnetic source itself.

During the early part of this investigation the Author proposed a new technique, as described further on, for detecting developing and/or existing rotor cage faults. A little later Hargis, Gaydon and Kamash[7] and Steele, Ashen and Knight[13], proposed <u>the same</u> technique. It is interesting to note that research workers so far removed from each other, and without any knowledge of each other's work, showed that this method of rotor cage fault detection is viable and practical. However the other researchers[7,13] do not give any indication of which additional harmonic components can be expected to appear in the stator current and how these shift in the spectrum with changes in speed.

This new method is based in the fact that electromagnetic asymmetries existing in an induction machine give rise to additional time harmonics in the spectrum of the primary current. This spectrum can be monitored periodically or continuously allowing developing faults to be detected. The analysis presented here only explains the origin of the additional current time harmonics that appear in the primary current spectrum, ie it allows the frequencies and frequency shifts due to changes in the slip of the motor to be predicted. It does not predict the amplitudes of these harmonics. It is the author's opinion that it is practically impossible to accurately predict the harmonic magnitudes, given the large number of unknown parameters involved. Hargis, etc.[7] give an expression for the value of the magnitude of the $(1-2s)f_{\beta}$ component that appears as a function of the number of broken bars. However, the values predicted by using this expression were found to be totally inconsistent with the measured values obtained from the experiments carried out in this project.

6.1 - Current harmonic spectrum

The approach followed here for the development of the equations describing the current spectrum is similar to that taken by Penman, Hadwick and Stronach[11,12]; the main difference being that the production of space harmonics due to the secondary asymmetry is also included. Therefore in this work the emphasis is on the negative sequence rotor induced currents and the space harmonic fields produced by them.

If the fundamental mmf space wave produced by the primary has a velocity with respect to the stator of $V1s$ and a wavelength $\lambda 1$, then the velocity of the "t"th space harmonic field with respect to the stator is:

$$Vts = V1s/t$$

and the wavelength is

$$\lambda t = \lambda 1/t$$

The rotor moves with velocity Vr, with respect to the stator, and hence the relative velocity of the stator produced "t"th harmonic fields with respect to the rotor will be

$$Vtr = (V1s/t) - Vr$$

These stator fields will induce emf's and hence currents in the rotor circuit having frequencies given by

$$ftr = Vtr/\lambda t$$

However, these rotor currents will not form a balanced three phase set as long as there is some unbalance in the rotor cage. Consequently the unbalanced rotor currents can be split into positive and negative sequence componenets[27,28,29]. Each of these component currents will give rise to a family of harmonic fields in the airgap, the positive sequence of order "t" giving rise to one set of harmonic fields and the negative sequence harmonic currents of order "t" giving rise to a second set of harmonic fields rotating in the opposite direction. It should be noted that the positive sequence rotor currents produce some fields that rotate forward and some that rotate backwards. Likewise the negative sequence rotor currents produce fields of the same harmonic order but each of these rotates in the opposite direction to that of its positive sequence current produced counterpart. The velocities of these fields relative to the rotor are given by

$$Vqr = \pm Vtr/q = \pm [(V1s/t) - Vr]/q \qquad ....[6.1]$$

where

Vqr is the velocity of the "q"th space harmonic field produced by the rotor,

"q" is the rotor harmonic order,

the +/- signs take account of the respective directions of rotation of the fields due to the positive and negative sequence rotor currents.

The velocity of these space harmonic fields with respect to the stator is given by:

$$V = Vr \pm Vqr$$
$$= Vr \pm [(V1s/t) - Vr]/q \qquad \text{....[6.2]}$$

and the frequencies of the currents induced back into the primary (and hence into the supply) by these fields are given by

$$fp = (|t|/\lambda 1).\{Vr + [(V1s/t) - Vr]/q\}$$

for the fields due to the positive sequence rotor currents

and $$fn = (|t|/\lambda 1).\{Vr - [(V1s/t) - Vr]/q\}$$

for the fields due to the negative sequence rotor currents. Substituting $Vr=(1-s)V1s$ in the above expression gives:

$$fp = (|t|/\lambda 1).[t(q-1)(1-s) + 1]/(t.q) \qquad \text{....[6.3]}$$

$$fn = (|t|/\lambda 1).[t(q+1)(1-s) - 1]/(t.q) \qquad \text{....[6.4]}$$

where s is the slip of the motor.

Clearly the rotor unbalance emphasizes the negative sequence currents, and hence, their associated fields. Therefore the frequencies of the primary induced currents due to the rotor unbalance will be identified as in equation [6.4]. Also equations [6.3] and [6.4] may be combined to yield a general expression for the harmonic currents induced in the primary, ie:

$$f = f_o \,|[t\,q \mp 1)(1-s) \pm 1]/q| \qquad \ldots.[6.5]$$

Equations [6.3], [6.4] and/or [6.5] are general, but it should be realized that not all the values of "t" and "q" will exist for every motor due to the different winding factors, type of connections, etc. applicable to the respective motors. The values of "t" and "q" applicable for each case may be assessed by using the guidelines laid down by Landy[20].

It is interesting to note that the rate of change of the frequencies of the stator time harmonic currents with the slip, are different. This is easily seen by differentiating equation [6.5] with respect to the slip, ie:

$$|df/ds| = f_o \,|t(q \mp 1)/q| \qquad \ldots.[6.6]$$

It can be seen from equation [6.6] that for high primary space harmonic orders ("t" large) and low secondary space harmonic orders ("q" small) the frequency change (shift) with slip, of the time harmonic primary currents, will be large.

6.2 - Experimental verification of equations [6.5] and [6.6]

equations [6.3] and [6.4] may be combined to yield a general expression for the harmonic currents induced in the primary, ie:

$$f = f_o \,|[t(q \mp 1)(1-s) + 1]/q| \qquad \ldots.[6.5]$$

Equations [6.3], [6.4] and/or [6.5] are general, but it should be realized that not all the values of "t" and "q" will exist for every motor due to the different winding factors, type of connections, etc. applicable to the respective motors. The values of "t" and "q" applicable for each case may be assessed by using the guidelines laid down by Landy[20].

It is interesting to note that the rate of change of the frequencies of the stator time harmonic currents with the slip, are different. This is easily seen by differentiating equation [6.5] with respect to the slip, ie:

$$|df/ds| = f_o \,|t(q \mp 1)/q| \qquad \ldots.[6.6]$$

It can be seen from equation [6.6] that for high primary space harmonic orders ("t" large) and low secondary space harmonic orders ("q" small) the frequency change (shift) with slip, of the time harmonic primary currents, will be large.

6.2 - Experimental verification of equations [6.5] and [6.6]

In order to verify the frequencies and frequency shifts given by equations [6.5] and [6.6] tests were performed on a 8 pole, 220 Volt, star-connected, 10 BHP squirrel cage induction motor having 72 stator slots housing a single layer full pitched concentric winding. The squirrel cage is made up of a single layer of 47 bars butt-brazed to two endrings. The measurements were taken with no bars broken in the cage and then subsequently repeated with one, two and three adjacent bars broken at the same end.

Table 6.1 shows the calculated values of the frequencies of the harmonic currents as indicated by equation [6.5] together with the shift in frequency (as per equation [6.6]) for an assumed change in slip of 2% ie ds=0,02 (or 15 rpm for the eight pole motor tested). For each combination of "t" and "q" the table gives two harmonic frequencies and next to each one the shift value is given in brackets; the upper values being for the fields induced by the positive sequence rotor currents (equation [6.3]) and the lower values being for the fields induced by the negative sequence rotor currents (equation [6.4]). The harmonic orders "t" and "q" are consistent with the complete machine being taken as 'p' times the fundamental wavelength. In Table 6.1 only the lower order time harmonics of the stator current have been considered since the amplitudes of the these induced stator currents are inversely proportional to their harmonic order. Also, besides this, all harmonic amplitudes are dependent on their respective winding factors and the type of connection used (parallel or series).

When the motor was supplied at reduced voltage it ran at approximately 700 rpm, ie with a slip of 6,7%. Therefore this value of slip was chosen when evaluating the frequency values given in Table 6.1. (All values have been rounded to the nearest integer except for exact half values which have been left). In the table t=1 and q=1 correspond to the stator and rotor electrical fundamental respectively.

Figures 6.1, 6.2, 6.3 and 6.4 show the primary current spectrum of the test motor. All pictures were taken for similar voltage and slip conditions, namely 30 volt (line) with the motor running on no-load. Figure 6.1 is for the case when no broken bars were present in the squirrel cage. Figures 6.2, 6.3 and 6.4 are for one, two and three adjacent bars broken respectively. It is clear from these stator current spectra that new time harmonics appear and that their magnitudes are related to the degree of unbalance introduced into the rotor (eg a 43 Hz component appears).

It should be noted that not all the harmonics shown in the spectra are significant and need be taken into account because their magnitudes are very small (the vertical scale is logarithmic). In Figure 6.3, for example, the 20 Hz harmonic has an amplitude of only 0,126% of that of the fundamental while that of the 43 Hz harmonic is 10% of the fundamental. The larger harmonics are from the lower values of the "t" and "q" series so that they may easily be identified in Table 6.1.

The validity of the harmonic frequencies given in Table 6.1 is clearly established in Figure 6.3. For example for "t" and "q" both equal to one, the electrical fundamental fields, the frequency due to the positive sequence rotor current is, as expected, 50 Hz, while that due to the negative sequence rotor current is 43 Hz. (The agreement between the measured and predicted values is well within the frequency tolerance expected due to the assumed 2% difference in the slip between the actual measured speed and that used in the calculations). The other harmonics that appear in Figure 6.3 can be related to corresponding values in the table, but it is the author's opinion that the harmonic stator current due to the negative sequence fundamental rotor current should be used as the basis for analysing and identifying secondary machine unbalance. This is so because this is the largest harmonic present in the stator current spectrum that results from this form of unbalance.

Figure 6.5 shows the current spectrum for the motor under test with two adjacent broken bars (as was the case for Figure 6.3 but in this case the rotor current and motor slip were larger as the voltage was further reduced). Figure 6.6 is also for two broken bars, but here the voltage was increased, giving a corresponding reduction in the rotor current and slip. If the spectra in figures 6.3, 6.5 and 6.6 are compared, it is clearly seen that the harmonics shift in frequency, as expected, due to the change in slip. Some harmonics shift to the left of the spectrum and some to the right in accordance with the direction in which their constituent space harmonics rotate in the airgap of the machine.

Table 6.1 - Table of frequencies (in Hz) of stator current time harmonics due to both positive (upper values) and negative (lower values) sequence rotor currents for the 8 pole, 10BHP motor. - Slip: 6,7%; ds = 2% -

t \ q	1/2	1	2	3	4	5
-5	333 (5) 800 (15)	50 (0) 517 (10)	92 (2,5) 375 (7,5)	139 (3) 328 (6)	162,5(4) 304 (6)	177 (4) 290 (6)
-2	193 (2) 380 (6)	50 (0) 236 (4)	22 (1) 165 (3)	46 (1) 141 (2)	57,5(1) 129(1,5)	65 (2) 122 (3)
1	53 (1) 40 (3)	50 (0) 43 (2)	48 (0,5) 45 (1,5)	48 (1) 46 (1)	47,5(1) 46 (1)	47 (1) 46 (1)
1/2	77(0,5) 30(1,5)	50 (0) 3 (1)	37 (≅0) 10 (1)	32(≅0) 1 (1)	30 (≅0) 17 (1)	29(≅0) 18 (1)
1/4	88 (≅0) 65 (1)	50 (0) 27(0,5)	31 (≅0) 7,5(≅0)	24(≅0) 1(≅0)	21 (≅0) 2 (≅0)	19 (≅0) 2(≅0)
4	87 (4) 460 (12)	50 (0) 323 (4)	118 (2) 255 (6)	141 (2) 232 (5)	152,5(3) 221 (5)	159 (3) 214 (5)
7	227 (7) 880 (21)	50 (0) 603 (14)	188 (3,5) 465 (10)	234 ( ) 419 ( )		

The results clearly demonstrate that this technique of examining the stator (primary) current spectrum is quite feasible for detecting asymmetry in the cage of a squirrel cage induction motor. The method of examining the axial flux produced has been used to determine stator faults only[11,12], but axial fluxes are produced by both stator and rotor asymmetries.

Clearly it is not always possible to predict the magnitude of the current harmonics in the stator because of the uncertainty in the nature of the fault, eg broken bars or broken rings or any combination of these. However, this method lends itself to a comparison technique where previous and recent spectra can be compared to evaluate the state of the rotor cage and hence assess whether any fault is present or developing.

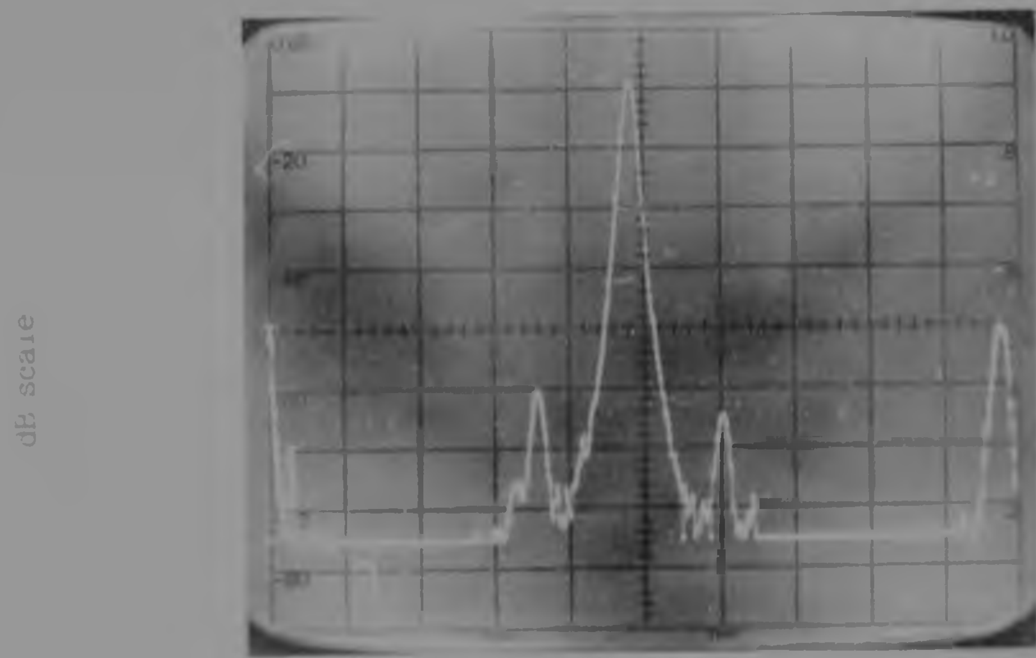

Figure 6.1 - Primary current spectrum - NO BROKEN BARS -

VERTICAL: logarithmic scale
HORIZONTAL: linear scale (10 Hz per Div.)
NOTE: In all spectra shown the trace is shifted approximately 2 Hz to the left

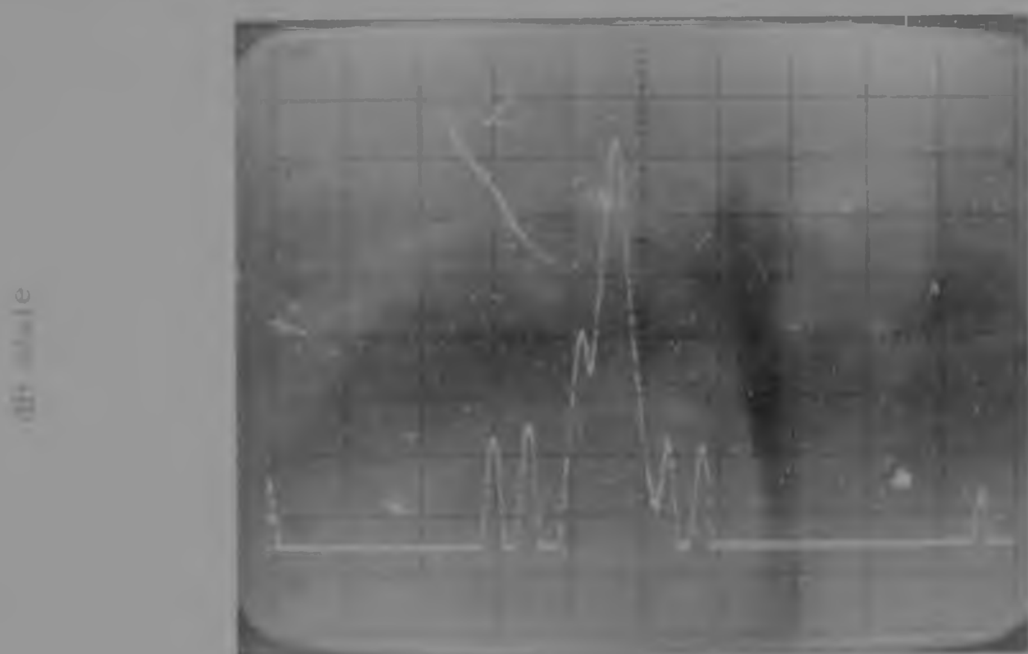

Figure 6.2 - ONE BROKEN BAR -
Scales as for Figure 6.1

dB scale

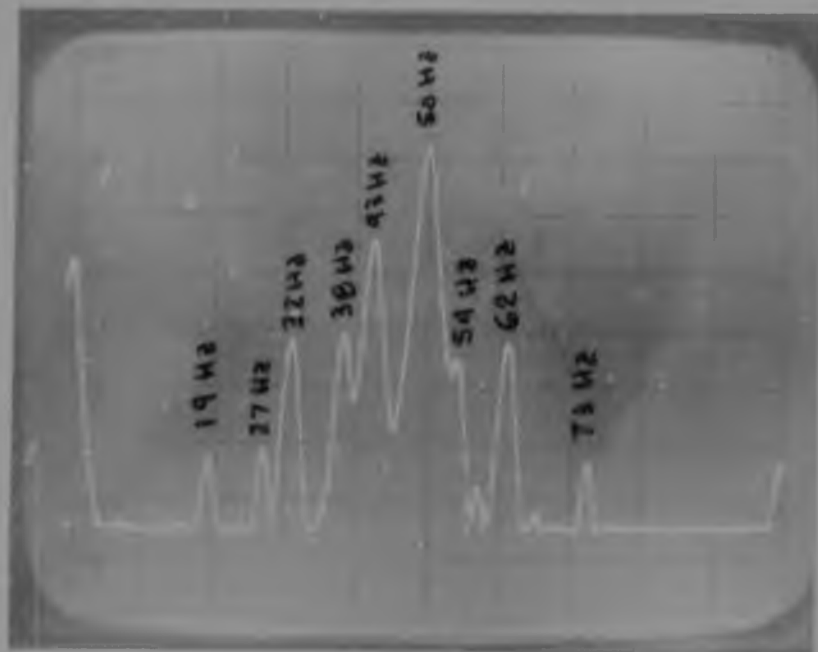

Figure 6.3 - TWO ADJACENT BROKEN BARS -
Scales as for Figure 6.1

dB scale

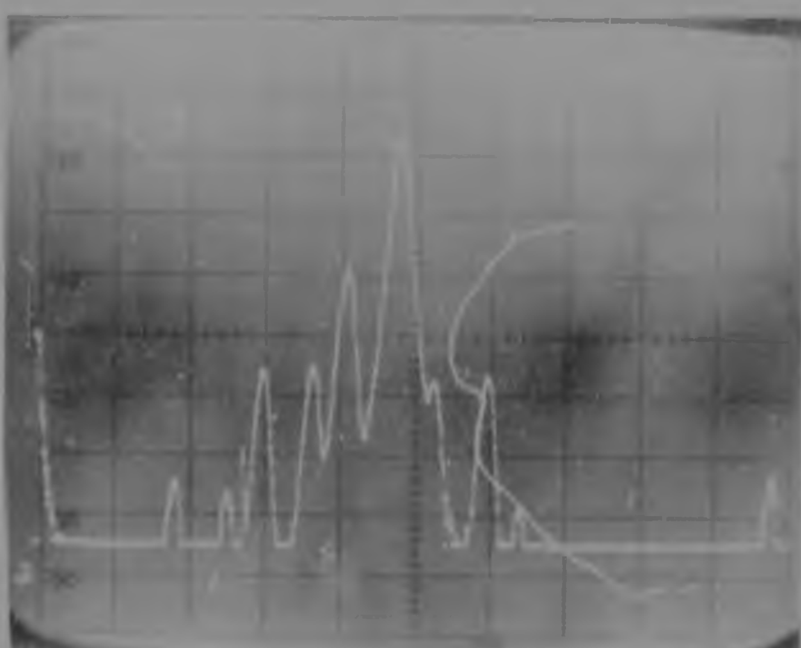

Figure 6.4 - THREE ADJACENT BROKEN BARS -
Scales as for Figure 6.1

Figure 6.5 - TWO ADJACENT BROKEN BARS, voltage
slightly lower than in Figure 6.3
Scales as for Figure 6.1

Figure 6.6 - TWO ADJACENT BROKEN BARS, voltage
slightly higher than in Figure 6.3
Scales as for Figure 6.1

CHAPTER 7

CONCLUSIONS

The main objective of this project was to investigate the effects produced in a squirrel cage induction motor having unbalance in the secondary winding impedance. In surveying the literature it soon became evident that the models proposed by the previous researchers to explain the phenomena observed were inadequate because they neglected the presence of inter-bar currents in the iron. As the initial measurements taken showed that substantial inter-bar currents were present, it became clear that in order to adequately explain the consequences of having such unbalance in the rotor cage (usually a broken bar or endring), these currents had to be taken into account. The approach followed in this project and the model presented take account of these inter-bar currents and thereby provide full explanations for many of the phenomena observed, the presence of which were previously not predictable. The excellent agreement achieved in every case between the measured results and those predicted using the proposed techniques clearly demonstrates that the main objective of this project has been realised. Also, once the observed effects of having a broken bar and/or endring could be adequately explained, it became possible to propose a method to diagnose the presence of such a fault in a motor.

The existence of inter-bar currents when analysing squirrel cage motors having faulty cages has been neglected by the previous researchers. In this investigation it has been shown that in most cases this assumption is erroneous, particularly in large industrial machines. The effects of having inter-bar currents present are that there is no significant reduction in the starting torque, there may be a substantial reduction in the pull-out torque, substantial axial vibrations are produced which are load dependent and the rotor laminations in the region adjacent to the fault could be burnt. In order to be able to fully assess these effects it is imperative to predict, with reasonable accuracy, the magnitude of these inter-bar currents and their distribution along the axial length of the rotor core. The theory and equations developed in this work enable these currents and their distribution along the core to be predicted. In this respect it is interesting to note in Figure 4.5, page 4.16, that the bulk of the inter-bar current exists in the core at the end closest to the fault. It is shown that the concentration of the inter-bar current at the end closest to the fault is governed by the rotor geometrical and electrical parameters. Also it is shown that this non-uniform current distribution in the axial direction gives rise to a corresponding non-uniform axial distribution of the radial airgap flux. That is, the airgap radial flux density varies along the machine in the axial direction and must give rise to resultant axial fluxes which are the source of additional axial vibrations. This aspect has not been recognised by the previous researchers.

The understanding gained by investigating and analyzing the inter-bar currents present in a rotor having a cage fault led to the development of the diagnostic procedure for detecting such faults. It has been shown in this project and almost simultaneously by the other researchers[7,13] that when such faults occur additional stator current harmonics appear. However, if substantial inter-bar currents exist implying that current flows in the broken bar, these induced stator harmonic currents may not be emphasized. This implies that this method of detecting cage faults is not singularly conclusive. When these inter-bar currents are present then, as has been shown in Chapter 5, substantial axial vibrations are produced. Therefore the diagnostic procedure recommended in this project is to measure both the axial vibration and the spectrum of the stator current. In this way no anomaly occurs as when the inter-bar currents are large, the axial vibrations will be large while the induced stator harmonic currents will be small and vice versa when the inter-bar currents are small. The current distributions described by equations [4.5] and [4.7] hold for the case where the bar is broken adjacent to one endring (which is the more common of such faults). For other types of cage faults (eg a broken bar midway along the core) the current distribution will be different. However it is the author's belief that significant inter-bar currents and their associated effects will still occur. This aspect forms the basis for further research which is at present being undertaken.

There is no doubt that there are considerable financial benefits to be gained if such faults can be detected before the motor finally fails. Therefore the author sincerely hopes that the results presented in this project will be beneficial to the manufacturers and users of large induction motors.

APPENDIX A

CALIBRATION OF THE TOROIDAL COILS

The amplifier-integrator circuit of Figure A.1 was previously developed and succesfully used by Landy[20]. In the present investigation a gain of 100 for the amplifier and a gain of 100 for the integrator circuit was used during the tests carried out on industrial motor A. Landy[20] tested the toroidal coil calibration and the measuring circuit for frequencies of up to 5 kHz and showed that the currents could be measured with an accuracy of 0,5%.

The calibration constant of each toroidal coil was obtained by passing known sinusoidal currents through a segment of bar, identical to that of the rotor-bars, and on which the toroidal coils were wrapped. The output of the toroidal coils was first amplified and then integrated.

Tables A.1 to A.4 show the measured calibration values for the sinusoidal current of 50 Hz. These measured values were used to plot the calibration curves given in figures A.2 and A.3. It is seen from these curves that the response of this current measuring system is linear. The resultant calibration constants are tabulated in Table A.5. Figure A.4 shows the circuit used for the calibration of the toroidal coils. The waveform obtained from the integrator circuit was compared with the actual waveform as displayed on an oscilloscope via a shunt in the circuit. The difference in the calibration constants obtained for the toroidal coils are due to the different number of turns and mean length of each of the coils. A typical current waveform and spectrum obtained by using this method are shown in figures D.7 and D.9, pages D.16 and D.18 respectively.

Table A.1 - Results of calibration of toroid B

Bar current A	Integrator o/p mV
26	15
50	29
64	41
100	52

Table A.2 - Results of calibration of toroids A and C

Bar current A	Integrator o/p mV
31	15
51	27
76	39
100	51

Table A.3 - Results of calibration of toroid D

Bar current A	Integrator o/p mV
31	16
51	27
74	40
100	54

Table A.4 - Results of calibration of toroid E

Bar current A	Integrator o/p mV
34	17
51	26
74	37
100	50

Table A.5 - Average calibration constant obtained from the curves in figures A.2 and A.3

Toroidal coil	Average calibration constant A/mV
B	1,74
A and C	1,92
D	1,87
F	1,98

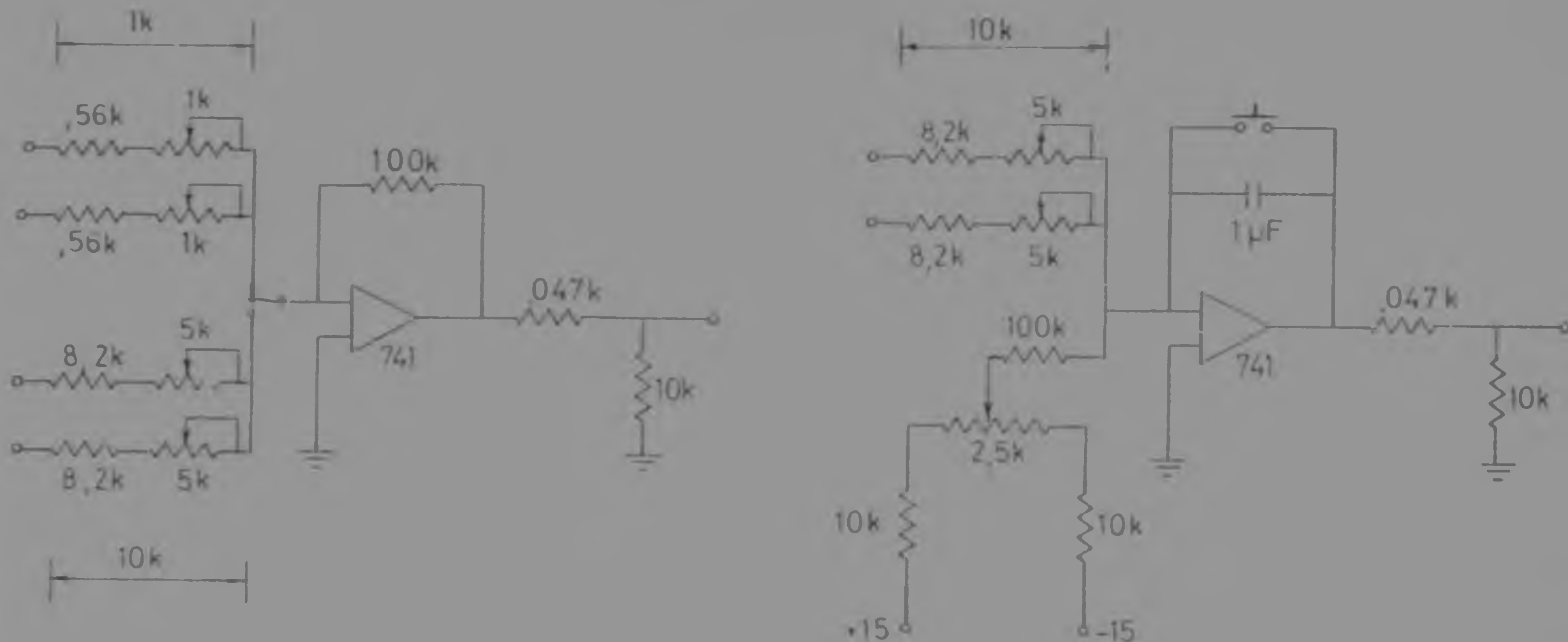

Figure A.1 Circuit diagram of typical amplifier/integrator unit constructed for flux and current measurements.

(After Tanev[20])

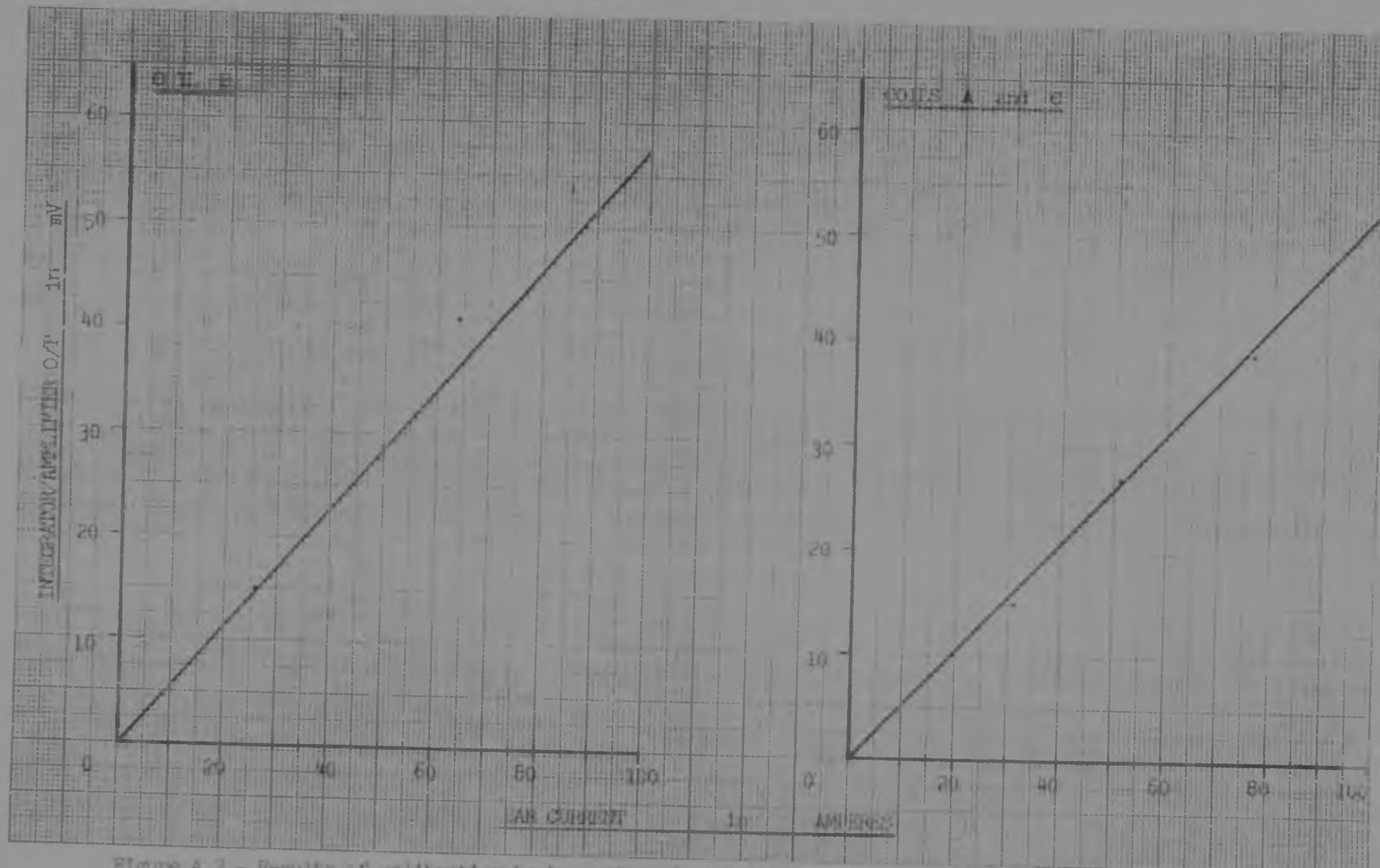

Figure A.2 – Results of calibration tests performed on toroids A, B and C (tables A.1 and A.2)
Calibration constant: coil B = 1,74 A/mV
coils A and C = 1,92 A/mV

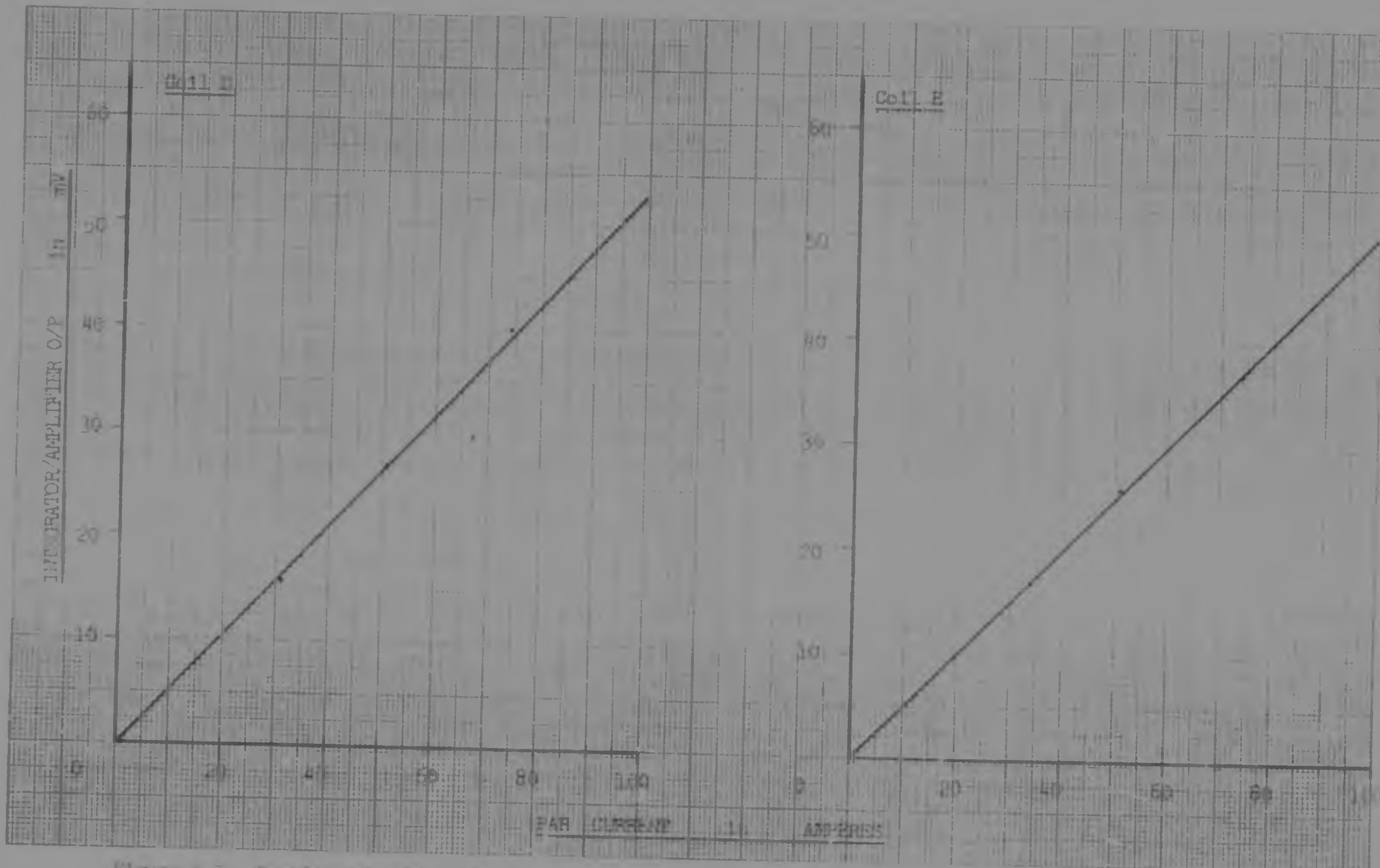

Figure A.3 – Results of calibration tests performed on toroids D and E. (Tables A.3 and A.4).
Calibration constant: coil D = 1,87 A/mV
coil E = 1,98 A/mV

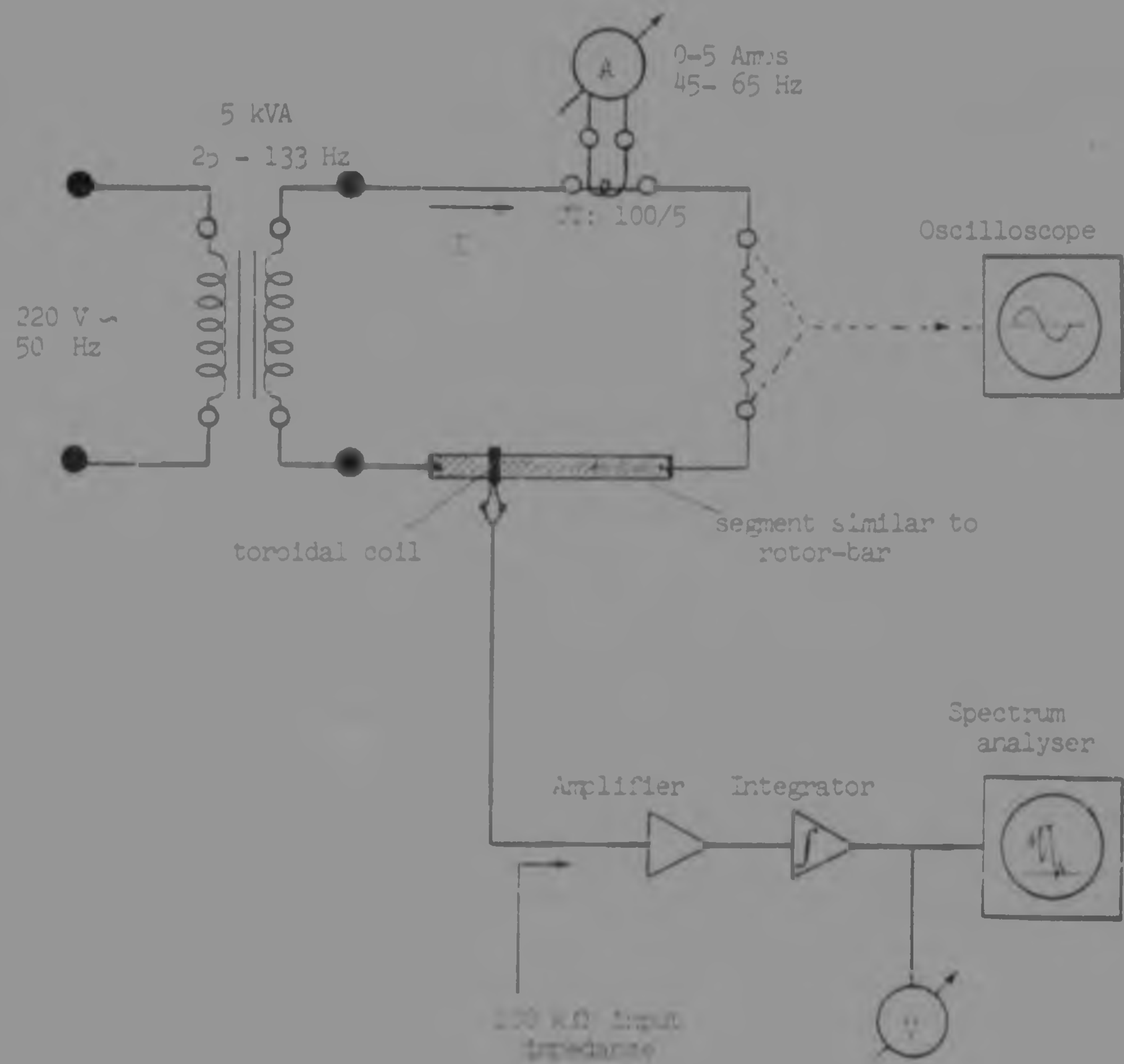

Figure A.4 - Circuit used for the calibration of the toroidal coils

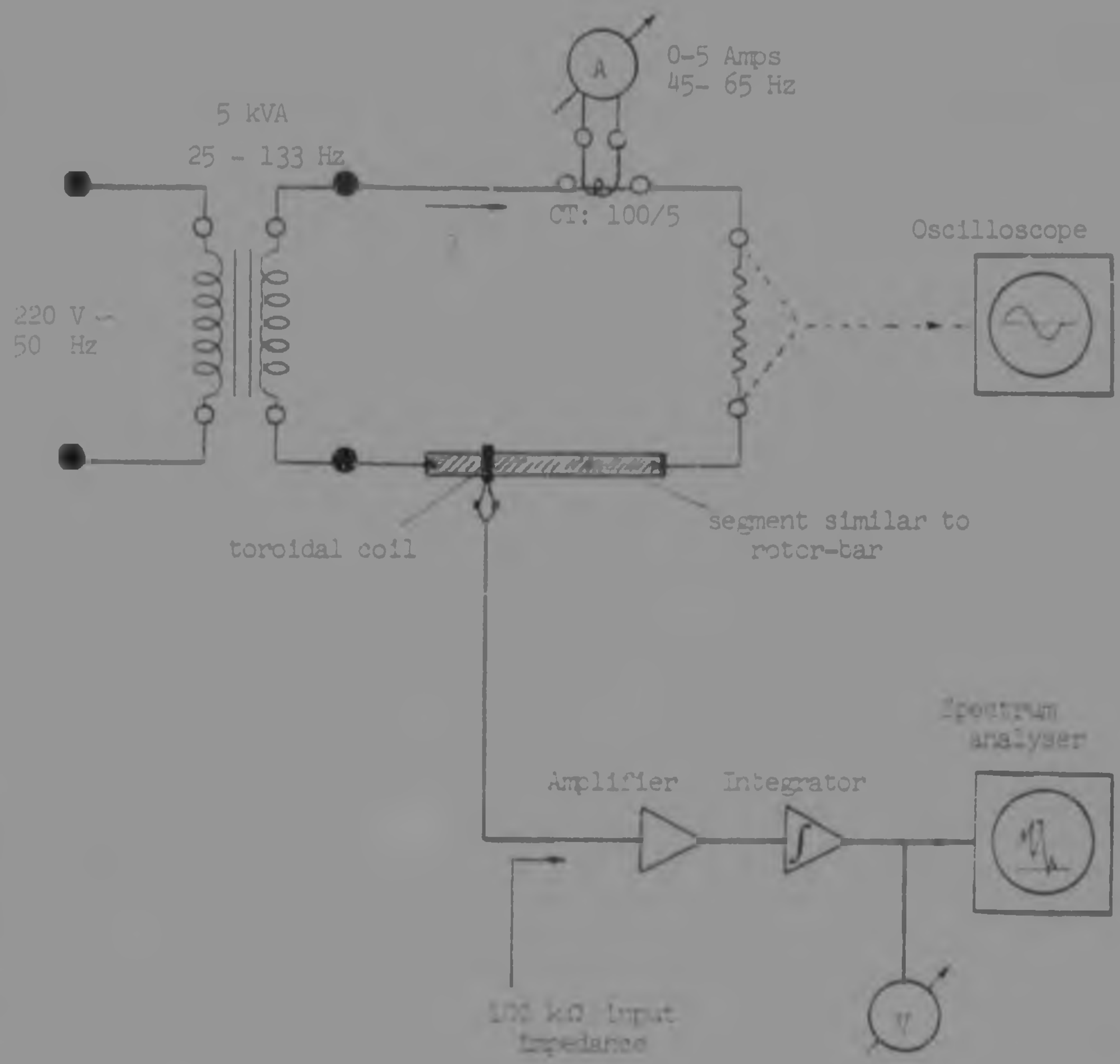

Figure A.4 - Circuit used for the calibration of the toroidal coils

APPENDIX B

CALCULATION OF INTER-BAR RESISTANCE FOR A CIRCULAR CORE WITH INNER DIAMETER EQUAL TO ZERO

In Chapter 2, two different methods for the calculation of the core resistance between two rotor-bars $R(\alpha_0)$ were discussed. One of the methods, developed below, assumes that in two pole motors the inner diameter of the laminations can be taken as zero. This assumption is valid due to the relatively high curvature of these motors, which results in the ratio -outer diameter/inner diameter- being fairly large. Therefore, the error introduced in calculating $R(\alpha_0)$, assuming zero inner diameter, is negligible for all practical purposes. Hence $R(\alpha_0)$ is determined as follows:

Due to symmetry the electric field pattern will be described by arcs of circles, with centers on the $\hat{y}$ axis and passing through M and N (see Figure B.1).

Assume two infinitely long charged lines (in the $\hat{z}$ direction) passing through M and N and having a charge per unit of length of Q_+ on M and Q_- on N. Then the Electric field intensity E(x,y) at any point T on the $\hat{x}$ axis is given by

$$\bar{E}_T(x,0) = \bar{E}_{Q+}(x,0) + \bar{E}_{Q-}(x,0)$$
$$= (Q/2\pi\epsilon)[1/(d+x) + 1/(d-x)] \quad \ldots.[B.1]$$

Let $K1 \doteq Q/2\pi\epsilon$ ... [B.2]

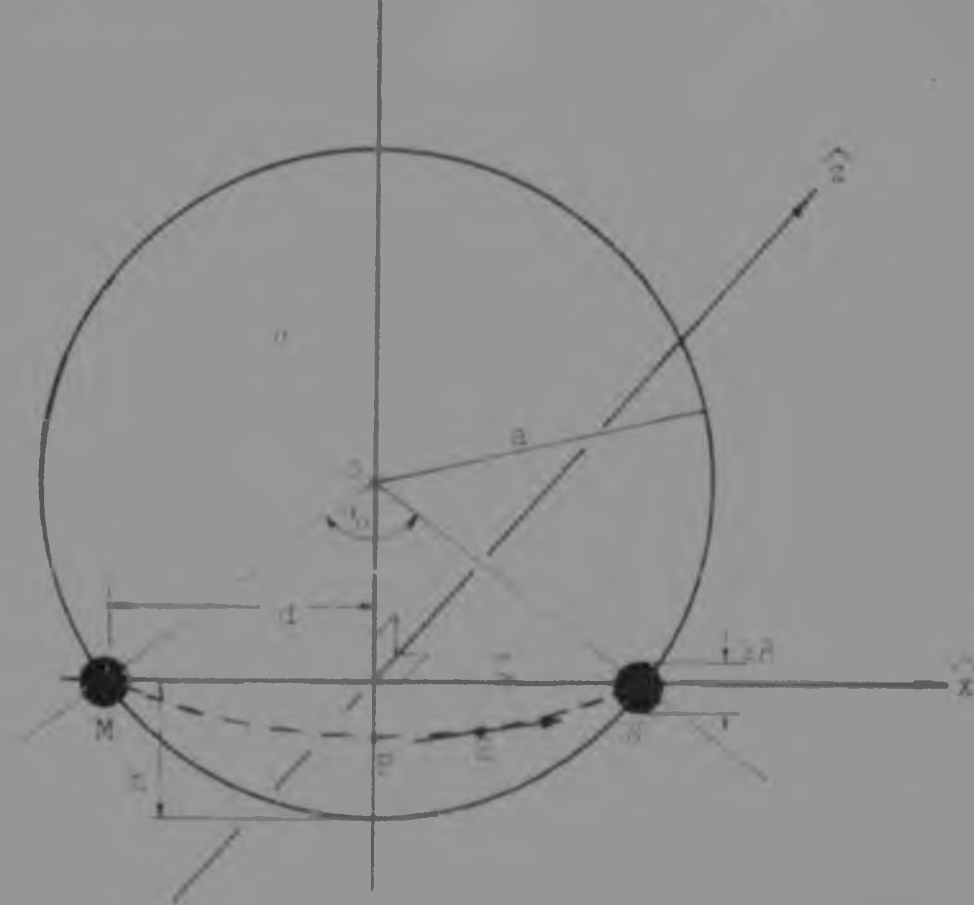

Figure B.1 - Schematic cross sectional view showing the rotor core and two bars M and N. The inner diameter is assumed to be zero.

a: radius of lamination

R: equivalent radius of conductor

σ: conductivity of lamination material

ϵ : permittivity of lamination material ($= \epsilon_r \epsilon_0$)

The potential that will exist between M and N is

$$V_{MN} = \int_{-d+R}^{d-R} E.dl$$

for any path of length l in the lamination between M and N

Therefore for the particular path on the $\hat{x}$ axis

$$V_{MN} = \int_{-d+R}^{d-R} E_T(x,0).dx$$

$$= K1.[\int dx/(d+x) + \int dx/(d-x)]\Big|_{-d+R}^{d-R}$$

$$= K1.[\ln(d+x) - \ln(d-x)]|$$

$$= K1.[2\ln(2d-x) - 2\ln R]$$

$$= 2.K1.\ln[(2d-R)/R] \qquad ....[B.3]$$

Substituting for K1 from equation [B.3] into [B.2] gives

$$Q = \pi.\epsilon.V_{MN}/\ln[(2d-R)/R]$$

and substituting into [B.1] gives

$$\bar{E}(x,0) = \{V_{MN}/2\ln[(2d-R)/R]\}.[1/(d+x)+1/(d-x)]$$

Now let $K2 \doteq V_{MN}/2\ln[(2d-R)/R]$

and for any point P on the $\hat{y}$ axis the electric field intensity in the $\hat{x}$ direction is

$$\bar{E}_P(0,y) = 2.K2.(1/\overline{MP}).(d/\overline{MP}) = 2.K2.d/(d^2+y^2)$$

The current density $\bar{J}$ at any point along the $\hat{y}$ axis is

$$\bar{J} = \bar{E}(0,y).\sigma$$

giving
$$I = \int_{y=-h}^{y=2a-h} 2.K2.\sigma.[d/(d^2+y^2)].dy$$

$$= 2.K2.\sigma.d.[(1/d).\arctan(y/d)]\Big|_{-h}^{2a-h}$$

$$= 2.K2.\sigma.d.\{\arctan[(2a-h)/d]+\arctan(h/d)\} \quad ..[B.4]$$

Therefore the equivalent resistance between M and N is

$$R(\theta_0) = V_{MN}/I$$

$$= \ln[(2d-R)/R]/\sigma.\{\arctan[(2a-h)/d]+\arctan(h/d)\}$$

per unit length of core

But

$$d = a.\sin(\theta_0/2)$$
$$h = a.[1-\cos(\theta_0/2)]$$
$$2a-h = a.[1+\cos(\theta_0/2)]$$

and
$$\arctan\{[1+\cos(\theta_0/2)]/\sin(\theta_0/2) + $$
$$+ \arctan\{[1-\cos(\theta_0/2)]/\sin(\theta_0/2)\} = \pi/2$$

Therefore

$$R(\theta_0) = (2/\pi\sigma)\ln\{[2a.\sin(\theta_0/2) - R]/R\} \quad ....[B.5]$$

per unit length of core

APPENDIX C

CALCULATION OF THE INTER-BAR INDUCTANCE

As shown by Christofides[15] and also from measurements done by the author in this project, the inter-bar impedance includes a frequency dependent element. A simplified model is developed in this Appendix for the calculation of the inductance existing between two adjacent rotor-bars. The geometric configuration used in the model consists of two parallel rectangular sheets, representing the two bars, separated by a magnetic medium which represents the core (see Figure C.1). This configuration was choosen for the model because it is simple to solve and any other configuration may be approximated to it, eg round bars. The calculation of the magnetic field distribution was done assuming a magnetostatic situation, ie a direct current exists which is uniformly distributed in the conducting medium between the two sheets. An alternating current will have a different distribution due to the 'depth of penetration' effect resulting in a reduction of the inductance 'L'. Nonetheless, as long as the value of the depth of penetration $\delta = (\omega \sigma \mu)^{-1/2}$ is larger than the thickness of the rotor laminations the error in the value of L calculated using the D.C. approximation will be small. Seeing that at normal working speed the frequency of the rotor currents is low, the model will give reliable results.

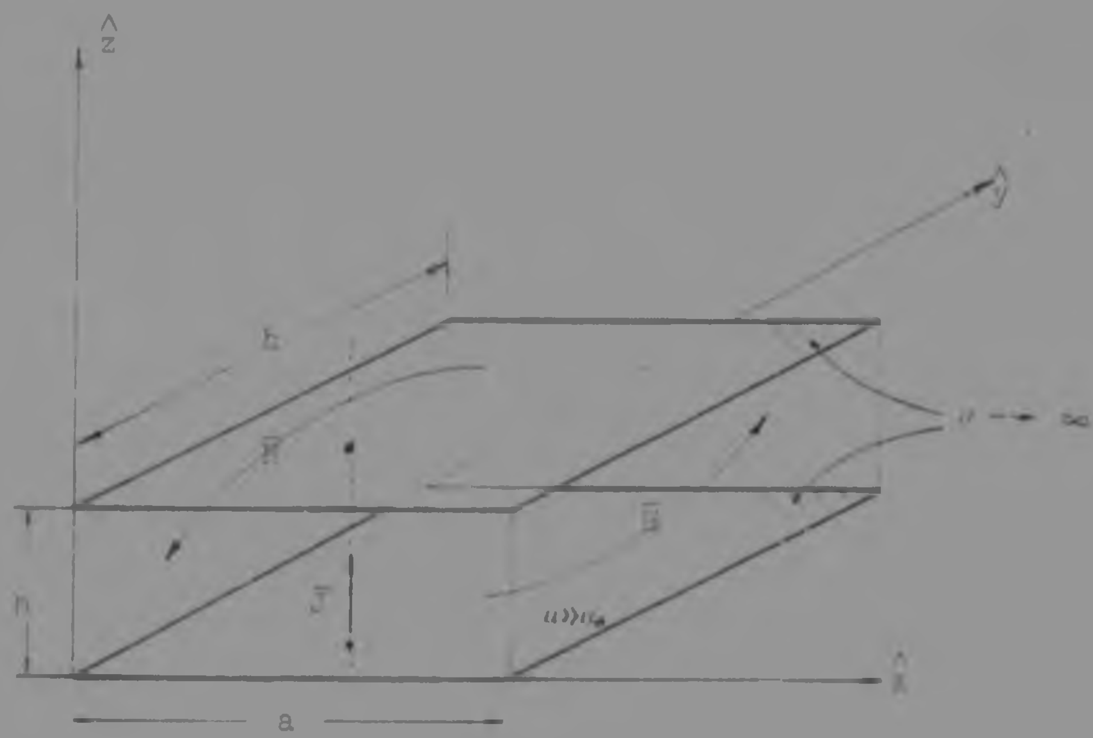

Figure C.1 - Geometric configuration of two rectangular conducting sheets of infinite conductivity separated by a ferromagnetic medium.

Using Maxwell's field equations for the magnetostatic situation gives

$$\text{curl } \bar{H} = \bar{J} \qquad \text{....[C.1]}$$

and

$$\text{div } \bar{H} = 0 \qquad \text{....[C.2]}$$

Therefore from [C.1]

$$\partial Hy/\partial x - \partial Hx/\partial y = J(x,y) = \text{constant} \qquad \text{....[C.3a]}$$

and from [C.2]

$$\partial Hx/\partial x + \partial Hy/\partial y = 0 \qquad ....[C.4a]$$

Using the `separation of variables' method gives

$$Hx(x,y) = Xx.Yx$$

$$Hy(x,y) = Xy.Yy$$

Hence [C.3a] and [C.4a] may be written as

$$Xy'.Yy - Xx.Yx' = J \qquad ....[C.3b]$$

$$Xx'.Yx - Xy.Yy' = 0 \qquad ....[C.4b]$$

Differentiating [C.3b] w.r.t. x and [C.4b] w.r.t. y and rearranging gives:

$$Xy''.Yy + Xy.Yy'' = 0$$

Hence $\quad Xy''/Xy = - Yy''/Yy$

The boundary conditions applicable in this case are:

(i) $\quad Hx(x=0) = Hx(x=a) = Hy(y=0) = Hy(y=b) = 0$

(ii) $\quad Hy(a/2,y) = Hx(x,b/2) = 0$

Incorporating these conditions gives the solution for the magnetic field intensity as

$$Hyn(x,y) = bn.\sin(n\pi y/b).\sinh[(n\pi/b)(x-0{,}5a)] \qquad ....[C.5]$$

$$Hxn(x,y) = an.\sin(n\pi x/b).\sinh[(n\pi/a)(y-0,5b)] \quad ....[C.6]$$

Since $\mu >> \mu_0$ the magnetic field form will follow the contour of the rectangular iron. Therefore as $\oint H.dl$ = Ienclosed, H(around the perimeter) = J.a.b. From this value of H, the values of bn and an can be found. Given the fact that for most practical purposes b (the length of the bar) is many times greater than a (the width of the bar), the end effects along the axial ($\hat{y}$) direction may be neglected. This means that Hx is practically constant along $\hat{y}$.

For the calculation of the flux in the core it is sufficient to take Hy at any point where the component in the $\hat{x}$ direction is equal to zero. Such a point occurs when y = b/2. From the above it is seen that Hyn(x=a,y=b/2) = J.a.b which gives:

$$bn = J.a.b \;/\; \sinh(n\pi a/2b)$$

and thus for any x,y

$$Hyn(x,y) \cong [J.a.b/\sinh(n\pi a/2b)].\sinh[(n\pi/b)(x-0,5a)]..[C.7]$$

To calculate the total magnetic flux present in the core, the flux density B is integrated along the $\hat{x}$ direction from x = a/2 to x = a in the plane y = b/2

$$d\phi y = \mu.Hy.dArea$$
$$= \mu.Hy.h.dx$$

$$\Phi total = \frac{\mu . h . J . a . b}{\sinh(n\pi a/2b)} . \int_{a/2}^{a} \sinh[\frac{n\pi}{b}(x-a/2)]. dx$$

$$= \frac{\mu . h.J . a . b}{\sinh(n\pi a/2b)} . \frac{b}{n\pi} . [\cosh(n\pi a/2b) - 1]$$

It is clear that as $n \to \infty$, $L \to 0$ (ie the series converges) and as a first approximation for the value of L it is sufficient to take n = 1 which yields:

$$L \cong [\mu .h.b/\pi \sinh(\pi a/2b)].[\cosh(\pi a/2b) - 1]....[C.9]$$

Verification of expression [C.9]

Figure C.2 shows the actual geometric configuration of two adjacent round bars of the rotor of the experimental inverted-geometry motor. Superimposed is the approximated geometric configuration having rectangular bars that allows expression [C.9] to be used for calculating the inter-bar inductance. From the magnetization curve of the material used in the laminations of the rotor core it is found that for low values of the flux density (as was the case during the measurements) the value of the permeability is $\mu \cong 5500\mu_o$.

Therefore:

$$L \cong 5500 x 4\pi x 10^{-} x 8 x 10^{-} x 136 x 10^{-} x (1,061-1)/\pi x 0,353$$

$$= 416 x 10^{-9} \quad H$$

The actual average value measured at 50 Hz between two adjacent bars was 442×10^{-9} H. This is sufficiently close to the predicted value and lends weight to the validity of the assumptions made.

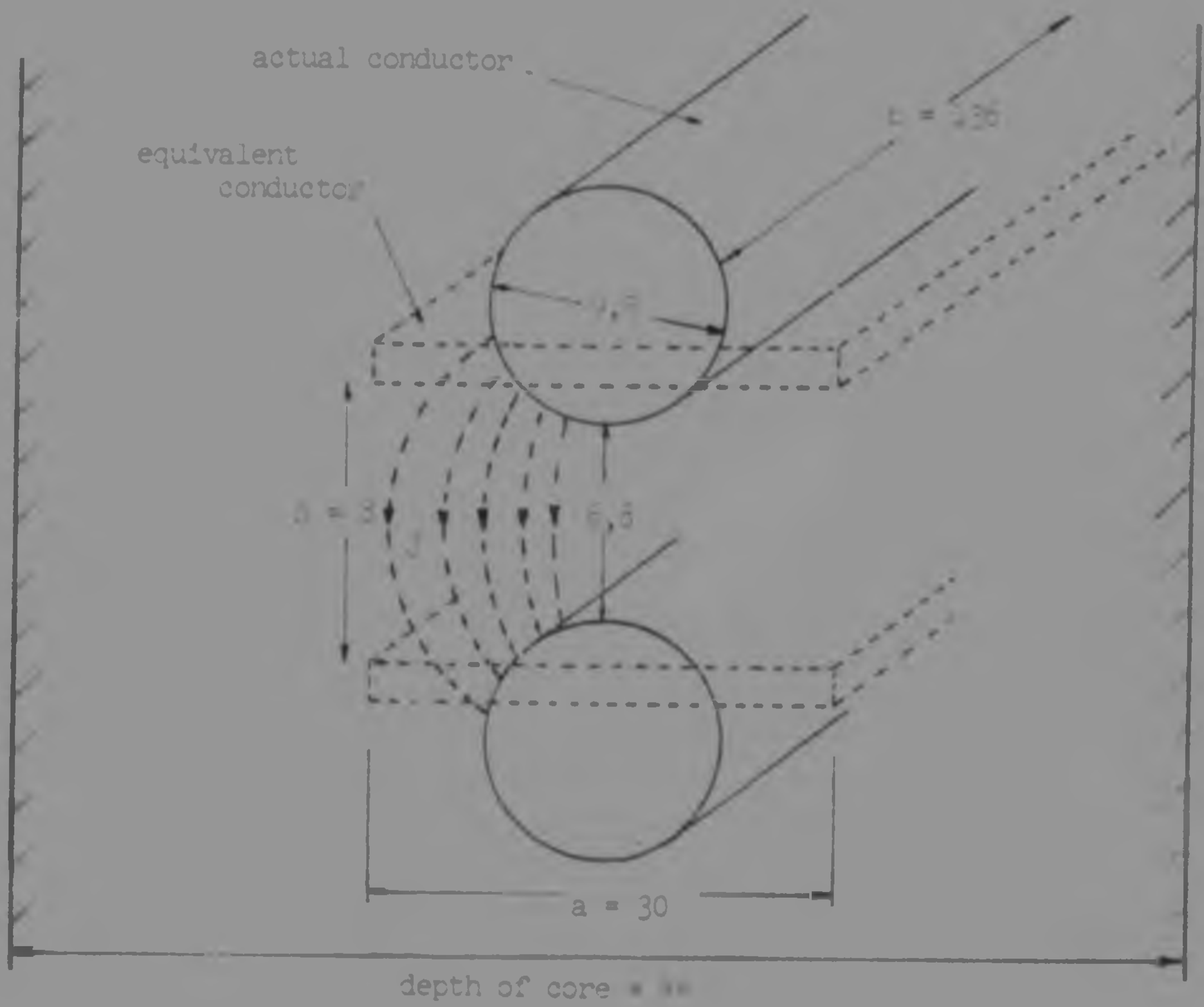

Figure C.2 - Actual and equivalent geometric configurations between two adjacent rotor-bars of the inverted experimental motor. All dimentions are in millimeters.

APPENDIX D

RESULTS OF MEASUREMENTS TAKEN ON THE INDUSTRIAL MOTORS

The two reasons for presenting all the results of the tests conducted on both industrial motors A and B in one appendix are:

(i) to present the results in such a way that the whole picture of the experimental procedure is brought out and,

(ii) as some of the results obtained are not directly relevant to the main topics covered in this work, they would otherwise be lost. In this way they are, at least, recorded and may be a source of information for subsequent researchers in this field.

D.1 - Tests on industrial motor A

D.1.1 - Measurement of the locked-rotor rotor-bar currents

As already stated in section 3.1.1, in this test the following were measured and recorded:

1- Primary (stator) current
2- Amplifier/integrator output
3- Photographs of the rotor-bar current waveforms
4- Photographs of the harmonic content of the rotor-bar current waveforms

Tables D.1 to D.5 contain the measured values of the primary current and the output from the integrator together with the calculated secondary current using the calibration constants found in Appendix A. During the test all the three phases of the primary current were measured, but due to the fact that no measurable differences were found, only one value common for all three phases appears in the tables. The positions of the toroidal coils placed on the various rotor-bars are shown in Figure 3.2, page 3.5.

The measured rotor-bar currents (obtained from tables D.1-D.5) are plotted against the primary currents in figures D.1-D.3. In this way a "measurement constant" (km) was found for each toroidal coil relating bar current to primary current. This averages out the measurement scatter. The average value is necessary because when the actual measured values were compared they were normalized to the same primary current of 100 A.

Table D.1 - Rotor-bar currents measured via toroidal coil A positioned on the `broken' bar.

Primary current Amps.	Integrator o/p mV	Rotor-bar current Amps.
26	158	303
50,4	312	599
74	461	885

Table D.2 - Rotor-bar currents measured via toroidal coil B positioned one bar away from the `broken' bar

Primary current Amps.	Integrator o/p mV	Rotor-bar current Amps.
25,2	154	268
51,2	312	543
74,4	456	793

Table D.3 - Rotor-bar currents measured via toroida[illegible] coil C positioned one bar away from the `broken' bar (opposite side to B)

Primary current Amps.	Integrator o/p mV	Rotor-bar current Amps.
25,8	162	311
50,2	315	605
74,6	463	889

Table D.4 - Rotor-bar currents measured via toroidal coil D positioned diametrically opposite the `broken' bar

Primary current Amps	Integrator o/p mV	Rotor-bar current Amps.
24,6	153	286
51,4	318	595
74,4	458	856

Table D.5 - Rotor-bar current measurement via toroidal coil E positioned two bars away from the `broken' bar

Pri-ary current Amps.	Integrator o/p mV	Rotor-bar current Amps.
25	138	273
50	274	543
74,2	423	838

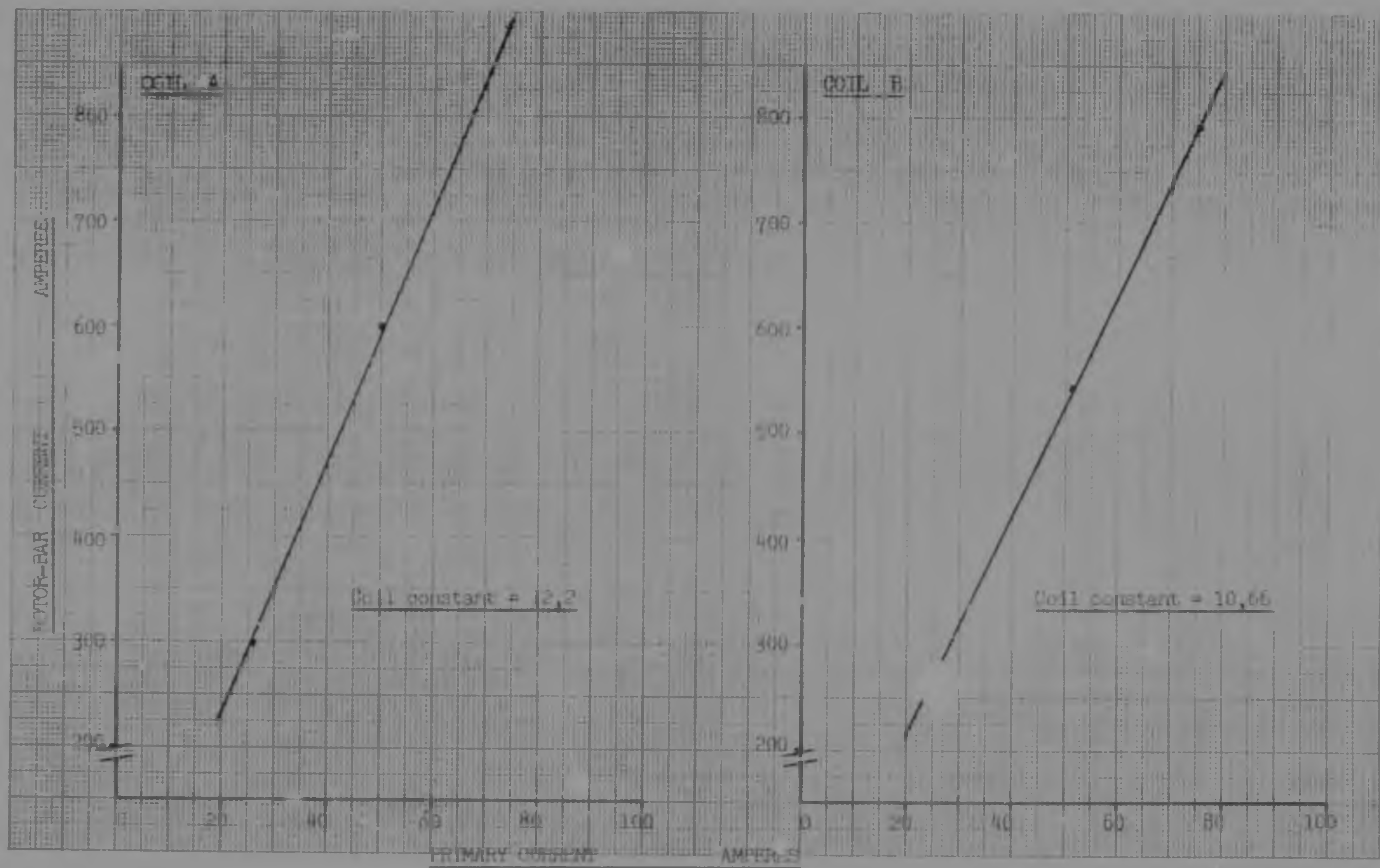

Figure D.1 - Locked-rotor bar current measurements on industrial motor A for coils A and B.

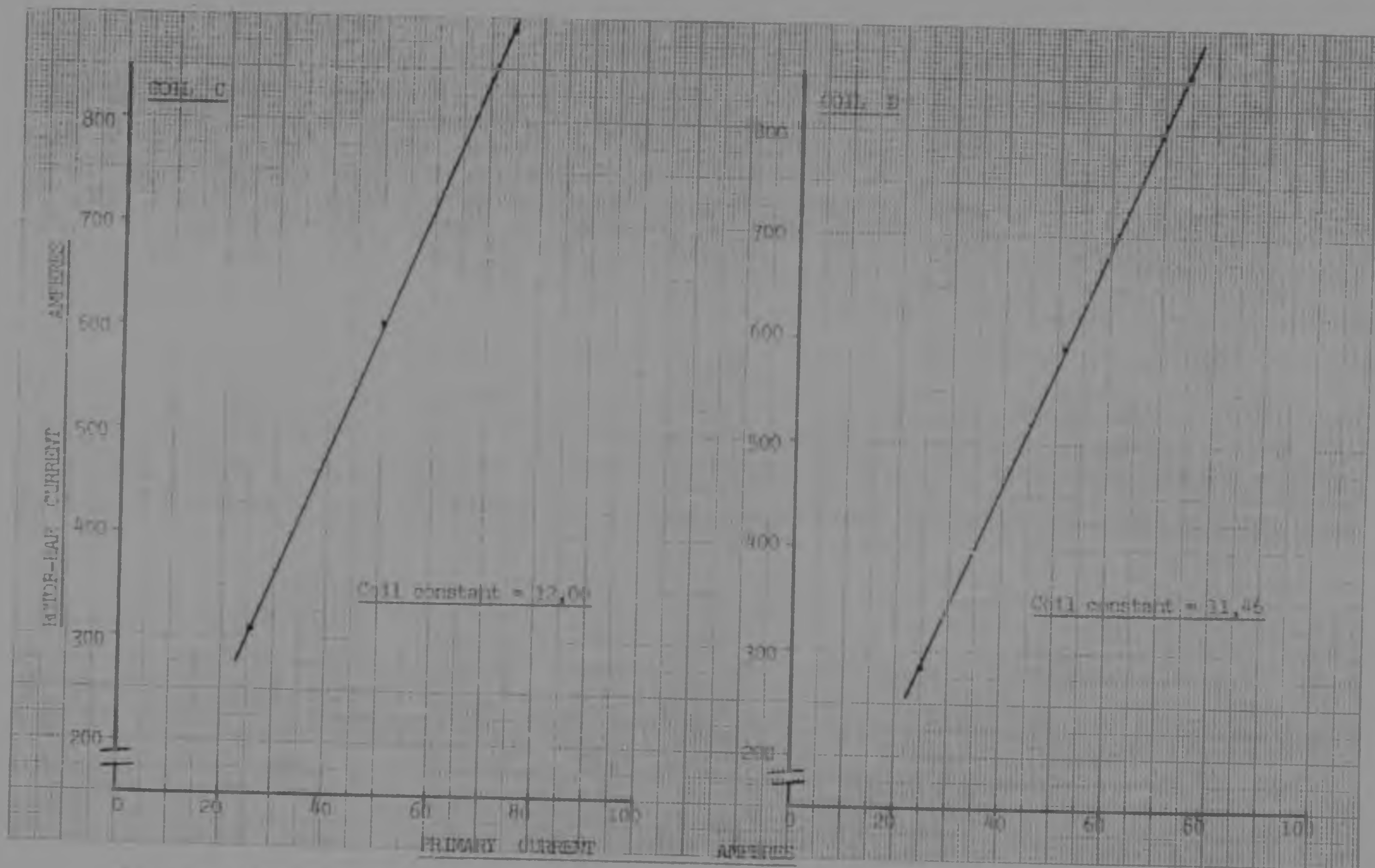

Figure D.3 - Locked-rotor bar current measurements on industrial motor A for coils C and D.

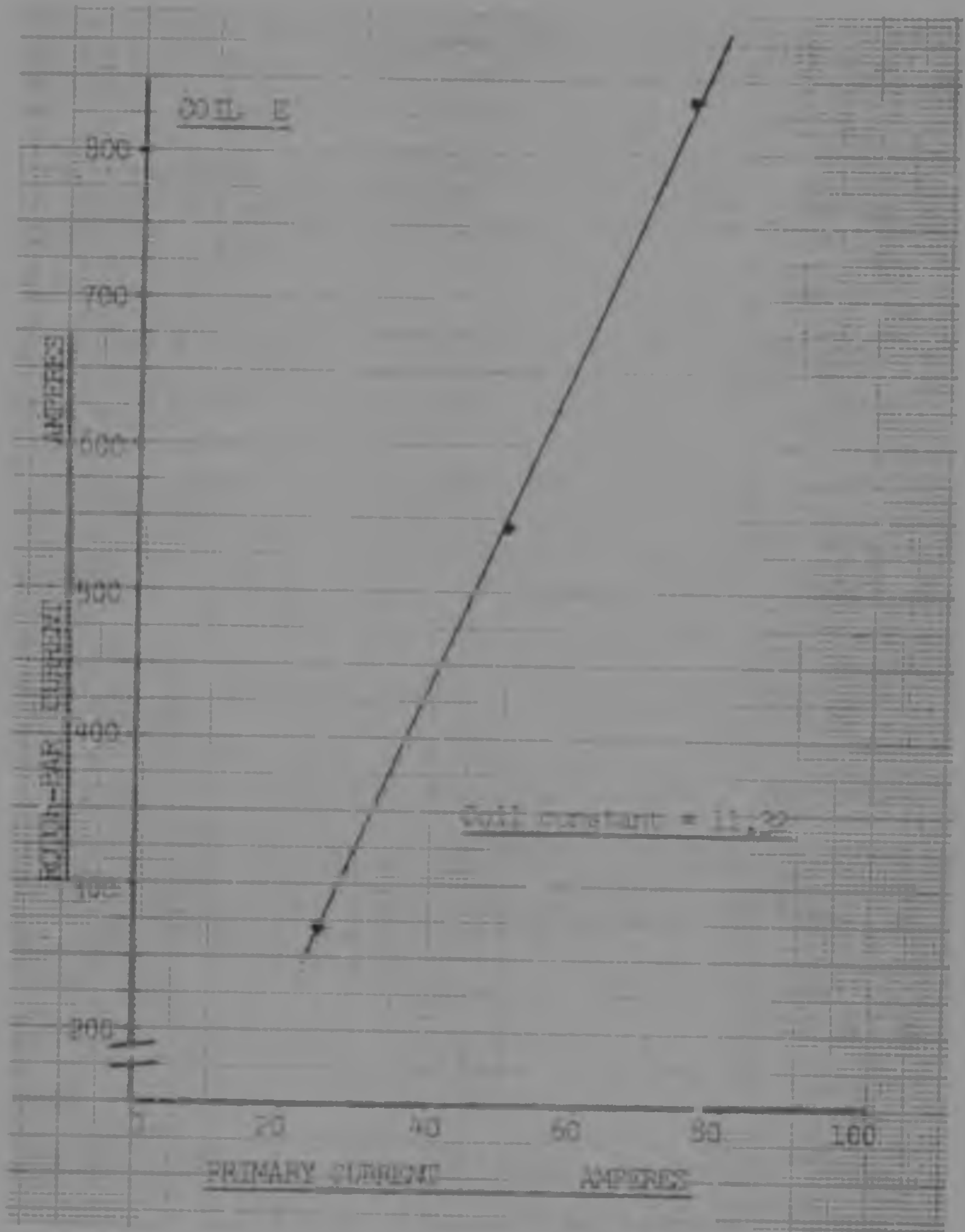

Figure D.3 - Locked-rotor bar current measurement on industrial motor A for coil E.

Table D.6 - Values of the "measurement constants" (km)
from figures D.1-D.3

Toroidal coil	"measurement constant" (km)
A	12,20
B	10,66
C	12,00
D	11,46
E	11,32

The ratio of the "measurement constants" between two different toroids should be identical to the ratio of their "calibration constants". Any difference is due to the errors in the measurement process. The "measurement constants", km, are tabulated in Table D.6, and in Table D.7 the percentage error of the ratio of km divided by the corresponding "calibration constant" ratio for all the toroidal coils is given. Table D.7 shows that the average error in the rotor-bar current measurement was 4,4% (the maximum error being approximately 7%). The magnitude of this error is quite acceptable in the context of this research as large current differences are investigated.

Table D.7 - Percentage error between the ratio of km values and corresponding ratio of calibration constants for all combinations of toroidal coils

$$\left|\Delta\ \%\right| = \left(\frac{\dfrac{\text{km of toroid x}}{\text{km of toroid y}}}{\dfrac{\text{calibration const. of toroid x}}{\text{calibration const. of toroid y}}} \right) \times 100$$

Combinations of toroids -x/y-	$\|\Delta\%\|$	
B/C	1,98	
B/A	3,58	
B/D	0,03	
B/E	7,16	
A/C	1,67	average $\|\Delta\%\|$=4,4
A/D	[illegible],00	
A/E	4,97	
C/D	1,99	
C/E	9,32	
D/E	7,19	

D.1.1a <u>Comparison between measured and calculated rotor-bar currents</u>

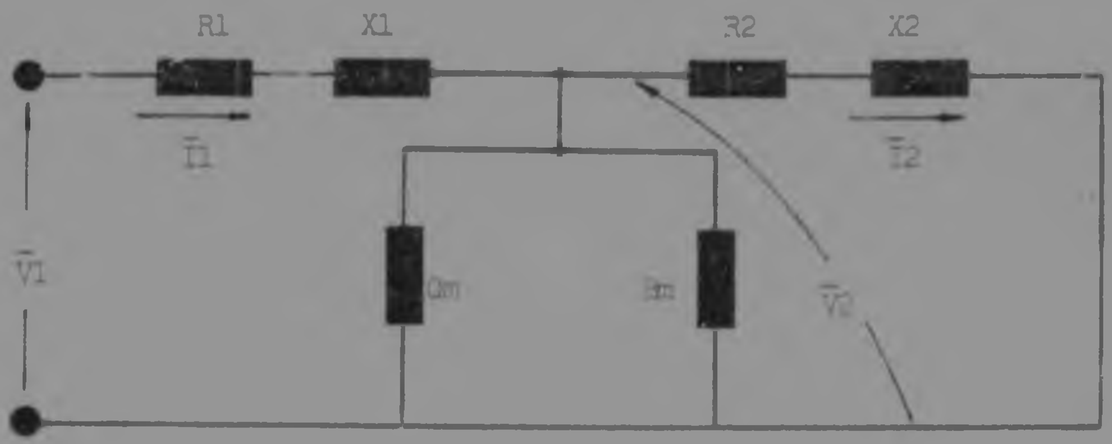

R1 = 0,0083 X1 = 0,1180

R2 = 0,0203 X2 = 0,0580

Gm = 0,0220 Bm = 0,2503

Figure D.4 - Fundamental per-phase equivalent circuit of industrial motor A with the rotor at stand-still.
All resistances and reactances are given in per-unit (1p.u. = 19,6 ohm)

As an extra check on the validity of the measured values of the rotor currents obtained via the toroidal coils, the magnitudes were predicted using the equivalent circuit of Figure D.4. The values of the circuit parameters were obtained from the design data as supplied by the manufacturer. These values are for stand-still conditions, ie they take into account the "penetration depth" effects within the squirrel cage bars. The parameter values were calculated for the condition where the leakage flux paths are saturated. In the actual machine, because smaller currents were used, the machine was not so saturated and this accounts for the slight differences recorded between the measured and the calculated values. The actual primary current values used during the tests were approximately 25, 50 and 75 Amperes and the equivalent circuit value of I1 was normalized to 75 Amps. The solution of the equivalent circuit for the case of I1 = 75 A gives:

$$\bar{V}1 = 585,6/\sqrt{3}\ e^{-j0}$$
$$\bar{I}1 = 75\ e^{-j81}$$
$$\bar{V}2' = 154/\sqrt{3}\ e^{-j10}$$
$$\bar{I}2' = 73,86\ e^{-j80,6}$$

The current I2' is the referred current and the actual secondary current flowing in the rotor-bars is (Say, Chapter 8, page 261)[24]:

$$Ibar = I2'.(6.kws.N1/S2) \qquad \text{....[D.1]}$$
$$= 73,86 \times 10,679$$
$$= 789 \text{ Amperes}$$

where

kws: stator winding factor (=kd.kp = 0,866 x 0,955)

N1 : number of stator turns in series per phase (=99)

S2 : number of rotor slots (=46)

This predicted value (789 Amps.) is in fair agreement with the measured values of approximately 800 A (tables D.1-D.5) and therefore shows that the measurements are meaningful. Similarly the equivalent secondary phase voltage is[24]

$$V2 = V2'.S2/kws.N1 \qquad \text{....[D.2]}$$

$$= 154/(\sqrt{3} \times 10,679) = 8,3 \text{ Volts}$$

From the graphs in figures D.1-D.3 values of rotor-bar currents for any particular value of primary current may be obtained. The values of the secondary currents thus obtained were normalized with the 'broken' bar current taken as the base value for normalization. These are shown in Table D.8 and are also plotted in Fig D.5.

Table D.8 - Normalized values of the measured rotor-bar currents under locked-rotor conditions. The current entering the `broken' bar is taken as 100. All other currents are normalized with this as base value.

Toroid/bar	$\left\{\frac{\text{Current through toroid/bar}}{\text{Current through `broken' bar}}\right\} \times 100$
A	100,0
B	88,3
C	99,4
D	95,6
E	93,3

It is seen from Table D.8 that all the values of the bar currents are within ten percent of each other. Figure D.6

shows the relative position between the stator and the rotor teeth. The relative position between the stator and the rotor remained unchanged for the rotor-bar current measurements taken on bars B, C, D and E. A change in the relative position between stator and rotor teeth produces a local change in the permeance thereby affecting the magnitude of the current in the bars. A treatment of this subject is given in Alger[25] (Chapter 9, page 336). If it is assumed that the relative stator/rotor position during the experiment was as shown in Figure D.6, then the variation in the bar current magnitudes as shown in Figure D.5 is as expected. Unfortunately, during the course of these measurements the toroidal coil around the 'broken' bar was damaged and had to be replaced. When the motor had been re-assembled it was not known whether the stator/rotor relative position was as before. Therefore the high magnitude of current obtained for the 'broken' bar (toroidal A) with relation to the rest of the measured bar currents, cannot be attributed with certainty to he relative stator/rotor position. At worst the position could have been similar to that of B (see Figure D.6) whence the magnitude would be less ($\approx$85 A). However, there is no doubt whatsoever that the current flowing into the 'broken' bar is substantial and is comparable with the current entering the 'healthy' bars.

Figures D.7 and D.8 show the waveforms of the current entering the 'broken' bar and 'healthy' bar D taken at stand-still with I1 $\approx$ 75 A.

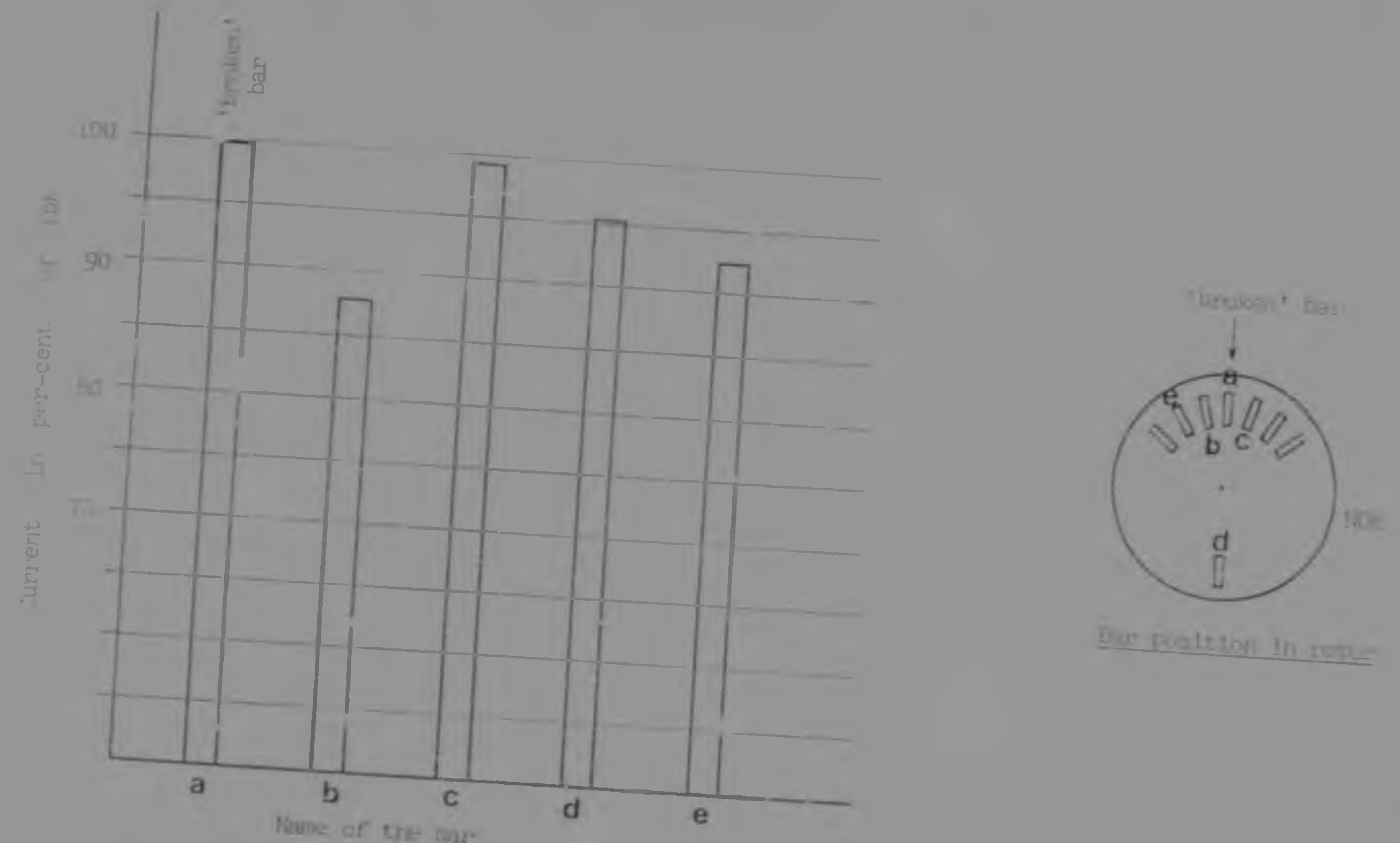

Figure D.5 - Measured values of $|I_{bb}/I_n|$ for industrial motor A. The bars were positioned around the machine as shown.

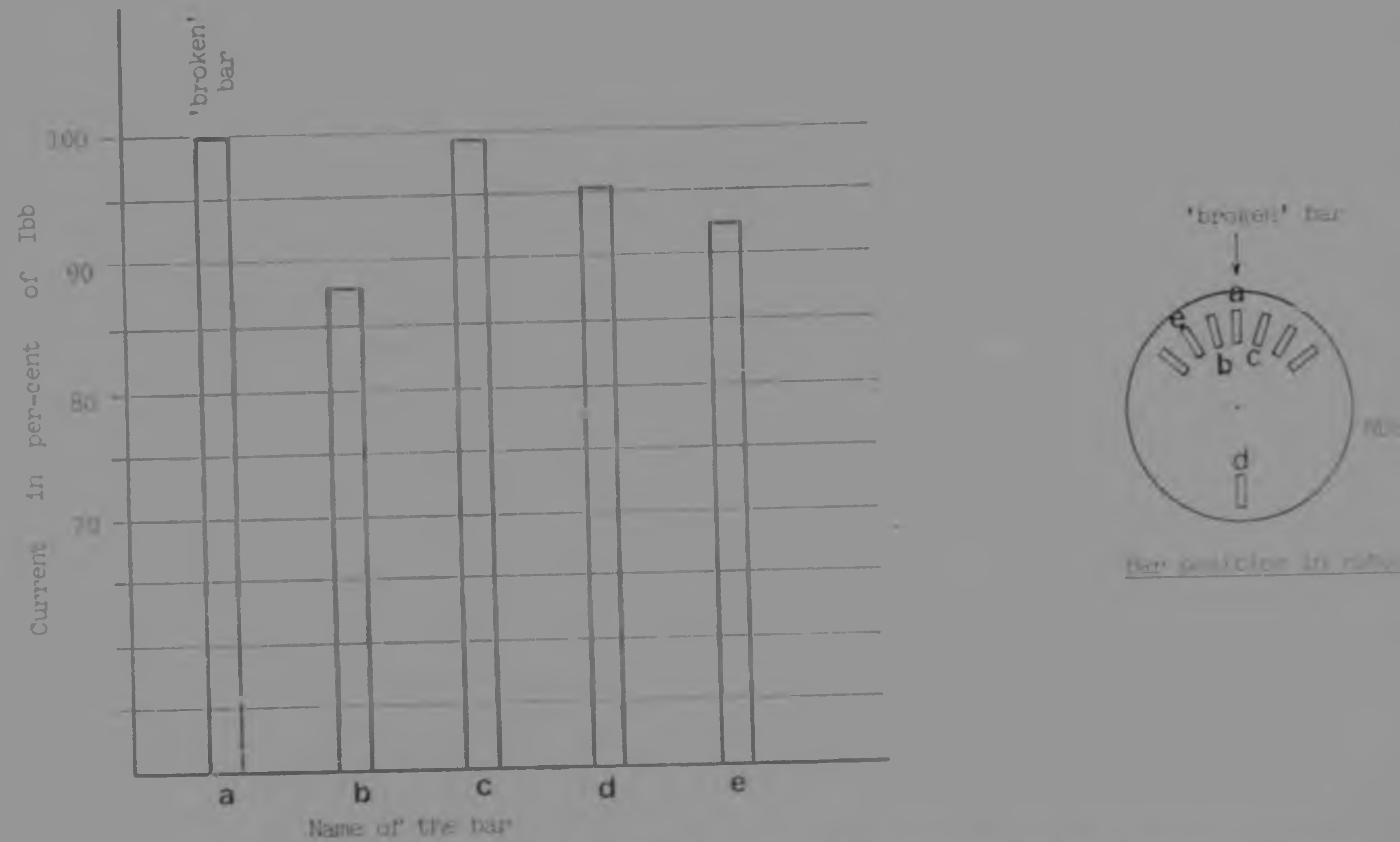

Figure D.5 – Measured values of Ibb/In [illegible] motor A. The bars were positioned around the machine as shown.

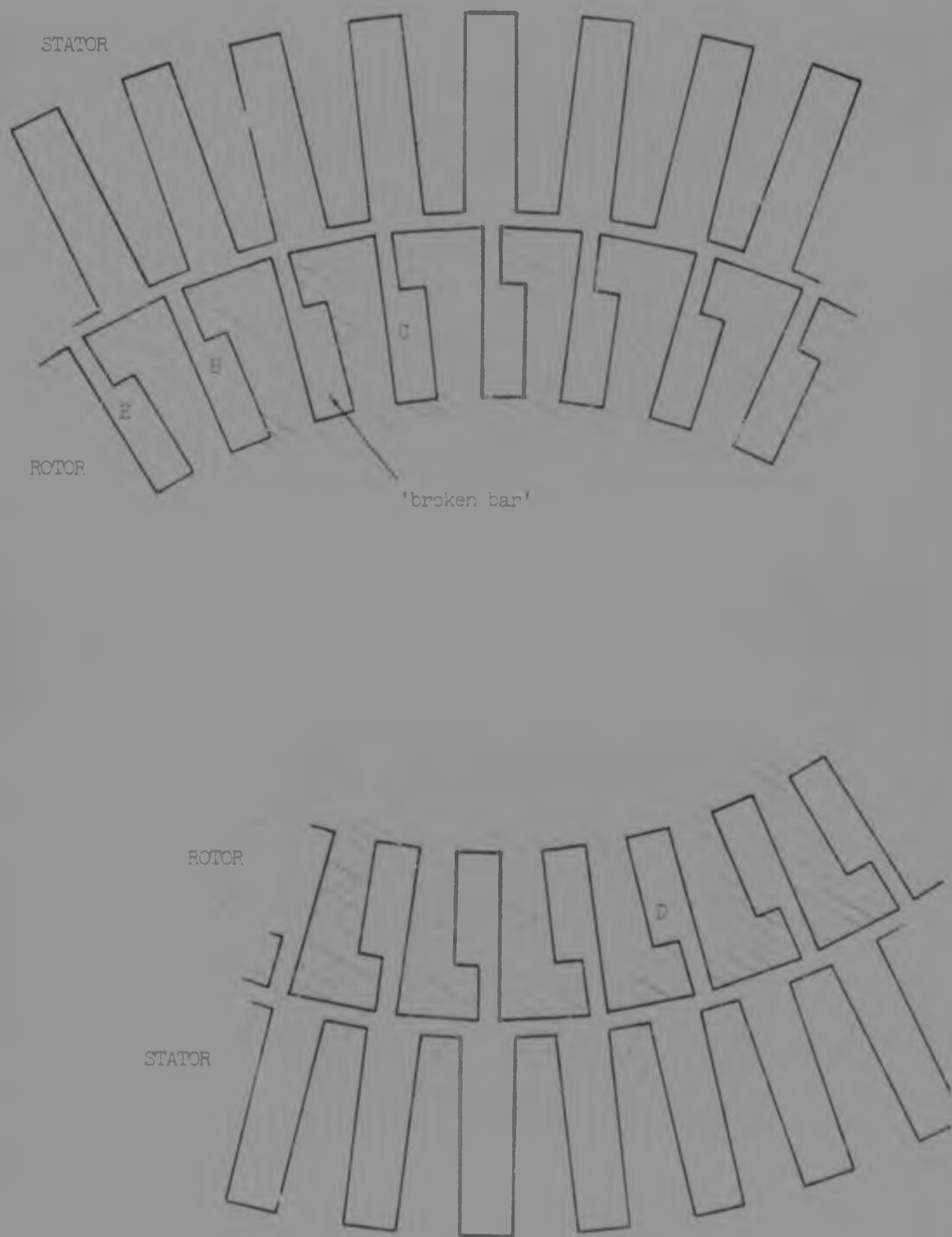

Figure D.6 - Relative position between stator and rotor teeth in industrial motor A during the bar current measurements.

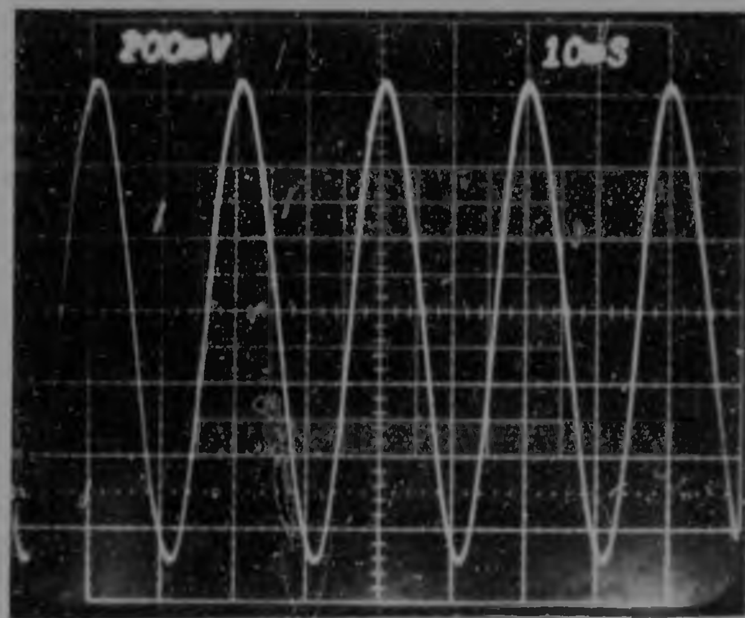

Figure D.7 - Waveform of the current flowing into the `broken' bar as measured during the locked-rotor test using the circuit described in Figure A.4. The primary current was ≃ 75 Amperes.

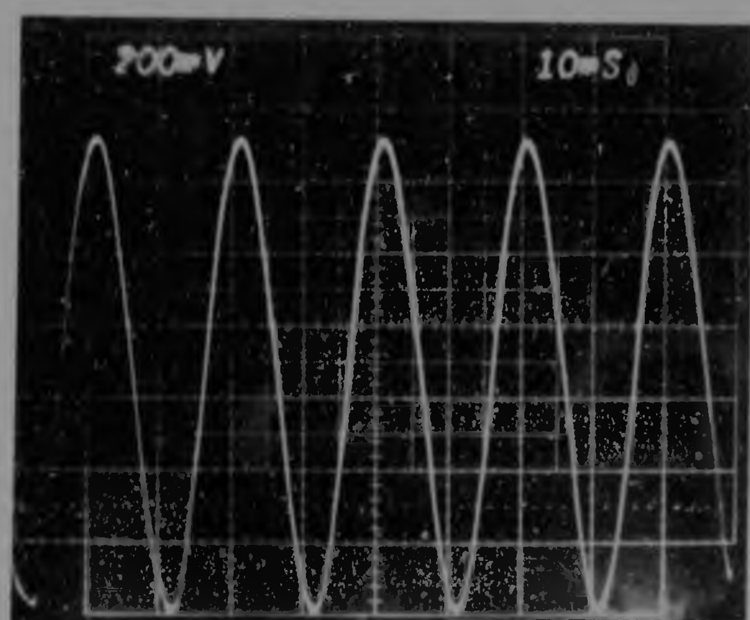

Figure D.8 - Waveform of current in `healthy' bar D measured at stand-still (I1 ≃ 75 A).

D.1.1b <u>Harmonic content of the rotor-bar currents measured during the locked-rotor test</u>

Figures D.9 and D.10 show the spectrum of the currents in the 'broken' bar and bar D taken at stand-still with I1 75 A. These figures show that a 3th harmonic component is present, but it must be realised that its magnitude is small when compared with that of the fundamental (40 dB less, see Table D.9). Table D.9 shows that the harmonic content of the measured bar currents is small.

Table D.9 - Comparison of rotor-bar harmonic content in per cent of the fundamental as measured on industrial motor A during the locked-rotor test.

Bar	Approx. primary current in Amps	Harmonic content in % of the fundamental						
		3th	5th	7th	11th	13th	17th	19th
A	75	0,04	0,915	0,061	0,019	0,012	0,010	?
B	50	0,04	1,807	0,081	0,052	0,028	0,013	0,010
C	50	0,179	1,789	0,085	0,053	0,028	0,013	?
D	75	0,069	0,921	0,062	0,018	0,012	0,011	?
E	50	0,065	1,813	0,073	0,058	0,024	0,015	0,012

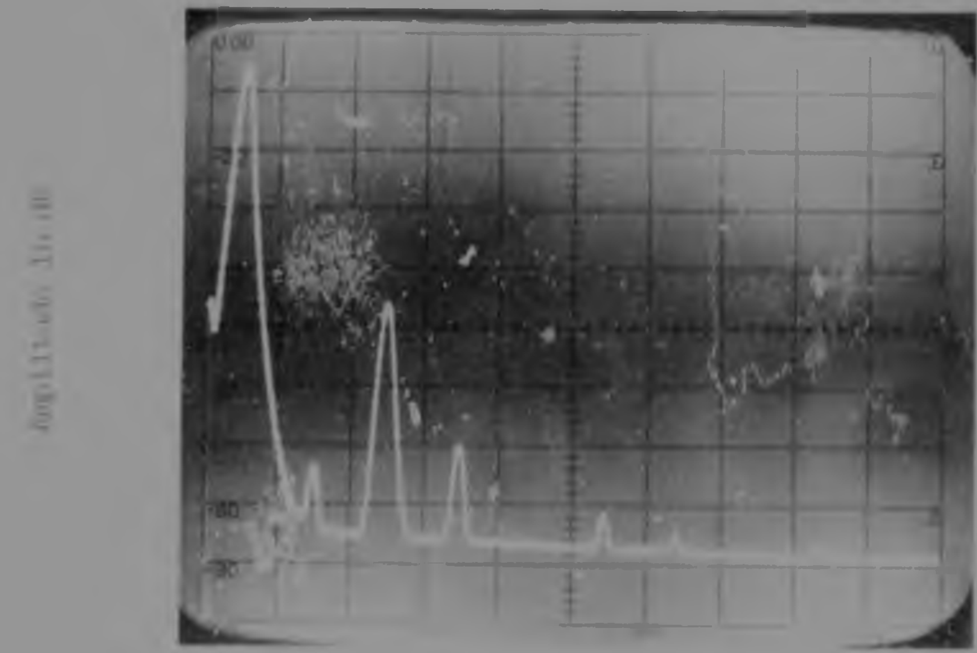

Figure D.9 - Picture of the rotor-bar current harmonic content measured during the locked-rotor test on industrial motor A. The current is the one flowing into the `broken' bar.

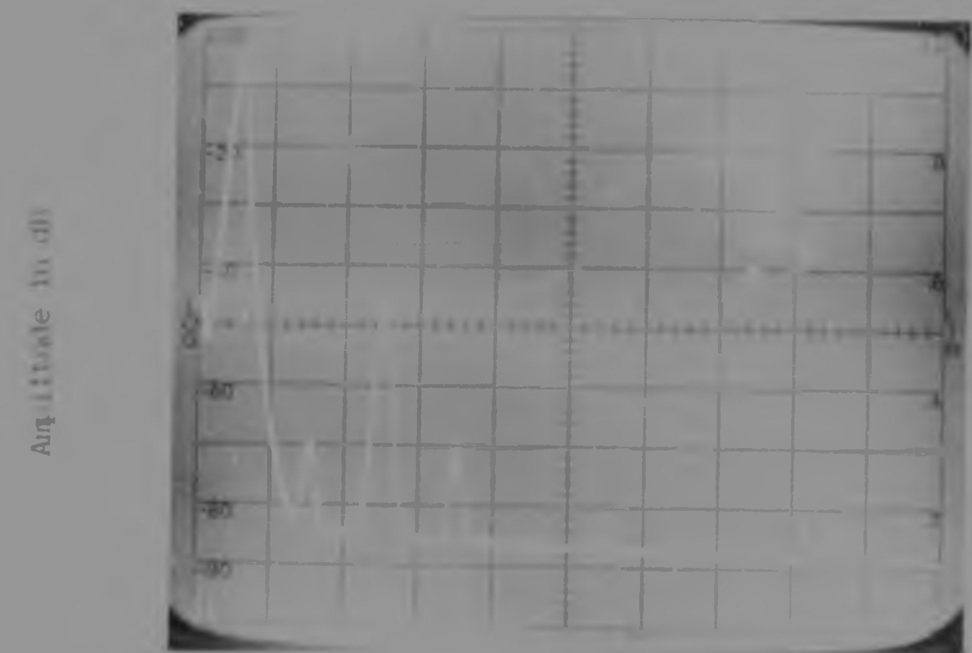

Figure D.10 - As for Figure D.9 but for rotor-bar D.

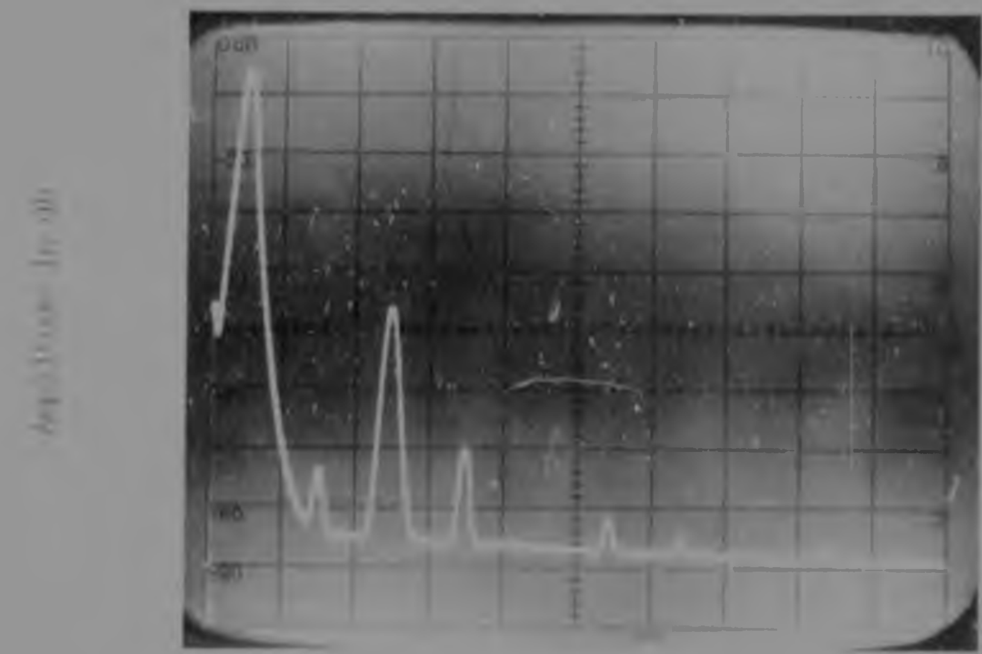

Figure D.9 - Picture of the rotor-bar current harmonic content measured during the locked-rotor test on industrial motor A. The current is the one flowing into the 'broken' bar.

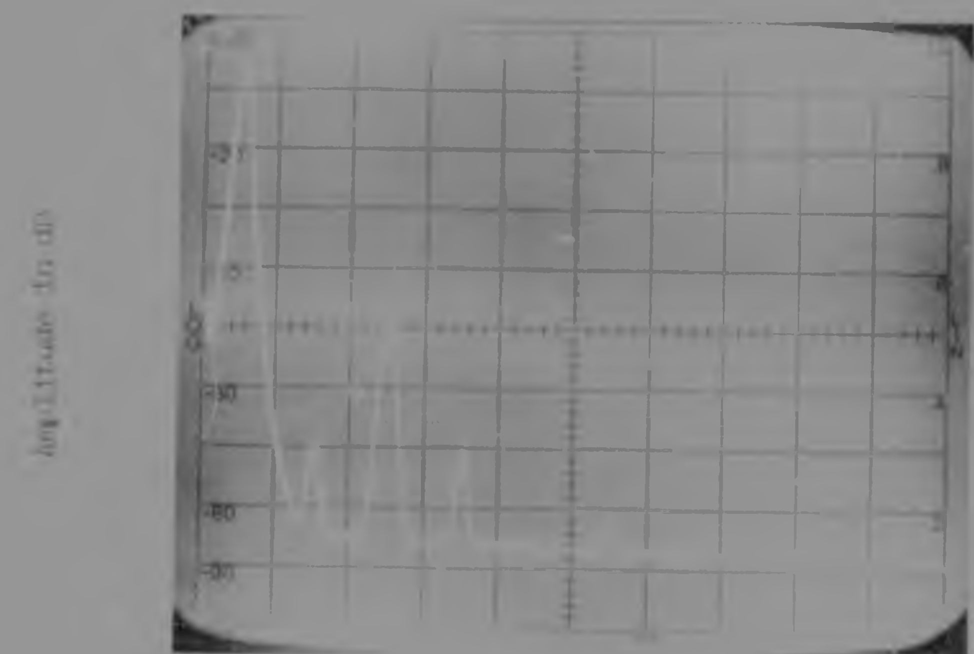

Figure D.10 - As for Figure D.9 but for rotor-bar D.

D.1.2 - Locked-rotor torque measurement

As already discussed in section 3.1.3 two different methods were used to determine the starting torque of industrial motor A:

(i) Direct method (using a torque-arm and a scale)

$$ST = (\text{measured torque}) \times (\text{rated voltage/test voltage})^2 / (\text{rated kW})$$

(ii) Indirect method (using the measured input kW's)

$$ST = (\text{input kW's} - 3.I1^2.R1/1000) \times 0{,}9 \times (\text{rated voltage/test voltage})^2/(\text{rated kW})$$

Where the 0,9 is an empirical factor allowing for the stray losses
and ST is the starting torque in per unit of full load torque (FLT).

The values of the starting torque obtained for the faulty and the normal cages are shown in Table D.10.

From the values of the starting torque tabulated in Table D.10 it is clear that no difference exist between the starting torque produced with one bar broken and that produced with a normal cage. As explained in Chapter 4 section 4.4, this is in accordance with the fact that the current flowing into the `broken' bar is practically equal to the current flowing into the healthy bars.

Table D.10 - Starting torque in p.u. of FLT measured on industrial motor A by two different methods. The voltage during the test was:

1200 Volts - 'broken' bar

900 Volts - 'normal' cage

	ST at rated voltage in p.u. of FLT	
	'broken' bar	'normal' cage
Direct method	0,87	0,87
Indirect method	0,94	0,94
Average	0,905	0,905

D.1.3 - Vibration measurements

D.1.3a - No-load vibration measurements ('broken' bar condition only)

The methods and the aims of these tests were explained in section 3.1.4. As indicated, the no-load vibration test was carried out on industrial motor A, only under the 'broken' bar condition.

Figure D.11 shows the vibration at the actual running speed plotted against the speed of the rotor as the motor coasts down from full speed to stand-still against its own inertia after the supply has been switched off. The maximum of the curve at 2338 rpm gives the first critical speed of the rotor. This is close to the full speed of the machine and therefore large changes in load, which are accompanied by relatively large changes in slip, will obviously have some detrimental effect on the motor. In this project the loading of the motor was such that the slip never went beyond 10 to 15 rpm. Therefore the effects arising from this first critical speed being close to the full load speed could safely be neglected.

D.1.3b - Comparison of vibration patterns taken at rated and reduced voltage

The motor was tested uncoupled and the positions of the vibration pick-ups were as indicated in Figure 3.5, page 3.13. The actual recordings are shown in figures D.12a-D.18b. The figures with subscript `a' are those recorded at rated voltage while those with subscript `b' were all recorded at the same reduced voltage.

The ratios of the amplitudes of the vibrations at rated and reduced voltage are summarised in tables D.11-D.16. The tables were compiled for all the measuring positions and only include the more conspicuous amplitudes. In these tables the frequencies of the vibrations are given in rpm or in multiples or submultiples of the actual motor speed (eg 1xRPM = 2980 rpm, 2xRPM = 5975 rpm, etc.). This vibration amplitude ratio is defined for each frequency as:

$$\frac{\text{Amplitude of vibration at reduced voltage}}{\text{Amplitude of vibration at rated voltage}}$$

Table D.11 - Results of no-load vibration test on industrial motor A having a `broken' bar.
Pick-up position: DEV

Approx. frequency of vibration	(1/3)xRPM =980rpm	1xRPM =2980rpm	2xRPM =5975rpm	9280rpm
Amplitude ratio	0,758	0,878	0,199	0,911

Table D.12 - As for Table D.11
Pick-up position: DEA

Approx. frequency of vibration	2980rpm	5965rpm
Amplitude ratio	1,8	0,288

Table D.13 - As for Table D.11
Pick-up position: DEH

Approx. frequency of vibration	1000rpm	2980rpm	5965rpm	9280rpm
Amplitude ratio	1,44	0,634	0,262	0,966

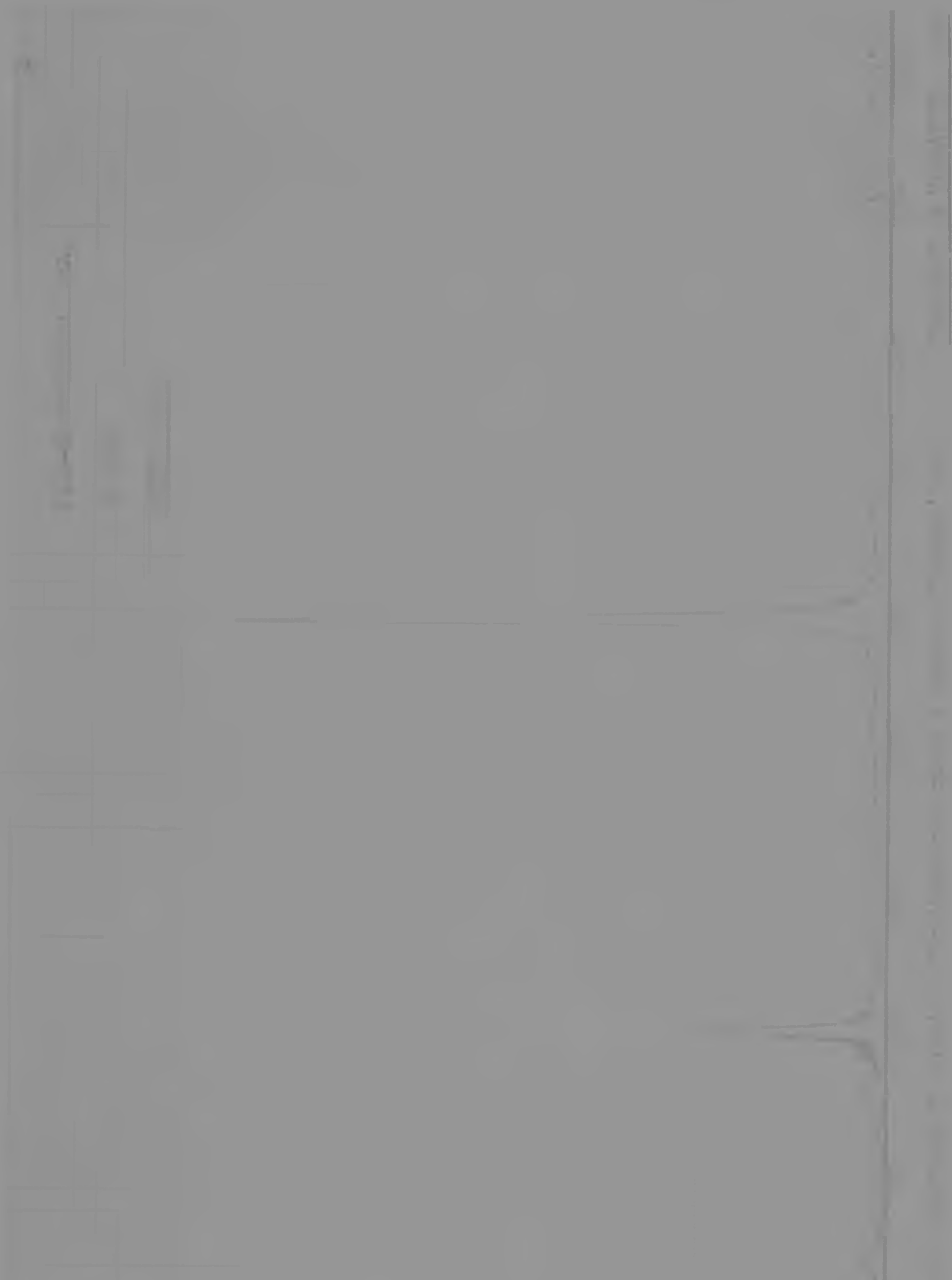

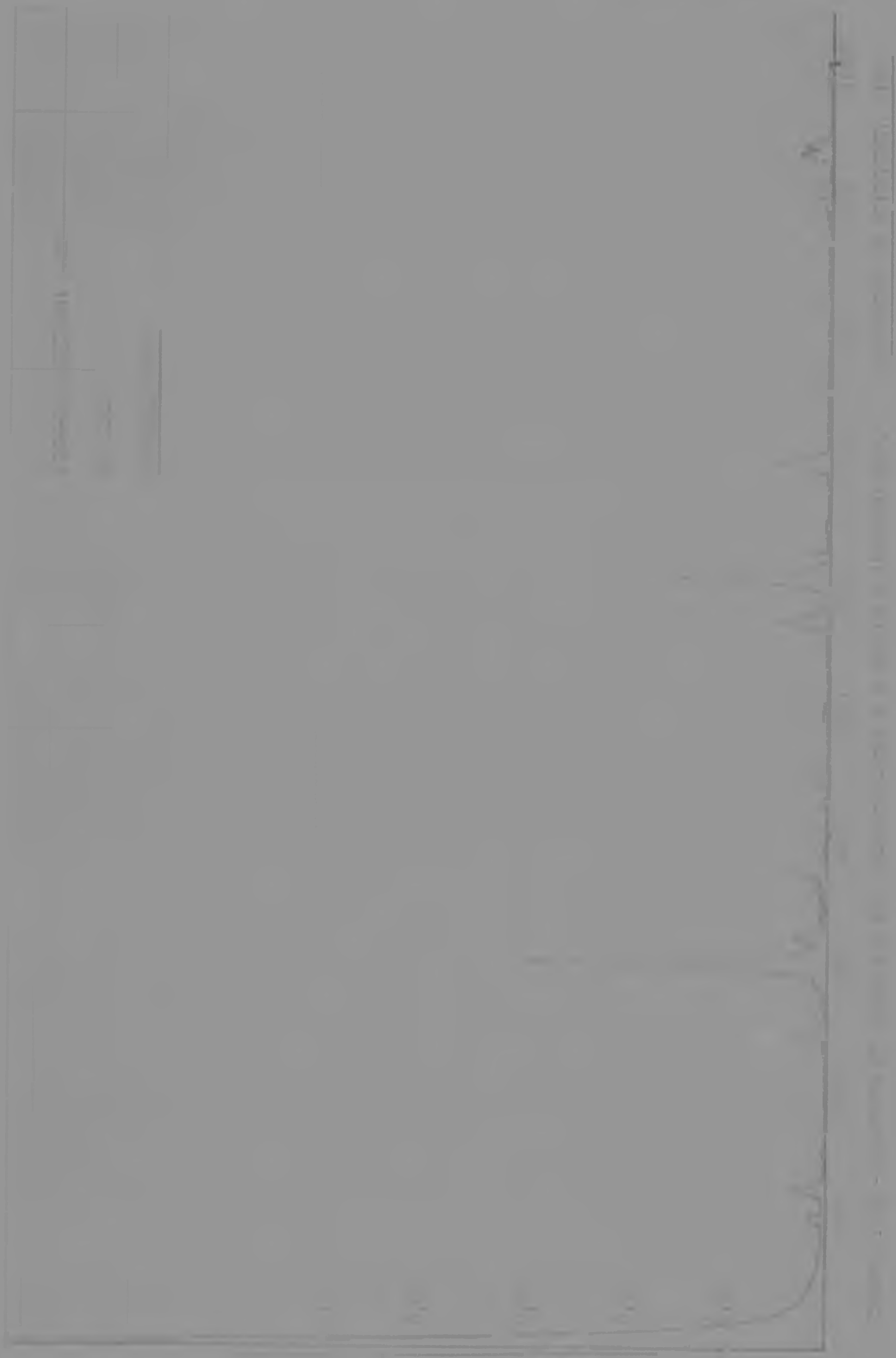

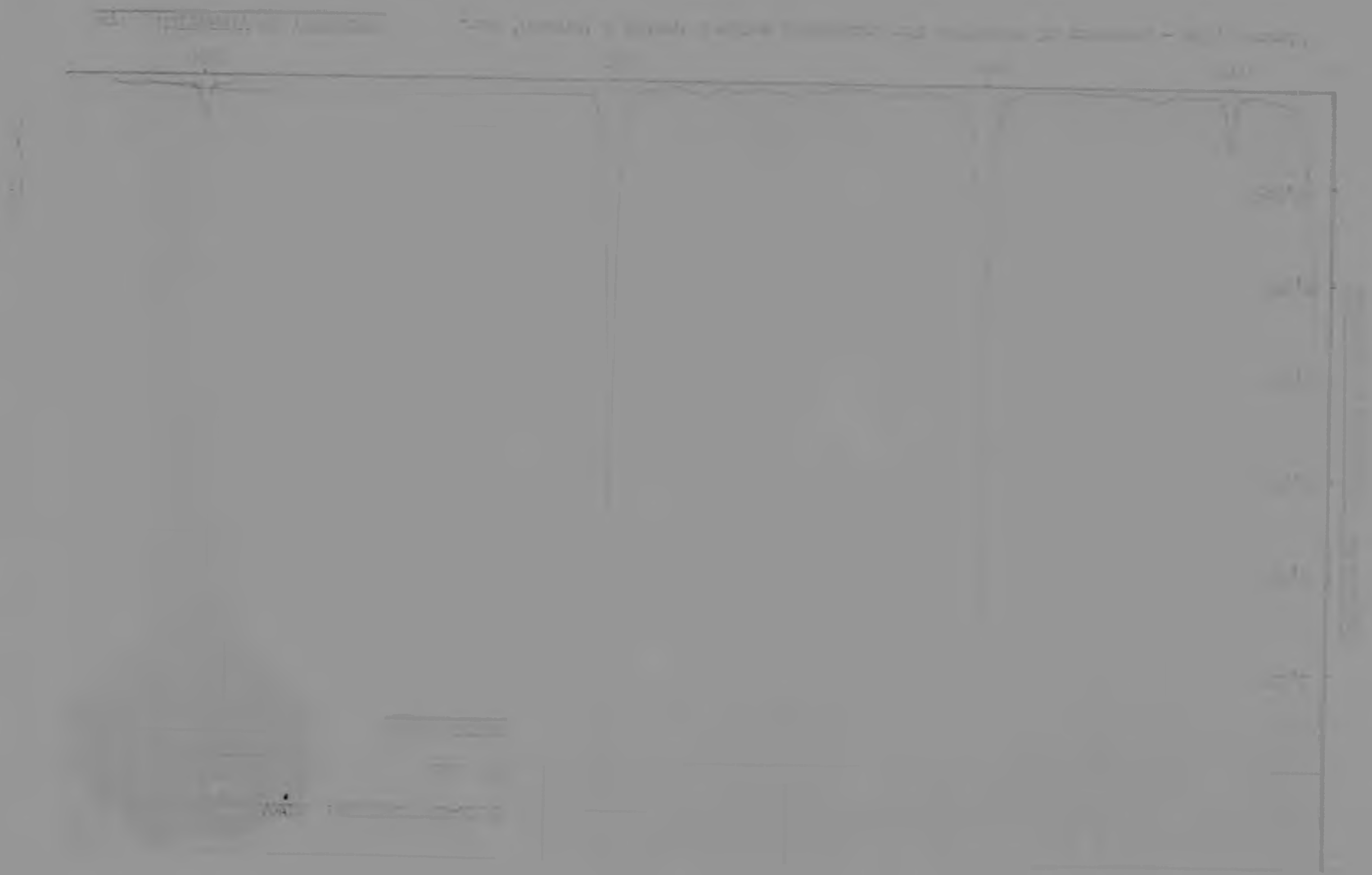

,528

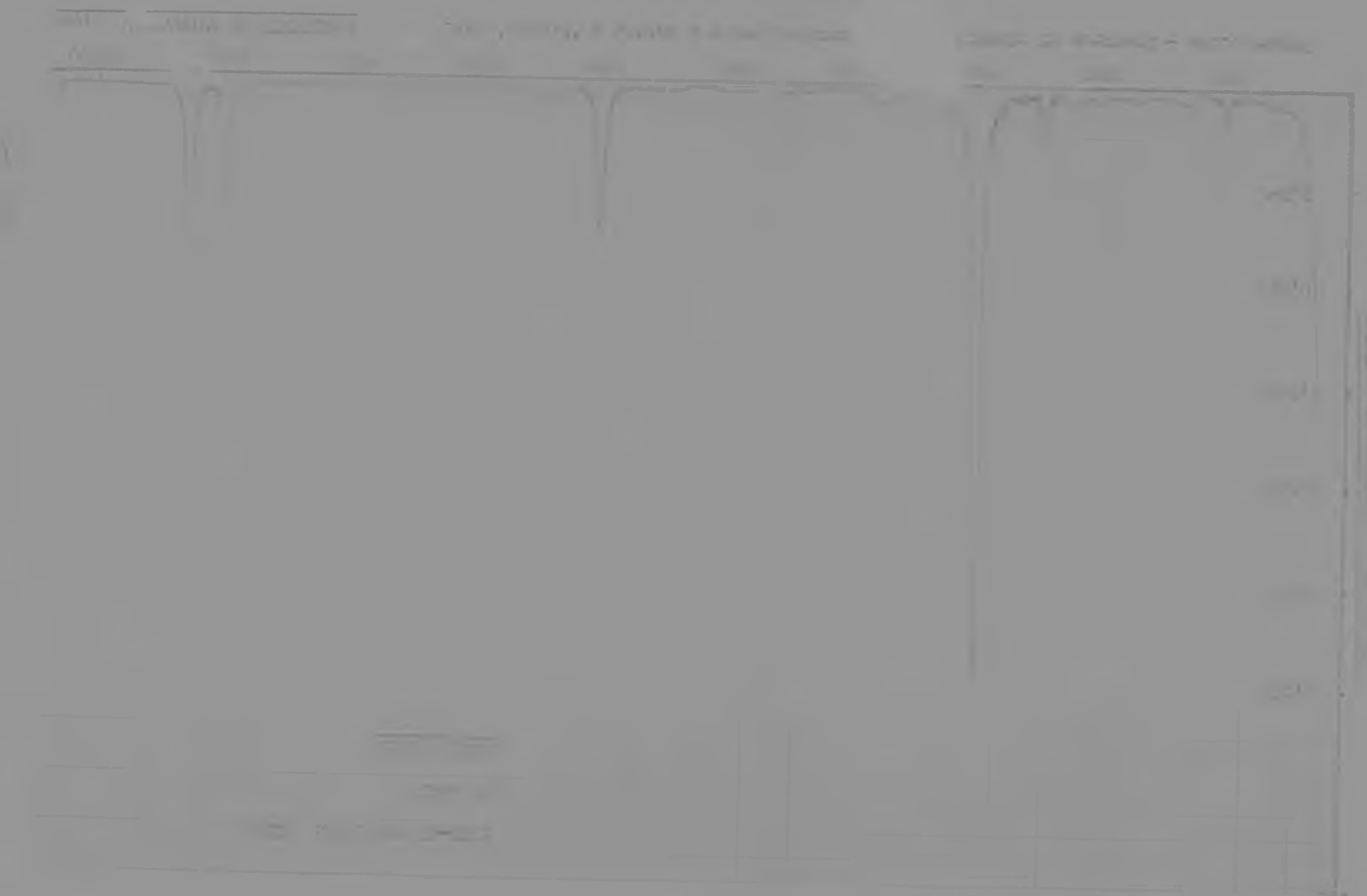

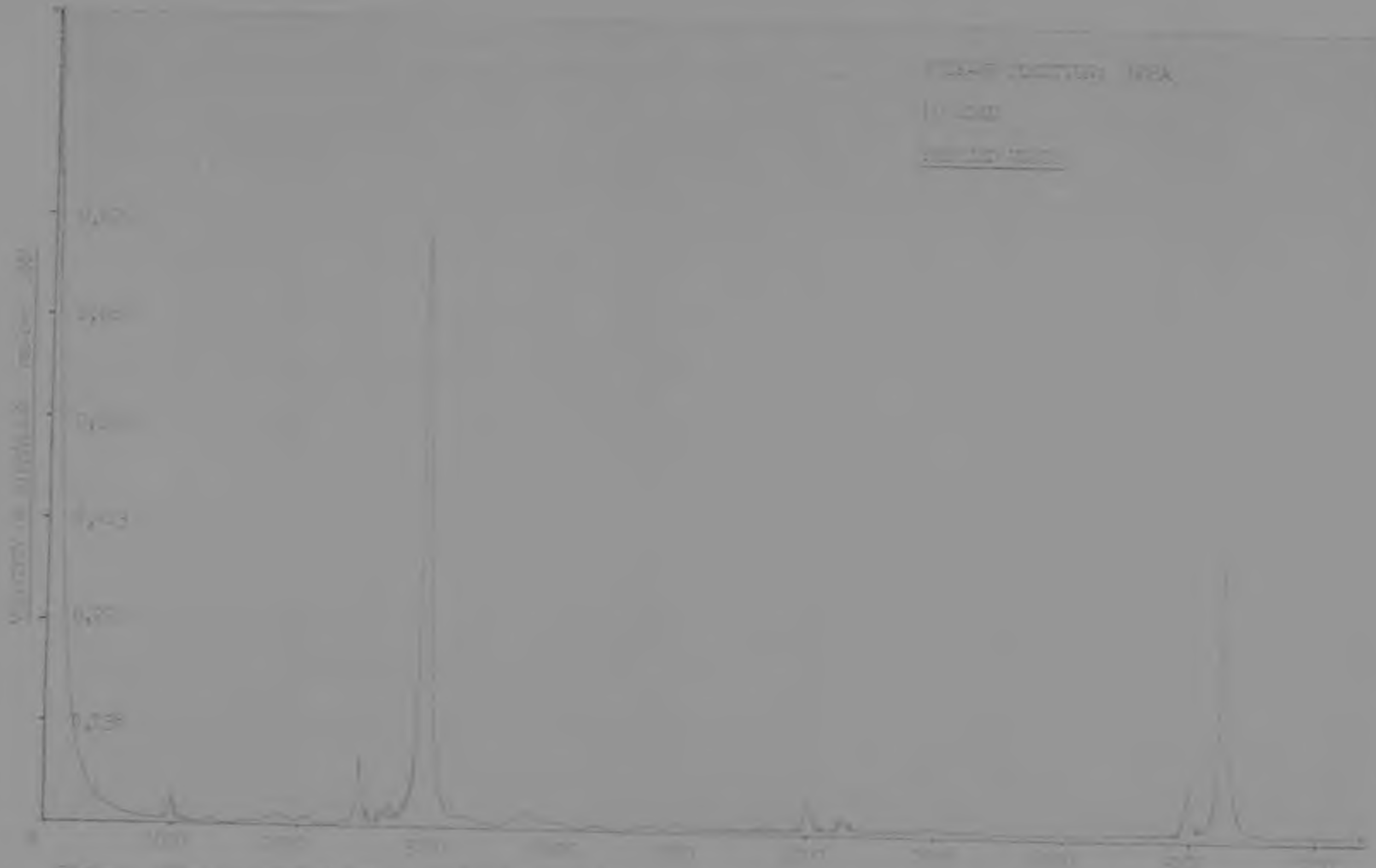

Table D.14 - As for Table D.11

Pick-up position: NDEV

Approx. frequency of vibration	1000rpm	3000rpm	6000rpm	9280rpm
Amplitude ratio	0,867	0,875	0,374	?

Table D.15 - As for Table D.11

Pick-up position: NDEA

Approx. frequency of vibration	1000 rpm	2465 rpm	2955 rpm	6000 rpm	8995 rpm	9280 rpm
Amplitude ratio	0,854	1,247	0,932	0,178	0,365	1,502

Table D.16 - As for Table D.11

Pick-up position: NDEH

Approx. frequency of vibration	1000rpm	2975rpm	6000rpm	9280rpm
Amplitude ratio	0,713	0,898	0,221	1,745 ?

The question mark (?) appearing in the tables indicates unclear readings.

Table D.17 was compiled from figures D.17a and D.17b which are recordings taken with the pick-up in the same position as for Figure D.11a and Figure D.11b. In this case the range of frequencies recorded was extended to 60000 rpm to assess whether any changes in the higher frequency vibrations were significant. Table D.17 shows that this was not the case.

Table D.17 - Results of no-load vibration test on industrial motor A having a 'broken' bar. (Extended frequency range).
Pick-up position: DEV

Approx. frequency of vibration	960rpm	2890rpm	5900rpm	9155rpm	11700rpm	15840rpm	18190rpm ?	49080rpm
Amplitude ratio	0,969	0,419	0,155	0,972	0,566	0,977	0,878	0,660

Tables D.11 to D.17 indicate the degree of change on the vibration amplitudes for a particular frequency due to the change in the terminal voltage. To develop further insight into the phenomena involved, tables D.18-D.24 were compiled where the amplitude of vibration at certain frequencies is compared with the amplitude of vibration at 1xRPM (for the same voltage). This was done for rated voltage and for reduced voltage. In this way it becomes clear which of the vibrations change in magnitude relative to the 1xRPM vibration with a change in the supply voltage.

Table D.18 - Comparison of vibrations at other frequencies relative to that at 1xRPM.
No-load vibration test on industrial motor A with a 'broken' bar condition.
Pick-up position: DEA

	Approx. vibration freq.(rpm)	2980	5965
Rated voltage	$\frac{\text{Amplitude at frequency......}}{\text{Ampl. at 1xRPM(=0,333mm/sec)}}$	1,000	3,126
Reduced voltage	$\frac{\text{Amplitude at frequency......}}{\text{Ampl. at 1xRPM(=0,600mm/sec)}}$	1,000	0,500

Table D.19 - As for Table D.18

Pick-up position: DEV

	Approx. vibration freq.(rpm)	980	2980	5975	9285
Rated	Amplitude at frequency......	0,916	1,000	5,336	2,573
voltage	Ampl. at 1xRPM(=0,131mm/sec)				
Reduced	Amplitude at frequency......	0,791	1,000	1,209	2,670
voltage	Ampl. at 1xRPM(=0,115mm/sec)				

Table D.20 - As for Table D.18

Pick-up position: DEH

	Approx. vibration freq.(rpm)	1000	2980	5965	9270
Rated	Amplitude at frequency......	0,145	1,000	4,662	0,387
voltage	Ampl. at 1xRPM(=0,922mm/sec)				
Reduced	Amplitude at frequency......	0,330	1,000	1,928	0,590
voltage	Ampl. at 1xRPM(=0,585mm/sec)				

Table D.21 - As for Table D.18

Pick-up position: NDEV

	Approx. vibration freq.(rpm)	1000	2950	5990	9280
Rated voltage	Amplitude at frequency...... / Ampl. at 1xRPM(=1,034mm/sec)	0,116	1,000	0,786	0,080
Reduced voltage	Amplitude at frequency...... / Ampl. at 1xRPM(=0,905mm/sec)	0,115	1,000	0,336	?

Table D.22 - As for Table D.18

Pick-up position: NDEH

	Approx. vibration freq.(rpm)	1000	2975	6000	9280
Rated voltage	Amplitude at frequency...... / Ampl. at 1xRPM(=1,262mm/sec)	0,102 ?	1,000	1,518	0,148 ?
Reduced voltage	Amplitude at frequency...... / Ampl. at 1xRPM(=1,133mm/sec)	0,081	1,000	0,373	0,283

Table D.23 - As for Table D.18

Pick-up position: NDEA

	Approx. vibration freq. (rpm)	1000	2465	2955	6000	8995	9280
Rated voltage	Amplitude at frequency...... / Ampl. at 1xRPM (=0,860mm/sec)	0,056	0,089	1,000	0,267	0,228	0,305
Reduced voltage	Amplitude at frequency...... / Ampl. at 1xRPM (=0,800mm/sec)	0,051	0,119	1,000	0,051	0,090	0,491

D.1.3c - <u>Vibration measurements on load</u>

The procedure used in these tests was as explained in section 3.1.6.

Figures D.19a-D.22b show the vibration recordings taken on industrial motor A at the different positions. In the original recordings the different traces are in different colours making it easy to distinguish between the two. In the copies shown in the text one of the traces, namely those for a load of 300 kW, has been overdrawn in red for clarity. Each set of recordings was repeated for two different load conditions, 300 kW (red trace) and 50 kW (black trace). Also these measurements were taken for the `healthy' cage (figures with subscript b) and `broken' bar (subscript a) conditions. The main features of the recordings are summarised in tables D.24-D.27.

Figures D.25-D.27 show recordings of the vibration amplitudes at various frequencies plotted against time for both load conditions and for the `broken' bar and `normal' cage conditions. No meaning can be attached to the phase shift between the traces because they were recorded sequentially and not simultaneously.

Note: It is important, when comparing the magnitudes of the vibrations for the different load conditions to be aware of any significant periodic changes in the vibration amplitudes. This is so because the recording at any particular frequency is almost an instantaneous indication of the vibration amplitude at that particular instant and is not an average value.

Table D.24 - Change in amplitude of vibration with load from results of on-load vibration tests on industrial motor A.

Pick-up position: DEH

Approx. freq. of vibration (rpm)		3000	6000	9000	12000
Change in the amplitude with increase in load from 50 kW to 300 kW	`broken' bar	0,829	3,154	-	7,75
	`normal' cage	0,680	1,224	-	2,846

Table D.25 - As for Table D.24

Pick-up position: NDEV

Approx. freq. of vibration (rpm)		3000	6000	9000	12000
Change in the amplitude with increase in load from 50 kW to 300 kW	`broken' bar	1,000	1,054	-	6,545
	`normal' cage	0,403	1,551	-	2,958

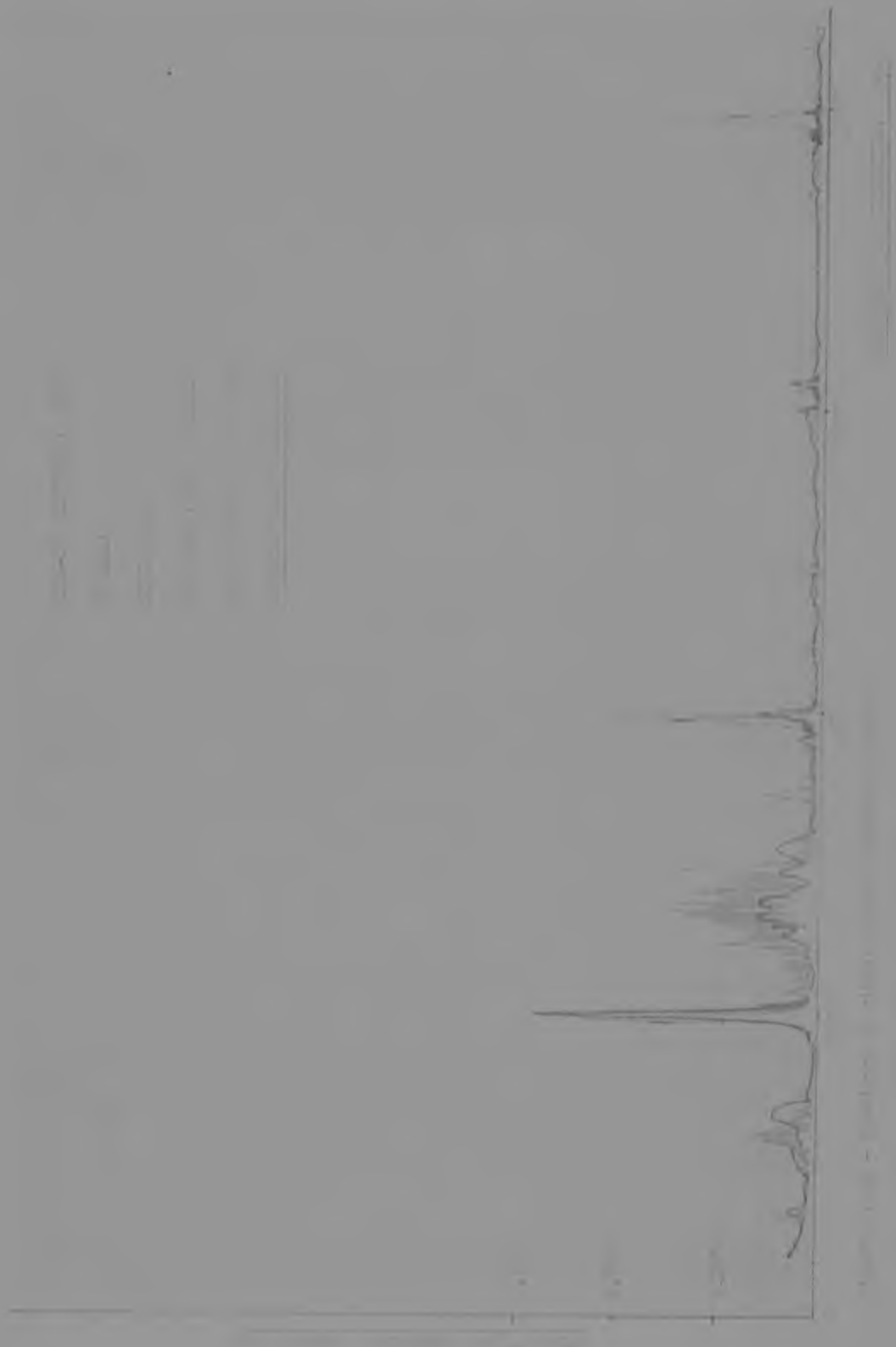

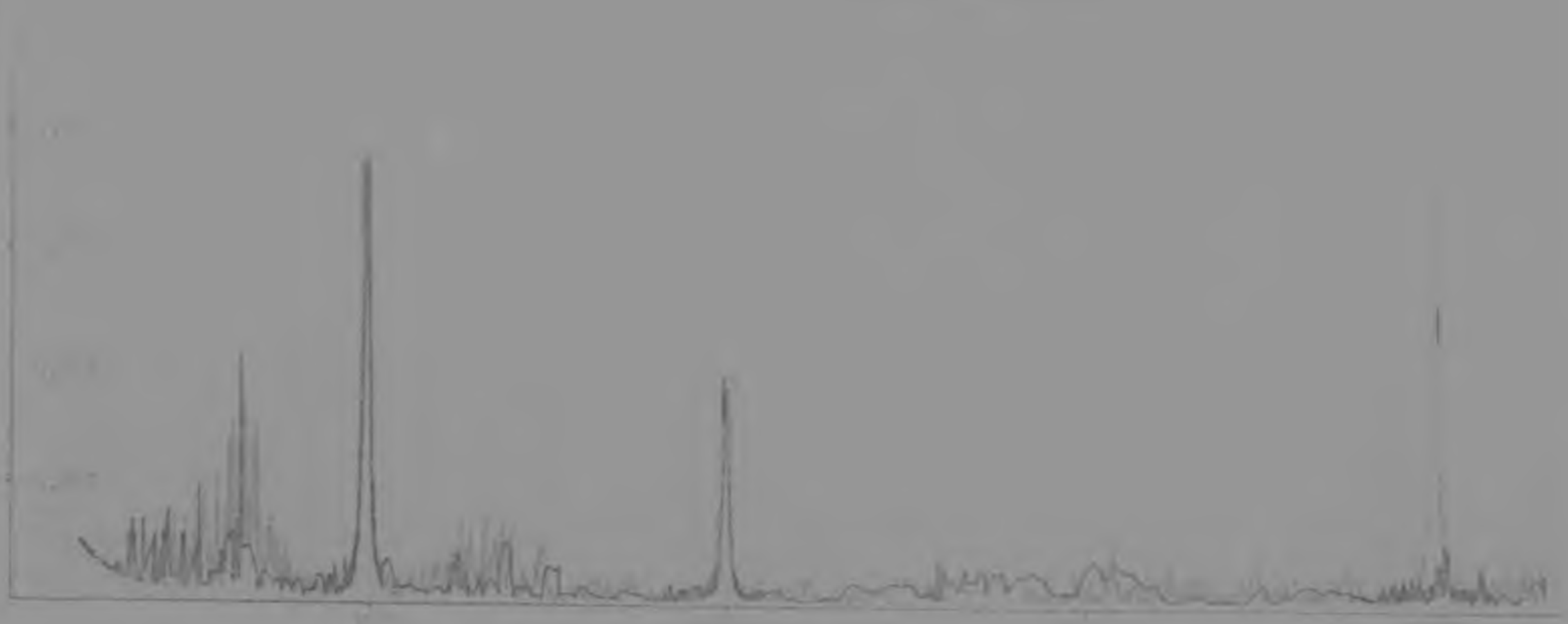

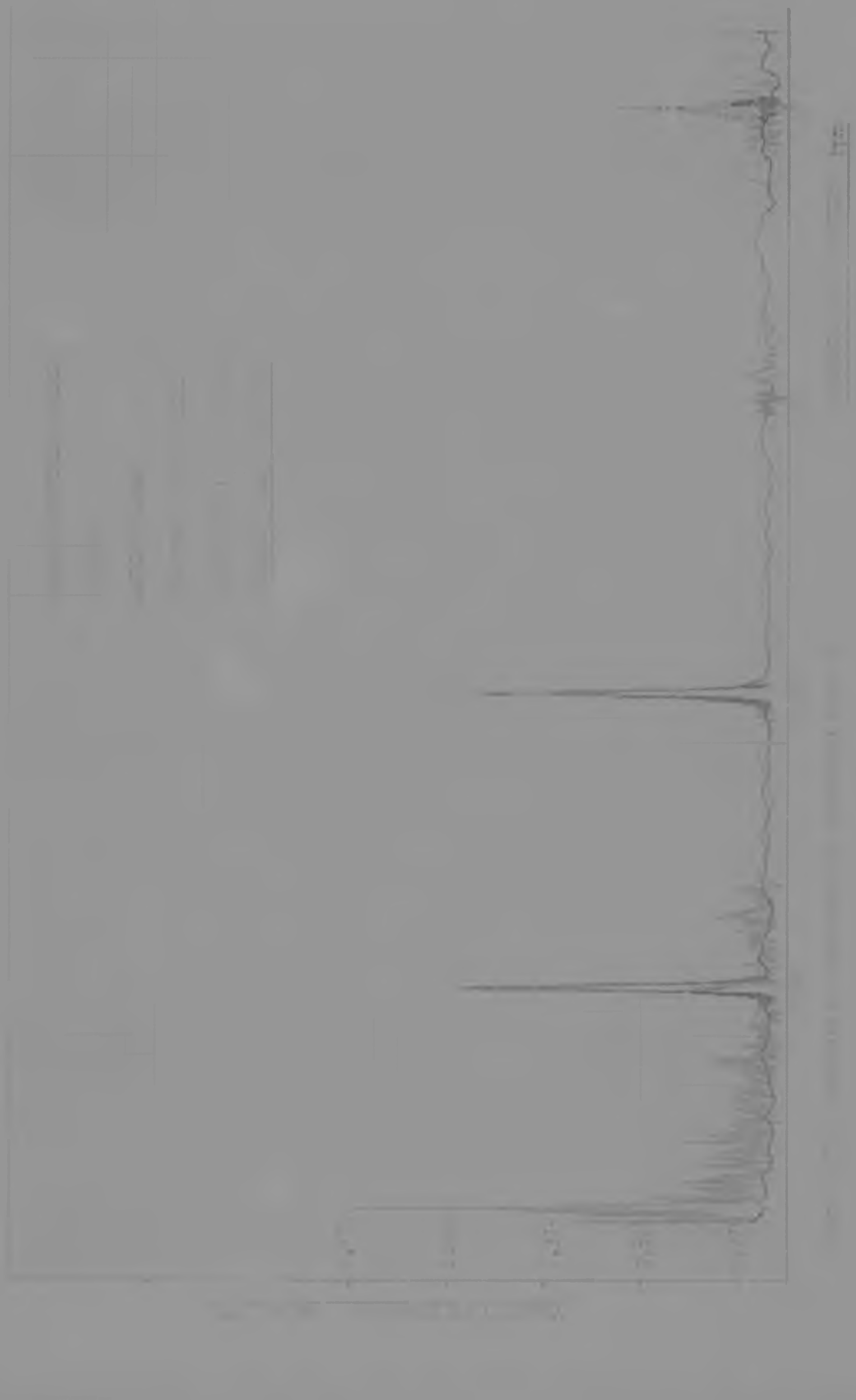

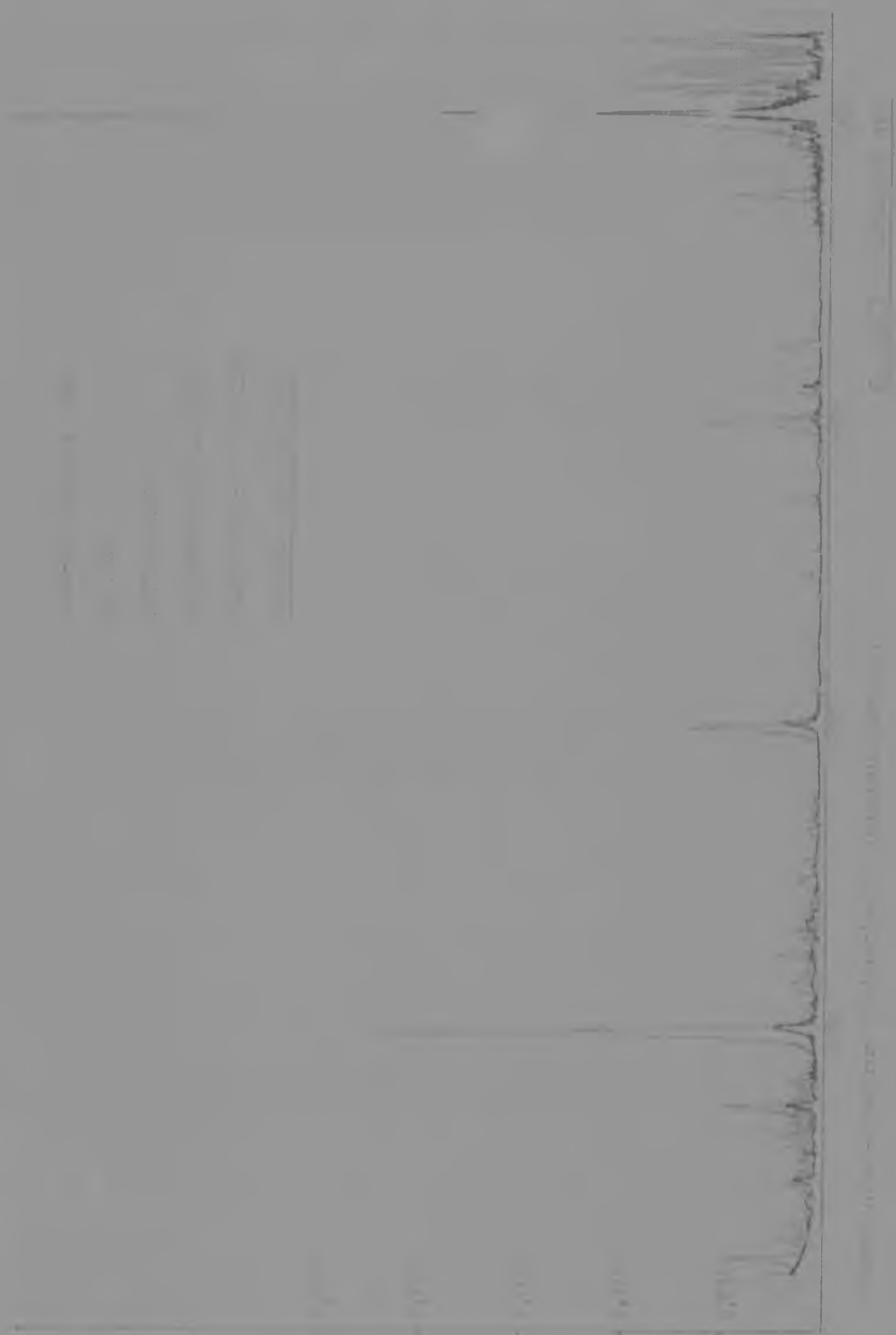

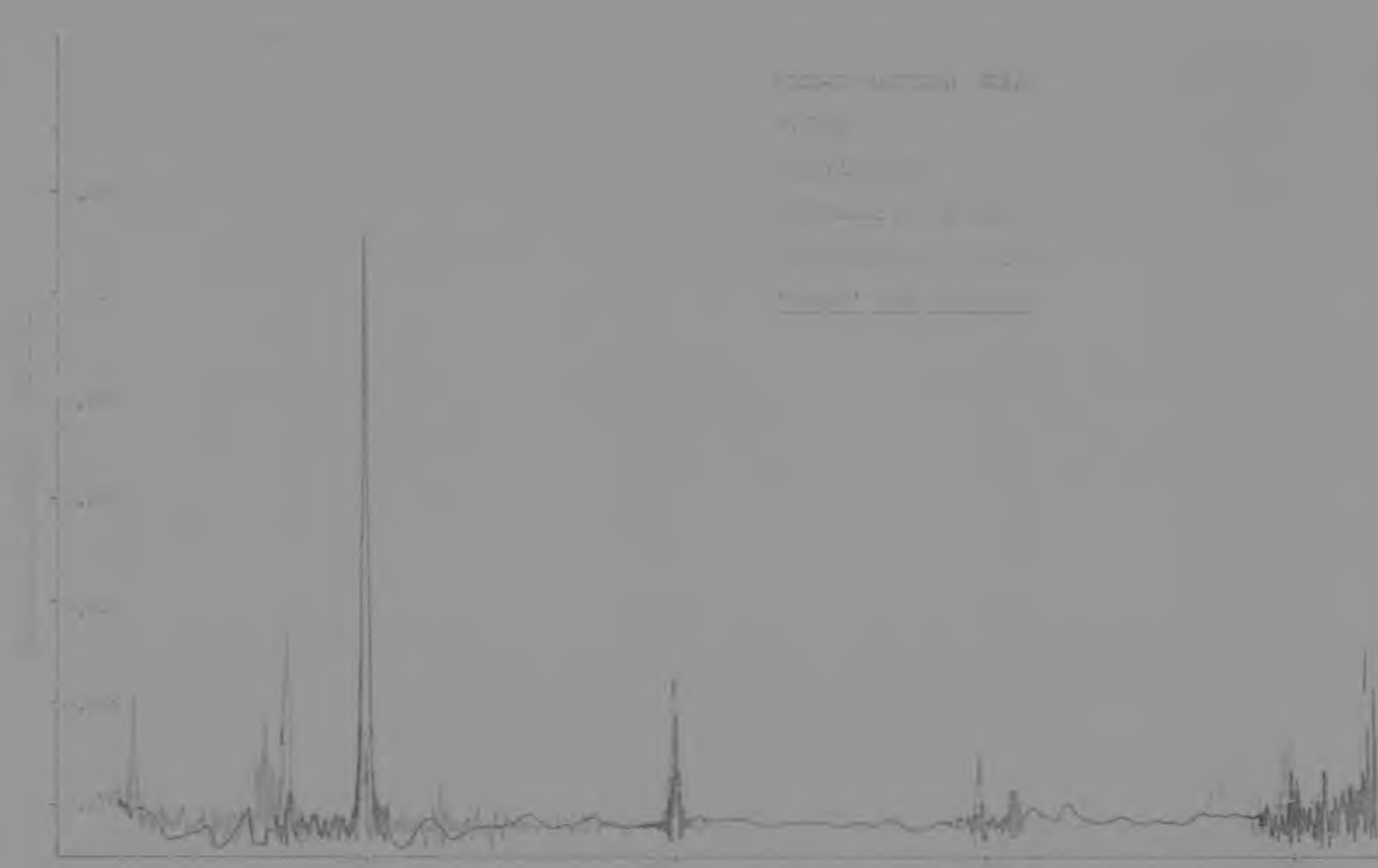

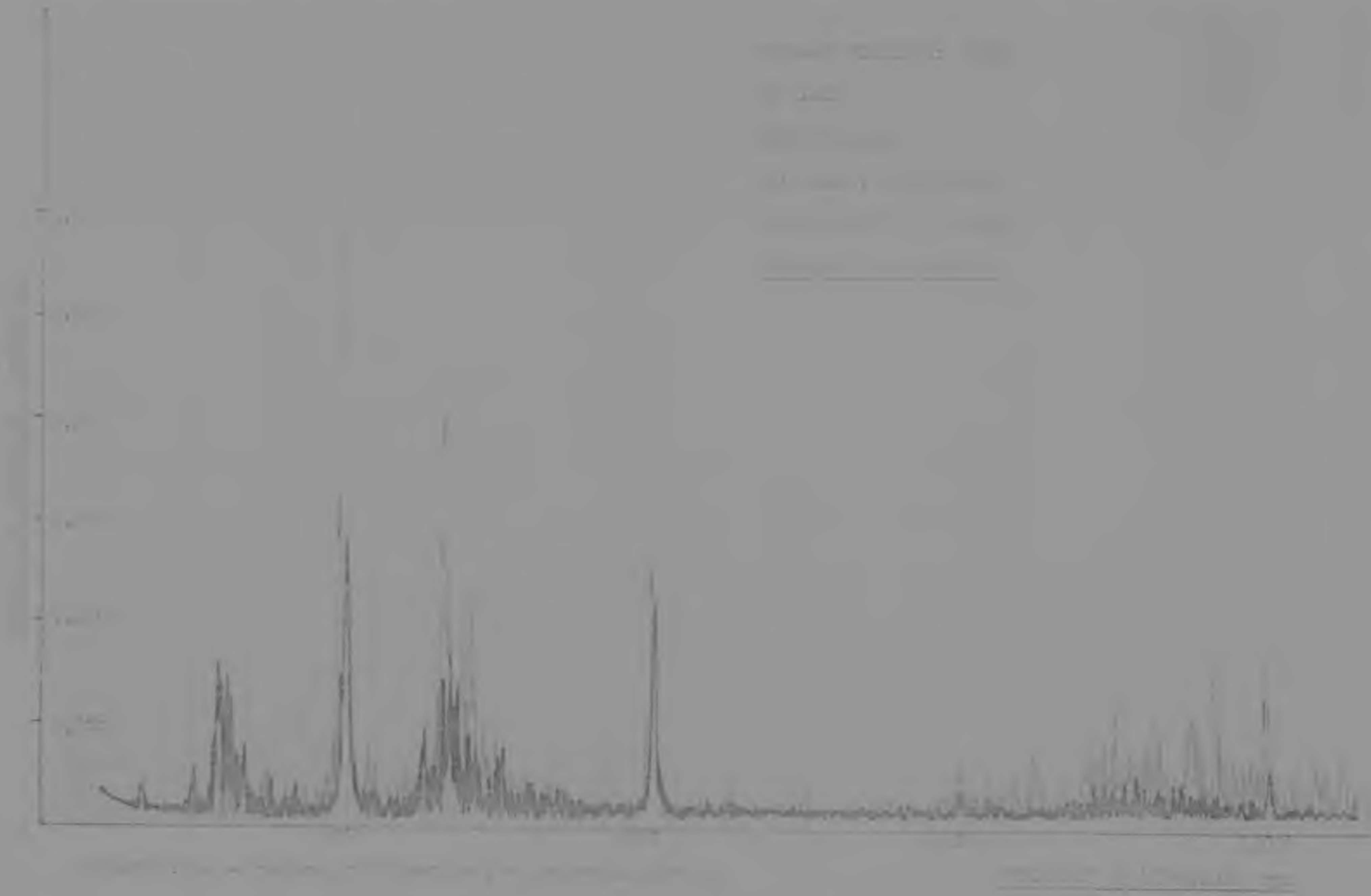

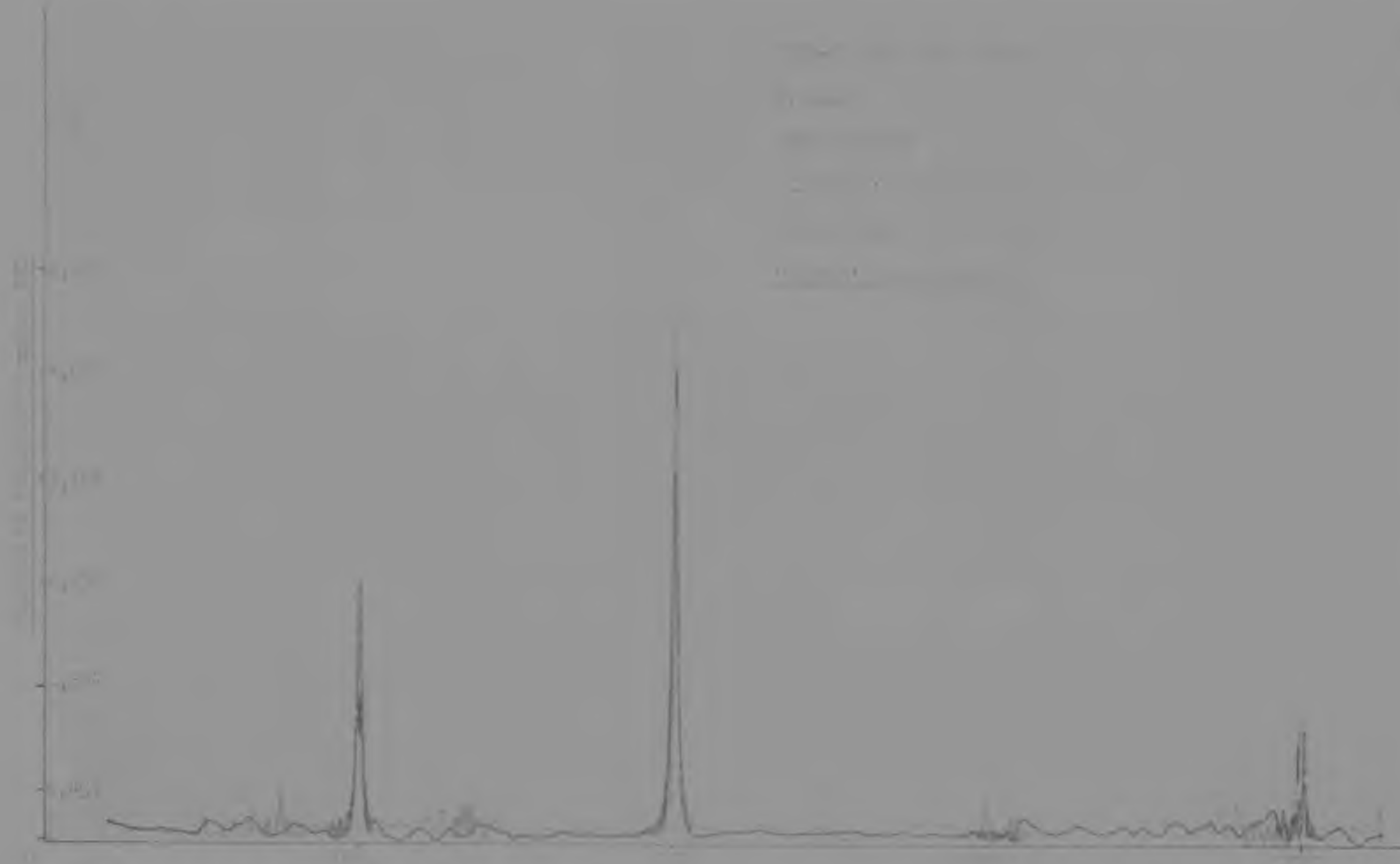

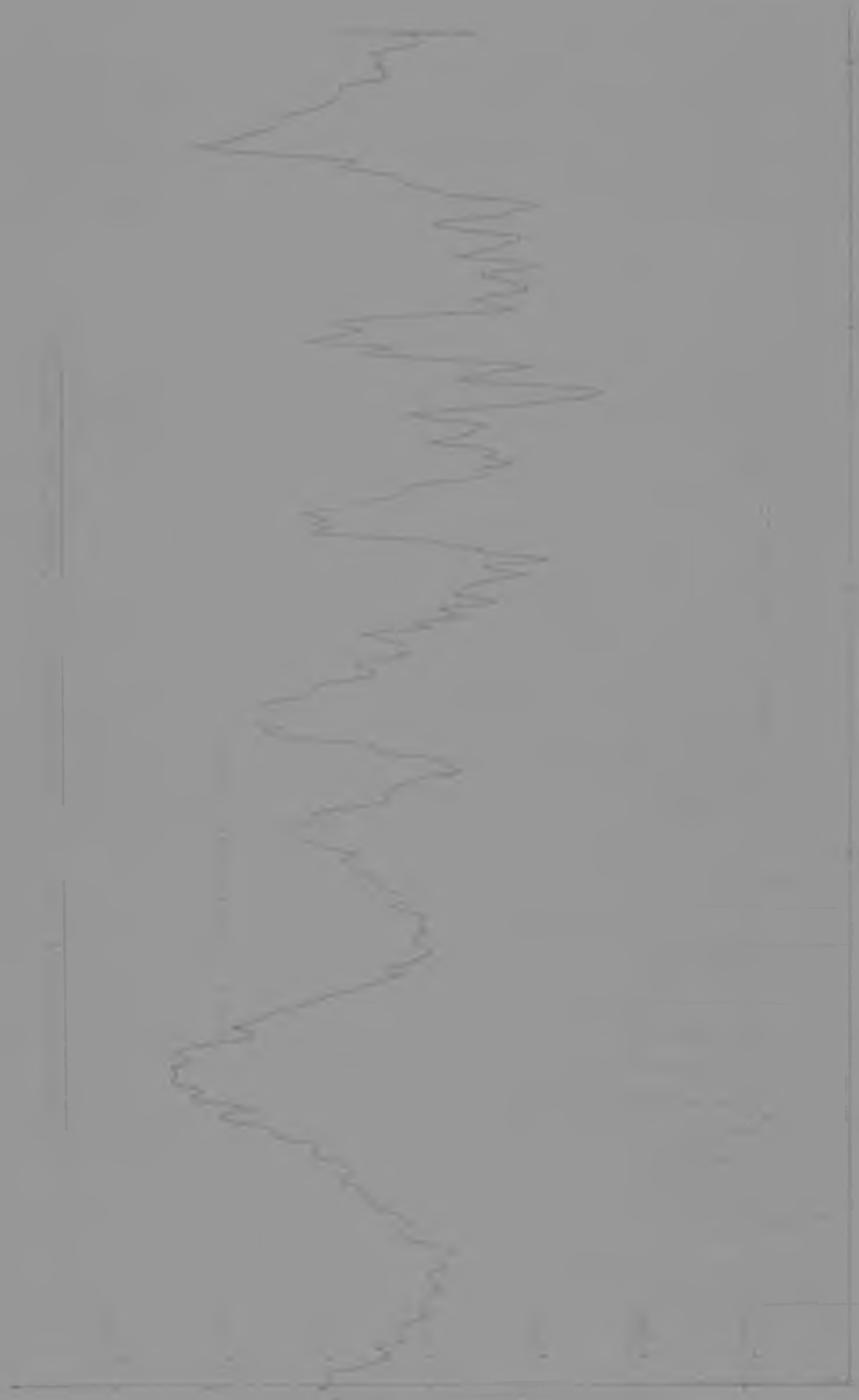

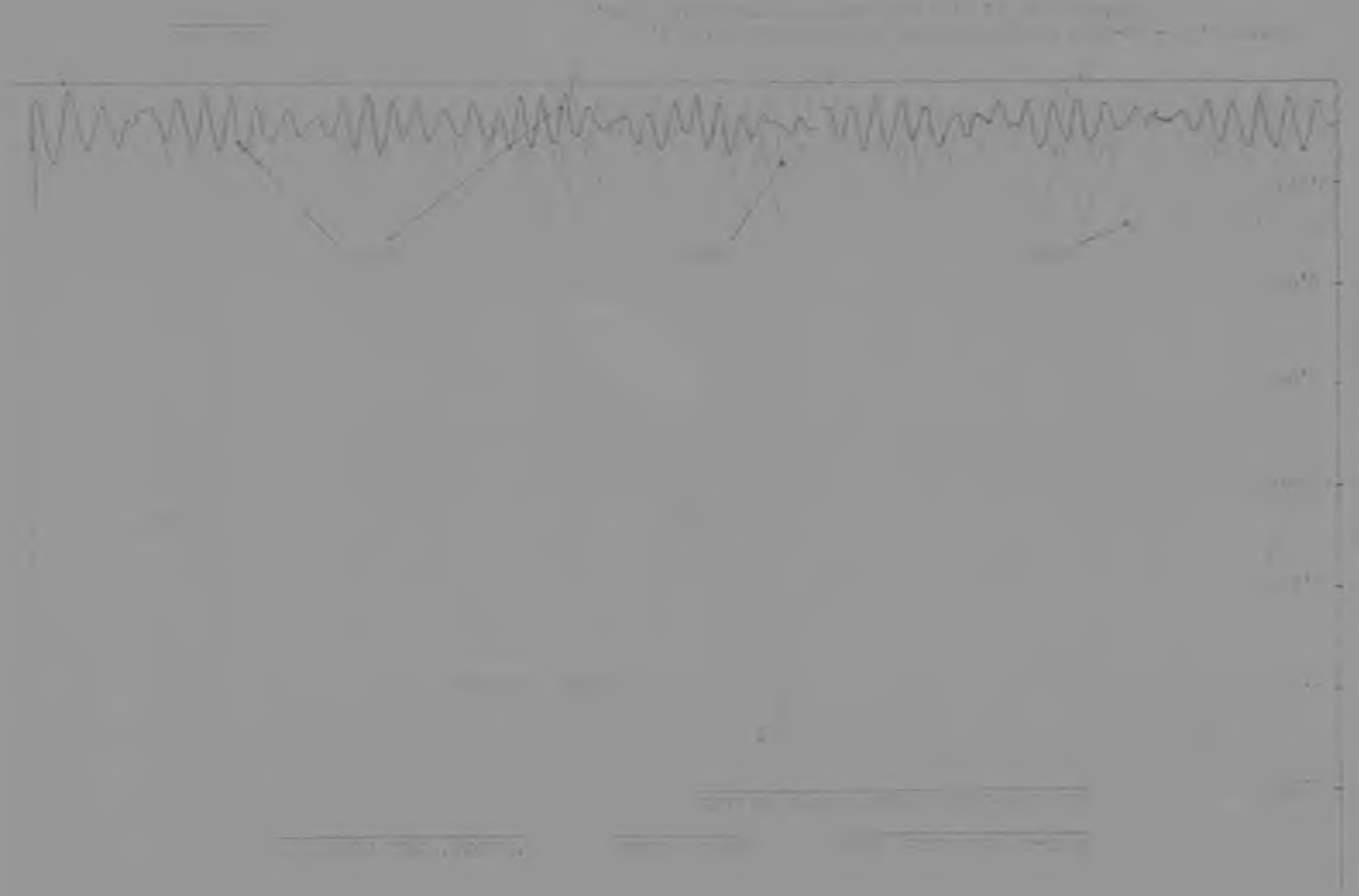

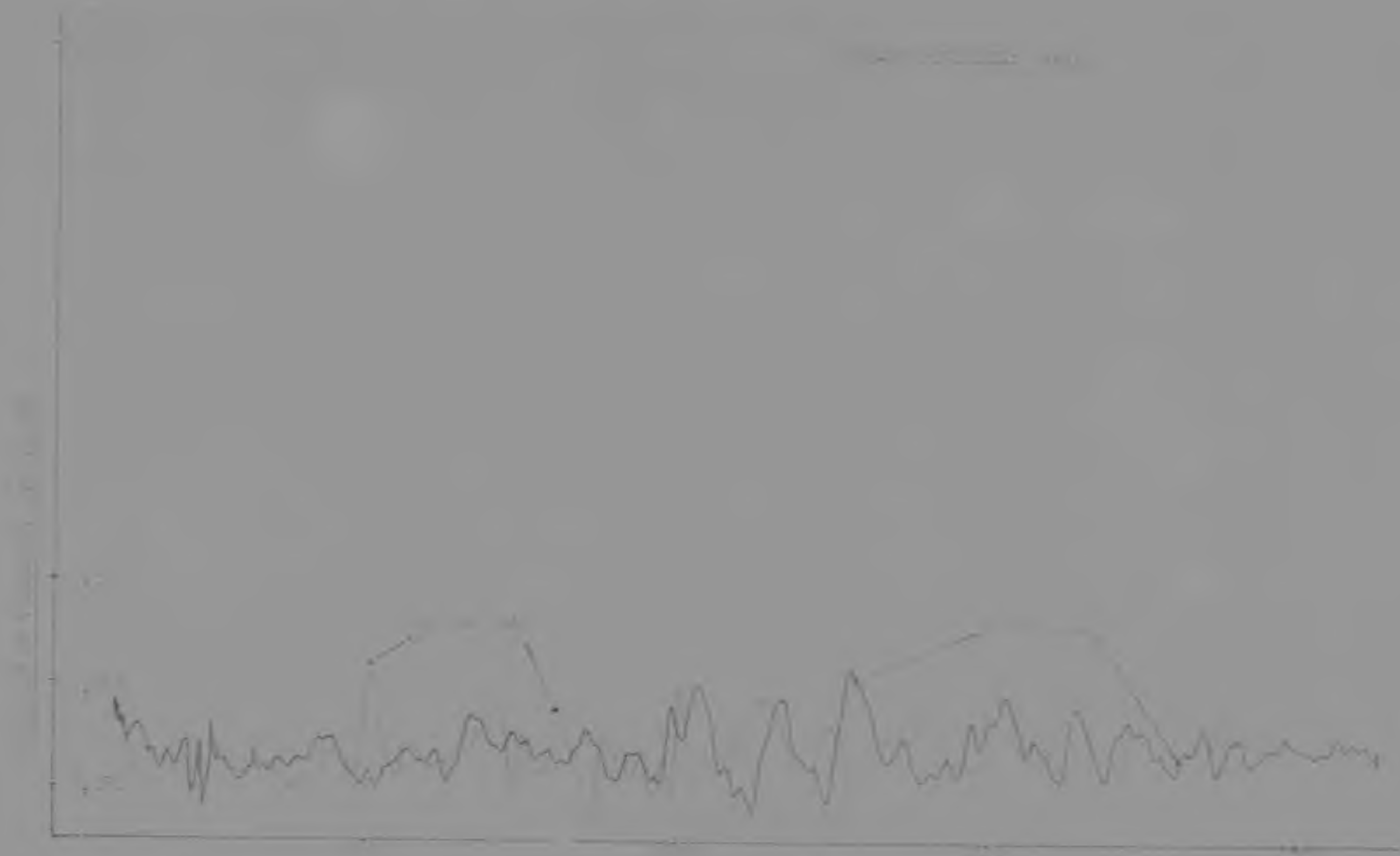

Table D.26 - As for Table D.24, but in this case the loading on the motor when tested with the `broken' bar was different that when tested with the `normal' cage.

Pick-up position: NDEH

Approx. freq. of vibration (rpm)		3000	6000	9000	12000
Change in amplitude for load change:50 to 150kW	`broken' bar	2,089	1,400	-	3,250
Change in amplitude for load change:50 to 300kW	`normal' cage	0,560	1,444	*	1,22[illegible]

Table D.27 - As for Table D.24

Pick-up position: NDEA

Approx. freq. of vibration (rpm)		2250	3000	3750	6000
Change in the amplitude with increase in load from 50 kW to 300 kW	`broken' bar	2,857	8,800	*	3,500
	`normal' cage	3,385	0,208	*	1,286

8250	9000	9250	9750	10250	12000
*	6,250	*	*	*	3,5+
*	1,864	*	-	*	1,471

The symbol * indicates a large change in amplitude but in absolute terms the magnitude is small when compared with the more conspicuous magnitudes.

Figures D.28 and D.29 show vibration spectra measured on the gearbox surface facing the motor under test. These show that no meaningful vibrations were transmitted into the motor from the gearbox.

D.1.4 - Measurement of the torque-speed characteristics

The procedure used for measuring the torque-speed curves of the industrial motor A has been explained in section 3.1.7. This gave U.V. recordings similar to that shown in Figure D.30, where the torque and the speed are recorded against the same time axis. From these recordings the torque-speed characteristics were extracted. Figures D.31 and D.32 show the torque-speed characteristics of industrial motor A for the 'broken' bar and 'normal' cage conditions respectively.

Figure D.30 - Copy of U.V. Recorder trace of speed and acceleration measurement taken on the industrial motor A.

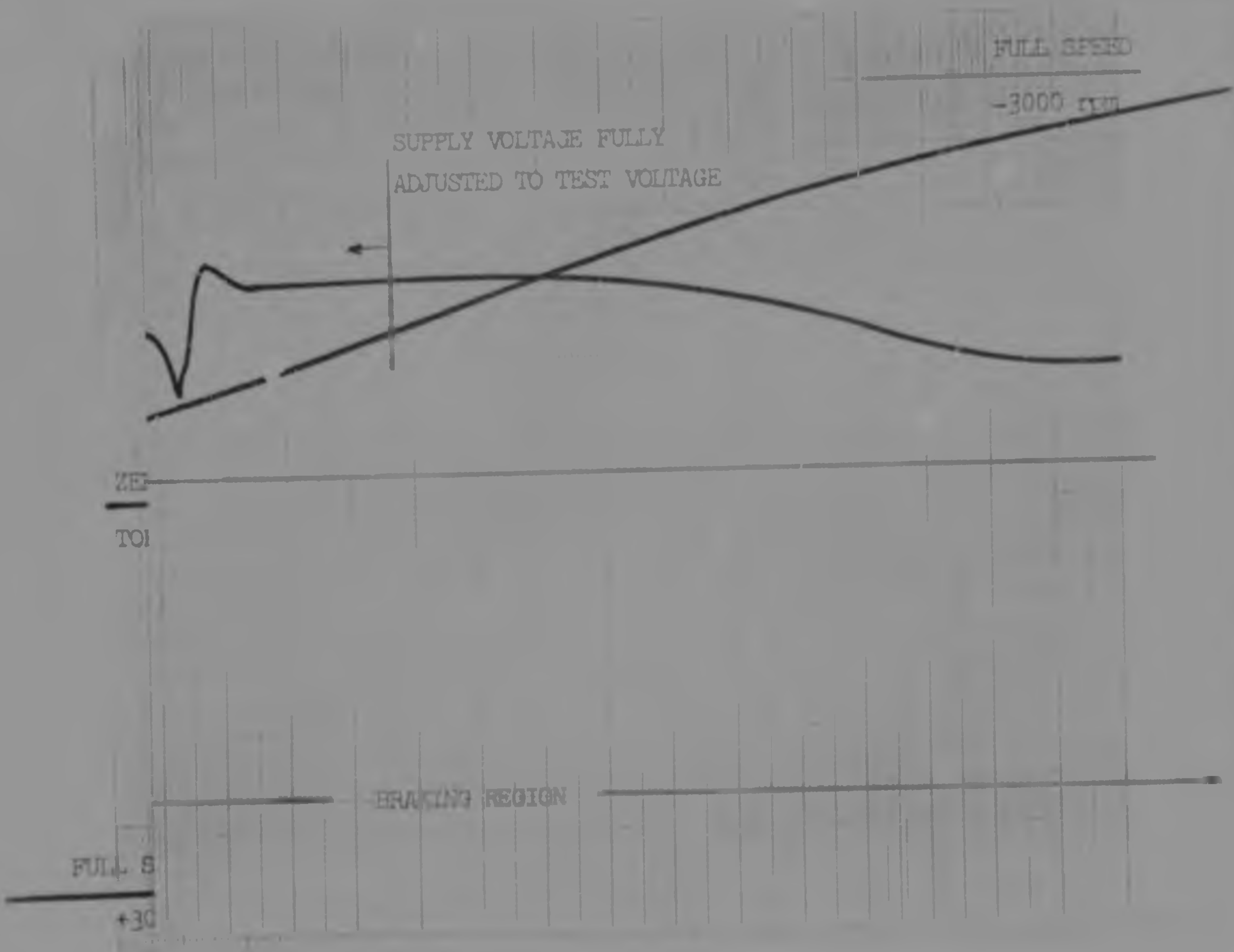

Figure D.30 - Copy of U.V. Recorder trace of speed and acceleration measurements taken on the industrial motor A.

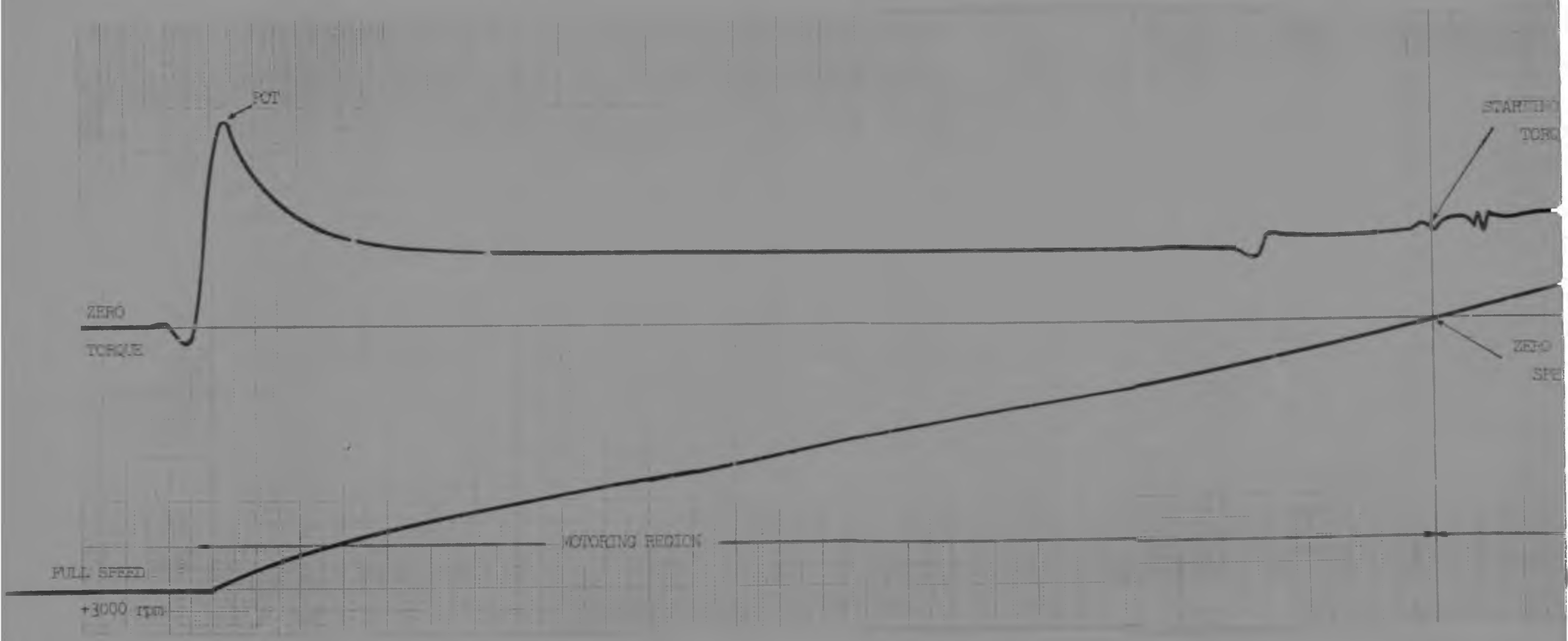

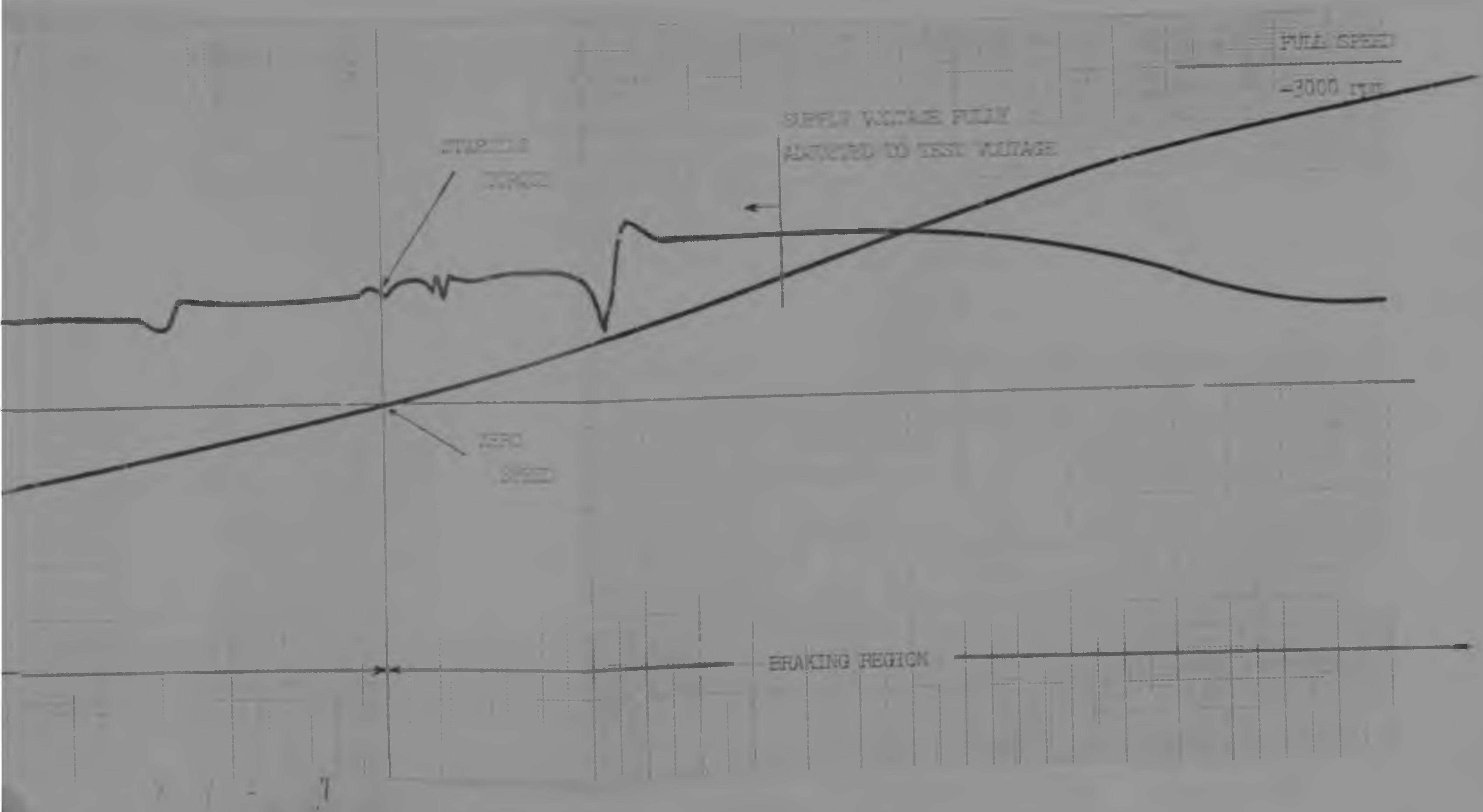
FULL SPEED
=3000 rpm
SUPPLY VOLTAGE FULLY
ADJUSTED TO TEST VOLTAGE
STARTING
TORQUE
ZERO
SPEED
BRAKING REGION

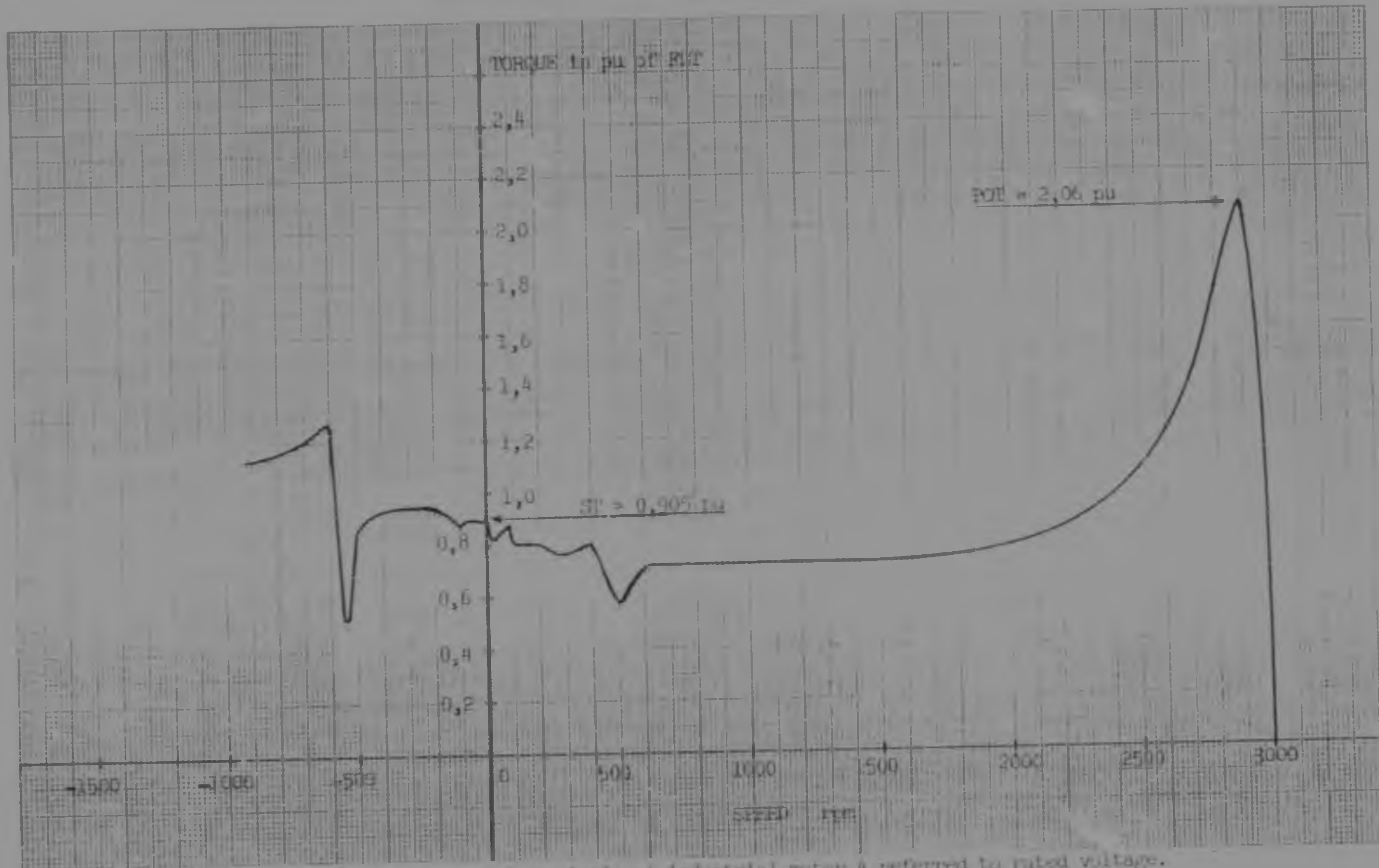

Figure D.31 - Measured torque-speed characteristic of industrial motor A referred to rated voltage. 'Broken' bar condition.

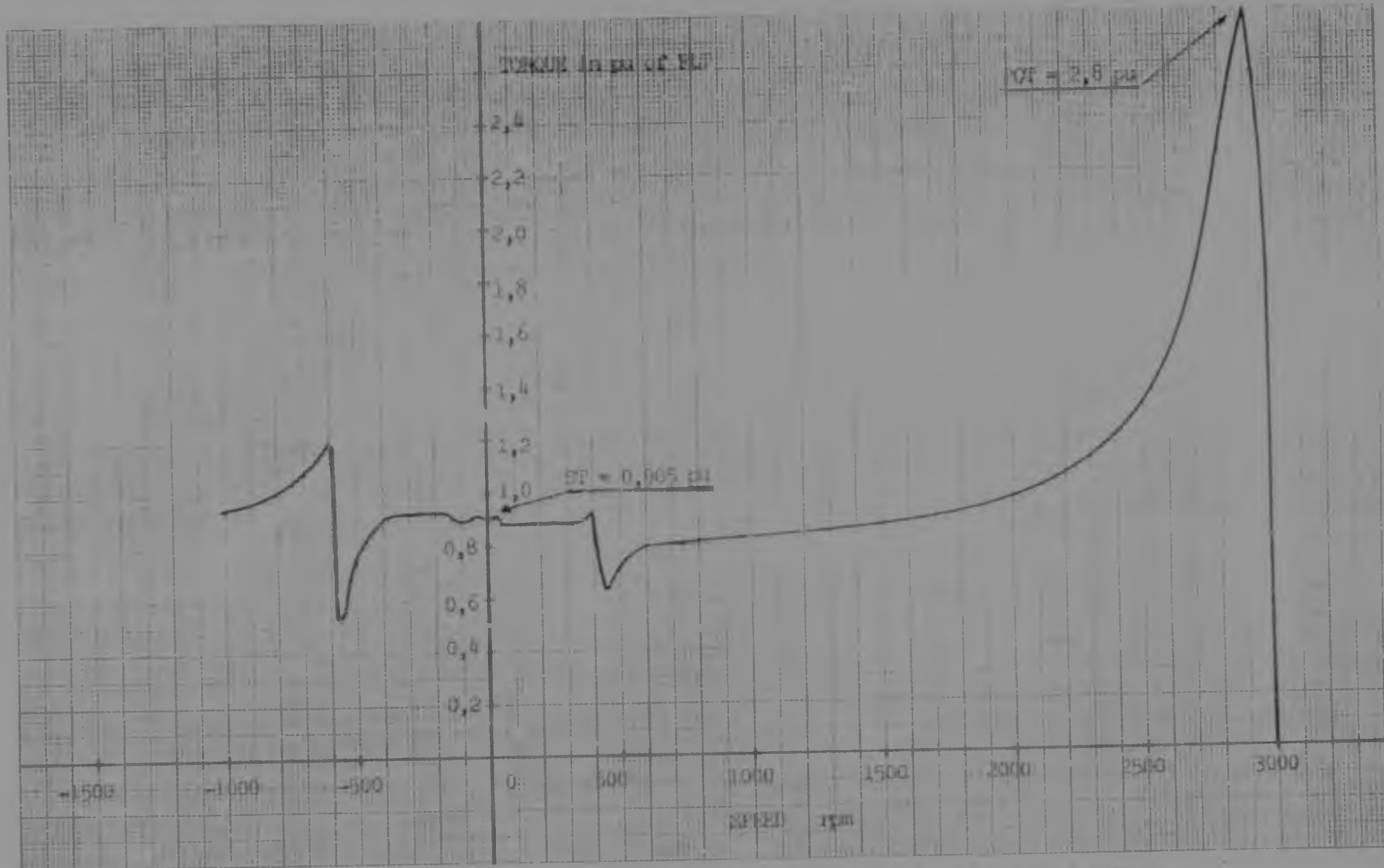

Figure D.32 - Measured torque-speed characteristic of industrial motor A referred to rated voltage.
'Normal'cage condition .

Table D.28 - Table of Harmonic Content for industrial motor A.
3-phase, 2 pole, 54 stator slots, 46 rotor slots, 18/27 pitch.
ms and mr are the stator and rotor produced space harmonics respectively.
K5 and K6 define which space harmonics will exist[20].
The dashed numbers are the stator and rotor slot harmonics.

	K6-->	-1	0	+1
K5	ms	mr = 46 K6 + ms		
-20	-59	-105	- 59	- 13
-18	-53	- 99	- 53	- 7
-16	-47	- 93	- 47	- 1
-14	-41	- 87	- 41	5
-12	-35	- 81	- 35	11
-10	-29	- 75	- 29	17
- 8	-23	- 69	- 23	23
- 6	-17	- 63	- 17	29
- 4	-11	- 57	- 11	35
- 2	- 5	- 51	- 5	41
0	1	- 45	1	47
2	7	- 39	7	53
4	13	- 33	13	59
6	19	- 27	19	65
8	25	- 21	25	71
10	31	- 15	31	77
12	37	- 9	37	83
14	43	- 3	43	89
16	49	3	49	95
18	55	9	55	101
20	61	15	61	107

The vertical axis is calibrated in per-unit of full load torque (FLT) and the horizontal axis represents the rotor speed in rpm. Both plots are for rated voltage and the friction and windage effects have been included, as per section 3.1.8.

Table D.28 is the Table of Harmonic Content of motor A. (The procedure and theory behind the construction of this table is given by Landy[20]). From the analysis of the table and the winding factors for this machine, relatively large dips in the torque-speed curve are expected due to the -5th and +7th space harmonic fields. These are evident in the measured curves.

The main features of the torque-speed characteristics for industrial motor A are that under both conditions, ie with one bar broken and with all the bars normally brazed, the starting torque is the same, but there is a reduction of approximately 26% in the pull-out-torque (POT) for the 'broken' bar condition.

D.2 - Tests on industrial motor B

D.2.1 - Measurement of impedance unbalance under locked-rotor

In this motor one rotor-bar was isolated from both endrings and it was suspected that a relatively large regional asymmetry in the field would appear in the airgap. This asymmetry became noticeable in the measurement of the input impedance taken when the rotor was locked at different angles, namely every 30 degrees.

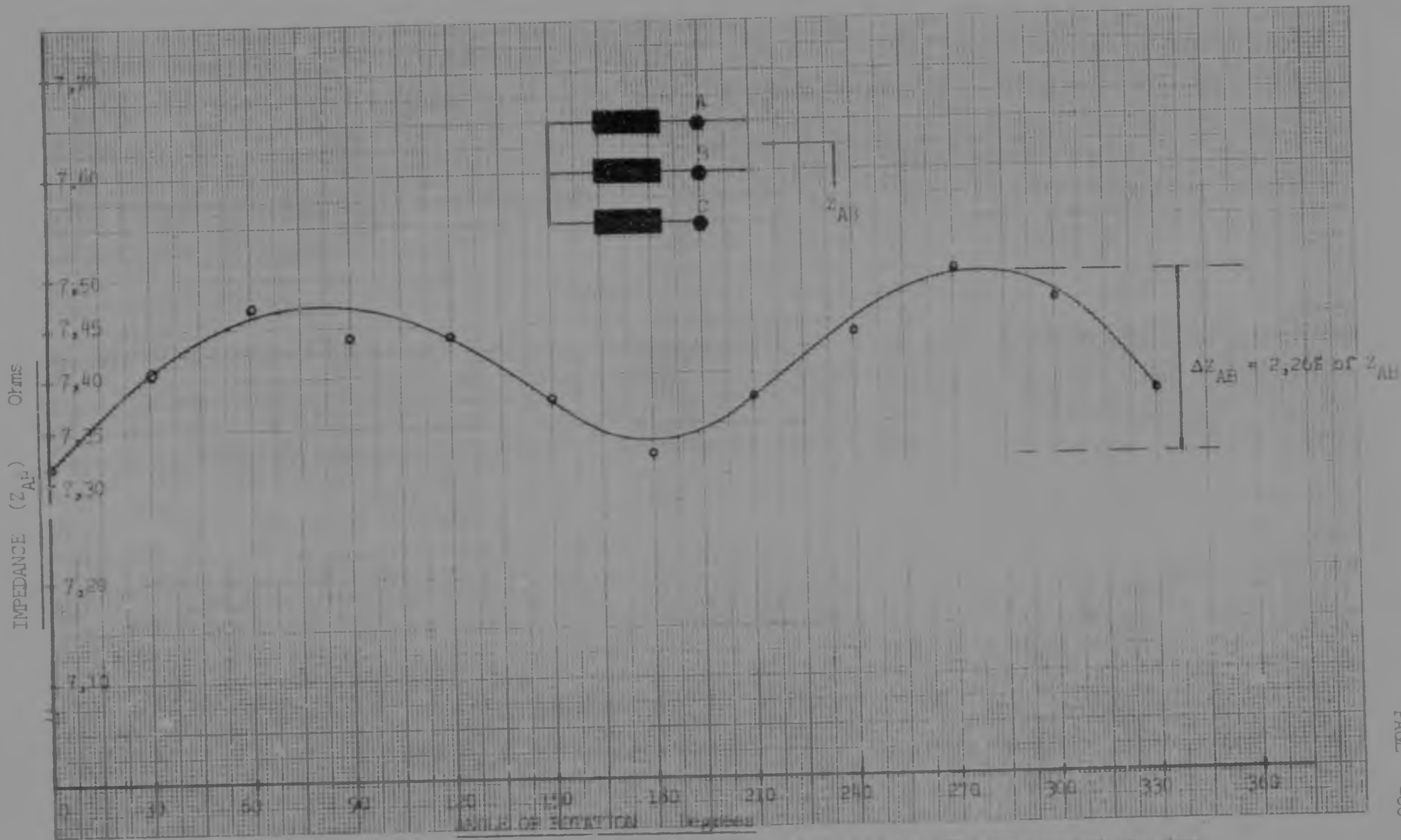

Figure D.33 - Measurement of Z_{AB} for industrial motor B having one isolated bar. The measurement was done with the rotor locked at 30 degrees intervals.

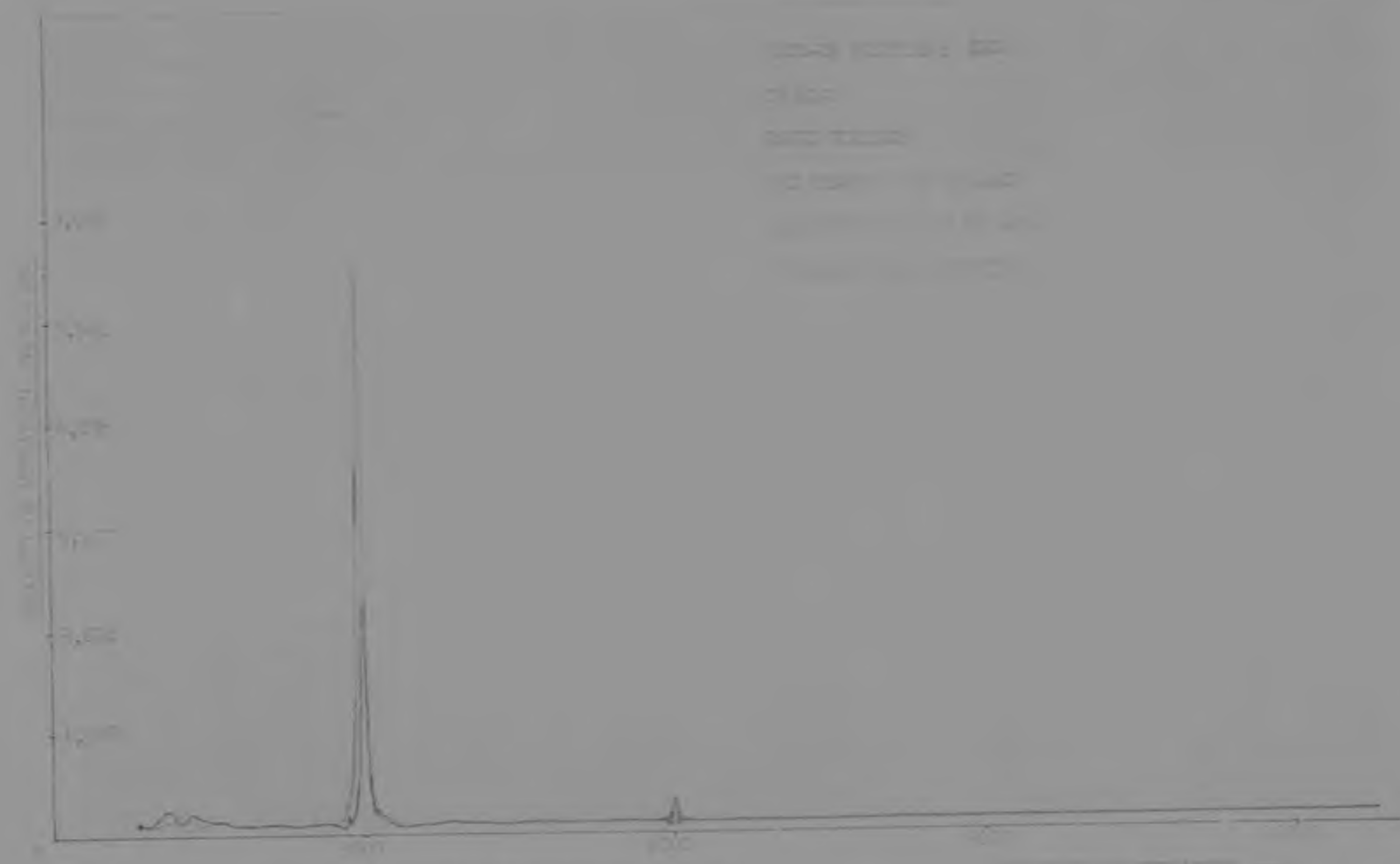

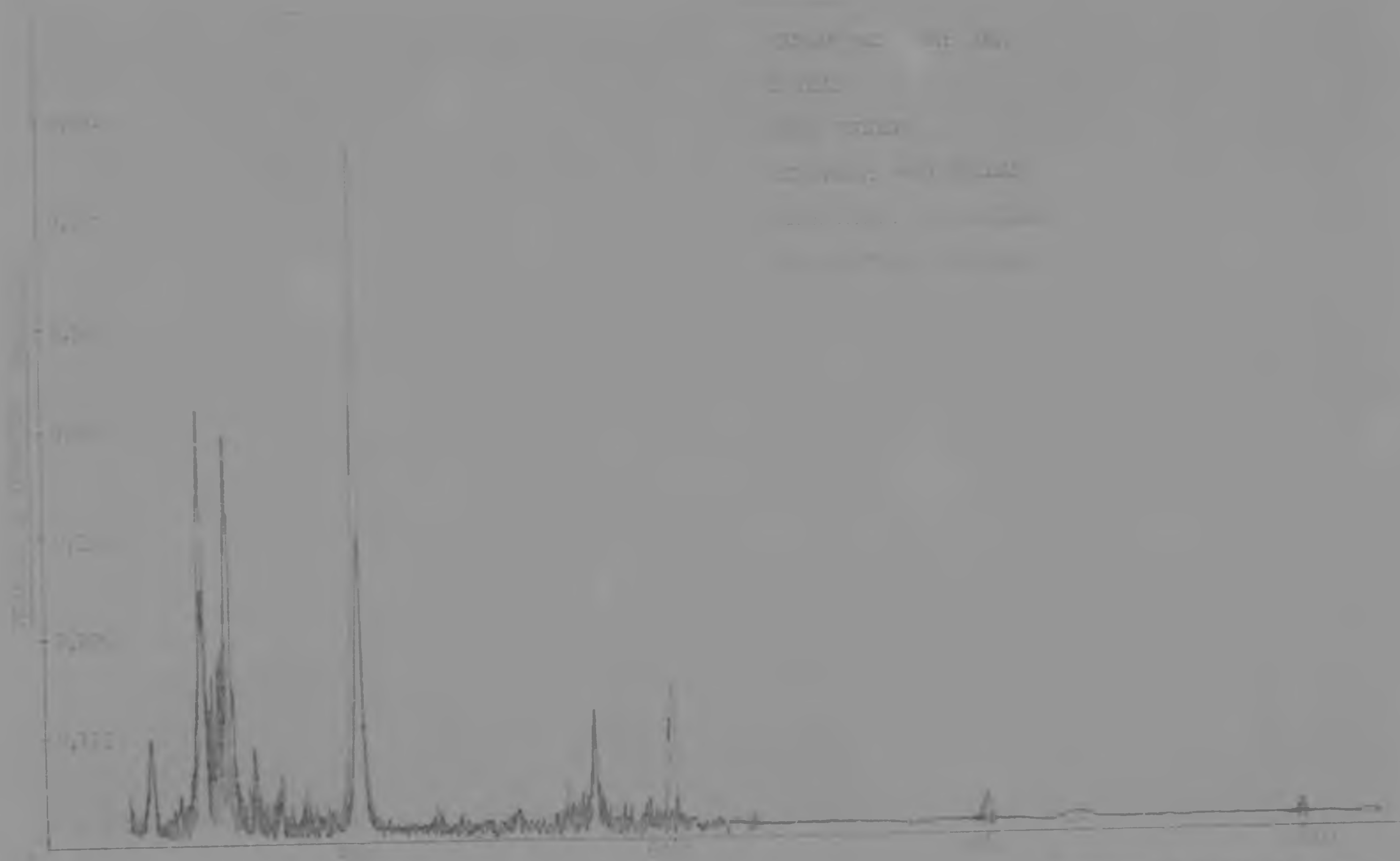

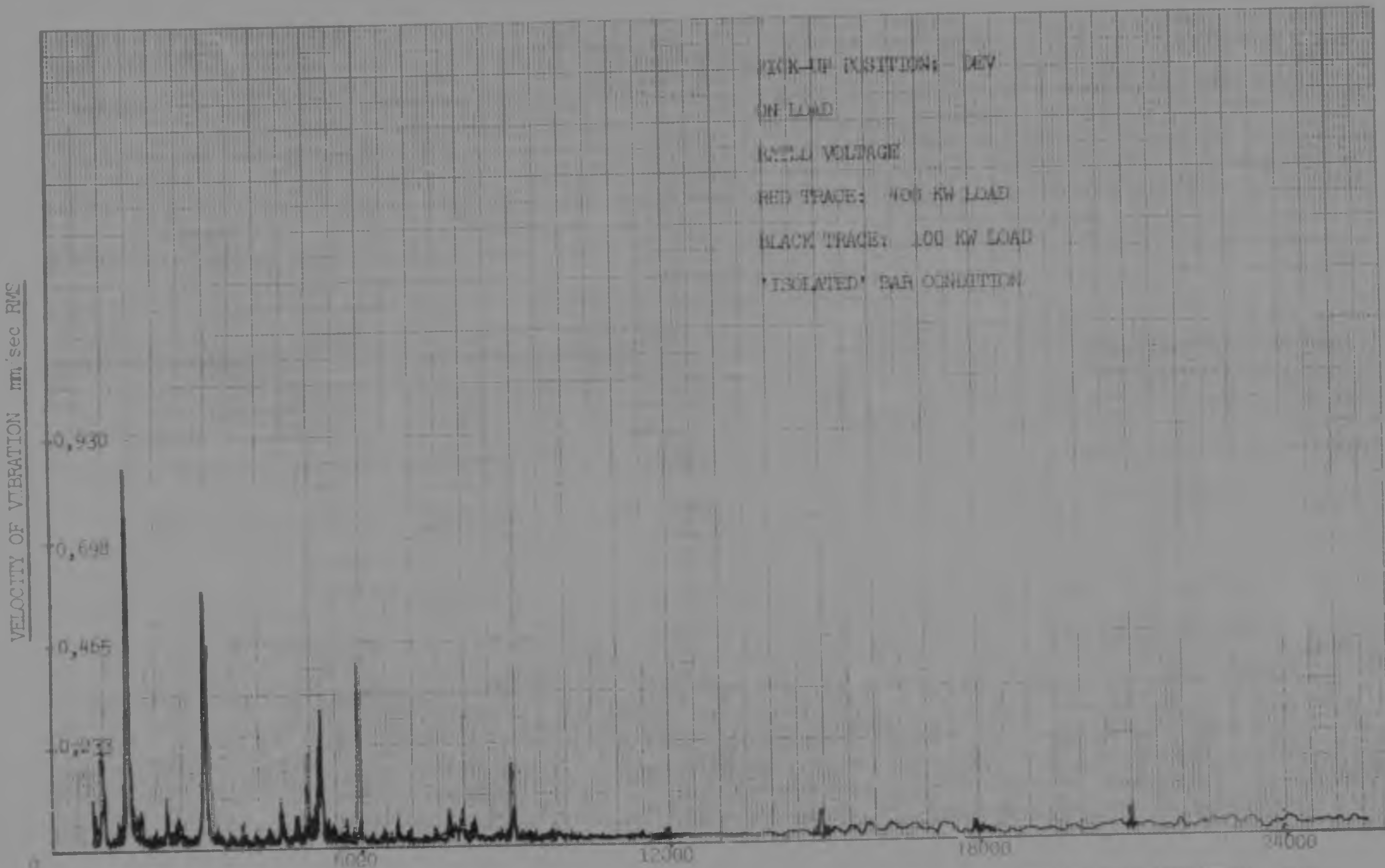

Figure D.36 - Spectrum of vibration for industrial motor B.

The machine is a two pole motor having the primary windings chorded by approximately 55% with the result that at any one time more than one stator phase is influenced by the rotor asymmetry. Hence the impedance measurements were carried out with only two phases excited. The test was carried out with the primary voltage kept constant and the rotor rotated at intervals of 30 degrees. Figure D.33 shows the plot of the impedances measured for each of the angular positions in which the rotor was locked. This shows the impedance varied by the relatively large margin of 2,2%.

D.2.2 - Measurement of vibrations on load

The positions at which the vibrations were measured are as shown in Figure 3.5 page 3.13. This motor had one rotor-bar totally electrically isolated from both endrings by actually cutting it next to each of the endrings. The mesurements were taken for two different loads, namely 100 and 400 kW. Figures D.34-D.36 show the vibration recordings, and the more important features are tabulated in tables D.29-D.31.

Table D.29 - Results of vibration test on industrial motor B having one isolated bar.
In the table the change in amplitude of vibration as a result of the increase in the motor load is shown.
Rated voltage.
Pick-up position: DEH

Approx. vibration freq.(rpm)	3000	6000	9000	12000
Change in amplitude with change in load: 100 to 400kW	2,391	1,33	-	-

Table D.30 - As for Table D.29
Pick-up position: DEA

Approx. vibration freq.(rpm)	1000	1500	1750	3000	5250	6000	9000	12000
Change in amplitude with change in load: 100 to 400kW	1,000	0,478	0,507	2.233	1,000	3,756	?	?

Table D.31 - As for Table D.29

Pick-up position: DEV

Approx. vibration freq.(rpm)	1000	1500	3000	5250
Change in amplitude with change in load: 100 to 400kW	1,667	0,360	0,740	0,630

6000	9000	12000	15000	18000	21000	24000
6,000	2,429	-	*	?	?	-

APPENDIX E

TECHNICAL DATA OF THE INDUSTRIAL AND EXPERIMENTAL MOTORS

E.1 – Industrial motor A (Figure E.1)

Figure E.1 - Photograph of industrial motor A.

General data:

Rated Voltage:	3300 Volts
Rated output:	475 kW
Number of poles:	2
Rated speed:	2978 rpm
Gross core length:	450 mm
OD of rotor:	302,8 mm
ID of rotor:	142 mm

The rotor was shrunk and keyed onto the solid shaft.

Figure E.2 - Photograph of industrial motor A showing the diamond type coils forming the primary winding.

Stator winding:

The stator winding (Figure E.2) is of the diamond type, double layer and narrow spread. It has an integral number of slots per pole per phase. The coils are short-chorded by 18/27 ie of span 1 to 19. A schematic diagram of the winding arrangement is shown in Figure E.3.

Rotor winding:

The rotor winding consists on a non-insulated squirrel cage formed by 46 "L" type copper bars of 100% conductivity housed in a single layer of 46 slots, and butt-brazed to two endrings. Figure E.4 shows the actual rotor construction.

U1,U2 } incomming leads
V1,V2 } to the two
W1,W2 } parallel circuits

SU1,SU2 } star connected
SV1,SV2 } ends
SW1,SW2 }

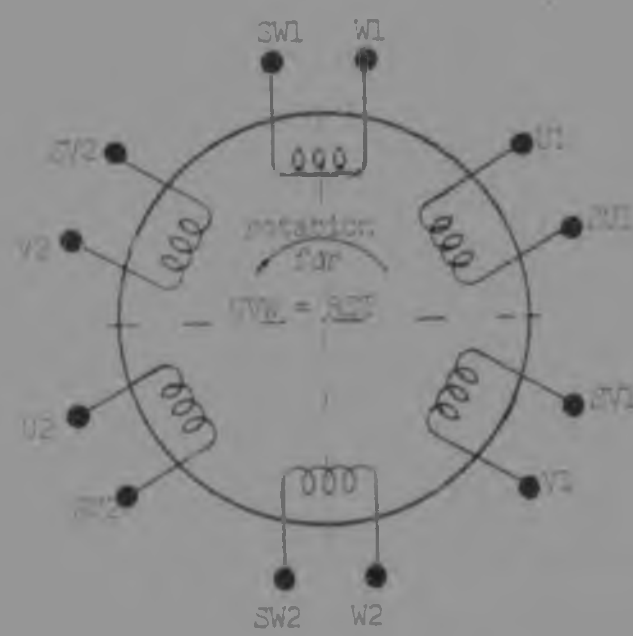

Figure E.3 - Schematic diagram of the primary winding arrangement of industrial motor A.

For this research project the cage was built with the length of the bars on the drive end side approximately eight millimeters longer than on the non-drive end side. However one bar was kept short and thus was left unbrazed from the DE side endring giving a physical clearance of a few millimeters, see Figure E.5. This produced a similar effect to that when a bar is broken adjacent to one endring (one of the more common cage faults). After the tests performed with the `broken' bar were completed, the drive-end-side endring was removed and all the bars on this side were machined back to the normal length and a new endring fitted.

Calculations were carried out with aid of a computer program to assess whether the additional 8 mm bar length affected the motor performance significantly (the `broken' bar being ignored). No noticeable effect was found.

Bearings:

The bearings are of the anti-friction type.

The NDE bearing is a "ball" type.

The DE bearing is a "roller" type.

The fact that the motor had one axial locating bearing (the "ball" type bearing) is of importance because it gave precise measurements of the axial vibrations produced in the motor. This was very suitable for this project in which the axial vibrations were important.

Figure E.4 - Cage of industrial motor A.

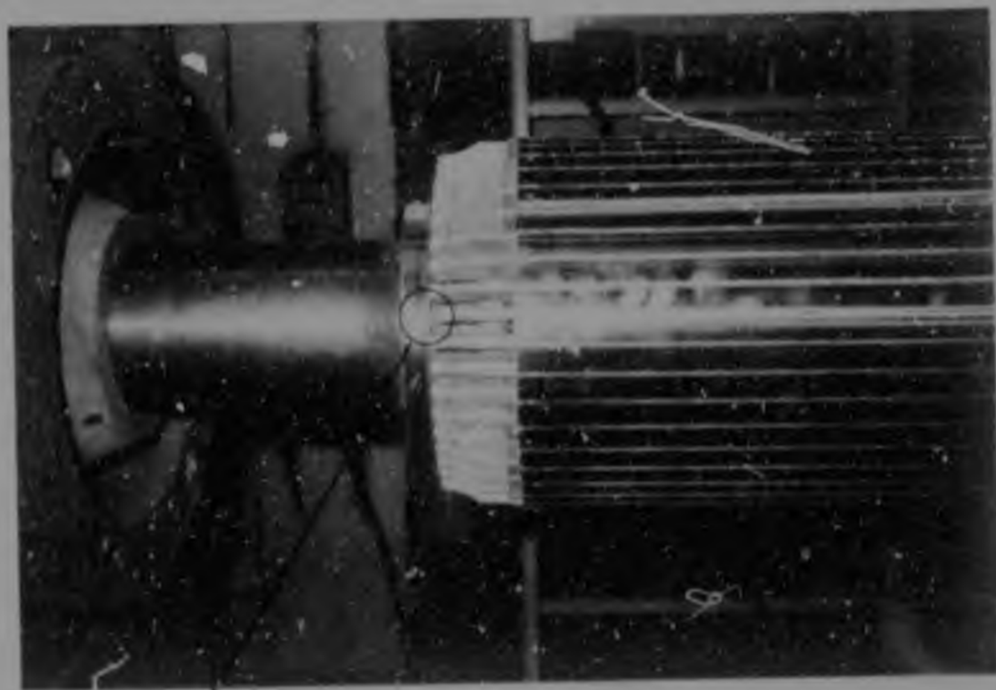

Shortened rotor-bar. No contact with endring.

Figure E.5 - View of the rotor of industrial motor A showing the 'broken' bar.

E.2 - Industrial motor B (Figure E.6)

General data:

Rated voltage:	3300 Volts
Rated output:	1257 kW
Number of poles:	2
Rated speed:	2988 rpm
Gross core length:	820 mm
OD of rotor:	442,9 mm

The rotor was shrunk and keyed onto the solid shaft.

Stator winding:

The stator winding is of the diamond type, double layer and narrow spread. It has an integral number of slots per pole per phase and has two parallel star connected sections. The coils are short chorded by 15/24.

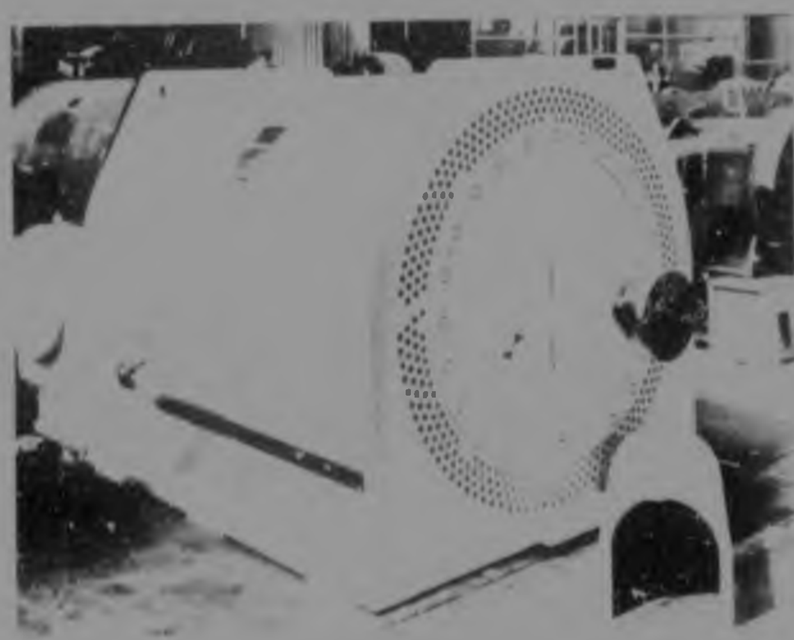

Figure E.6 - Photograph of industrial motor B.

Rotor winding:

It is a non-insulated single layer squirrel cage of 38 "T" shaped copper bars of 100% conductivity with their end butt-brazed to the two endrings. For the purposes of the present research one rotor-bar was isolated from both endrings by cutting the bar next to each of the endrings. The slot/bar clearances are similar to those of industrial motor A resulting in similar values of inter-bar impedances.

Bearings:

Both bearings are of the friction (sleeve) type without having an axial locating point.

E.3 - Inverted-geometry experimental motor

This machine, designed by Cormack[26], has a rotating primary housed in twenty four slots and is supplied via three sliprings. The squirrel cage is constructed from thirty six round copper bars and two endrings bolted onto the bars. It is housed in thirty six single layer slots on the stationary member. The stationary member housing the squirel cage is mounted on an inner frame which is itself attached to the fixed outer frame via three spring-steel plates. The relative rotation possible between the two frames allows the developed torque to be measured by means of the position transducer, see Figure E.7. The mechanical system is damped by two electromagnetic dampers. A detailed description of the machine layout as well as its operation is given by Landy[20].

The stationary member housing the squirrel cage can be easily changed. For the present research the core built and fitted into the machine had slot dimensions and lamination material similar to those used in the construction of large squirrel cage induction motors. The copper bars were choosen to have the same slot/bar clearances as in large motors. These small clearances together with the natural staggering of the laminations results in the bars having a positive interference fit, ie the bars are held very tight in the slots giving a contact resistance per unit length practically the same as in the large motors. For this project one bar was shortened by a millimeter and left unbolted from one endring giving an effect similar to that introduced into industrial motor A. Figure E.8 shows the construction of the secondary member.

The inter-bar impedance was measured by using a method similar to that described by Christofides[15] and Weppler[30]. This was done for various pairs of adjacent bars. The measurements were done for three different frequencies, viz. DC, 50 Hz and 400 Hz. The average of the results obtained gave a DC inter-bar resistance per unit of effective core length of 26,9 $\mu\Omega$ and an inter-bar inductance per unit of effective core length of 39,1 nH. It must be realised that the value of the inter-bar inductance changes with frequency; as has been explained in Appendix C. For a frequency of 400 Hz the value of L will be lower than at lower frequencies (due to the "skin" effect).

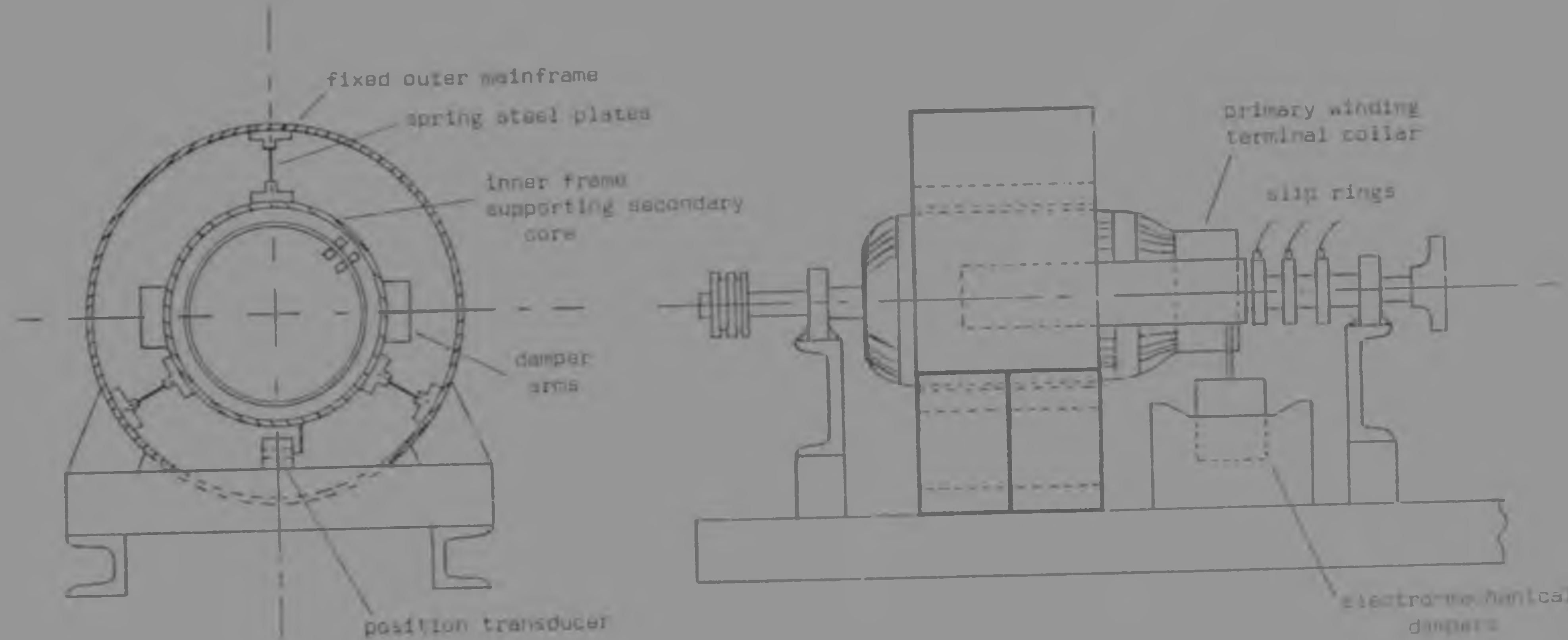

Figure E.7 Schematic diagram showing the basic construction of experimental machine

(After Landy[20])

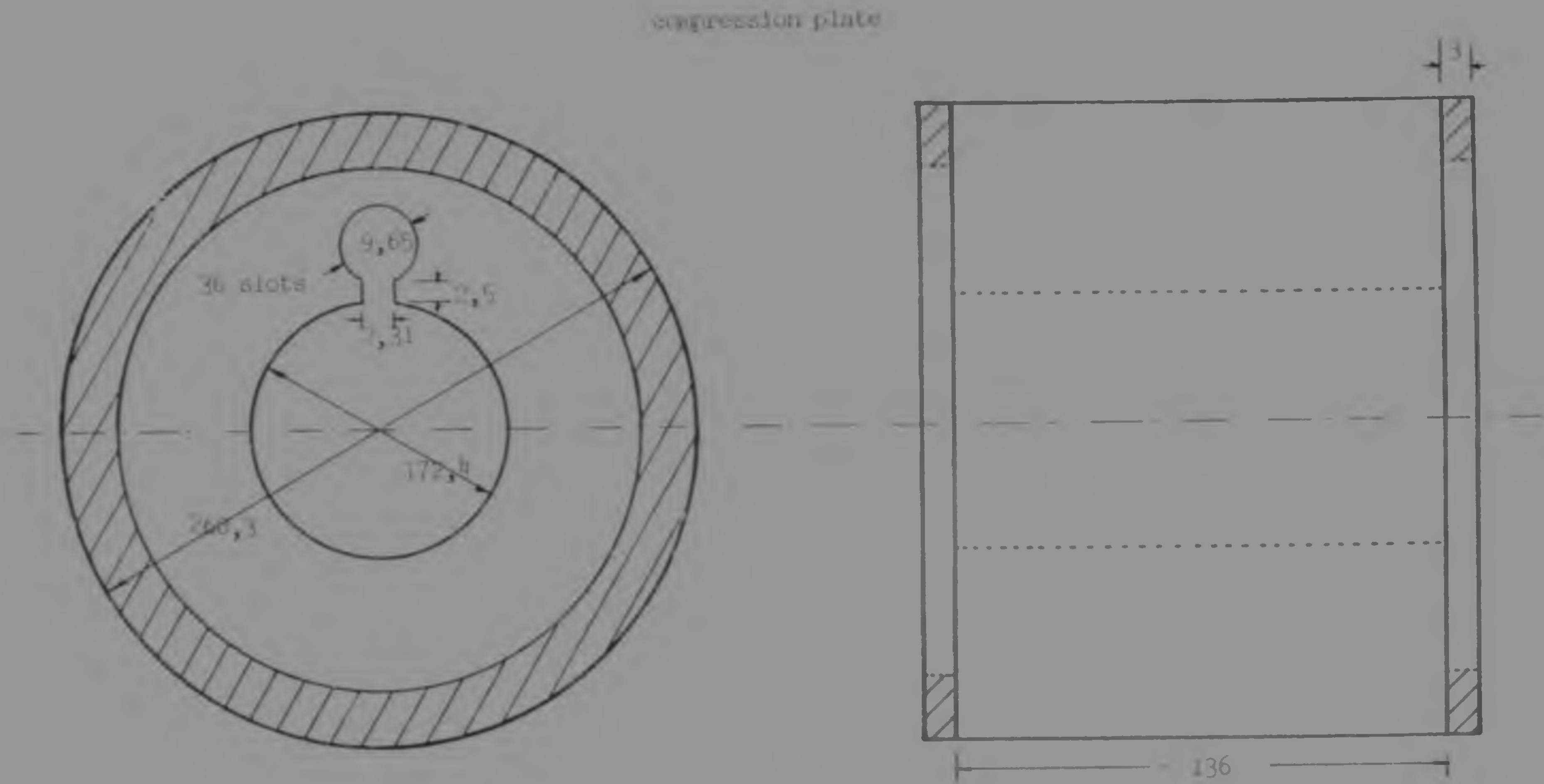

Figure E.8 - Construction of the secondary core of the experimental inverted geometry motor.

All dimensions in millimeters.

REFERENCES

1. GORGE, H.: `Uber Drehstrommotoren mit Verminderter Tourenzahl', Elektrotechnische Zeitung, 1896, 17, p. 517.

2. GABARINO, H.L., and GROSS, E.T.: `The Gorges Phenomena - Induction Motors with Unbalanced Rotor Impedances', Trans. AIEE, 1950, 69, p. 1569.

3. WEICHSEL, H.: `Squirrel Cage Motors with Split Resistance Rings', Journal of the AIEE, August 1928, pp. 606-610.

4. VAS, P.: `Performance of three-phase squirrel-cage induction motors with rotor asymmetries', Period. Polytech. Electr. Eng., 1975, 19, pp. 309-315.

5. POLOUJADOFF, M.: `General rotating mmf theory of squirrel cage induction machines with non-uniform airgaps and several non-sinusoidally distributed windings', IEEE Ind. Applics. Soc. Anual Meeting, Ohio, USA, Sep-Oct. 1980, Pt. II, pp. 1292-1304.

6. WILLIAMSON, S., and SMITH, A.: `Steady-state analysis of three-phase cage motors with rotor-bar and endring faults', Proc. IEE, 129, May 1982, pp. 93-100.

7. HARGIS, C., GAYDON, B.G., and KAMASH, K.: `The detection of rotor defects in induction motors', Conference of the Proc. of the IEE, London, July 1982, p. 216.

8. GAYDON, B.G.: `An instrument to detect induction motor rotor circuit defects by speed fluctuation measurements', Electronic Test and Measurement Instrumentation, Testamax 79 Conference Papers, 1979, pp. 5-8.

9. POZANSKI, A.: `Acoustic measurement of three-phase asynchronous motors with a broken bar in the cage rotor', Zesz. Navk. Politech. Lodz. Elektr., 1977, 60, pp. 121-131.

10. BINNS, K.J., and BARNARD, W.R.: `Some aspects of the use of Flux and Vibration Spectra in electrical machines', Conference on Applications of Time-Series Analysis, University of Southampton, Sept. 1977, pp. 17.1-17.12.

11. PENMAN, J., HADWICK, J.G., and BARKER, B.: `Detection of faults in electrical machines by examination of axially directed fluxes', Third Int. Conf. on Electr. Machines, Brussels, 1978.

12. PENMAN, J., HADWICK, J.G., and STRONACH, A.F.: `Protection strategy against the occurrence of faults in electrical machines', IEE Conf. Publ. 185, 1980, pp. 54-58.

13. STEELE, M.E., ASHEN, R.A., and KNIGHT, L.G.: 'An electrical method for condition monitoring of motors', Conf. of the Proc. of the IEE, July 1982, London.

14. VAS P., and VAS J.: `Transient and Steady-State Operation of Induction Motors', Archiv fur Elektrotechnik, 59, 1977, pp. 55-60.

15. CHRISTOFIDES, N.: `Origins of load losses in induction motors with cast aluminium rotors', Proc. IEE, Vol. 112, 12, 1965, pp. 2317-2332.

16. STRINGER, L.S.: `Unbalanced magnetic pull and shaft voltages in electromagnetic rotating machines', Enginner, April 1968, p. 631.

17. DE JONG, H.C.J.: `AC motor design - with conventional and converter supplies', Oxford University Press, 1976, p. 63, book.

18. GILTAY, J., and DE JONG, J.: `The influence of the pole number on the axial flux tendency in radial-gap rotating machines', Holectechniek, 3, 1973, pp. 24-27.

19. LANDY, C.F.: `Analysis of rotor-bar currents as a mean of evaluating torque produced in a squirrel-cage induction motor', Proc. IEE, 1977, 124, [II], p. 1078.

20. LANDY, C.F.: `An investigation of an induction motor with a view to leakage effects and developed torque', Ph.D. Thesis, University of the Witwatersrand, 1978.

21. ELLISON, D.H., EXON, J.L.T. and WARD, D.A.: `Protection of slipring induction motors', North Eastern Region, SSD of the CEGB, IEEE, 1980, p. 49.

22. STOLL, R.L.: `Method of measuring alternating currents without disturbing the conducting circuit', Proc. IEE, 1975, 122, [10], p. 1066.

23. DANNAT, C., and REDFEARN, S.W.: `A new form of rotational accelerometer', Met. Vick. Gazette, 1932, 13.

24. SAY, M.G.: `Alternating current machines', Pitman, 1978, book.

25. ALGER, P.L.: `Induction machines', Gordon and Breach, 1969, book.

26. CORMACK, W.: `The measurement of the torque slip curves of induction motors', Trans. S.African IEE, 1955, 46, [5], p. 127.

27. BARTON, T.H., and DOXEY, B.C.: `The operation of three-phase induction motors with unsymmetrical impedance in the secondary circuit', Proc. IEE, 1955, 102A, pp. 71-79.

28. ELGERD, O.: `Non-uniform torque in induction motors caused by unbalanced rotor impedances', AIEE, December 1954, p. 340.

29. VICKERS, H.: `The Induction Motor', Pitman, London, book, (p. 340).

30. WEPPLER, R.: `Influence of Inter-bar Rotor Currents on the Performance of Single-phase and Polyphase Induction Motors', Siemmens Forsch. -u. Entwickl.- Ber. Bd. 4 (1975) Nr. 2.

31. SUMMERS, E.W.: `Vibration in two-pole induction motors related to slip frequency', Trans. AIEE, 74, Part III, 1955, pp. 69-72.

32. MAXWELL, J.H.: `Diagnosing induction motor vibration', Hydrocarbon Processing, January 1981, pp. 117-120.

33. ITO, M., FUJIMOTO, N., OKUDA, H., TAKAHASHI, N., and WATAHIKI, S.: `Effect of Broken Bars on Unbalanced Magnetic Pull and Torque of Induction Motors', Electrical Engineering in Japan, Vol. 100, Nr. 1, 1980, pp. 42-49.

34. VERMA, S.P., and GIRGIS, R.S.: `Experimental verification of resonant frequencies and vibration behaviour of stators of electrical machines', (Part 1, 2, and 3), IEE Proc., Vol. 128, Nr. 1, January 1981.

35. VAS, P.: `Steady-state and transient performance of induction motors with rotor asymmetry', Trans. IEEE, Vol. PAS-101, Nr. 9, 1982, pp. 3246-3251.

36. MISHKIN, E.: `Disturbances in the induction machine due to broken sqirrel-cage rings', J.Franklin Inst., 195 , 259, pp. 133-143.

37. SCHUISKY, W.: `Induktionmaschinen', Springer-Verlag, Wien, 1957, book.

38. HILLER, U.M.: `Einfluss fehlender Lauferstabe auf die elektrischen Eigenschaften van Kurzschlusslaufer-Motoren', ETZ Arch., 1962, 83, pp. 94-97.

39. D'ALESSANDRO, U., and PAGONO, E.: `Uber asynchronmotoren mit elektrisch unsymmetrischen Kaflglaufer', ETZ Ar [illegible] 9. 90, pp. 582-586.